

1999

**Evolution of Quaternary intraplate mafic lavas detailed using helium-3 surface exposure and argon-40/argon-39 dating, and elemental and helium, strontium, neodymium and lead isotopic signatures: Potrillo volcanic field, New Mexico, United States of America and San Quintin volcanic field, Baja California Norte, Mexico**

Wendi Joan Whitehead Williams  
*University of Texas at El Paso*, [wwilliam@southtexascollege.edu](mailto:wwilliam@southtexascollege.edu)

Follow this and additional works at: [https://scholarworks.utep.edu/open\\_etd](https://scholarworks.utep.edu/open_etd)



Part of the [Geology Commons](#)

---

**Recommended Citation**

Williams, Wendi Joan Whitehead, "Evolution of Quaternary intraplate mafic lavas detailed using helium-3 surface exposure and argon-40/argon-39 dating, and elemental and helium, strontium, neodymium and lead isotopic signatures: Potrillo volcanic field, New Mexico, United States of America and San Quintin volcanic field, Baja California Norte, Mexico" (1999). *Open Access Theses & Dissertations*. 3949.  
[https://scholarworks.utep.edu/open\\_etd/3949](https://scholarworks.utep.edu/open_etd/3949)

This is brought to you for free and open access by ScholarWorks@UTEP. It has been accepted for inclusion in Open Access Theses & Dissertations by an authorized administrator of ScholarWorks@UTEP. For more information, please contact [lweber@utep.edu](mailto:lweber@utep.edu).

**EVOLUTION OF QUATERNARY INTRAPLATE MAFIC LAVAS DETAILED  
USING  $^3\text{He}$  SURFACE EXPOSURE AND  $^{40}\text{Ar}/^{39}\text{Ar}$  DATING, AND  
ELEMENTAL AND HE, SR, ND, AND PB ISOTOPIC SIGNATURES:  
POTRILLO VOLCANIC FIELD, NEW MEXICO, U.S.A., AND  
SAN QUINTÍN VOLCANIC FIELD,  
BAJA CALIFORNIA NORTE,  
MÉXICO**

by

WENDI JOAN WHITEHEAD WILLIAMS, B.Sc., M.Sc.

DISSERTATION

Presented to the Faculty of the Graduate School of  
The University of Texas at El Paso  
in Partial Fulfillment  
of the Requirements  
for the Degree of  
DOCTOR OF PHILOSOPHY

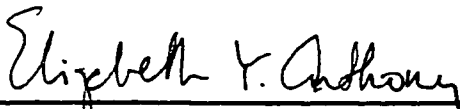
Department of Geological Sciences  
UNIVERSITY OF TEXAS AT EL PASO

May 1999

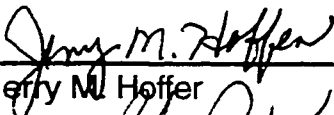
**EVOLUTION OF QUATERNARY INTRAPLATE MAFIC LAVAS DETAILED  
USING  $^3\text{He}$  SURFACE EXPOSURE AND  $^{40}\text{Ar}/^{39}\text{Ar}$  DATING, AND  
ELEMENTAL AND HE, SR, ND, AND PB ISOTOPIC SIGNATURES:  
POTRILLO VOLCANIC FIELD, NEW MEXICO, U.S.A., AND  
SAN QUINTÍN VOLCANIC FIELD,  
BAJA CALIFORNIA NORTE,  
MÉXICO**

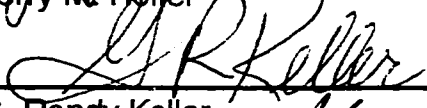
WENDI JOAN WHITEHEAD WILLIAMS  
Department of Geological Sciences


APPROVED:

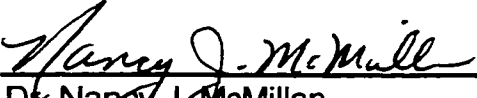
  
\_\_\_\_\_  
Dr. Elizabeth Y. Anthony, Chair

  
\_\_\_\_\_  
Dr. Kenneth F. Clark

  
\_\_\_\_\_  
Dr. Jerry M. Hoffer

  
\_\_\_\_\_  
Dr. G. Randy Keller

  
\_\_\_\_\_  
Dr. Leonard W. ter Haar, Chemistry

  
\_\_\_\_\_  
Dr. Nancy J. McMillan  
New Mexico State University

---

Associate Vice President  
for Graduate Studies

**COPYRIGHT©**  
**By Wendi J. W. Williams**  
**16 April 1999**

## DEDICATION

*Time has brought a close to this endeavor.*

*This is dedicated to those who were there for the start of this pursuit  
but not at its fruition. Each person added sense to my life.*

*Beloved Family Members*

*Graffie Jordan*

*Donald Whitehead*

*Mary Whitehead*

*Ruby Williams*

*And Champions of Student Success as well as Friends*

*John Anthony*

*Patricia Clark*



*For the youngsters who have since joined us*

*Eliza-Lee*

*Haley*

*Patricia*

*Sarah*

*Thomas*

*and have many sunrises ahead.*

## ACKNOWLEDGEMENTS

This study has benefited from many fine educators and researchers. Your time, patience and tutelage are much appreciated and have made a lasting impression upon me. Advisor Libby Anthony has generously provided of her talents and many times made the fog of complex issues dissipate. I believe that I am a better scientist for this interaction. I thank my Committee Members for interest and insight.

The  $^3\text{He}$  and  $^{40}\text{Ar}/^{39}\text{Ar}$  geochronology would not have been possible without Jane Poths and Bill McIntosh, respectively. Sr, Nd and Pb isotopic analyses were due to the efforts of Todd Housh. Paleomagnetic information was provided by Mick Whitelaw and John Geissman. Jim Luhr, Jorge Aranda-Gomez and Todd Housh made sampling the San Quintín volcanoes and the local cuisine a “cyclonic” event. Thank you. Early encouragement to pursue volcanoes to higher degrees was from John Wolff and Steve Self. Thank you for bringing things global and for your mentorship.

Financial support has been provided by a Patricia Roberts Harris Fellowship through the U.S. Department of Education, sundry teaching and research assistantships through the UTEP Department of Geological Sciences, stipends from the Association of Western Universities and the Texas Advanced Research Program, and a Herbert

Hoover Scholarship/Loan through the Women's Auxiliary of the Society of Mining Engineers (WAAIME).

There have been many friends along the way. In particular, my appreciation extends to UTEP-ers Michelle Barnes, Arturo Burgos, Rudy Machorro, Joseph Miller, Mark Ouimette, Mick and Julie Whitelaw, and Virginia Wong. Linnea Fletcher, Robert Blodgett and Cindy Carr Mathis have provided much guidance and encouragement during my most recent life between Austin and El Paso. I thank my family far and wide for their unselfish efforts and their many ways of motivation and support.

*The greatest waves of gratitude and continued love are sent to lift my husband Jeffrey and our daughter Sarah Gayle toward the moon and stars, beyond where the sky touches the horizon. You keep me afloat and alive with your ways.*

This dissertation was successfully defended on 16 April 1999.

## Part I: Potrillo Volcanic Field, New Mexico, U.S.A.

### ABSTRACT

The Pleistocene Potrillo volcanic field (PVF) resides within the southern axis of the Rio Grande Rift, New Mexico, U.S.A., near the eastern extent of the Basin and Range Province. Its alkalic mafic volcanism has resulted in several hundred cones, flows and maars distributed over approximately 4,600 km<sup>2</sup>. Alignments are segregated into two halves relative to the East Robledo fault system that dissects this field. Three of the five maars have brought peridotitic and lower to upper crustal xenoliths to the surface; several older, non maar-related flows from the west half of the field host ultramafic clots. Stratigraphic relationships, <sup>3</sup>He surface exposure dating and <sup>40</sup>Ar/<sup>39</sup>Ar methods confirm this area has been active since 1 Ma ago to as recently as 20 ka ago. The Kilbourne Hole maar was dated at 28 ka by the acquisition of exhumation ages of deposits using age differences between syn-maar and proximal non-maar deposits.

Elemental and isotopic signatures indicate source heterogeneity coupled with varying degrees of partial melting and polybaric crystal fractionation events. Melts underwent early clinopyroxene fractionation within the mantle, but then the easternmost volcanic complexes experienced a second, shallow-level olivine fractionation history. Fundamental differences existing between the east and west half of the field are further established by <sup>87</sup>Sr/<sup>86</sup>Sr (0.703087 - 0.703917), <sup>143</sup>Nd/<sup>144</sup>Nd (4.4 – 6.7 ε<sub>Nd</sub>), <sup>206</sup>Pb/<sup>204</sup>Pb (18.363 – 19.081), <sup>207</sup>Pb/<sup>204</sup>Pb (15.520 – 15.584), <sup>208</sup>Pb/<sup>204</sup>Pb (38.192 – 38.699), and



magmatic  $^3\text{He}/^4\text{He}$  (5 – 15  $R/R_a$ ) isotopic data for ten lavas. Two isotopic groups are observed: Group I is characterized by higher  $\epsilon_{\text{Nd}}$  and Pb isotopes and lower  $^{87}\text{Sr}/^{86}\text{Sr}$ . Group II melts display the opposite trends. At least three mantle reservoirs may have contributed to the melts: (1) PREMA, (2) HIMU, and (3) either EM1 or Lower Crust for Group II. The primitive (Mg # < 64) lavas have relatively high  $\text{Al}_2\text{O}_3$  and Yb associated with low La/Yb and  $\text{CaO}/\text{Al}_2\text{O}_3$ , similar to the San Quintín volcanic field in Baja California Norte, México (Luhr *et al.*, 1995). These observations are consistent with progressive partial melting of spinel lherzolite at unusually shallow mantle levels.

A complex magmatic history for the Potrillo volcanic field is now elucidated from combining improved Quaternary dating methods with detailed geochemical studies and structural information. The magma dynamics model integrates temporal, spatial and chemical evidence in light of magma emplacement and neotectonic parameters. Five phases of volcanism are recognized. The punctuated volcanic activity, presence of both monogenetic and polygenetic centers, and evidence for shifting eruption foci across 30 km lateral distances during approximately  $10^6$  year time frames are explained in terms of a crack coalescence model by Takada. Changes in magma input rates and/or differential stress fields are invoked. These findings for the Potrillo volcanic field are all causes for concern with respect to prediction of future activity trends within small mafic fields in intraplate extensional terranes.

## TABLE OF CONTENTS

Acknowledgements.....	iii
Abstract.....	v
Table of Contents.....	vii
List of Tables.....	x
List of Figures.....	xi
List of Appendices.....	xiv
<hr/>	
Part I: Potrillo Volcanic Field, New Mexico, United States of America	
Chapter 1 Introduction.....	1
Chapter 2 Geologic Setting and Previous Studies.....	5
2.1 Geologic Setting.....	5
2.2 <sup>3</sup> He Surface Exposure Dating.....	11
2.3 Geochemistry and Isotopic Signatures.....	15
Chapter 3 Analytical Methods.....	18
3.1 Geochronology.....	18
3.1.1 <sup>3</sup> He Surface Exposure Dating.....	18
3.2 Geochemical Analyses.....	21
3.2.1 Major Element Analyses Using ICP-ES.....	22
3.2.2 Trace Element Analyses Using INAA.....	22

3.2.3 Sr, Nd and Pb Isotopes.....	23
Chapter 4. Analytical Results: Geochronology.....	26
4.1 <sup>3</sup> He Surface Exposure Dating.....	26
4.2 <sup>40</sup> Ar/ <sup>39</sup> Ar Dating.....	36
4.3 Comparison of <sup>3</sup> He and <sup>40</sup> Ar/ <sup>39</sup> Ar Determinations.....	40
4.4 Dating Maar Eruptions.....	45
Chapter 5 Analytical Results: Geochemistry.....	53
5.1 Major Elements and Normative Mineralogy.....	53
5.2 Trace Element Analyses.....	63
5.2.1 Enrichment Diagrams.....	63
5.2.2 Rare Earth Element Diagrams.....	71
5.2.3 Incompatible Elements: H versus H.....	74
5.2.4 Incompatible Elements: H/M versus H.....	84
5.3 Relationship of Major and Trace Elements.....	91
5.4 Isotopes.....	97
5.4.1 Global Reservoirs.....	99
5.4.2 Potrillo Volcanic Field.....	105
5.5 Correlation of Isotopes and Elemental Data.....	114
Chapter 6 Discussion and Conclusions.....	120

6.1 Physical, Spatial and Temporal Evolution.....	120
6.2 Elemental and Isotopic Geochemical Evolution.....	127
6.3 Integrated Magma Dynamics Model.....	135
References.....	142
Appendices.....	152
<hr/>	
Part II: San Quintín Volcanic Field, Baja California Norte, México	
Abstract.....	176
Introduction.....	178
Analytical Mehtods and Results.....	180
Discussion.....	184
Conclusions.....	189
Acknowledgments.....	190
References.....	191
<hr/>	
Curriculum Vitae.....	194

## LIST OF TABLES

### Part I: Potrillo Volcanic Field, New Mexico, U.S.A.

Table 1. $^3\text{He}$ Surface Exposure Dating Summary.....	27
Table 2. $^{40}\text{Ar}/^{39}\text{Ar}$ Dating Summary.....	37
Table 3. $^3\text{He}$ and $^{40}\text{Ar}/^{39}\text{Ar}$ Corresponding Samples.....	41
Table 4. Major Element Analyses and Normative Mineralogy.....	54
Table 5. High Silica and Low Silica Group Members.....	60
Table 6. Trace Element Analyses.....	64
Table 7. Strontium, Neodymium and Lead Isotope Analyses.....	98
Table 8. Isotopic Group I and Group II Attributes.....	133

### Part II: San Quintín Volcanic Field, Baja California Norte, México

Table 1. Noble Gases for $^3\text{He}$ Dates.....	183
Table 2. Sample Descriptions and $^{40}\text{Ar}/^{39}\text{Ar}$ Information.....	186

## LIST OF FIGURES

### Part I: Potrillo Volcanic Field, New Mexico, U.S. A.

Figure 1.	Regional Map .....	2
Figure 2	Satellite Image of Potrillo Volcanic Field.....	6
Figure 3	Simplified Geologic Map of Vicinity.....	7
Figure 4	Local Volcanic Complex Map with Alignment Designations.....	10
Figure 5a.	<sup>3</sup> He Concentration Versus Date Build-Up.....	13
Figure 5b.	Erosion Effects on <sup>3</sup> He Build-Up.....	13
Figure 6.	Map with <sup>3</sup> He Dates and Generalized Sample Locations.....	30
Figure 7.	Map with <sup>40</sup> Ar/ <sup>39</sup> Ar Dates and Generalized Sample Locations..	39
Figure 8.	<sup>3</sup> He and <sup>40</sup> Ar/ <sup>39</sup> Ar Dates Comparison .....	42
Figure 9a.	Dating Central Maars: Kilbourne and Hunt's Holes .....	47
Figure 9b.	Dating Western Maars: Riley, Malpais, and Potrillo.....	47
Figure 10a.	Total Alkalis Versus Silica.....	58
Figure 10b.	Normative Nepheline Versus Normative Anorthite .....	58
Figure 10c.	Mg # Versus SiO <sub>2</sub> .....	58
Figure 10d.	Normative Nepheline versus Mg # with Fo (10 kbars).....	58
Figure 11.	Enrichment Diagrams.....	68
Figure 12.	Phenocryst Modal Percentages.....	70
Figure 13.	Rare Earth Element Diagrams.....	72
Figure 14.	C <sub>02</sub> Versus C <sub>01</sub> : Source(s).....	77
Figure 15.	C <sub>02</sub> Versus C <sub>01</sub> : Magmatic Processes.....	77
Figure 16.	Cerium Versus Lanthanum.....	78
Figure 17.	Tantalum Versus Niobium.....	78
Figure 18.	Niobium Versus Zirconium.....	79
Figure 19.	Cerium Versus Thorium.....	79
Figure 20.	Lanthanum Versus Thorium.....	80

Figure 21.	Samarium Versus Lanthanum.....	80
Figure 22.	Hafnium Versus Zirconium.....	81
Figure 23.	Tantalum Versus Zirconium.....	81
Figure 24.	Rubidium Versus Lanthanum.....	82
Figure 25.	Barium Versus Strontium.....	82
Figure 26.	Theory behind Partition Coefficients.....	83
Figure 27.	H/M Versus H: Magmatic Process Identification.....	85
Figure 28.	La/Sm Versus La.....	87
Figure 29.	Ce/Yb Versus Ce.....	87
Figure 30.	La/Yb Versus La.....	88
Figure 31.	Nb/Yb Versus Nb.....	88
Figure 32.	Sr/Yb Versus Sr.....	89
Figure 33.	Ta/Yb Versus Ta.....	89
Figure 34.	Th/Yb Versus Th.....	90
Figure 35.	Zr/Yb Versus Zr.....	90
Figure 36a.	Mg # versus Sr.....	92
Figure 36b.	Mg # versus Sc.....	92
Figure 37.	Thorium versus CaO, Al <sub>2</sub> O <sub>3</sub> and CaO/ Al <sub>2</sub> O <sub>3</sub> .....	94
Figure 38.	Mg # versus Nickel and K <sub>2</sub> O.....	96
Figure 39.	SiO <sub>2</sub> (wt %) versus Rubidium and La/Sm.....	96
Figure 40a.	Global Reservoirs: $\epsilon_{Nd}$ Versus $^{87}Sr/^{86}Sr$ .....	101
Figure 40b.	Global Reservoirs: $\epsilon_{Nd}$ Versus $^{206}Pb/^{204}Pb$ .....	101
Figure 40c.	Global Reservoirs: $^{207}Pb/^{204}Pb$ Versus $^{206}Pb/^{204}Pb$ .....	101
Figure 41.	PVF and Crustal Xenoliths: $^{87}Sr/^{86}Sr$ Versus $^{206}Pb/^{204}Pb$ .....	103
Figure 42.	PVF and Crustal Xenoliths: $^{208}Pb/^{204}Pb$ Versus $^{206}Pb/^{204}Pb$ ...	104
Figure 43a.	Global Reservoirs: $^3He/^4He$ (R/R <sub>a</sub> ) Versus $\epsilon_{Nd}$ .....	106
Figure 43b.	Global Reservoirs: $^3He/^4He$ (R/R <sub>a</sub> ) Versus $^{87}Sr/^{86}Sr$ .....	106

Figure 43c .	Global Reservoirs: $^3\text{He}/^4\text{He}$ (R/R <sub>a</sub> ) Versus $^{206}\text{Pb}/^{204}\text{Pb}$ .....	106
Figure 44 .	$\epsilon_{\text{Nd}}$ , $^{87}\text{Sr}/^{86}\text{Sr}$ , $^{207}\text{Pb}/^{204}\text{Pb}$ , $^{206}\text{Pb}/^{204}\text{Pb}$ Versus $^{206}\text{Pb}/^{204}\text{Pb}$ ....	108
Figure 45.	$\epsilon_{\text{Nd}}$ Versus $^{87}\text{Sr}/^{86}\text{Sr}$ and $^{207}\text{Pb}/^{204}\text{Pb}$ .....	109
Figure 46a.	$^3\text{He}/^4\text{He}$ (R/R <sub>a</sub> ) Versus $^{87}\text{Sr}/^{86}\text{Sr}$ .....	110
Figure 46b.	$^3\text{He}/^4\text{He}$ (R/R <sub>a</sub> ) Versus $^{207}\text{Pb}/^{204}\text{Pb}$ .....	110
Figure 46c.	$^3\text{He}/^4\text{He}$ (R/R <sub>a</sub> ) - $\epsilon_{\text{Nd}}$ Pairing.....	111
Figure 46d,	$^3\text{He}/^4\text{He}$ (R/R <sub>a</sub> ) Versus $^{206}\text{Pb}/^{204}\text{Pb}$ .....	112
Figure 46e.	$^3\text{He}/^4\text{He}$ (R/R <sub>a</sub> ) Versus $^{208}\text{Pb}/^{204}\text{Pb}$ .....	112
Figure 47.	Mg # Versus $^{87}\text{Sr}/^{86}\text{Sr}$ and $^{206}\text{Pb}/^{204}\text{Pb}$ .....	115
Figure 48.	La/Sm Versus $\epsilon_{\text{Nd}}$ , $^{87}\text{Sr}/^{86}\text{Sr}$ and $^{206}\text{Pb}/^{204}\text{Pb}$ .....	117
Figure 49.	La/Sm Versus $^3\text{He}/^4\text{He}$ (R/R <sub>a</sub> ).....	118
Figure 50.	Evolution of the PVF: Spatial, Temporal, and Paleomagnetic Signatures.....	122
Figure 51.	Volcanic Phases and Episodicity in East Half .....	125
Figure 52.	Volcanic Phases and Part of Field on La Versus La/Sm.....	129
Figure 53.	Volcanic Phases and Part of Field on Sr Versus Sc.....	129
Figure 54.	Yb Versus La/Yb for Primitive Samples.....	131
Figure 55.	Elemental and Isotopic Evolution with Time.....	134
Figure 56.	Mechanism of Emplacement:  Takada's Crack Coalescence Model.....	136
Figure 57.	Integrated Magma Dynamics Model.....	141
<hr/>		
Part II: San Quintín Volcanic Field, Baja California Norte, México		
Figure 1.	Regional and Local Map for SQVF.....	181
Figure 2.	Distribution of $^3\text{He}$ Dates Suggests Episodicity.....	185



## APPENDIX

### Part I: Potrillo Volcanic Field, New Mexico, U.S.A.

Table A.	<sup>3</sup> Helium Surface Exposure Dating.....	152
Table B.	Comprehensive Major Element Analyses and Normative Mineralogy.....	154
Table C.	Comprehensive Major Element Analyses by Various Methods.....	160
Table D.	Comprehensive Trace Element Analyses.....	166
Table E.	Comprehensive Sr, Nd and Pb Isotopic Data.....	175

## **Part I: Potrillo Volcanic Field, Rio Grande Rift, New Mexico, U.S.A.**

### **Chapter 1**

#### **INTRODUCTION**

Part I of this dissertation study focuses on the Potrillo volcanic field (PVF). This Quaternary mafic volcanic field is situated in the southern portion of the Rio Grande rift (RGR) and is thus close to the eastern extent of the Basin and Range Province within the United States (Figure 1). Although small volume, the field contains over 200 centers. These centers present a diversity of eruption styles: fissure-fed flows to coalesced platforms, scoria cones with and without breach flows, a shield volcano, spatter ramparts, and maars with varying combinations of pre-, syn-, and post-maar deposits. Several maars have brought peridotitic and lower to upper crustal xenoliths to the surface, and several older, non maar-related flows host ultramafic clots.

Qualitative assessment of geomorphic surfaces suggests episodic volcanism with activity perhaps as recent as the late Pleistocene. Previous geochronologic and isotopic studies of the Potrillo volcanic field have been dominantly reconnaissance-style. In contrast, a substantially greater major and trace element data set is available for the eastern half of this field (summarized in Chapter 2). Recent advances in Quaternary dating methods allow for a more detailed quantitative understanding of eruption timing than was possible with

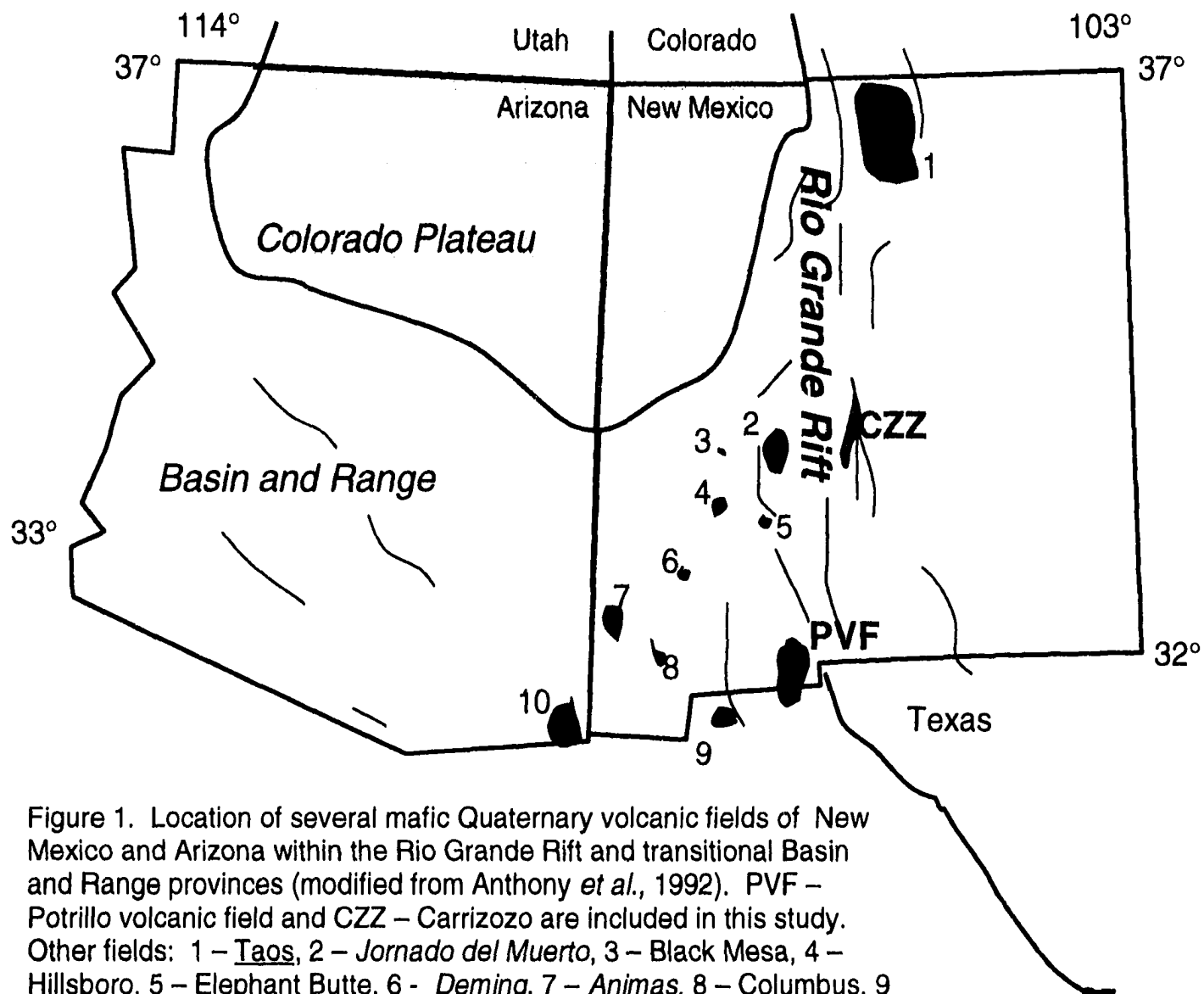


Figure 1. Location of several mafic Quaternary volcanic fields of New Mexico and Arizona within the Rio Grande Rift and transitional Basin and Range provinces (modified from Anthony *et al.*, 1992). PVF – Potrillo volcanic field and CZZ – Carrizozo are included in this study. Other fields: 1 – Taos, 2 – *Jornado del Muerto*, 3 – Black Mesa, 4 – Hillsboro, 5 – Elephant Butte, 6 – *Deming*, 7 – *Animas*, 8 – Columbus, 9 – Palomas, and 10 – Geronimo. Underline indicates both alkaline and subalkaline group. Italics indicate *subalkaline* group.

more traditional radiometric methods, such as K/Ar. This refined dating, in turn, provides a framework for an enhanced petrological understanding utilizing new and previously acquired geochemical and isotopic data.

My intent in Part I, therefore, is threefold:

- To better determine the timing and distribution of volcanic events forming the Potrillo volcanic field.
- To contribute additional insight concerning the geochemical and isotopic signatures of the melts representing the entire eruption history.
- To propose a comprehensive magmatic evolution model.

$^3\text{He}$  surface exposure dating was used with  $^{40}\text{Ar}/^{39}\text{Ar}$  determinations on samples collected based on previously mapped stratigraphic relationships in order to explore temporal and spatial relationships. A more robust understanding of eruption timing has resulted from the blending of these three methods. This study also addresses the application of cosmogenic helium to the dating of maar events. This was accomplished through the acquisition of exhumation ages of maar-related deposits by using differences between those determinations and ages for proximal non maar-related deposits; further explanation is presented in Section 4.4.

Major element, trace element and isotopic data have been acquired in order to achieve the second goal concerning insight to chemical evolution. The new major

and trace element data are for the western alignment and four maars. This information is integrated with data obtained by Chen (1991) for lavas from the central and eastern parts of the field. The new isotopic data comprise  $^{87}\text{Sr}/^{86}\text{Sr}$ ,  $^{143}\text{Nd}/^{144}\text{Nd}$ ,  $^{206}\text{Pb}/^{204}\text{Pb}$ ,  $^{207}\text{Pb}/^{204}\text{Pb}$ ,  $^{208}\text{Pb}/^{204}\text{Pb}$ , and *magmatic*  $^3\text{He}/^4\text{He}$  for ten lavas from the central and western alignments. Collectively, this breadth of additional data permits a more thorough characterization of source reservoir signatures recorded by the melts. Finally, the third objective is to propose a magma dynamics model specific to the Potrillo volcanic field. This is resolved using the temporal, spatial and chemical evidence in light of magma emplacement and neotectonic parameters.

## Chapter 2

### GEOLOGIC SETTING AND PREVIOUS STUDIES

#### 2.1 Geologic Setting

The study area lies near the juncture of the Basin and Range province and the Rio Grande rift and is within the axial portion of the rift proper (Figure 1). The Rio Grande rift is a tectonically active structure (Seager and Morgon, 1979), as indicated by high heat flow, youthful volcanism, and deep normal fault-bounded basins. It has evolved during two stages. The initial phase was from 36 Ma to 15 Ma ago and is responsible for approximately thirty to fifty percent extension. Associated volcanism included basaltic andesites, andesites and silicic ash flow tuffs. The second phase initiated 10 Ma ago and continues to the present, thus far resulting in about ten percent extension (Keller et al., 1990). Mafic volcanism is associated with the current stage.

The Potrillo volcanic field is an example of volcanism associated with the second stage of the Rio Grande rift extension. A false-color satellite image of the area is presented in Figure 2. The generalized geology of this field is provided in Figure 3 and is based on studies by Hoffer (1976), Mack and Seager (1995), Salyards (1991), and my own observations. There are six units in the area, with the



Figure 2. False-color satellite image (R:4, G:3, B:2; 23 July 1994) of the Potrillo volcanic field. Courtesy of the Pan-American Center for Earth and Environmental Studies (PACES) Program at the University of Texas at El Paso (<http://paces.geo.utep.edu/> ).

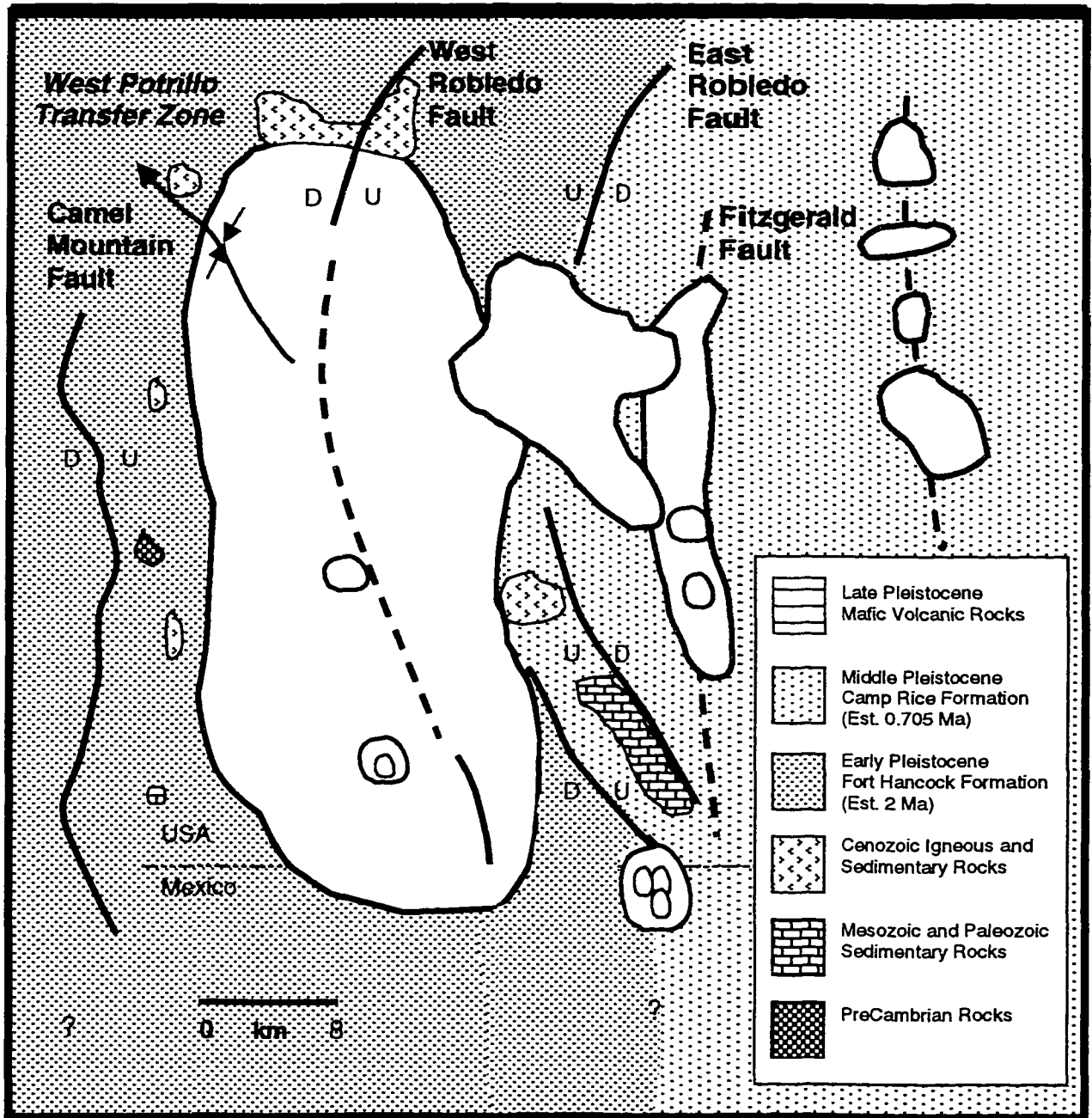


Figure 3. Simplified geology local to the Potrillo volcanic field. Fault information, stratigraphic units, and ages from Hoffer (1976), Salyards (1991), and Mack and Seager (1995).



three oldest being exposed by normal faulting. From oldest to youngest, the units are:

- Undifferentiated Precambrian rocks (Mack and Seager, 1995).
- Mesozoic (clastic) and Paleozoic (dominantly carbonate) sedimentary rocks.
- Cenozoic igneous (volcanic and plutonic) and clastic sedimentary units.
- The early Pleistocene Fort Hancock Formation. This unit is estimated to be 2 Ma old (Salyards, 1991) and forms the flat “La Mesa” surface west of the East Robledo fault.
- The middle Pleistocene Camp Rice Formation which forms the “La Mesa” surface east of the East Robledo fault. Gile *et al.* (1981) document tuff within this formation and correlate it to the Peach Springs eruption occurring 700 ka ago.
- The late Pleistocene alkaline mafic volcanic rocks of the Potrillo volcanic field.

The fault-bounded grabens have a north-south orientation, which is typical of the Rio Grande rift and many areas of the Basin and Range province. Mack and Seager (1995) evaluated several zones within the Rio Grande rift as representing “transfer zones,” designating the southernmost as the “West Potrillo transfer zone.” They suggest that the western part of the Potrillo volcanic field lies within a northwest-plunging syncline and that fractures trending northeast may control vent alignments within the West Potrillo Mountains area.

There are a number of normal faults in the study area, with the dominant one being the Robledo fault system. This system consists of two main features: (1) the West Robledo fault, which underlies the West Potrillo Mountains, and (2) the East Robledo fault. The East Robledo fault traverses beneath some of the central eruption complexes, then separates into two splays at its southern extent. One splay is the boundary fault for the eastern Potrillo Mountains (a block of Paleozoic units) and the other splay dissects Quaternary volcanic deposits associated with Potrillo Maar. Mack *et al.* (1991) estimated the slip rate for the Robledo fault as 0.01 mm/yr. Other inferred faults in the area include the Fitzgerald fault, which is potentially a structural control for the central volcanic alignment, and an unnamed fault inferred to connect the easternmost volcanic centers (Hoffer, 1976).

For this study, the Potrillo volcanic field is subdivided into three geographic areas (Figure 4): the eastern, central and western alignments. This subdivision is based on the essentially north – south distribution of volcanic centers, which is particularly delineated by units east of the East Robledo fault. Traversing from north to south, the eastern alignment includes Santo Tomas (SM), San Miguel (SM), Little Black Mountain (LBM), and Black Mountain (BM). This eastern alignment is dominantly scoria cones with and without breach flows with pahoehoe surfaces. Paleodrainage trends are obvious, with flows terminating in the direction of the modern Rio Grande valley.

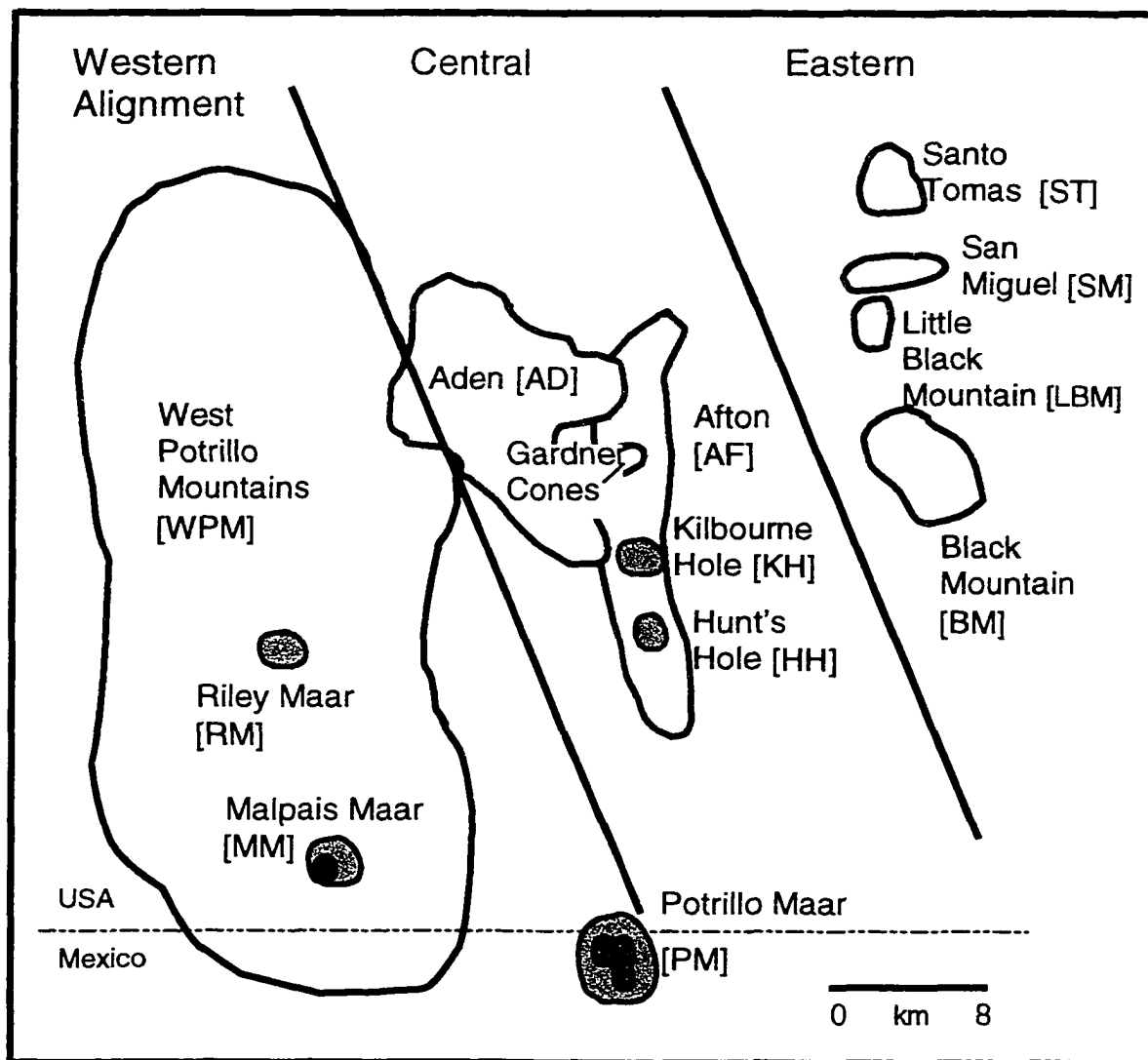


Figure 4. Potrillo volcanic field units, divided into “geographic” labels: western, central and eastern alignments. Dark lines indicate boundaries and are not faults. Abbreviations used throughout this document are included in brackets next to the name of each studied volcanic center.

The central alignment includes Aden (AD), Afton (AF), the Gardner cones, and the two maars Kilbourne Hole (KH) and Hunt's Hole (HH). The two maars erupted through portions of the pre-existing Afton series. The Afton flows may be a fissure-emplaced series upon which the Gardner cones were built. Aden is a shield volcano with a parasitic spatter rampart and well-preserved lava lake. It is also the site of numerous tube-fed lavas with explosion features (Hoffer, 1976). The western alignment comprises the West Potrillo Mountains, a cavalcade of several hundred coalescing cones and flows built upon an older, thick platform resulting from possibly fissure-fed stacked flows. Also within the western sector are several maars: Riley (RM), Malpais (MM) and Potrillo (PM). Potrillo maar is included with the western alignment due to its position west of the East Robledo fault (Figure 3).

## 2.2 $^3\text{He}$ Surface Exposure Dating

Most radiometric dating techniques are inappropriate for application to recent volcanic events since they use isotopes with long half-lives. K/Ar dating, for example, has yielded ages too old to fit the geomorphology in several late Quaternary mafic volcanic fields; fortunately, this problem becomes less significant for volcanic suites older than 1 Ma (Harland *et al.*, 1990). The  $^{40}\text{Ar}/^{39}\text{Ar}$  method is potentially more accurate than conventional K/Ar dates for young mafic systems.  $^{14}\text{C}$  is a radioisotope with a short half-life and is useful in dating material deposited up to 45,000 years ago; for example, the dating of plants carbonized by the heat from an overriding lava flow can yield an eruption age. Chronometers such as

surface exposure dating (which uses the build-up of cosmogenic nuclides), thermoluminescence and U-series disequilibria are alternative dating methods that attempt to close the gap between 1 Ma and 45 ka (Anthony, 1993).

Surface exposure dating is made possible by recent improvements in mass spectrometry (including the development of accelerator mass spectrometry). The more refined equipment provides a way to measure the radionuclides produced by cosmic ray reactions within rocks exposed at the earth's surface (Lal, 1987, 1988). Surface exposure techniques rely on the fact that the concentration of cosmogenic isotopes is a function of the amount of time that the material has been exposed to cosmic rays. Cosmic ray bombardment of rock surfaces results in nuclear reactions forming cosmogenic nuclides that are evenly distributed in a crystal. A spallation reaction yields cosmogenic  $^3\text{He}$  (Figure 5a, inset), which builds up in concentration with continued cosmic ray bombardment. Therefore the abundance of such isotopes is proportional to the age of the surface, as has been demonstrated by Kurz (1986b), Cerling (1990) and Lal (1991).

*In situ* lava surfaces must have been continually exposed in order for the exposure age to be equivalent to eruption age. Shielding by subsequent deposition or removal of material by erosion, for instance, can result in an underestimation of age (Figure 5b). To illustrate this point, consider a lava flow that erupted 100 ka ago and has undergone erosion at a rate of 1.0 cm/ka since cooling. The sampled

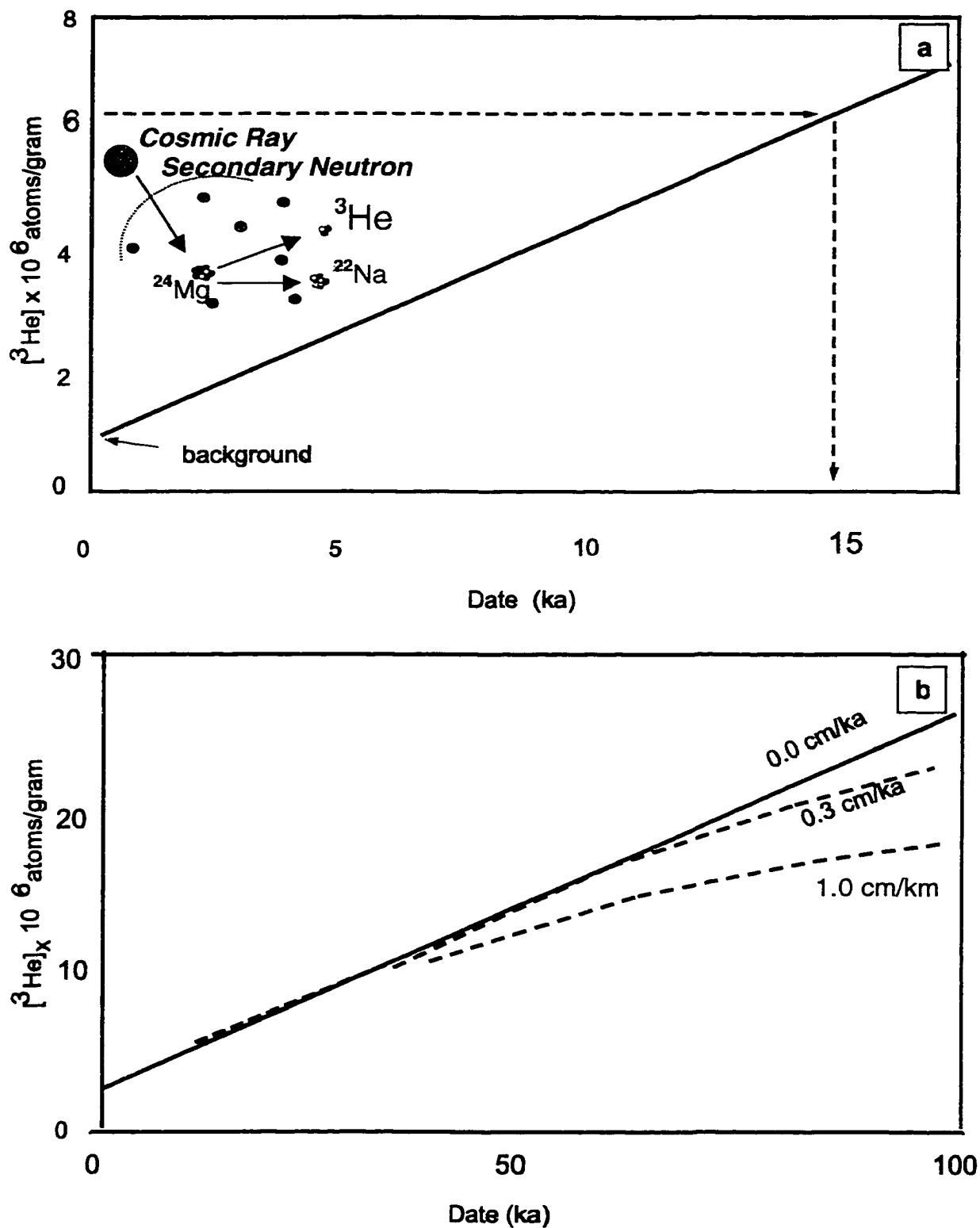


Figure 5. Accumulation of cosmogenic  $^3\text{He}$  with time and erosion effects. (a) A cosmic secondary neutron bombardment creates the  $\alpha$  particle  $^3\text{He}$ . Continuous bombardment yields a linear accumulation of this isotope with time. (b) Removal of surface by erosion, resulting in an underestimation of eruption age.

surface has  $10 \times 10^6$  atoms of cosmogenic  $^3\text{He}$  per each gram of rock less than predicted for a flow surface having undergone no erosion. Hence, the eruption “age” determined for this sample would be approximately 40 ka too young.

A number of studies document the use of surface exposure dating. These include Leavy (1987), who measured  $^{36}\text{Cl}$  build-up in young basalt flows in southern New Mexico and determined ages which are in general agreement with geomorphic and soil evidence. Phillips, Dunbar and Zreda (1997) applied  $^{36}\text{Cl}$  methods to basaltic lavas; their results for the Carrizozo flows of New Mexico are in close agreement with  $^3\text{He}$  dates reported in Chapter 4 (Table 1) and in Anthony *et al.* (1998). Staudacher and Allègre (1993) have used a combination of  $^3\text{He}$  and  $^{21}\text{Ne}$  to evaluate basalts at Réunion, located in the Indian Ocean. Bierman (1994) suggests that cosmogenic surface exposure dating will be of significant value to geomorphologists and tectonicists, particularly in determining erosion rates. Quaternary meteor impact features (Nishiizumi, 1991; Phillips *et al.*, 1991) have also been dated using cosmogenic  $^{36}\text{Cl}$ ,  $^{14}\text{C}$ ,  $^{10}\text{Be}$ , and  $^{26}\text{Al}$ . Examples of other applications may be found in Craig and Poreda (1986), Kurz (1986b), Nishiizumi *et al.* (1986 and 1990), Marti and Craig (1987), Sarda *et al.* (1993), Staudacher and Allègre (1993), Zreda *et al.* (1993), Laughlin *et al.* (1994), and Williams *et al.* (1995 and in revision).

Anthony and Poths (1992) began applying  $^3\text{He}$  surface exposure dating to lavas from the eastern and central parts of the Potrillo volcanic field. The area was selected due to the existence of clearly mapped stratigraphic relationships (Hoffer, 1976), the availability of well-preserved young lava flows, low erosion rates, and lack of coverage of surfaces by later depositional processes. Duplicate samples from a single flow surface (e.g. Afton flows) and for several samples from a single volcanic center (e.g. Aden complex) showed good reproducibility. Their surface exposure dates agreed with known stratigraphy, estimates of pedogenic carbonate build-up (Giles, 1987) and some K/Ar dates. The work by Anthony and Poths (1992) indicated the applicability of the  $^3\text{He}$  surface exposure dating technique to these mafic extrusive products.

### **2.3 Geochemistry and Isotopic Signatures**

Overview articles on the timing, tectonics and magmatism of the Rio Grande rift may be found in Heatherington (1988) and Gibson *et al.* (1992). Geochemical investigations more specific to the northern Rio Grande rift include Dungan *et al.* (1986), Perry *et al.* (1990), Duncker *et al.* (1991), Johnson and Thompson (1991), Menzies *et al.* (1991), and Wolff (1997).

Anthony *et al.* (1992) show that mafic volcanism during the past 5 Ma in the southern Rio Grande rift has been represented by two compositional groups. Individual volcanic fields in the rift (Figure 1) generally belong to one group or the



other and no pattern in geochemistry, position or age can be discerned. The first group consists of a subalkaline basalt suite; examples are the Animas, Deming, Jornada del Muerto, and Taos fields. The second assemblage consists of an alkaline suite of basanite, alkali basalt and trachybasalt. Examples of alkaline fields are the Potrillo, Columbus, Hillsboro, Black Mesa, Elephant Butte, Taos, and Palomas.

Isotopic studies in the southern rift have been reconnaissance in style. The studies have been divided into provinces, concentrating on the Basin and Range, Colorado Plateau, Sierra Nevada, and the Rio Grande rift (see Menzies *et al.*, 1983; Perry *et al.*, 1987 and 1988; Roden, 1988), or combined to reflect the southwestern United States (e.g. Reid and Graham, 1996). Interpretations for the rift include the existence of mantle heterogeneity (Menzies *et al.*, 1983). Perry *et al.* (1987) propose that areas undergoing less lithospheric extension yield alkali basalts from enriched lithospheric mantle and that depleted mantle sources are characteristic of greater extension.

With respect to the Potrillo volcanic field specifically, major and trace element geochemical studies of the eastern and central parts of the Potrillo volcanic field have been reported by Hoffer (1976), Chen (1992), and Anthony *et al.* (1992). Long's thesis (1994) documented the geochemistry of spinel-bearing mantle xenoliths from Kilbourne Hole. Previous studies for the area also include DeHon

(1965a,b,c), Reeves and DeHon (1965), Renault (1970), Hoffer (1971), Page (1973 and 1975), Bersch (1977), Ortiz (1981), and Sheffield (1981). Very little isotope information has been published for the Potrillo field. Whole rock  $\epsilon_{Nd}$  and  $^{87}Sr/^{86}Sr$  values reported include: +6.9 and 0.703 (Crowley and others, 1986), +6.5 to +13.3 and 0.703 (Jagoutz and others, 1980), and +6 and 0.703 (Roden, 1988).

## Chapter 3

### ANALYTICAL METHODS

#### 3.1 Geochronology

##### 3.1.1. $^3\text{He}$ Surface Exposure Dating

Well-preserved surface samples from breach-flow, lava lake and fissure-fed flows were collected from eight volcanic centers. Surface samples were selected such that the following criteria were met.

- The rock surface was *in situ*.
- Subsequent deposits did not previously, or do not currently, cover the site.
- Taller, near-vicinity features that can cause horizon effects did not shield the locality.
- The surface was deemed the original top displaying little to no erosion or weathering features.

The last parameter was very carefully considered by reconnaissance of the flow(s) before site selection. In some instances, several surfaces from a single flow were collected. In addition to these surface samples, four samples for dating maar eruptions were collected. These were from Hunt's Hole, Kilbourne Hole, Potrillo Maar, and Malpais Maar. Details for each of the four centers will be provided in Section 4.4.

For all sample surfaces, “tops” comprised the upper 3 to 5 cm. This was ensured by carefully marking the orientation of samples in the field prior to their removal. Once back at the laboratory, a rock saw was used to remove material representing lava deeper than 5 cm from the surface. This step was taken to remove progressively shielded material, which would retain an incomplete cosmogenic record due to attenuation of cosmic rays. Then each 3 to 5 cm thick sample was crushed using a chipmunk followed by further reduction using clean ceramic plates set at a 2 mm gap. The resulting glassy matrix and phenocryst mixture was then separated according to size by using dry sieving techniques.

Olivine and pyroxene grains (250 $\mu$  - 420 $\mu$  fraction) were later separated from matrix material using density columns with dimethylene iodine. Occasional (~ 1% by volume) magnetite grains were found in the mix and were removed using a hand magnet. Olivine and pyroxene crystals were then thoroughly cleaned with multiple acetone rinses and allowed to air-dry before analyses. For additional analytical procedures, see Anthony and Poths (1992) and Laughlin and others (1994).

Analyses were performed with Dr. Jane Poths at Los Alamos National Laboratory. The concentration and isotopic compositions of helium were determined for the trapped component (*i.e.* magmatic) by crushing approximately 0.3 grams of mineral separates on-line to a Nier mass spectrometer. The

resulting powder was melted under vacuum, releasing a mixture of cosmogenic and residual trapped components. Cosmogenic  $^3\text{He}$  was determined by subtracting the trapped values from the total  $^3\text{He}$  released during the melt procedure. This trapped helium was assumed to be equal to the amount of  $^4\text{He}$  released in the melt step multiplied by the  $^3\text{He}/^4\text{He}$  released in the crush step.

All data are corrected for mass discrimination and blank. Errors are reported as one sigma standard deviation analytical uncertainties. The concentration of cosmogenic  $^3\text{He}$  and the dates include propagated uncertainties for analysis, blank, and correction for the trapped  $^3\text{He}$  in the melt step. The trapped  $^3\text{He}/^4\text{He}$  values vary for different flows and therefore have not been averaged for the trapped correction. Data reduction included production rates based on work by Cerling and Craig (1994) of 440 atoms/grams/year at 1445 m and 39°N latitude, adjusted for actual sample latitude and altitude (Lal, 1991). Based upon conclusions drawn by Laughlin and others (1994), production of  $^3\text{He}$  in olivine and clinopyroxene was considered identical within analytical error. Further, the production rate has been decreased by 18% to incorporate the recalibration of the  $^{14}\text{C}$  time scale by Bard *et al.* (1990).

### 3.2 Geochemical Analyses

Geochemical samples were selected to be representative of the holocrystalline, interior portion of lava flows or xenocryst-poor bomb coatings adhering to xenoliths collected at maar centers. It is important to note that material used for geochemical analyses *are not* splits from surface geochronology samples; selection criteria of samples for the two studies are vastly different. Flow samples were ~ 1000 times greater in volume than the largest phenocryst. Bomb coatings were consistently removed from similar xenoliths at a given center. Specifically, I used coatings only from lherzolites at Kilbourne Hole and from mudstone clasts at Hunt's Hole.

Samples were mechanically fragmented to roughly 1 cm<sup>3</sup> pieces using a VD Bico-Braun crusher. A Bico-Braun UD pulverizer with ceramic plates was then used to grind fragments to a fine-grained sand size. A quartered split of the pulverized material was powdered for twelve minutes using a Spex 8000 mixer/mill with a ceramic ball mill assembly, resulting in approximately 50 gm of material. At all stages of grain size reduction, the equipment was cleaned and pre-contaminated with each sample.

The geochemical investigation involved whole rock major and trace element analyses primarily done as two experiments: WPVFA and WPVFB. Also

included in this study are additional samples run as experiments MAOVL, CHEN and CLKHA. Data are tabulated and presented in two forms: appendix tables and tables within the mainbody of the text. A comparison of techniques (e.g. INA versus ICP-ES) or duplicate analyses are in the appendix tables. Further, these appendices indicate all analyses by experiment code, averages and reported values for each technique. Final reported concentrations are then provided as tables in the main body of the text (see Chapter 4).

### **3.2.1 Major Elements Using ICP-ES**

Melanie Barnes analyzed samples for major elements and selected trace elements using the inductively coupled plasma facilities at Texas Tech University. Procedures are detailed in Omenda (1997). Note that rubidium was determined using atomic adsorption spectroscopy at Texas Tech University.

### **3.2.2 Trace Elements Using INAA**

Trace element concentrations were primarily determined using instrumental neutron activation analysis at the University of Texas at El Paso. Several samples were run by Weiping Chen using x-ray fluorescence technique through the New Mexico Bureau of Mines and Geology (denoted in appendix Table D). INAA data reduction was performed by a program developed by W. V. Boynton, University of Arizona, licensed to E. Y. Anthony.

INA experiments each consisted of twelve unknowns and four standards. Sample and standard powders were weighed to five significant figures on a Mettler AE163 dual range balance. Weights ranged from 0.6 to 0.8 grams. Powders were then encapsulated in airtight vials and irradiated at the Nuclear Sciences Center, Texas A & M University – College Station.

Once irradiated, samples were evaluated for degree of radioactivity using UTEP's GeLi gamma ray detector for approximately three minutes. Samples were then arranged in order of increasing radioactivity such that those with lesser counts would be analyzed sooner to minimize dead time counts. Each sample was counted in series of six, eight, and twenty-four hours, allowing for both short- and long-lived radionuclide counting. Consistency of the INAA results were monitored by comparison of observed and reported values for standards, unknown duplicates across both experiments, and checked by Omenda (1997).

### **3.2.3 Sr, Nd and Pb Isotopes**

Strontium, neodymium and lead analyses were conducted on a subset of geochemical samples. Splits for the isotopic analyses were taken from the powders used for the major and trace element analyses. Ten samples were selected to represent centers from the central and western alignments that spanned the oldest to youngest eruption dates documented by this dissertation



study. Values for  $^{87}\text{Sr}/^{86}\text{Sr}$ ,  $\epsilon_{\text{Nd}}$ ,  $^{206}\text{Pb}/^{204}\text{Pb}$ ,  $^{207}\text{Pb}/^{204}\text{Pb}$ , and  $^{208}\text{Pb}/^{204}\text{Pb}$  were determined for each lava. Analyses were conducted using Finnigan MAT 261 mass spectrometer facilities with Dr. Todd B. Housh at the University of Texas at Austin.

Sr was loaded with  $\text{H}_3\text{PO}_4$  onto a Ta filament and the isotopic composition was measured in static multicollection mode. Sr isotopic compositions were corrected for mass fractionation using an exponential fractionation law and normalizing to  $^{86}\text{Sr}/^{88}\text{Sr} = 0.1194$ . Multiple analyses ( $n = 7$ ) of NIST SRM987 concurrent with the analyses of these samples resulted in a mean value of  $^{87}\text{Sr}/^{86}\text{Sr} = 0.710240 \pm 25$  ( $2\sigma$ ). On the basis of the long-term reproducibility of the standard and samples, uncertainties for the Sr isotopic analyses are estimated to be approximately  $0.000026$  ( $2\sigma$ ).

Nd was loaded with  $\text{H}_3\text{PO}_4$  onto a Re side filament of a double-filament assembly, and the isotopic composition was measured in dynamic multicollection mode. Nd isotopic compositions were corrected for mass fractionation using an exponential fractionation law and normalizing to  $^{146}\text{Nd}/^{144}\text{Nd} = 0.7219$ . The mean value for a La Jolla standard ( $n = 3$ ) is  $^{143}\text{Nd}/^{144}\text{Nd} = 0.511866 \pm 10$  ( $2\sigma$ ) and for CIT nNd $\beta$  ( $n = 4$ ) is  $^{143}\text{Nd}/^{144}\text{Nd} = 0.511915 \pm 8$  ( $2\sigma$ ). These correspond to  $\epsilon_{\text{Nd}} = -15.06$  and  $-14.10$ , respectively. On the basis of the long-term reproducibilities of

the La Jolla and CIT  $n\text{Nd}\beta$  standards, the estimated uncertainty for a given analysis is approximately 0.000013 ( $2\sigma$ ), corresponding to approximately 0.25  $\epsilon$  units.

Pb was loaded with silica gel and  $\text{H}_3\text{PO}_4$  on a Re filament and the isotopic composition was measured in static multicollection mode. The measured Pb isotopic compositions have been corrected for  $\alpha = 0.11$  %/amu based upon multiple analyses of NIST SRM981. Uncertainties for the Pb isotopic compositions are estimated to be 0.05 %/amu ( $2\sigma$ ).

## Chapter 4

### ANALYTICAL RESULTS: GEOCHRONOLOGY

#### 4.1 $^3\text{He}$ Surface Exposure Dating

A comprehensive summary of helium surface exposure dating conducted in the Potrillo volcanic field is provided in Table 1 and depicted in Figure 6. This compilation includes new data generated by this study as well as that previously determined by Anthony and Poths (1992). Their results have been revised to reflect recalibration of the  $^{14}\text{C}$  time scale (Bard *et al.*, 1990) and are reported here. Sample descriptions are provided in appendix Table A. There are two types of duplicates documented. One type involved collection of more than one sample from a given flow, usually separated by approximately 100 meters. This was done in order to test the extent of surface preservation of a single flow surface through duplicate sampling. The other type of duplication involved running separate analyses for mineral splits from a single surface sample, thus allowing for the evaluation of laboratory uncertainties (*i.e.* reproducibility and precision). For all helium dates, errors are reported as  $1\sigma$ . For the remainder of this section, results will be discussed for each volcanic complex in the following order of alignments: eastern, central, then western.

Table 1. <sup>3</sup>Helium Surface Exposure Dating Summary

Potrillo Volcanic Field Eruptive Center	Crush		Melt				Production Rate (atoms/g)	Age (ka)
	[ <sup>4</sup> He] (10 <sup>-9</sup> cc/g)	<sup>3</sup> He/ <sup>4</sup> He R/R <sub>a</sub>	[ <sup>4</sup> He] (10 <sup>-9</sup> cc/g)	[ <sup>3</sup> He] (10 <sup>-12</sup> cc/g)	[ <sup>3</sup> He] <sub>o</sub> surface '10 <sup>-6</sup> atoms/g)	<sup>3</sup> He/ <sup>21</sup> Ne		
<b>Little Black Mountain</b>								
29#1 {LBM2}	2.49	10.2 +/- 3.5	3.0 +/- 0.2	1.43 +/- 0.09	38.6 +/- 2.5	--	282	137 +/- 9
29#2 {LBM2}	1.18	10 +/- 6	4.4 +/- 0.3	1.24 +/- 0.08	33.1 +/- 2.6	2.72 +/- 0.45	282	117 +/- 9
<b>Black Mountain</b>								
21T(92) {BM5}	5.5	16 +/- 13	18 +/- 1.8	1.05 +/- 0.05	28.3 +/- 1.4	2.8 +/- 0.6	289	98 +/- 5
21B(92) {BM5}	10.3	14 +/- 8	5.4 +/- 1.0	1.19 +/- 0.06	29.9 +/- 2.6	3.2 +/- 0.5	289	104 +/- 9
27#1(92) {BM1}	20.2	13 +/- 4	3.6 +/- 0.6	1.02 +/- 0.06	26.5 +/- 1.9	2.8 +/- 0.5	300	88 +/- 6
27#2 {BM1}	--	--	14.7 +/- 0.8	1.01 +/- 0.08	23.7 +/- 2.3	2.8 +/- 1.1	300	79 +/- 7
<b>Aden Flows</b>								
23C#1(92)	16.7	14 +/- 6	2.3 +/- 0.9	0.259 +/- 0.038	6.0 +/- 1.2	2.7 +/- 1.3	281	21.4 +/- 4.3
23C#2(92)	16.8	10 +/- 5	2.3 +/- 0.6	0.246 +/- 0.030	5.7 +/- 1.0	--	281	20.3 +/- 3.6
24B(92)	57	7.8 +/- 1.7	4.6 +/- 0.7	0.272 +/- 0.027	6.0 +/- 0.8	--	303	19.9 +/- 2.6
24C(92)	109	8.4 +/- 1.5	7.1 +/- 1.0	0.332 +/- 0.032	7.0 +/- 1.0	1.6 +/- 0.5	303	22.9 +/- 3.3
25A(92) {AD1}	62	8.9 +/- 1.6	7.7 +/- 1.0	0.342 +/- 0.042	6.9 +/- 1.2	--	296	23.3 +/- 4.1
65B#1 {AD6}	8.4	7.9 +/- 1.7	5.8 +/- 0.3	0.305 +/- 0.035	6.8 +/- 1.0	2.5 +/- 1.2	283	24.2 +/- 3.5
65B#2 {AD6}	12.0	5.3 +/- 1.0	--	--	--	--		
Notes:	#1,2	Duplicate analyses on same mineral separate.						
	A, B, C	Different sample locations on the same flow surface.						
	(92)	Reported in Anthony and Poths (1992); corrected for revision to 14Carbon timescale.						
	{ }	Sample designation used in chemical analyses series from this study or theses by Chen (1992), Long (1994), and Waggoner (1991).						
	1	Ejected interior block of Afton flow; see Section 4.4 for discussion.						
	2	"By Difference Dating" involving a shielded Afton flow; see Section 4.4 .						
	**	Shielded Sample (See Section 4.4)						

Table 1. <sup>3</sup>Helium Surface Exposure Dating Summary

Potrillo Volcanic Field Eruptive Center	Crush		Melt				Production Rate (atoms/g)	Age (ka)
	[ <sup>4</sup> He] (10 <sup>-9</sup> cc/g)	<sup>3</sup> He/ <sup>4</sup> He R/R <sub>a</sub>	[ <sup>4</sup> He] (10 <sup>-9</sup> cc/g)	[ <sup>3</sup> He] (10 <sup>-12</sup> cc/g)	[ <sup>3</sup> He <sub>e</sub> ] surface '10 <sup>-6</sup> atoms/g)	<sup>3</sup> He/ <sup>21</sup> Ne		
<b>Afton Flows</b>								
<b>22B#1(92) {AF826}</b>	22	14 +/- 4	3.0 +/- 0.7	0.99 +/- 0.05	25.7 +/- 1.5	2.6 +/- 0.3	281	91 +/- 5
<b>22B#2 {AF826}</b>	21.9	8 +/- 4	4.6 +/- 0.3	1.18 +/- 0.07	30.9 +/- 2.0	2.8 +/- 0.4	281	110 +/- 7
<b>22D(92) {AF826}</b>	4.2	15 +/- 6	2.7 +/- 0.9	1.11 +/- 0.05	29.0 +/- 1.5	2.5 +/- 0.3	281	103 +/- 5
<b>58A#1 **</b>	4.8	10.9 +/- 2.2	10.2 +/- 0.8	1.04 +/- 0.06	25.4 +/- 2.0	1.8 +/- 0.4	275	93 +/- 7
<b>58B#1</b>	7.5	7.2 +/- 1.6	2.9 +/- 0.2	1.23 +/- 0.09	32.9 +/- 2.3	3.2 +/- 0.5	275	120 +/- 8
<b>58B#2</b>	8.9	7.5 +/- 1.4	--	--	--	--	275	
<b>58C#1</b>	9.5	8.9 +/- 1.6	2.7 +/- 0.2	1.17 +/- 0.07	31.3 +/- 1.8	2.47 +/- 0.28	275	114 +/- 7
<b>28#2 ** {AF4}</b>	4.7	7.8 +/- 2.1	2.5 +/- 0.5	0.83 +/- 0.06	22.4 +/- 1.9	2.1 +/- 0.4	294	76 +/- 6
<b>Syn-Hunt's Hole<sup>1</sup></b>								
<b>62C#1</b>	73	7.8 +/- 0.5	78 +/- 4	1.06 +/- 0.06	3.9 +/- 2.0	1.2 +/- 0.8	276	14 +/- 7
<b>62C#2</b>	75	8.5 +/- 0.5	64 +/- 3	0.94 +/- 0.09	4.8 +/- 2.6	--	276	17 +/- 9
<b>Syn-Kilbourne Hole<sup>2</sup></b>								
<b>KHPRS1</b>	2.4	5 +/- 4	5.0 +/- 0.3	0.95 +/- 0.06	24.1 +/- 1.7	--	281	Afton: 88 +/- 6
<b>Spatter Near Hunt's Hole</b>								
<b>63A#1</b>	51	7.4 +/- 0.5	--	--	--	--		
<b>Post-Potrillo Maar</b>								
<b>52A#1 {PM823}</b>	12.9	7.2 +/- 1.2	6.1 +/- 0.4	0.91 +/- 0.06	23.3 +/- 1.6	--	283	82 +/- 6
<b>52A#2 {PM823}</b>	18.6	9.0 +/- 1.2	--	--	--	--		
<b>52C#1 {PM823}</b>	15.9	8.4 +/- 1.1	7.3 +/- 0.5	0.80 +/- 0.06	19.8 +/- 1.7	3.6 +/- 1.0	283	70 +/- 6

Table 1. <sup>3</sup>Helium Surface Exposure Dating Summary

Potrillo Volcanic Field Eruptive Center	Crush		Melt				Production Rate (atoms/g)	Age (ka)
	[ <sup>4</sup> He] (10 <sup>-9</sup> cc/g)	<sup>3</sup> He/ <sup>4</sup> He R/R <sub>a</sub>	[ <sup>4</sup> He] (10 <sup>-9</sup> cc/g)	[ <sup>3</sup> He] (10 <sup>-12</sup> cc/g)	[ <sup>3</sup> He] <sub>o</sub> surface '10 <sup>-6</sup> atoms/g)	<sup>3</sup> He/ <sup>21</sup> Ne		
<b>Post-Potrillo Maar</b>								
56A#1	2.85	9.0 +/- 2.8	7.1 +/- 0.4	0.75 +/- 0.06	18.3 +/- 1.8	--	277	66 +/- 6
56A#2	7.1	9.0 +/- 0.9	1.7 +/- 0.6	0.72 +/- 0.05	19.3 +/- 1.6	2.6 +/- 0.7	277	70 +/- 6
56A#3	4.2	6.8 +/- 2.2	--	--	--	--	--	--
56B#1	5.0	10.0 +/- 2.2	2.9 +/- 0.2	0.77 +/- 0.06	20.0 +/- 1.6	2.6 +/- 0.5	277	72 +/- 6
<b>Post-Malpais Maar</b>								
M3#1** (M3)	5.2	9.8 +/- 2.8	25.8 +/- 1.4	0.90 +/- 0.06	14.9 +/- 3.0	1.7 +/- 1.1	287	52 +/- 10
M5#1 (M5)	18.9	6.6 +/- 0.8	15.4 +/- 0.8	2.99 +/- 0.13	78.6 +/- 3.3	2.68 +/- 0.20	279	282 +/- 12
M5#2 (M5)	--	--	10.2 +/- 0.7	2.79 +/- 0.13	74.2 +/- 4.4	2.24 +/- 0.22	279	266 +/- 15
<b>Carrizozo, New Mexico</b>								
CF1#1	12.0	5.5 +/- 1.1	3.6 +/- 0.2	0.093 +/- 0.022	1.8 +/- 0.6	--	369	4.8 +/- 1.7
CF2#1	11.7	5.9 +/- 1.0	--	--	--	--	--	--

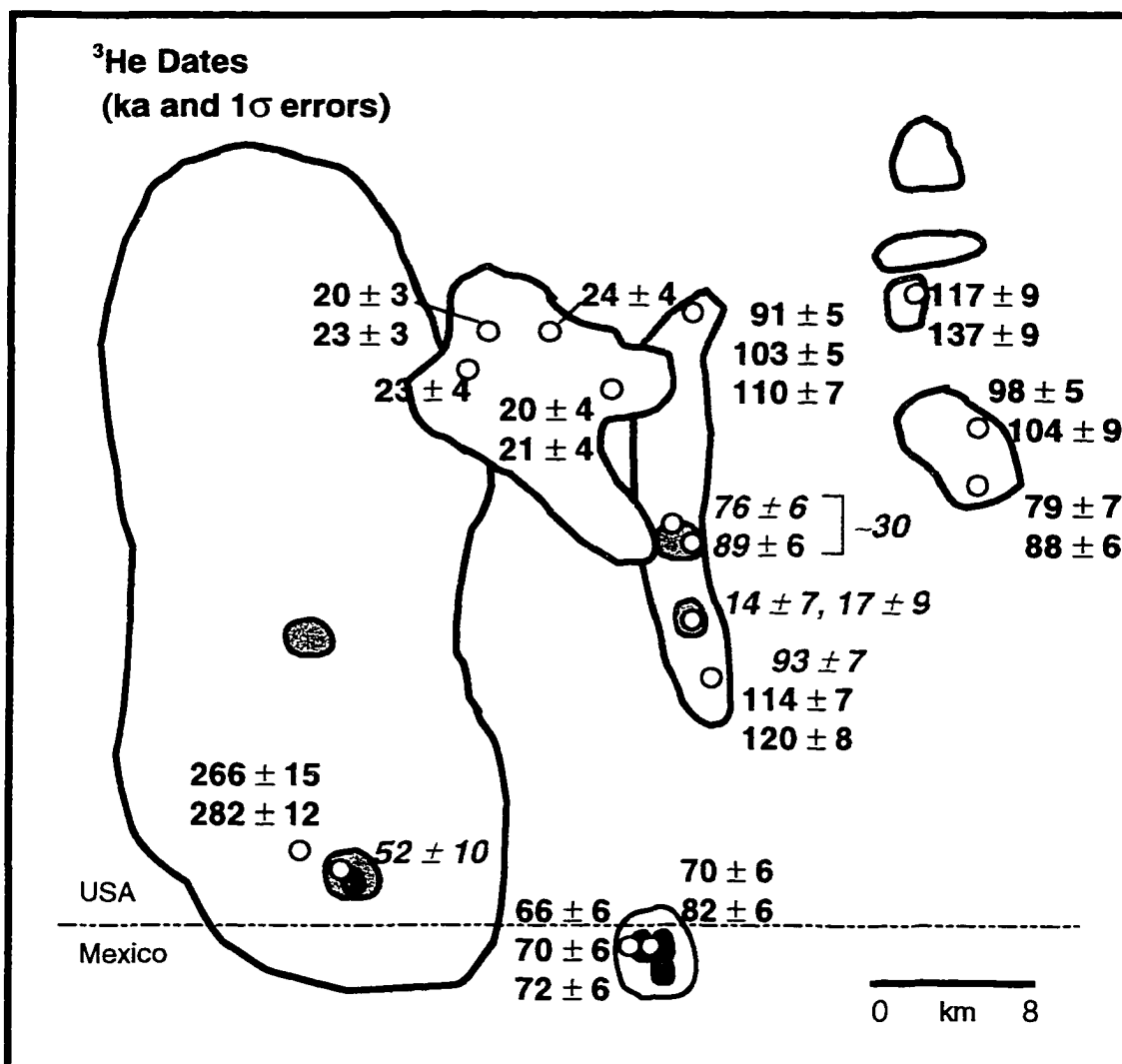


Figure 6. Results of  $^3\text{Helium}$  surface exposure dating for the Potrillo volcanic field. One sigma errors are indicated. "Dates" indicated using a green, italicized font require special discussion (see text). Yellow dots are sample collection sites.

The eastern alignment is comprised of four eruptive centers. Of these, two complexes were selected for surface exposure dating: Little Black Mountain and Black Mountain. Splits of mineral separates taken from a single flow surface were analyzed for Little Black Mountain. These were run as two separate analyses. The dates determined are  $137 \pm 9$  ka (PVF-29#1) and  $117 \pm 9$  ka (PVF-29#2).

Two separate flow surfaces (one each from the north and south) were collected at Black Mountain. For each of those surfaces, there were two separate analyses. The northern of the two flows yielded duplicate analyses on sample PVF-21 in the following sense. This sample was selected for a test of attenuation effects at shallow surface depths. From the same 6 cm thick surface sample, two "splits" were taken by sawing and separating the upper 3 cm from the bottom 3 cm. The results are  $98 \pm 5$  ka and  $104 \pm 9$  ka, thus demonstrating an insignificant attenuation effect detectable for up to 6 cm depth from the surface. Determinations of  $79 \pm 7$  ka (PVF-27#1) and  $88 \pm 6$  ka (PVF-27#2) for the southern Black Mountain flow represent a split of the mineral separates obtained from a single 5 cm thick surface sample.

The central part of this field is also a roughly north-south alignment of centers and is located approximately 10 km to the southwest of the eastern alignment. The following comments address the northern centers then work southward.



Surface samples were selected to represent the various eruption styles preserved at the Aden complex. These include the main spatter rampart, the well-preserved lava lake within that spatter ring, a hornito atop the lava lake, and proximal flow material that breached the main spatter ring. The Aden surfaces were sampled and analyzed in the following ways:

- (1) two separate surfaces collected from the spatter rampart gave  $19.9 \pm 2.6$  ka (PVF-24B) and  $22.9 \pm 3.3$  ka (PVF-24C);
- (2) one analysis from a single surface collected from the lava lake yielded  $23.3 \pm 4.1$  ka (PVF-25A);
- (3) a surface from the hornito produced a  $24.2 \pm 3.5$  ka date (PVF-65B#1);  
and
- (4) one breach flow yielded  $21.4 \pm 4.3$  ka (PVF-23C#1) and  $20.3 \pm 3.6$  (PVF-23C#2), reflecting two separate analyses on mineral splits from a single surface sample.

The Afton flows are part of the next complex to the south. Three flows have been mapped by Hoffer (1976), one of which is proximal to the Gardner cones and more than likely has been shielded for a part of its exposure history. Therefore, the flow is not included in this study. The other two flows are more distal and thus were selected for inclusion in this study. Samples collected from the northern, and stratigraphically younger (Hoffer, 1976), flow were analyzed both as (1) several samples from a given flow surface and (2) mineral splits from

a single surface. PVF-22B is the first surface sample and was run as splits #1 and #2. These yielded dates of  $91 \pm 5$  ka and  $110 \pm 7$  ka, respectively. PVF-22D is a second surface sample from the same flow surface and gave a date of  $103 \pm 5$  ka. These determinations are within  $2 \sigma$  agreement with work by Gile (1987). He estimated the age of this Afton flow to be 100 ka based upon carbonate build-up in materials exposed near the southern rim of Kilbourne Hole.

The Kilbourne Hole eruption pierced the southern Afton flow hence the maar emplacement post-dates it. A second Afton sample (PVF-28#2) was collected at the NNE rim of Kilbourne Hole, interior to the present coverage of the tuff ring. The sample was selected to demonstrate the young date one can determine when a portion of a sample's cosmogenic isotope build-up history has been interrupted. In this particular case, the lack of continuous build-up is related to burial beneath tuffaceous material emplaced during the phreatomagmatic eruption. Some indeterminate time later, exhumation by erosional processes allowed the cosmogenic nuclide accumulation on the flow surface to resume. The resultant low date of  $76 \pm 6$  ka determined will be further addressed in Section 4.4.

The stratigraphically older of the two Afton flows crops out to form the southern extent of the Afton complex. Three different samples were collected from this single flow surface at approximately 100 meters from one another. Sample PVF-

58B#1 yielded  $120 \pm 8$  ka and PVF-58C#1 yielded  $114 \pm 7$  ka. These agree within error. However, the first sample (PVF-58A#1) yielded a date of  $93 \pm 7$  ka, which is younger than the previously reported two ages. In retrospect, this sample did not fulfill the collection criteria described in Chapter 3. We have observed at several Quaternary volcanic fields in the southwestern U.S.A. and Baja California Norte, México, that pahoehoe flows erode by losing thin layers. The thickness of any given layer is presumably a function of the cooling rates involved; it varies in the fields we have worked from 5 to 15 cm thick layers. Each level subsequently exposed retains ropey features. These are termed here as “pseudoropes” in the sense that they do not represent the uppermost (original) flow surface textures.

The pseudoropes show degradation that is subtle in the first ~ 5 cm removal of the flow surface. Review of field notes leads me to believe that sample PVF-58A#1 was not the original top. Rather, pseudoropes may have been collected. Therefore, the low date from this particular Afton sample is an excellent example of how important it is to follow sample selection criteria and to collect multiple samples. The remaining volcanoes in the central alignment are maars. Surface exposure methods can be applied to maars that have not produced syn-eruption flow material; see Section 4.4. As discussed in that section, Kilbourne Hole erupted roughly 30 ka ago based upon the “by difference” method, and Hunt’s Hole formed roughly 16 ka ago based upon dating of an ejecta block.

The geomorphology of volcanic deposits forming the western alignment suggests an eruption history that began substantially before any activity in the central or eastern sectors and extended to quite recently. Although the West Potrillo Mountains include some complexes youthful enough to retain well-preserved surfaces, it was decided that the majority of surfaces more than likely had seen removal of original tops by erosion of the pahoehoe layers. Therefore, helium surface exposure dating was not extensively applied in the West Potrillo Mountains and was limited to the southern extent. The lavas comprising the West Potrillo Mountains were dated using  $^{40}\text{Ar}/^{39}\text{Ar}$  methods (see Section 4.2).

The three sites where helium dating was done are associated with the eruptions forming Malpais and Potrillo maars. Two of the sites are from the Malpais locality and the third is from Potrillo Maar. In discussing these samples, I define “cogenetic” as eruption products emanating from the same general edifice, regardless of time interval between events, and do not call upon matching geochemical fingerprints. At Malpais, data collected include:

- (1) mineral splits from a non-cogenetic lava capping the tuffaceous material emplaced by this maar, yielding dates of  $282 \pm 12$  ka (M5#1) and  $266 \pm 15$  ka (M5#2); and

- (2) a cogenetic lava breaching a syn-maar scoria cone built within the tuff ring. This “date” of  $52 \pm 10$  ka (M3#1) is problematic and will be discussed in Section 4.4.

The third sample is from the Potrillo locality and within the maar depression, thus considered cogenetic activity. These post-maar breach flows are roughly 70 ka old. Further comments regarding the specifics for both maars will be deferred to Section 4.4 .

Finally, Table 1 reports data for a flow not within the Potrillo volcanic field. It is the upper flow from the two mapped Carrizozo flows of the Carrizozo volcanic field (Figure 1) in New Mexico. Data was collected and analyzed while I was studying the Potrillo volcanic field. The  $^3\text{He}$  date of  $4.8 \pm 1.7$  ka places the Carrizozo flow as the second youngest documented in New Mexico (Williams *et al*, 1992; Anthony *et al*,1998), with the McCarty’s flow near Grants being the youngest.

## 4.2 $^{40}\text{Ar}/^{39}\text{Ar}$ Dating

A combination of whole rock and anorthoclase xenocryst  $^{40}\text{Ar}/^{39}\text{Ar}$  dating was done on numerous lavas throughout the Potrillo volcanic field (Table 2; Figure 7) in collaboration with Dr. William C. McIntosh, New Mexico Institute of Technology. Most of the data, however, are for the West Potrillo Mountains where both normal and reversed polarity flows have been documented by

Table 2. <sup>40</sup>Argon/<sup>39</sup>Argon Dating Summary

<i>Alignment</i> <b>Complex</b>	<sup>40</sup> Ar/ <sup>39</sup> Ar <b>Date ± (ka)</b>	<sup>40</sup> Ar/ <sup>39</sup> Ar <b>Sample #</b>	<sup>3</sup> He <b>Sample #</b>	<b>Chemistry</b> <b>Sample #</b>	<b>Comments</b>
<i>West</i>					
Potrillo maar	59 ± 10	PVF-52	PVF-52	Post.16	w
West Potrillo Mountains	840 ± 15	NM1168	---	NM1168	w, n
	916 ± 67	NM1167	---	NM1167	w, r
	847 ± 2	NM1167	---	NM1167	a
	870 ± 18	NM1169	---	NM1169	w, r
	885 ± 16	NM1170	---	NM1170	w, r
	720 ± 180	NM1171	---	NM1171	w, n
	500 ± 20	NM879	---	WPM8, WPM9	w, n
	520 ± 17	NM879	---	NM879	a, n
	860 ± 15	NM880	---	NM880	w
	680 ± 20	NM1103	---	NM1103	w, n
262 ± 12	NM877	---	NM877	w	
Riley maar	624 ± 47	NM1174	---	NM1174	a, syn-
Malpais maar and Vicinity	610 ± 10	MPRS6	---	MPRS6	w, pre-, nc
	310 ± 30	M5	M5	M5	w, post-, nc
	360 ± 17	M5	M5	M5	w, post-, nc
	433 ± 17	NM878	M3	M3	w, post-, c
	510 ± 40	M3	M3	M3	w, post-, c

Notes: w - whole rock      n - normal polarity      c - co-genetic  
a - anorthoclase      r - reverse polarity      nc - not co-genetic

Table 2. <sup>40</sup>Argon/<sup>39</sup>Argon Dating Summary

<b>Alignment Complex</b>	<b><sup>40</sup>Ar/<sup>39</sup>Ar Date ± (ka)</b>	<b><sup>40</sup>Ar/<sup>39</sup>Ar Sample #</b>	<b><sup>3</sup>He Sample #</b>	<b>Chemistry Sample #</b>	<b>Comments</b>
<b>East</b>					
Little Black Mountain	167 ± 21	NM1162	PVF-29	LBM1	w
	188 ± 9	NM1163	---	---	w
Black Mountain	125 ± 11	NM 875	PVF-21	BM4/5	w
	180 ± 110	PVF-27	PVF-27	---	w
	193 ± 11	NM876	---	---	w
<b>Central</b>					
Aden	41 ± 6	NM1166	PVF-25	AD3	w
Afton	70 ± 14	NM1164	PVF-22	AF2	w

Notes: w - whole rock      n - normal polarity      c - co-genetic  
a - anorthoclase      r - reverse polarity      nc - not co-genetic

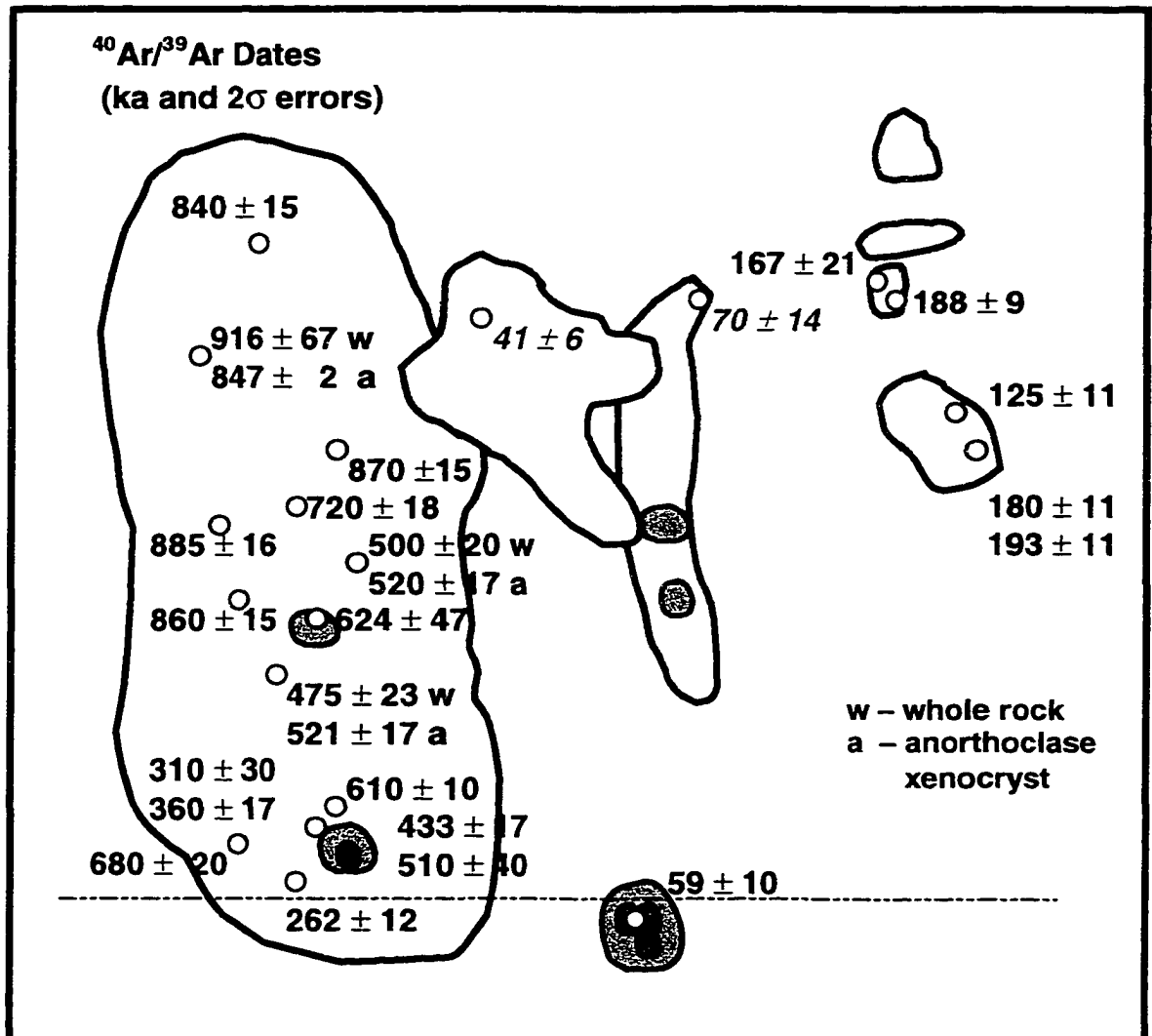


Figure 7.  $^{40}\text{Ar}/^{39}\text{Ar}$  dating results for the Potrillo volcanic field (W.C. McIntosh, Personal Communication). Two sigma errors reported. Yellow dots are sample locations. Note that samples are presumed whole rock unless anorthoclase xenocryst is indicated.



Mick Whitelaw and John Geissman (Williams *et al*, 1992). An attempt was made to sample for both polarity flows, to sample from north to south along the alignment, and to develop a reconnaissance-style geochemistry set for the West Potrillo Mountains. The geochemical data are reported in Chapter 5. Two main results are to be noted for the  $^{40}\text{Ar}/^{39}\text{Ar}$  dating. First, the dating documents eruptions from roughly 916 ka to 70 ka for the West Potrillo Mountains. Secondly, dates derived from whole rock and anorthoclase separates for a given flow agree within analytical error (e.g. sample NM879).

### **4.3 Comparison of $^3\text{He}$ and $^{40}\text{Ar}/^{39}\text{Ar}$ Determinations**

As previously discussed, the helium dating was primarily directed toward the east and central alignments where youthful looking surfaces are abundant. In contrast, argon dating was used on the older deposits dominant in the west part of the field. Several sites, however, were purposefully dated using both methods in order to test the accuracy of both methods. Table 2 provides corresponding helium and chemistry sample numbers, when applicable. The following comments will address localities where direct comparisons (Table 3; Figure 8) were possible. Again, the discussion is organized to move from the eastern to western alignment.

In the eastern alignment, the same flow at Little Black Mountain was sampled for

**Table 3.  $^3\text{He}$  and  $^{40}\text{Ar}/^{39}\text{Ar}$  Dating Comparisons**

<b>Center</b>	<b><math>^3\text{He}</math> Sample</b>	<b><math>^3\text{He}</math> Date (1 <math>\sigma</math> Errors)</b>	<b><math>^{40}\text{Ar}/^{39}\text{Ar}</math> Date (2 <math>\sigma</math> Errors)</b>	<b><math>^{40}\text{Ar}/^{39}\text{Ar}</math> Sample</b>
<b><i>Little Black Mountain</i></b>	PVF-29#2	117 +/- 9	167 +/- 21	NM1162
	PVF-29#1	137 +/- 9		
<b><i>Black Mountain</i></b>	PVF-21T	98 +/- 5	125 +/- 11	NM875
	PVF-21B	104 +/- 9		
<b><i>Aden</i></b>	PVF-27#1	88 +/- 6	180 +/- 110	PVF27
	PVF-25A	23 +/- 4		
<b><i>Afton</i></b>	PVF-22#1	91 +/- 5	70 +/- 14	NM1164
	PVF-22#2	110 +/- 7		
<b><i>Potrillo Maar</i></b>	PVF-52C#1	70 +/- 6	59 +/- 10	PVF52
	PVF-52A#1	82 +/- 6		
<b><i>Malpais Maar</i></b>	M3#1	52 +/- 10	433 +/- 17	NM878
	M3#1		510 +/- 40	M3
	M5#2	266 +/- 15	310 +/- 30	M5
	M5#1	282 +/- 12	360 +/- 17	M5

**Note: See Section 4.3 .**

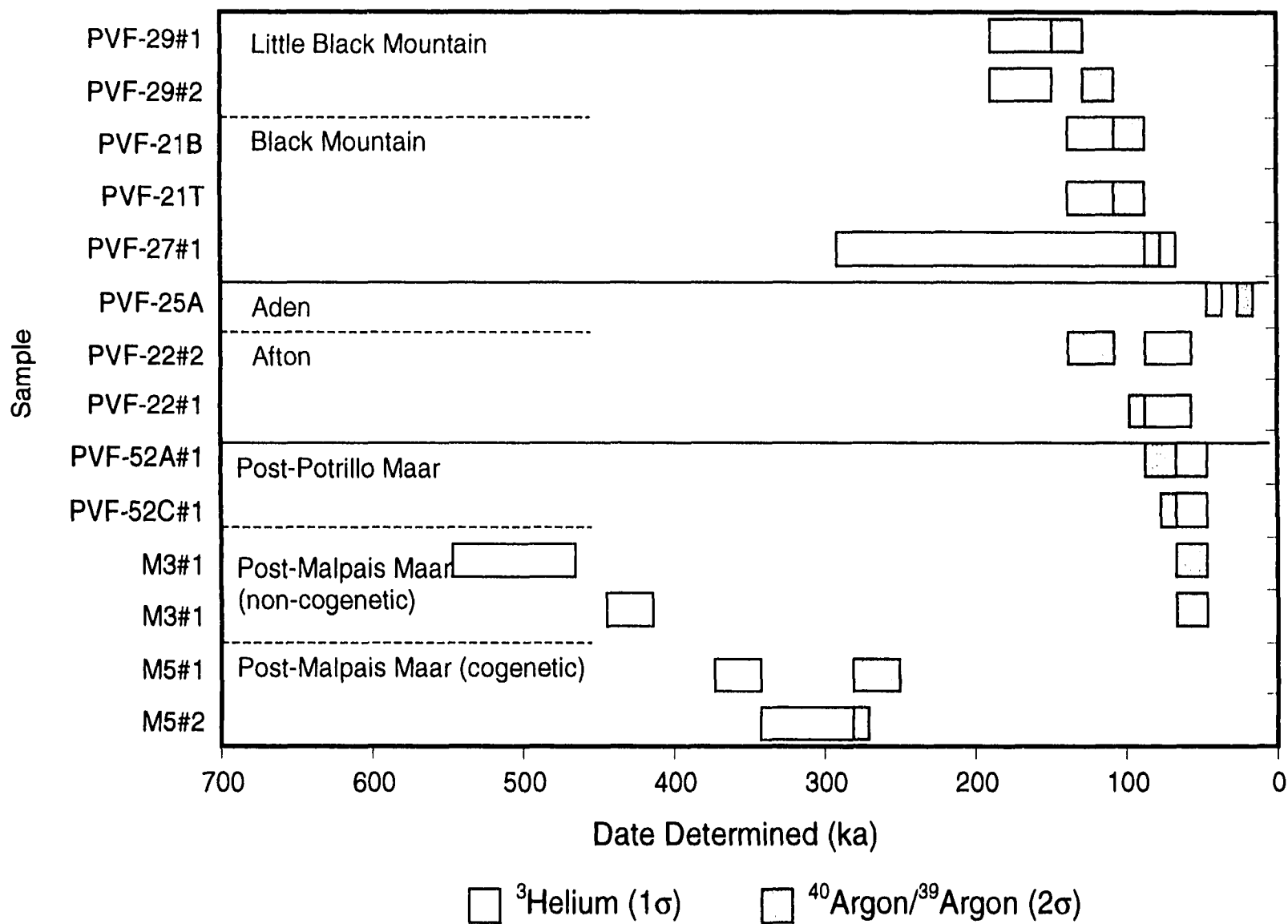


Figure 8. Comparison of the  $^3\text{He}$  and  $^{40}\text{Ar}/^{39}\text{Ar}$  methods for same sample locations. Bars provided for qualitative comparison. See corresponding Table 3 for quantitative limits.

both helium and argon. The average  $^3\text{He}$  determination is  $127 \pm 9$  ka ( $1\sigma$ ) and  $^{40}\text{Ar}/^{39}\text{Ar}$  is  $167 \pm 21$  ka ( $2\sigma$ ). These agree within  $2\sigma$  errors. Similar agreement was found at Black Mountain, where determinations are  $101 \pm 7$  ka ( $1\sigma$ ) using  $^3\text{He}$  and  $125 \pm 11$  ka ( $2\sigma$ ) using  $^{40}\text{Ar}/^{39}\text{Ar}$ . In contrast, work on a second flow has resulted in a large discrepancy between the results from the two methods. With respect to the helium study, this was one of the first flows sampled by Anthony and Poths. It was taken from a non-vesicular outcrop, which stands above the main breach flow surface as a resistant pressure ridge. Based on what we have learned about sampling criteria, we now believe that this helium sample was not from a flow surface. The helium date determined was  $85 \pm 7$  ka. This determination is an under estimation of eruption age. At a later field visit, a sample was taken specifically for argon analysis. That analysis determined a crystallization age of  $193 \pm 10$  ka for the feature. An archived chip sample split originally selected for geochemical study was sent for yet another argon analysis. This was done in an attempt to resolve the difference in dates. The second argon analysis yielded  $180 \pm 110$  ka. Even with its large error, the second date is more similar to the first argon value than to the helium value.

Moving to the central alignment, helium dating suggests the Aden center erupted approximately  $22 \pm 4$  ka before present. Five separate argon samples yielded  $41 \pm 6$  ka,  $13 \pm 11$  ka,  $70 \pm 8$  ka,  $120 \pm 30$  ka, and  $88 \pm 10$  ka. The argon spectra yield imprecise steps and are therefore considered very poor (McIntosh,

Personal Communication). In this case, the lack of agreement between the two dating methods results from pushing the argon method to such young lavas in 1994.

Lastly, both Malpais and Potrillo maars were included from the western alignment. Two flows were studied at Malpais maar. Flow M3 is the first. It is designated cogenetic to the maar eruption, based on the fact that the activity occurred within the depression. M3 yields vastly varying ages between the two dating methods used. The helium date is  $52 \pm 10$  ka ago, whereas the  $^{40}\text{Ar}/^{39}\text{Ar}$  dates are  $433 \pm 17$  ka and  $510 \pm 40$  ka.

Based on a better understanding of field relations, it is now recognized that the  $^3\text{He}$  date for M3 was unreliable. This flow breached the cone at its western flank but then was abruptly diverted southward. This abrupt change in direction may have been due to the advancing flow deflecting off the interior moat walls of the tuff ring. I suggest that this impact caused a portion of the syn-maar tuff ring to collapse onto the flow surface thus causing the post-maar flow surface to be shielded from cosmogenic nuclide accumulation. The tuffaceous material has since been eroded, leaving the M3 lava surface currently exposed.

In retrospect, the older appearance of the M3 surface in conjunction with the advanced rill and apron development on its associated cone does not support the

young  $^3\text{He}$  date. The older argon dates appear to be more in keeping with the dates of other eruptive products in this area. This is, again, an example that stratigraphic relationships must be understood for correct and meaningful application of the helium surface exposure technique. Although not the original intent, this helium date does represent exhumation timing and therefore is useful for elucidating geomorphologic processes.

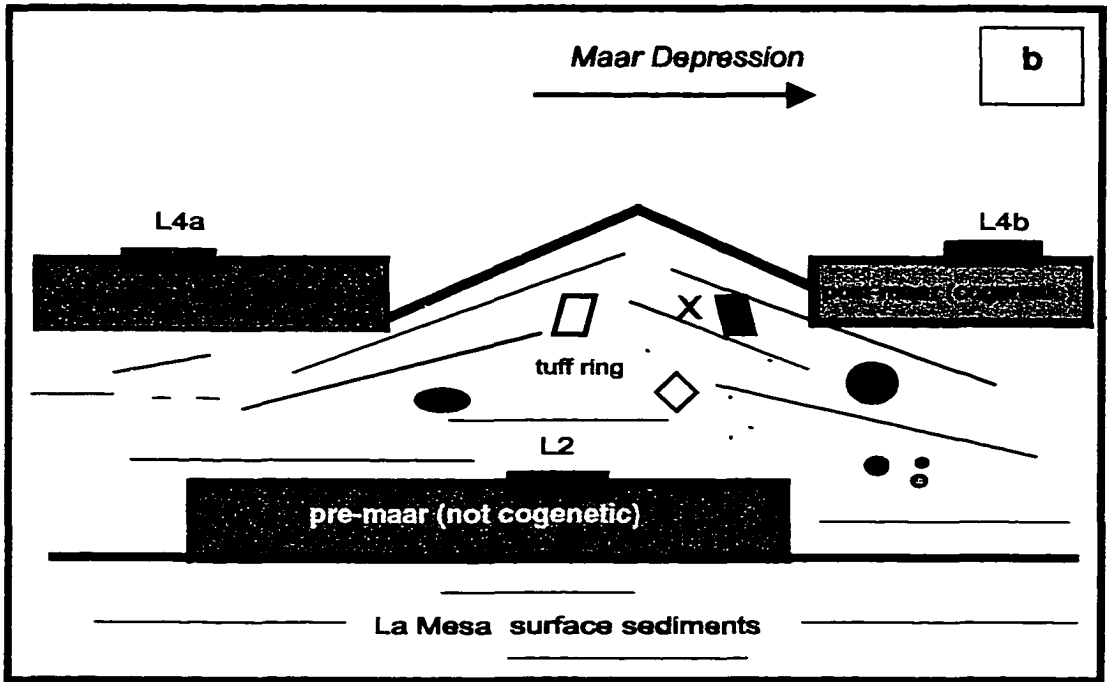
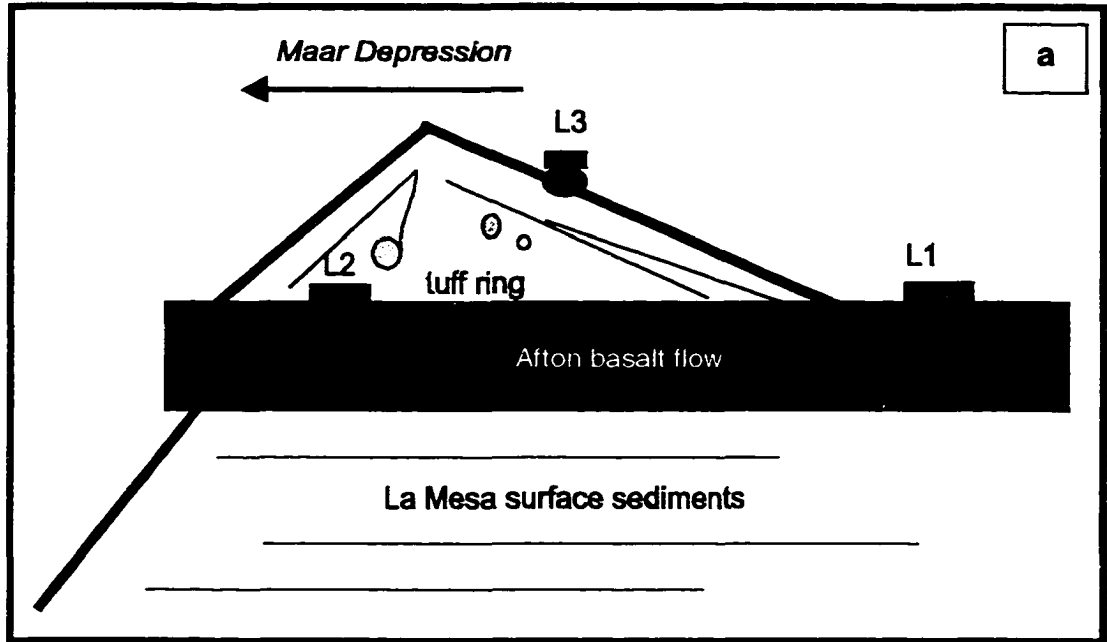
55

The second flow considered using both dating methods is M5, a post-maar flow capping the Malpais tuff ring on its western exposure. I have mapped M5 back to a doubly-breached, highly degraded cone to the northwest of the maar using pahoehoe flow indicators. Therefore this flow can not be considered cogenetic using the criteria previously discussed. Helium dates of  $266 \pm 15$  ka and  $282 \pm 12$  ka were determined from splits of mineral separates and run as two separate helium analyses. Two separate samples from this flow yield argon dates of  $310 \pm 30$  ka and  $360 \pm 17$  ka. There is agreement at the  $2\sigma$  level from dates by the two methods. Finally, the third locality in the western trend is the post- Potrillo maar flows, breached from cones within the depression. The two methods do agree even with  $1\sigma$  reporting for helium:  $^3\text{He}$  yields  $76 \pm 6$  ka and  $^{40}\text{Ar}/^{39}\text{Ar}$  yields  $59 \pm 10$  ka.

#### 4.4 Dating Maar Eruptions

The potential exists to constrain the eruption ages for maars using a variety of techniques and materials. Five maar eruptions (two along the central alignment, one in the “middle” of the west, and two in the southernmost part of the west) have been evaluated using a combination of helium and argon dating methods, as will be outlined in the following text and accompanying figures 9a and 9b.

Traditionally, helium surface exposure dating of mafic eruptions involves sampling tops of flows. Many maar eruptions, however, are violently phreatomagmatic and do not have associated flows as syn-maar deposits. Nor do many such volcanoes have post-maar deposits. Therefore, a different application of the helium method has been used to assess such maars. Within the Potrillo field, that includes those in the central alignment: Kilbourne and Hunt’s Holes. First, consider Kilbourne Hole maar. A surface exposure sample was collected from the Afton flow, through which Kilbourne Hole erupted. In the case of both Kilbourne Hole and Hunt’s Hole, the eruptions pierced the southernmost Afton flow. Surface exposure dating suggests that the Afton flow erupted approximately 117 ka ago (Figure 6), based on surfaces sampled distal (Figure 9a, label L1) from the maars. If the Afton flow in its southern extent had been accumulating cosmogenic  $^3\text{He}$  across its entire exposed surface prior to the maar event (label L2), then the portion covered by maar deposits became



Figures 9. Scenarios used to determine age of maar eruptions within the Potrillo volcanic field; see text for details. Scenario "a" applies to those maars with pre-maar, but without post-maar, deposits; "by difference" surface exposure dating is used. Scenario "b" applies to those maars with pre- and post-maar deposits; helium and argon methods used.



sufficiently shielded from continued cosmic input. Thick cover provided by the tuff ring would not allow further cosmogenic build-up in that portion of the Afton flow surface, thus stopping the accumulation of  $^3\text{He}$ .

Density measurements for the Kilbourne Hole surge deposits were close to 2 g/cc. Using this information and considering cosmic ray attenuation effects (Lal, 1988; Poths, Personal Communication), it was calculated that a flow surface beneath roughly 2 meters and back 2 meters from a cliff exposure would be appropriately shielded within analytical error for the helium surface exposure dating method. Based upon these considerations, the tuff emplaced when the maar erupted has been dated using this "by difference" method. The Afton flow was sampled 2.3 meters below the present day eroded surge surfaces. The olivine and clinopyroxene mineral separates yield a helium date of roughly  $88 \pm 6$  ka (*i.e.* when the surge stopped the cosmogenic clock). Therefore Afton's 117 ka eruption age minus 88 ka supports a maar eruption forming Kilbourne Hole occurring 29 ka ago. This date is in close agreement with the 24 ka proposed by Gile (1987) based on pedogenic carbonate (*i.e.* caliche) build-up.

Another helium sample taken from the NNE rim of Kilbourne Hole is similar to the shielded sample just discussed. The southern Afton flow is presently exposed (PVF28#2) at this rim, exhumed from the tuff ring cover by erosional processes.

A surface from this flow yielded a date of  $76 \pm 6$  ka. This agrees within  $1\sigma$  error with the date obtained from the trenched sample, thus lending further credence to the methodology.

At Hunt's Hole, a different type of sample was collected. An ejecta block sampled by Jane Poths was found resting on the present day surface of the tuff ring (Figure 9a as L3). This material was identified as an interior portion of the southern Afton flow based on its modality, similar chemistry and non-vesicular texture. This field-based interpretation was later supported by laboratory observations during helium dating analysis. The crush step had an unusually high gas yield, suggestive of more interior magmatic gas retention. Prior to the maar event, the block was effectively shielded from cosmic input while still an *in situ* interior portion of the Afton lava. Since the ejecta block was incorporated into the tuff ring during the eruption then covered for a period of time, this date is viewed as representing an exhumation age. A surface exposure date from this ejecta block suggests that the maar eruption forming Hunt's Hole may have occurred as recently as approximately 16 ka (Figure 6).

The remainder of this section considers maars from the western alignment. Dating of Riley Maar was achieved using  $^{40}\text{Ar} / ^{39}\text{Ar}$  techniques. McIntosh analyzed an anorthoclase xenocryst (Figure 9b, Label X) collected from the surge deposits. Based on our work concerning anorthoclases and hosting lavas

from other parts of the field, we believe that this xenocryst had been substantially de-gassed during the maar eruption so that older argon signatures were obliterated and the clock was reset. This crystal yielded a syn-maar date of  $624 \pm 47$  ka, based on the  $^{40}\text{Ar}$  accumulation since resetting.

Malpais maar is located in the southern extent of the West Potrillo Mountains and has been mapped by Page (1973). It has had episodes of post-maar cone and flow development within the maar depression proper, unlike the three previously discussed maars. There has also been both pre- and post-maar activity in the near vicinity of Malpais.  $^{40}\text{Ar}/^{39}\text{Ar}$  dating has primarily been used at this complex since lavas at Malpais maar are considerably older and not generally appropriate for surface exposure methods. By dating samples collected from pre- and post-maar flows, it was possible to better surmise when Malpais maar formed. Mapping indicates that a flow from a cinder cone northwest of the maar depression caps the tuff ring deposits. Helium and argon dating of that non-cogenetic flow (M5) yield its emplacement around 280 ka before present (Figures 6 and Figure 9b, label L4a).

However, to better constrain the age of syn-maar activity, two additional samples

were evaluated using argon dating. These are:

- MPRS6, yielding  $610 \pm 10$  ka. This is from a pre-maar breach flow lying directly beneath tuff (Figure 9b, label L2), which is presently exposed in an arroyo bottom.
- M3, yielding  $510 \pm$  ka. This is from the post-maar breach flow residing within the tuff ring (Figure 9b, label L4b).

The pre-maar flow MPRS6 and its associated cone are presently exposed from beneath the tuff deposits. Their geomorphologies are deceptively young due to the protective mantling afforded by the surge deposits until fluvial exhumation. However, argon dating reveals the older age, which is the upper limit. Field evidence does not help rectify whether or not the events emplacing MPRS6 and the maar event are synchronous. There is no indication of scoria - lava and tuff fluidization textures, but it is readily apparent that the surge washed up and over the cone based upon the tuff bedding orientations exposed in the arroyo cut. The results of this study indicate that the Malpais maar-forming eruption occurred between 610 ka and 510 ka ago (Figure 7). The temporal aspects of these events and episodicity ramifications will be explored later in Chapter 6, particularly with respect to hazards planning studies.

Finally, Potrillo Maar was also investigated. Both helium and argon have been used to obtain dates for the post-maar flows associated with scoria cones developed within the Potrillo maar depression. The sampling scenario is

analogous to L4b in Figure 9b. These dates provide a lower limit to the maar formation. One breach flow was sampled in two different areas along its surface. Ages determined are  $82 \pm 6$  ka (PVF-52A#1) and  $70 \pm 6$  ka (PVF-52C#1). The second flow was also sampled in two different areas along the same surface. But in this case, mineral separates for one of the samples were split and run as separate analyses: PVF-56A#1 and PVF-56A#2 splits yielded  $66 \pm 6$  ka and  $70 \pm 6$  ka, respectively. The second surface was sample PVF-56B#1 and yielded a  $72 \pm 6$  ka date, which is consistent within  $1\sigma$  error to the first surface determinations.

## Chapter 5

### ANALYTICAL RESULTS: GEOCHEMISTRY

#### 5.1 Major Elements and Normative Mineralogy

A total of sixty geochemical analyses were collected as part of this study and during Chen's thesis work (1991). Data are reported in Table 4 and appendix Tables B and C. In order to assess the complete evolution of this field, the full dataset has been used for plotting. Lavas include basanites (modal plagioclase of  $>an_{50}$ ; Chen, 1991), basalts and trachybasalts according to the total alkalis versus silica classification shown by Figure 10a (Irving and Baragar, 1971; Le Bas *et al.*, 1986). The normative nepheline versus normative feldspar classification diagram indicates lavas are basanites, alkali basalts, trachybasalts, and lesser nepheline hawaiites (Figure 10b; following the CIPW normative scheme of Best and Brimhall, 1974). As can be seen from both figures, the magmas have been consistently alkaline for the life of this field. In fact, Anthony *et al.* (1991; 1998) suggest that these are some of the most alkaline Quaternary volcanic deposits in New Mexico.

I have chosen to group samples on the basis of weight percent  $SiO_2$  (e.g. Figures 10a and 10c). Samples with less than 45.5 weight percent  $SiO_2$  are assigned to the Low Silica Group (LSG), whereas those with greater amounts are considered

Table 4. Potrillo Volcanic Field Major Element Chemistry for the Western Alignment and Maars

<b>Sample</b>	<b>NM 1103</b>	<b>NM1167</b>	<b>NM1168</b>	<b>NM1169</b>	<b>NM1171</b>	<b>PVF1</b>	<b>PVF7</b>	<b>PVF8</b>	<b>PVF10</b>	<b>PVF11</b>
<b>SiO<sub>2</sub></b>	46.05	46.24	46.77	46.11	43.58	46.13	45.68	45.64	44.90	44.54
<b>TiO<sub>2</sub></b>	2.44	2.37	2.24	2.33	2.54	2.68	2.66	2.48	2.61	2.45
<b>Al<sub>2</sub>O<sub>3</sub></b>	13.78	14.61	14.90	14.69	13.76	15.63	14.99	14.98	15.18	14.00
<b>Fe<sub>2</sub>O<sub>3</sub> (Total)</b>	11.44	11.83	11.55	10.47	11.39	12.35	11.77	10.53	11.98	11.06
<b>MnO</b>	0.19	0.20	0.19	0.17	0.18	0.20	0.20	0.17	0.19	0.17
<b>MgO</b>	9.66	8.44	7.74	10.09	10.16	7.76	8.85	9.91	8.93	11.52
<b>CaO</b>	11.27	10.06	8.57	10.33	11.21	9.90	9.31	10.42	10.16	11.00
<b>Na<sub>2</sub>O</b>	3.23	4.03	3.69	3.01	2.31	3.82	3.81	3.27	3.49	2.48
<b>K<sub>2</sub>O</b>	0.84	0.96	1.77	1.70	0.77	1.76	1.96	1.58	1.65	1.45
<b>P<sub>2</sub>O<sub>5</sub></b>	0.44	0.51	0.52	0.46	0.46	0.56	0.59	0.57	0.53	0.38
<b>LOI</b>	1.37	1.78	0.93	0.75	3.69	0.74	0.87	0.95	0.47	0.88
<b>Total<sub>(Fe Tot)</sub></b>	100.71	101.03	98.87	100.11	100.05	101.54	100.69	100.49	100.09	99.93
<b>Mg#</b>	66.74	62.46	61.25	68.97	67.58	59.65	63.29	68.97	63.37	71.03
<b>Or</b>	4.96	5.67	10.45	10.04	4.55	10.40	11.58	9.33	9.75	8.56
<b>Ab</b>	15.45	18.06	20.44	12.42	13.12	13.49	12.25	11.84	10.23	7.66
<b>An</b>	20.62	18.93	18.86	21.55	24.90	20.30	18.01	21.52	20.88	22.78
<b>Ne</b>	6.43	8.68	5.83	7.06	3.47	10.19	10.82	8.57	10.45	7.21
<b>Di</b>	18.01	14.48	10.37	15.43	15.68	12.74	13.11	15.25	13.96	17.27
<b>He</b>	8.26	8.05	6.17	6.11	6.73	7.83	6.66	6.10	7.24	6.33
<b>Fo</b>	11.00	10.02	10.13	12.59	12.63	9.40	11.18	12.33	11.04	14.49
<b>Fa</b>	6.38	7.04	7.63	6.30	6.86	7.30	7.17	6.23	7.24	6.72
<b>Mt</b>	2.76	2.87	2.79	2.53	2.76	3.00	2.87	2.56	2.91	2.68
<b>Il</b>	4.63	4.50	4.25	4.42	4.82	5.08	5.05	4.71	4.95	4.65
<b>Ap</b>	1.04	1.20	1.23	1.08	1.08	1.32	1.39	1.35	1.25	0.90
<b>Total</b>	99.54	99.50	98.15	99.53	96.60	101.05	100.09	99.79	99.90	99.25

Note: All concentrations expressed in weight percent.

Mg # based on  $Fe^{2+} = Fe_T * 0.85$ .

See Appendix Table C for NAA and ICP Comparisons.

Table 4. Potrillo Volcanic Field Major Element Chemistry for the Western Alignment and Maars

<b>Sample</b>	<b>PVF15A</b>	<b>NM877</b>	<b>NM878</b>	<b>NM879</b>	<b>NM880</b>	<b>NM1170</b>	<b>MPRS6</b>	<b>MPRS7</b>	<b>MSYN8</b>	<b>KHSYN1</b>
<b>SiO<sub>2</sub></b>	46.02	46.61	45.03	45.18	45.10	44.32	44.78	44.50	44.98	46.12
<b>TiO<sub>2</sub></b>	2.59	2.52	2.66	2.33	2.08	2.54	2.45	2.53	2.61	2.34
<b>Al<sub>2</sub>O<sub>3</sub></b>	14.33	15.79	15.34	15.47	14.96	14.94	14.37	15.27	15.51	14.51
<b>Fe<sub>2</sub>O<sub>3</sub> (Total)</b>	11.39	11.46	11.04	11.88	11.15	11.89	11.51	11.22	11.48	12.21
<b>MnO</b>	0.18	0.19	0.18	0.21	0.20	0.19	0.18	0.18	0.19	0.20
<b>MgO</b>	10.18	9.41	10.44	8.91	8.68	10.00	9.94	8.94	9.47	11.10
<b>CaO</b>	10.00	9.32	10.21	10.09	9.71	10.95	10.41	10.59	10.29	9.91
<b>Na<sub>2</sub>O</b>	3.38	3.82	3.63	3.61	3.20	3.76	2.97	3.47	3.72	3.57
<b>K<sub>2</sub>O</b>	1.00	2.09	1.90	1.55	0.88	0.78	1.38	1.81	1.80	1.75
<b>P<sub>2</sub>O<sub>5</sub></b>	0.45	0.58	0.64	0.52	0.43	0.45	0.56	0.58	0.65	0.62
<b>LOI</b>	1.77	-0.02	0.20	1.05	2.81	1.39	1.19	1.48	0.31	-0.10
<b>Total<sub>(Fe Tot)</sub></b>	<b>101.28</b>	<b>101.77</b>	<b>101.27</b>	<b>100.80</b>	<b>99.20</b>	<b>101.21</b>	<b>99.74</b>	<b>100.57</b>	<b>101.01</b>	<b>102.23</b>
<b>Mg#</b>	<b>67.62</b>	<b>65.84</b>	<b>68.99</b>	<b>63.46</b>	<b>64.45</b>	<b>66.71</b>	<b>66.95</b>	<b>65.72</b>	<b>65.59</b>	<b>67.99</b>
<b>Or</b>	5.90	12.35	11.22	9.15	5.20	4.60	8.15	10.69	10.63	10.34
<b>Ab</b>	17.13	11.92	6.72	11.16	19.36	10.12	12.11	7.39	7.96	9.74
<b>An</b>	20.97	19.76	19.95	21.42	23.85	21.58	21.80	20.74	20.30	18.39
<b>Ne</b>	6.21	11.05	12.99	10.49	4.17	11.75	7.05	11.89	12.73	11.08
<b>Di</b>	14.58	12.55	15.39	13.43	11.53	16.57	14.67	15.41	14.73	15.04
<b>He</b>	6.20	5.83	6.01	7.10	5.95	7.59	6.54	7.31	6.74	6.58
<b>Fo</b>	13.02	12.34	13.21	11.18	11.40	12.06	12.58	10.59	11.73	14.48
<b>Fa</b>	7.01	7.25	6.52	7.47	7.44	6.98	7.09	6.36	6.79	8.01
<b>Mt</b>	2.76	2.76	2.66	2.87	2.69	2.87	2.78	2.71	2.76	2.95
<b>Il</b>	4.91	4.78	5.05	4.42	3.95	4.82	4.65	4.80	4.95	4.44
<b>Ap</b>	1.06	1.37	1.51	1.23	1.01	1.06	1.32	1.37	1.53	1.46
<b>Total</b>	<b>99.75</b>	<b>101.96</b>	<b>101.23</b>	<b>99.92</b>	<b>96.55</b>	<b>100.00</b>	<b>98.74</b>	<b>99.26</b>	<b>100.85</b>	<b>102.51</b>



Table 4. Potrillo Volcanic Field Major Element Chemistry for the Western Alignment and Maars

<b>Sample</b>	<b>KHSYN2</b>	<b>HHSYN1</b>	<b>HHSYN2</b>	<b>WPM6</b>	<b>WPM7</b>	<b>WPM8</b>	<b>WPM10</b>	<b>M4</b>	<b>M2</b>	<b>MWC3</b>
<b>SiO<sub>2</sub></b>	44.85	47.64	47.00	44.18	46.33	43.66	45.67	45.36	43.66	44.54
<b>TiO<sub>2</sub></b>	2.23	2.16	2.30	2.37	2.01	2.27	2.48	2.52	2.33	2.48
<b>Al<sub>2</sub>O<sub>3</sub></b>	14.56	14.68	15.03	15.56	16.12	15.69	15.64	15.16	14.44	15.7
<b>Fe<sub>2</sub>O<sub>3</sub> (Total)</b>	11.89	10.86	11.25	11.61	11.22	12.82	11.58	12.40	12.78	11.41
<b>MnO</b>	0.19	0.18	0.19	0.17	0.18	0.21	0.16	0.17	0.18	0.17
<b>MgO</b>	10.45	9.49	10.16	10.86	8.56	6.98	10.08	10.74	10.99	9.22
<b>CaO</b>	9.74	9.80	10.28	10.34	9.26	8.93	9.78	10.39	10.68	9.73
<b>Na<sub>2</sub>O</b>	3.56	3.26	3.24	2.97	3.73	4.30	3.30	3.44	2.36	3.86
<b>K<sub>2</sub>O</b>	1.70	1.80	1.68	1.8	1.3	2.19	1.75	1.68	1.63	1.96
<b>P<sub>2</sub>O<sub>5</sub></b>	0.57	0.50	0.42	0.61	0.47	0.73	0.56	0.52	0.55	0.56
<b>LOI</b>	0.02	0.31	0.33	0.86	1.8	1.69	0.13	-0.49	0.53	-0.32
<b>Total<sub>(Fe Tot)</sub></b>	99.76	100.68	101.88	101.33	100.98	99.47	101.13	101.89	100.13	99.31
<b>Mg#</b>	67.55	67.28	67.43	67.80	64.46	54.58	66.83	66.06	65.72	65.33
<b>Or</b>	10.04	10.63	9.92	10.63	7.68	12.94	10.34	9.92	9.63	11.58
<b>Ab</b>	8.92	16.83	12.88	5.67	18.27	8.08	11.33	4.94	5.94	7.12
<b>An</b>	18.72	20.10	21.50	23.80	23.40	17.04	22.69	20.96	23.99	19.72
<b>Ne</b>	11.48	5.82	7.87	10.53	7.19	15.33	8.98	13.08	7.59	13.83
<b>Di</b>	14.40	14.10	15.11	13.41	10.35	10.60	12.46	16.90	14.04	13.71
<b>He</b>	6.56	6.35	6.53	5.58	5.49	7.91	5.48	7.60	6.56	6.48
<b>Fo</b>	13.55	11.98	12.82	14.59	11.57	8.73	13.54	13.25	14.61	11.63
<b>Fa</b>	7.80	6.82	7.01	7.68	7.77	8.24	7.53	7.53	8.63	6.96
<b>Mt</b>	2.87	2.62	2.72	2.81	2.71	3.10	2.79	3.00	3.08	2.75
<b>Il</b>	4.23	4.10	4.36	4.50	3.81	4.31	4.71	4.78	4.42	4.71
<b>Ap</b>	1.35	1.18	0.99	1.44	1.11	1.72	1.32	0.12	1.30	1.32
<b>Total</b>	99.92	100.53	101.71	100.64	99.35	98.00	101.17	102.08	99.79	99.81

Table 4. Potrillo Volcanic Field Major Element Chemistry for the Western Alignment and Maars

<b>Sample</b>	<b>M1</b>	<b>M3</b>	<b>M5</b>
<b>SiO<sub>2</sub></b>	45.85	44.34	44.9
<b>TiO<sub>2</sub></b>	2.47	2.52	2.5
<b>Al<sub>2</sub>O<sub>3</sub></b>	16.20	15.31	15.41
<b>Fe<sub>2</sub>O<sub>3</sub> (Total)</b>	11.29	10.72	11.31
<b>MnO</b>	0.16	0.17	0.17
<b>MgO</b>	9.39	9.98	9.47
<b>CaO</b>	9.11	10.12	9.97
<b>Na<sub>2</sub>O</b>	3.63	3.75	4.29
<b>K<sub>2</sub>O</b>	2.06	1.84	1.21
<b>P<sub>2</sub>O<sub>5</sub></b>	0.58	0.63	0.65
<b>LOI</b>	0.07	0.47	0.18
<b>Total<sub>(Fe Tot)</sub></b>	100.80	99.85	100.06
<b>Mg#</b>	65.76	68.62	66.16
<b>Or</b>	11.87	10.87	7.15
<b>Ab</b>	12.08	6.45	11.73
<b>An</b>	21.97	19.50	19.21
<b>Ne</b>	10.09	13.69	13.30
<b>Di</b>	10.80	15.33	14.49
<b>He</b>	4.95	6.13	6.57
<b>Fo</b>	12.87	12.43	11.81
<b>Fa</b>	7.46	6.28	6.77
<b>Mt</b>	2.72	2.59	2.74
<b>Il</b>	4.69	4.78	4.74
<b>Ap</b>	1.37	1.49	1.53
<b>Total</b>	100.87	99.54	100.04

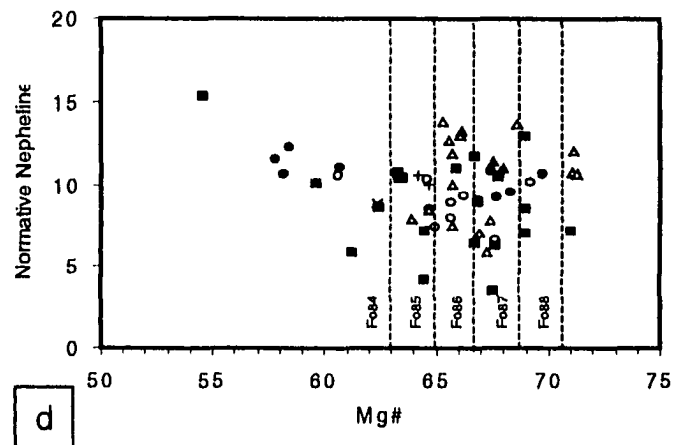
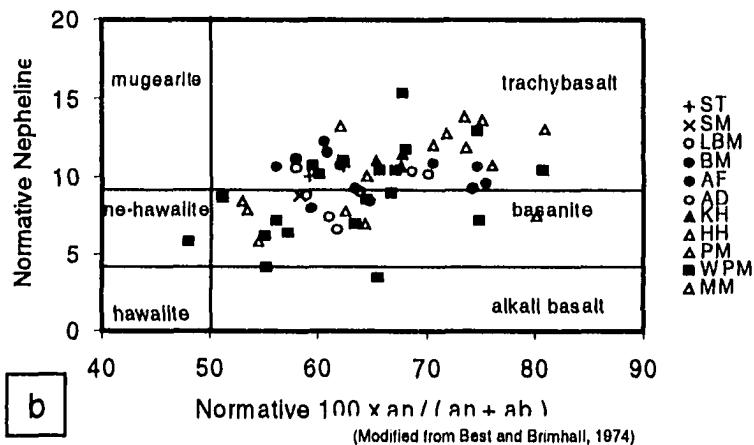
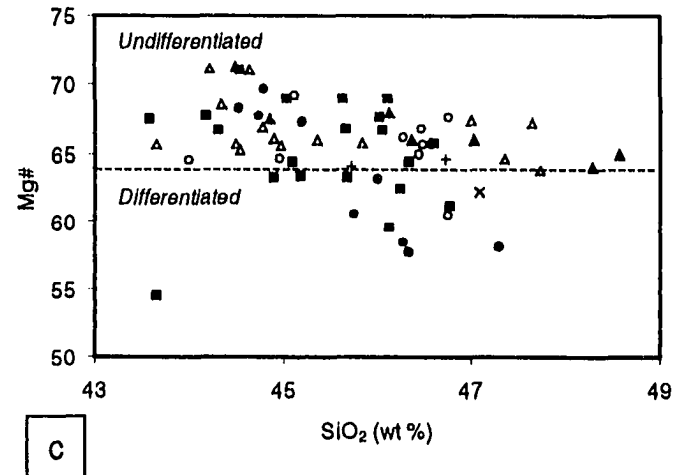
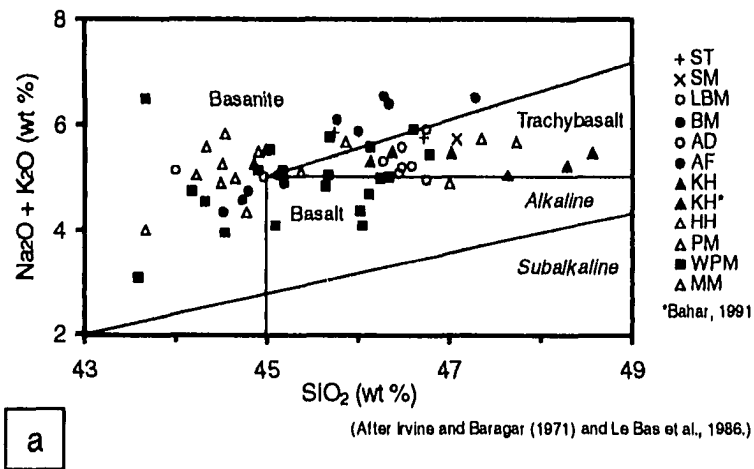


Figure 10. (a) Total Alkali Versus Silica Rock Classification (After Irvine and Baragar, 1971) with Alkaline Domain (LeBas *et al.*, 1986). (b) Normative Feldspar Versus Normative Nepheline Rock Classification (Modified from Best and Brimhall, 1974) (c)  $\text{SiO}_2$  Versus Mg # with Primitive Magmas (Mg # > 64 ; After Luhr *et al.*, 1995) (d) Mg # Versus Normative Nepheline with Corresponding Forsterite Contents in Equilibrium at 10 Kbar Pressure (Luhr *et al.*, 1995 using Ulmer (1989)).

part of a High Silica Group (HSG). The Low Silica Group (Table 5) includes deposits from three of the central complexes and many of the western alignment centers. It includes approximately half of the undifferentiated mapped units of the West Potrillo Mountains, all stages of deposition at Malpais Maar, and the pre- and syn-maar activity at Potrillo Maar. Considering all the analyses, approximately an equal number of lavas are within the High Silica Group. This includes all centers of the eastern alignment, all or part of three central complexes, and essentially half of lavas sampled in the West Potrillo Mountains including the post-eruption cones flows at Potrillo Maar. The nature of these groupings will be explored further in the discussion, particularly as to whether or not they are controlled by geochemistry, eruptive style, and/or age.

Whole rock Mg # is used to identify the most primitive (*i.e.* undifferentiated) melts in this field. Mg # is defined as  $[Mg/(Mg + (0.85 \times Fe_{Total})) \times 100]$ . The selection of Mg # equal to 64 as the lower limit for undifferentiated magmas is based upon defining primitive melts as those in equilibrium with olivine greater than or equal to Fo<sub>84</sub>. This follows the approach used by Luhr *et al.* (1995) in their evaluation of the San Quintín volcanic field. Most lavas in the Potrillo volcanic field are primitive according to this criteria (Figure 10c). Those displaying some differentiation include lavas from the West Potrillo Mountains and some of the eastern flows located at the Black Mountain and the San Miguel complexes. For both the lavas at Black Mountain in the eastern alignment and Potrillo Maar of

Table 5. Volcanic Centers Classified as Low or High Silica Group Members

Low Silica Group (< 45 weight % SiO <sub>2</sub> )			High Silica Group (> 45 weight % SiO <sub>2</sub> )		
Center	Geochemistry Sample	Eruption Style	Center	Geochemistry Sample	Eruption Style
<i>Eastern Alignment</i>			Santo Tomas	SAT 5, SAT4	breach flows
			San Miguel	SAM1	fissure flow
			Little Black Mountain	LBM1, LBM2	breach flows
			Black Mountain	BM5, BM5H, BM3 BM2, BM1	breach flows breach flows
<i>Central Alignment</i>					
Aden	AD4, AD3, AD2	proximal flows	Aden	AD1, AD1H AD6, AD5, AD3A	lava lake distal flows
Afton	AF4, AF8/26 AF2, AF1	fissure flows fissure flows			
Kilbourne Hole syn-	KHSYN2	coating	Kilbourne Hole syn-	KHSYN1 XPN1,2,3 & XP1A,1D	coating juvenile lapilli <sup>1</sup>
			Hunt's Hole syn-	HHSYN1, HHSYN2	coatings

<sup>1</sup> Bahar (1991)

Table 5. Volcanic Centers Classified as Low or High Silica Group Members

Low Silica Group (< 45 weight % SiO <sub>2</sub> )			High Silica Group (> 45 weight % SiO <sub>2</sub> )		
Center	Geochemistry Sample	Eruption Style	Center	Geochemistry Sample	Eruption Style
<i>Western Alignment</i>					
West Potrillo Mountains	NM878	unknown	West Potrillo Mountains	NM877	unknown
	NM879	(fissure or breach)		NM1103	(fissure or breach)
	NM880			NM1167	
	NM1170			NM1168	
	NM1171			NM1169	
	PVF10			PVF1	
	PVF11			PVF7	
	WPM6			PVF8	
WPM8		PVF15A			
				WPM7	
			WPM10		
Malpais Maar Vicinity pre-	M4 MPRS6, MPRS7	breach flows			
Malpais Maar syn-	MSYN8	coating cogenetic			
Malpais Maar post-	M1,M2, MWC3, M3	breach flows cogenetic			
Malpais Maar Vicinity post-	M5	breach flow not cogenetic			
Potrillo Maar pre-	USF8/24	flow cogenetic			
Potrillo Maar syn-	PM13, PM20	coatings cogenetic			
			Potrillo Maar post-	POST.16, 8/23	breach flow cogenetic

the western alignment, there is an indication of decreasing Mg # corresponding with increasing SiO<sub>2</sub> contents. For Potrillo Maar, we do have temporal control. In this case Mg # decreases going from older (pre- and syn-maar units) to younger (post-maar units), thus corresponding to increasing differentiation with time.

The relationship between normative nepheline and Mg # for the lavas is also considered (Figure 10d). Chen (1991) reports optical mineralogical evidence for Fo<sub>77-83</sub> phenocrystic olivine and Fo<sub>89-90</sub> xenocrystic olivine compositions. These determinations are supported by microprobe data collected by Kent Waggoner. Geophysical evidence indicates the Moho at 30 km beneath this area, which would be equivalent to 10 kilobars pressure. Therefore, dashed lines delimiting olivine compositions expected to be in equilibrium at 10 kilobar pressure for various whole rock Mg # (after Luhr *et al.*, 1995) are included in the figure. The majority of samples are not in equilibrium with depleted peridotites, since their compositions plot to the left of the Fo<sub>88</sub> field. But it does appear that several melts from the western alignment centers may have been in equilibrium with depleted peridotites (Fo<sub>84-88</sub>). This includes Potrillo maar and an undated flow from West Potrillo Mountains (PVF-11). Long (1994) studied the chemistry of mantle xenoliths from Kilbourne Hole; his data supports the hypothesis of mantle heterogeneity beneath the Potrillo volcanic field.

## 5.2 Trace Element Analyses

Trace element data are used to recognize enrichment patterns, compare the Potrillo volcanic field to chondritic values, and to evaluate the interrelationship of moderately and strongly incompatible elemental behavior for the purpose of constraining source contributions and magmatic processes recorded by the lavas. The following plots and discussion are based upon trace element concentrations provided in Table 6 and appendix Table D.

### 5.2.1 Enrichment Diagrams

A series of enrichment diagrams have been generated using trace element values normalized to Afton flow sample AF4 and are included as Figures 11a through 11d. Sample AF4 was selected due to its low La value, which indicates that it has a primitive composition. Enrichment diagrams are used to assess which elements behave as compatible versus incompatible in melts. For this section, the entire field is presented first with color-coding keyed to the three geographic zones, then by symbols for most individual centers.

The majority of the elements behave incompatibly with respect to the melt. The most highly incompatible elements include niobium, lanthanum, cerium, samarium, hafnium, tantalum, and thorium. Both Yb and Lu have similar incompatibilities to the middle rare earth elements Sm and Eu in these melts. The



**Table 6. Potrillo Volcanic Field Trace Element Chemistry for the Western Alignment and Maars**

Sample Experiment	NM 1103 WPVFA	NM1167 WPVFA	NM1168 WPVFA	NM1169 WPVFA	NM1171 WPVFA	PVF1 WPVFA	PVF7 WPVFA	PVF8 WPVFA	PVF10 WPVFA	PVF11 WPVFA	PVF15A WPVFA
Sc	30.4	26.3	25.4	29.4	30.0	25.3	24.4	29.4	27.7	33.5	28.6
Ti	2.5	--	--	--	--	--	--	--	--	--	--
V	244	233	205	230	263	208	212	213	225	242	225
Cr	302	300	258	348	328	152	258	274	166	378	307
Co	49.4	44.2	43.9	46.8	48.1	45.5	43.6	48.1	47.0	52.2	50.6
Ni	191	128	110	216	172	99	153	195	128	235	209
Cu	38.00	33.60	29.50	33.70	38.00	31.70	30.70	36.50	37.00	39.60	30.40
Zn	75.0	79.2	84.2	73.0	70.7	91.1	84.4	67.7	82.8	68.0	73.3
Rb	--	--	38	39	--	42	45	38	37	31	28
Sr	667	709	707	587	623	839	837	682	771	593	708
Zr	186	229	242	192	183	226	231	201	209	172	204
Nb	26	82	82	76	66	90	93	83	79	63	77
Ba	496	521	538	471	419	596	592	526	607	531	526
La	26.1	37.4	25.1	33.7	29.6	42.7	39.6	41.0	39.3	27.0	34.3
Ce	49.3	62.2	63.4	57.7	52.1	72.5	67.1	68.1	67.0	48.3	58.9
Nd	24.9	27.7	29.5	25.0	25.3	34.2	30.8	31.1	33.3	25.6	27.3
Sm	5.23	6.48	4.54	6.53	6.10	7.56	7.01	7.19	7.28	5.95	6.41
Eu	1.95	2.05	2.11	1.96	1.98	2.41	2.20	2.22	2.25	1.86	2.05
Y	26	27	26	29	26	29	28	29	30	26	26
Tb	0.75	0.78	0.78	0.82	0.78	0.92	0.83	0.85	0.86	0.76	0.81
Yb	1.946	2.146	1.890	2.257	2.017	2.419	2.261	2.289	2.276	1.948	2.039
Lu	0.30	0.35	0.31	0.36	0.33	0.37	0.37	0.36	0.37	0.31	0.32
Hf	4.44	5.73	6.09	4.85	4.59	6.03	5.94	5.12	5.22	4.36	5.15
Ta	3.48	4.34	4.45	3.69	3.41	4.72	4.70	4.14	4.12	3.23	3.98
Th	3.20	4.86	4.90	4.13	3.26	5.16	4.92	4.94	4.45	3.15	4.19
U	--	--	0.89	--	--	--	1.35	--	--	0.85	--

Note: All concentrations in ppm.  
NAA, ICP, XRF, and AAS analyses as specified in Appendix Table D.

Table 6. Potrillo Volcanic Field Trace Element Chemistry for the Western Alignment and Maars

Sample	NM877	NM878	NM879	NM880	NM1170	MPRS6	MPRS7	KHSYN1	KHSYN2	HHSYN1	HHSYN2
Experiment	WPVFB	WPVFB	WPVFB	WPVFB	WPVFB	WPVFB	WPVFB	WPVFB	WPVFB	WPVFB	WPVFB
Sc	26.2	28.9	27.5	25.5	31.3	29.8	27.9	26.4	26.1	27.5	29.3
Ti	2.5	2.7	2.3	2.1	2.5	2.4	2.4	2.3	2.2	2.1	2.2
V	204	225	203	163	197	223	208	207	198	202	216
Cr	267	272	232	257	320	310	230	388	414	244	253
Co	49.2	50.6	47.8	45.2	53.4	52.2	48.8	53.3	53.4	49.5	50.7
Ni	199	227	151	134	184	210	164	287	332	170	176
Cu	34.00	43.00	46.00	60.00	43.00	41.00	35.00	39.00	42.00	38.00	38.00
Zn	81.6	71.4	80.8	79.9	81.2	76.2	77.3	86.0	84.3	73.6	72.8
Rb	44	41	38	27	--	32	39	41	39	41	37
Sr	733	718	696	622	668	682	969	677	646	602	626
Zr	221	227	225	240	215	202	226	237	224	197	196
Nb	77	79	76	71	64	68	73	67	66	55	57
Ba	530	492	499	459	452	473	482	499	460	529	505
La	39.3	38.7	39.6	33.0	33.2	32.5	41.2	36.8	36.5	34.5	30.8
Ce	66.6	67.7	68.1	59.3	59.3	58.0	72.3	64.7	64.6	61.4	55.4
Nd	31.8	34.2	32.7	29.3	30.1	30.8	35.2	32.5	32.9	31.7	31.0
Sm	6.62	7.00	6.89	5.84	6.48	6.37	7.27	6.86	6.87	6.50	6.08
Eu	2.14	2.22	2.19	1.90	2.12	2.09	2.32	2.14	2.17	2.04	1.92
Y	27	30	30	29	29	29	30	31	31	29	30
Tb	0.85	0.89	0.91	0.78	0.86	0.83	0.97	0.92	0.89	0.87	0.80
Yb	2.175	2.215	2.307	2.190	2.158	2.106	2.319	2.476	2.373	2.333	2.209
Lu	0.34	0.34	0.36	0.35	0.34	0.32	0.37	0.39	0.37	0.36	--
Hf	5.34	5.09	5.25	5.19	4.87	4.54	5.27	5.37	5.07	4.73	4.40
Ta	4.15	4.19	3.97	3.76	3.52	3.39	3.93	3.74	3.63	3.11	3.09
Th	5.16	4.76	4.87	4.53	3.92	3.94	5.10	4.53	4.42	4.32	3.99
U	1.27	1.02	1.31	1.33	--	1.14	1.22	1.29	1.35	1.00	1.14

Table 6. Potrillo Volcanic Field Trace Element Chemistry for the Western Alignment and Maars

Sample Experiment	WPM6 MAOVL	WPM7 MAOVL	WPM8 MAOVL	WPM10 MAOVL	M4 CHEN	M2 MAOVL	MWC3 CHEN	M1 MAOVL	M3 NAA (Averaged)	M5 NAA (Averaged)	AF4 CHEN
Sc	29.6	26.7	21.0	28.0	30.1	31.0	28.5	27.5	28.4	27.5	29.5
Ti	--	--	--	--	--	--	--	--	--	--	--
V	--	--	--	--	--	--	--	--	228	--	--
Cr	278	231	91	255	282	346	229	241	253	253	358
Co	52.1	44.1	38.9	50.1	56.8	58.6	48.3	50.1	49.1	49.9	54.8
Ni	202	140	75	168	172	220	177	160	197	168	203
Cu	--	--	--	--	--	--	--	--	40	--	--
Zn	--	--	--	--	--	--	--	--	68	--	--
Rb	46	46	72	43	38	38	50	45	41	23	35
Sr	685	643	959	679	631	696	708	745	721	740	--
Zr	213	252	301	204	177	167	218	217	214	210	--
Nb	65	63	89	59	57	52	67	65	62	61	46
Ba	605	470	638	506	474	473	540	569	516	492	--
La	40.0	39.3	55.7	36.5	33.2	33.0	42.2	42.4	40.0	39.3	30.1
Ce	68.9	68.4	93.4	63.6	62.4	60.4	75.4	74.0	73.7	71.0	54.9
Nd	31.3	30.9	40.9	30.6	26.3	26.6	30.2	30.4	33.6	31.3	25.6
Sm	5.83	5.91	7.44	6.09	5.59	5.55	6.40	6.17	6.57	6.36	5.55
Eu	2.18	1.74	2.51	1.81	2.12	2.10	2.24	2.19	2.11	2.06	2.01
Y	26	27	31	28	25	25	28	26	30	29	26
Tb	0.89	0.86	0.98	0.92	0.90	0.81	1.01	0.90	0.904	0.868	0.95
Yb	2.470	2.440	2.630	2.330	2.280	2.090	2.360	2.230	2.25	2.24	2.14
Lu	0.34	0.37	0.40	0.35	0.35	0.35	0.37	0.35	0.34	0.34	0.36
Hf	5.16	5.76	6.61	4.88	4.31	4.19	4.86	5.10	4.70	4.73	4.08
Ta	--	3.77	2.17	3.29	3.13	2.93	3.91	3.88	4.21	4.02	2.66
Th	4.78	5.01	6.27	3.96	3.41	3.40	4.97	5.04	4.10	4.12	3.36
U	1.59	1.81	1.93	1.14	0.69	0.74	1.28	1.19	--	--	0.92

Table 6. Potrillo Volcanic Field Trace Element Chemistry for the Western Alignment and Maars

Sample	PM824	PM20	PM16
Experiment	CHEN	CHEN	CHEN
Sc	31.5	30.0	24.9
Ti	--	--	--
V	--	--	--
Cr	438	528	229
Co	61.9	63.2	44.7
Ni	306	340	106
Cu	--	--	--
Zn	--	--	--
Rb	34	34	36
Sr	--	--	--
Zr	--	--	--
Nb	49	49	50
Ba	--	--	--
La	35.8	35.2	37.4
Ce	65.4	65.1	68.7
Nd	27.3	27.9	27.3
Sm	5.89	5.97	5.68
Eu	2.21	2.23	2.09
Y	27	28	27
Tb	0.90	0.93	0.82
Yb	2.45	2.57	2.38
Lu	0.39	0.40	0.40
Hf	4.58	4.80	4.86
Ta	3.05	2.98	3.01
Th	3.73	3.52	4.05
U	0.84	0.80	0.99

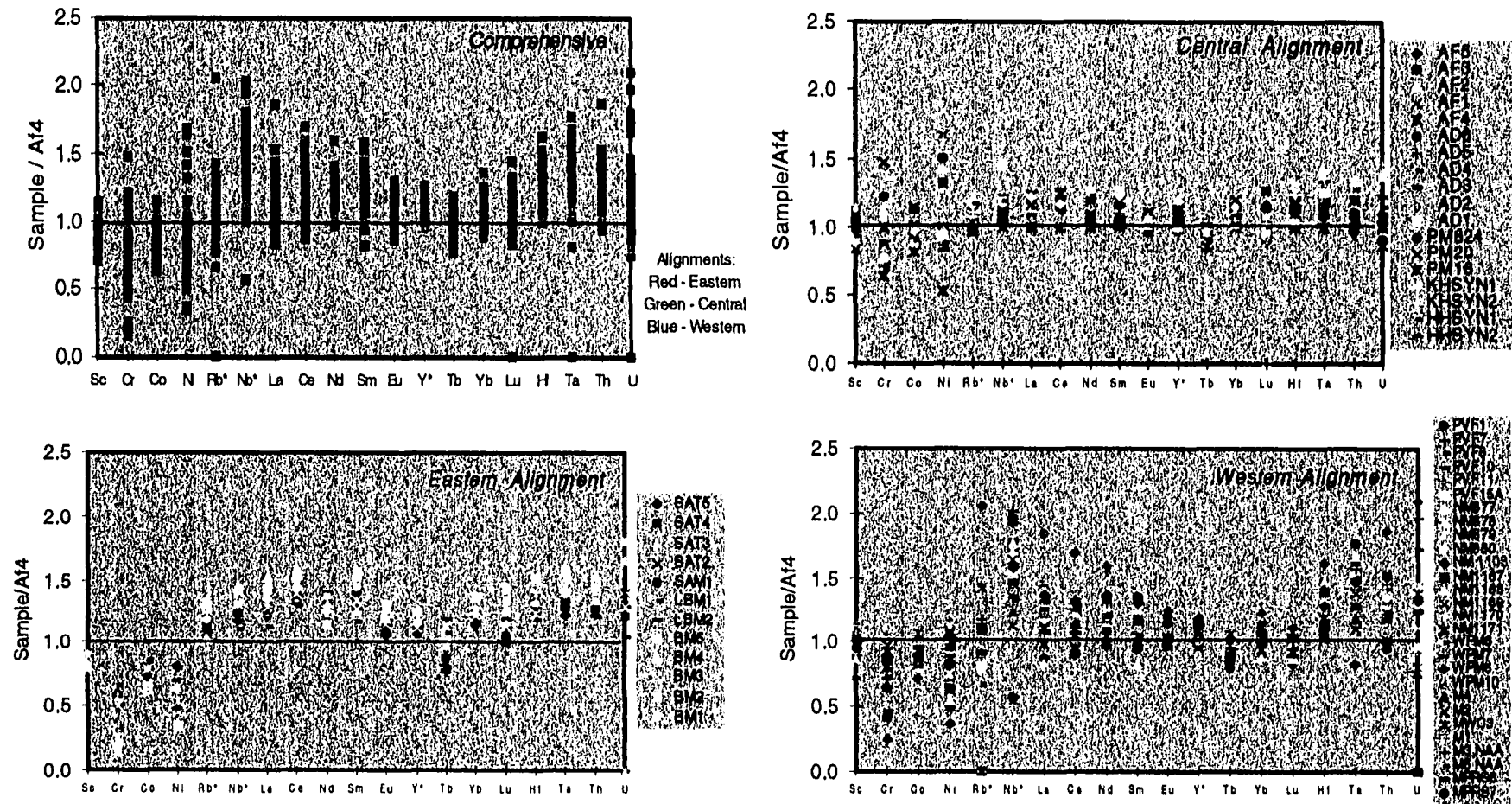


Figure 11. Trace element compatibility diagrams normalized to PVF sample Af4. (a) Comprehensive sample set with alignment affinity color-coded (b) Eastern alignment by sample numbers (b) Central alignment + Potrillo Maar by sample number (c) Western alignment by sample number.

Potrillo volcanic field melts are similar to San Quintín volcanic field in this regard. According to Luhr *et al.* (1995), the San Quintín volcanic field is different from many other intraplate volcanic suites in having been generated from spinel lherzolite rather than garnet lherzolite (see Section 6.2). This issue will be discussed more fully in Section 6.2.

The transition elements scandium, chromium, cobalt, and nickel are depleted (*i.e.* sample/AF4 < 1) and thus behave compatibly with respect to the melt. Depletion of chromium and nickel indicates that olivine (ol) precipitation, which is a low pressure phenomenon, has been important. This is particularly true for the central alignment and is supported by the modal mineralogy (Figure 12). The lesser degree of compatibility for both scandium and cobalt suggests higher pressure clinopyroxene (cpx) fractionation has also played a role, particularly for the central complexes. Again, this is reflected in the petrography by Chen (1991). She determined phenocrystic modes as:

- plagioclase  $\equiv$  olivine(>clinopyroxene) for the eastern volcanoes.
- olivine >> plagioclase(>clinopyroxene) for the central alignment.
- possibly olivine>> plagioclase (>clinopyroxene) for the West Potrillo Mountains lavas. This statement is based on using the post-Potrillo Maar lavas as representative for the other West Potrillo Mountain lavas.

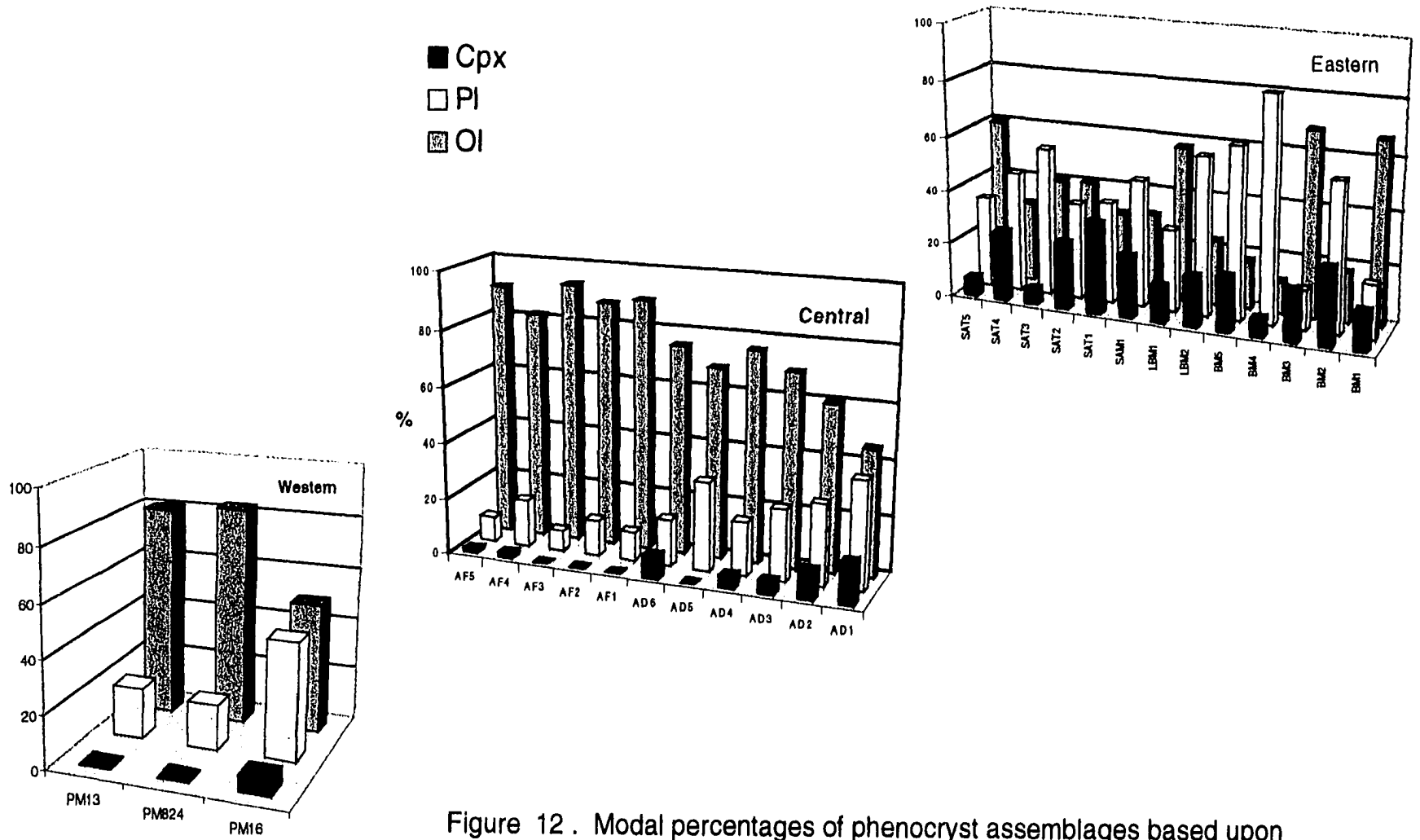


Figure 12 . Modal percentages of phenocryst assemblages based upon 350 points per thin section (data from Chen, 1991).

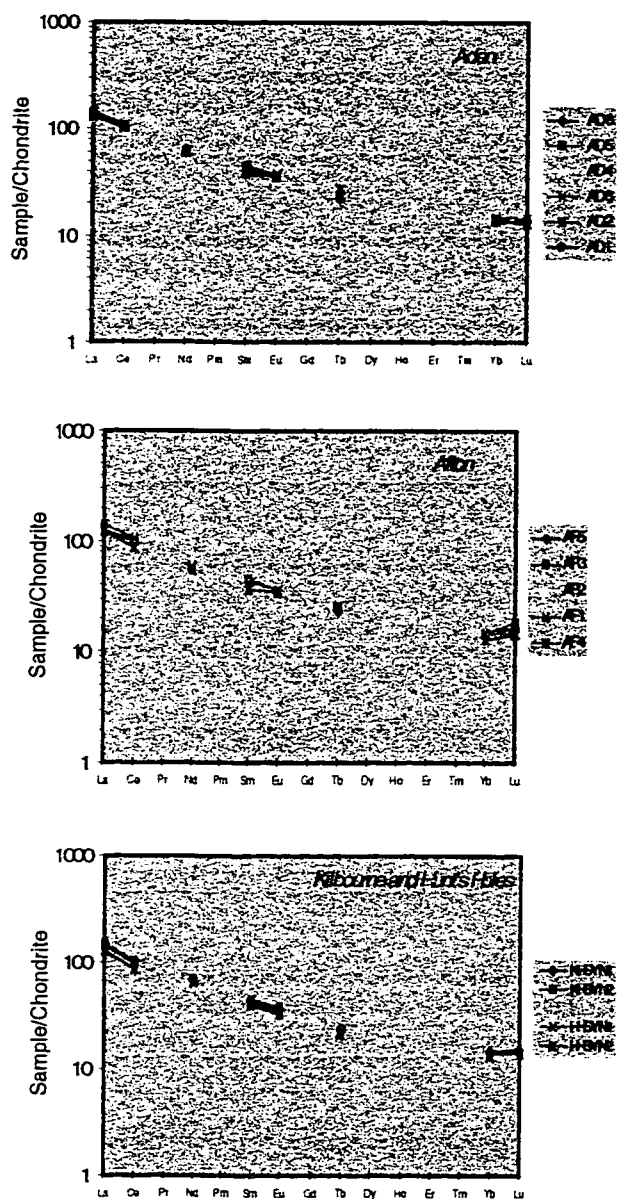
For two volcanoes, the enrichment plots indicate that the whole rock analyses have been affected by xenocrystic olivine. The syn-maar melts associated with both the Potrillo and Kilbourne Hole maars have significantly elevated chromium and nickel concentrations (i.e. sample/AF4 > 1), suggestive of mantle xenocrystic olivine contributions to the analyses.

### 5.2.2 Rare Earth Element Diagrams

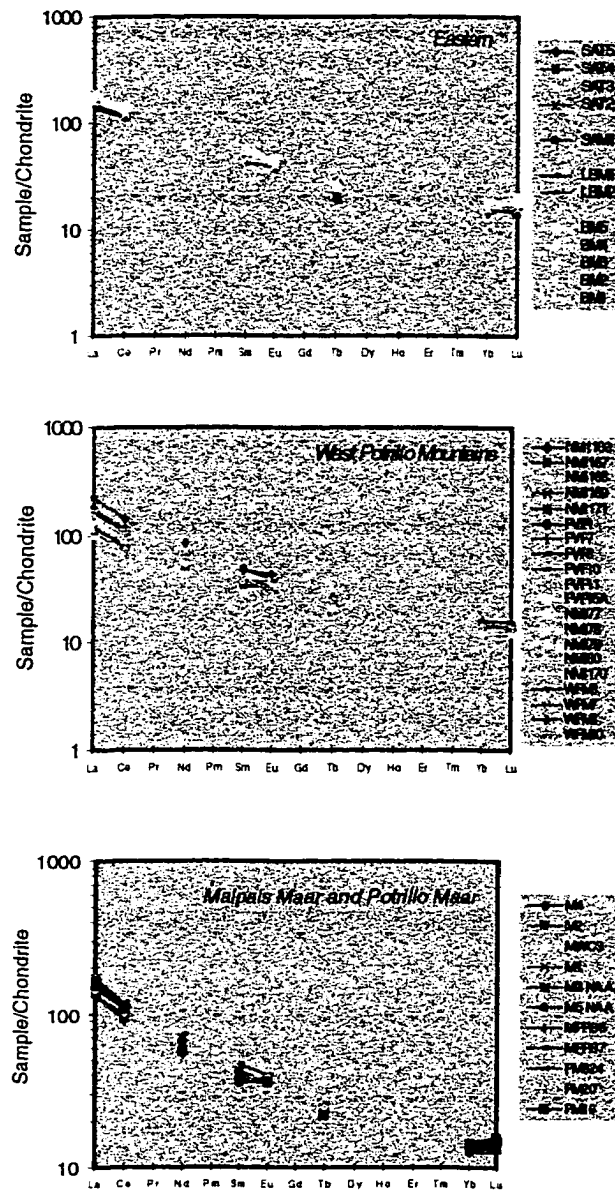
Rare earth elements (REE) have been normalized to chondritic values published by Anders and Ebihara (1982) and are provided as Figures 13a through 13f. Plots for individual samples are grouped by eruptive centers. Any given eruptive center in the eastern and central sectors has a limited range in rare earth element enrichment, closely clustering around 150 times chondrite for La. The western alignment spans 100 to 200 times chondrite for La. The greater range is probably due to these samples representing numerous eruptive centers. The implications for some of the West Potrillo Mountain samples having the highest concentrations of rare earth elements are discussed in the following sections. This high degree of enrichment follows with the overall alkaline nature of the Potrillo volcanic field (Anthony *et al.*, 1992, 1998).

The rare earth element patterns display no europium anomaly for the lavas, indicating that plagioclase has not played a significant role in their fractionation history. Only in the eastern complexes is phenocrystic plagioclase present,





Figures 13a. Rare Earth Element (REE) diagrams for the Central alignment.



Figures 13b. Rare Earth Element (REE) diagrams for the Eastern and Western alignments.

indicating a degree of feldspar fractionation. The lack of Eu anomaly implies precipitation for only a short time interval prior to eruption. Petrographic observations (Hoffer, 1976; Chen, 1991) and the enrichment patterns presented in the previous section corroborate these observations.

### 5.2.3 Incompatible Elements: H versus H

Treuil *et al.* (1977) demonstrated that trace elements can be used to discern:

- (1) whether or not source heterogeneity is suggested and
- (2) whether the magmatic processes have been dominated by partial melting or crystal fractionation.

The indices are illustrated using simple x-y scatter plots of two strongly incompatible elements from the same rock. The relationship is as follows for a single element:

$$C_L = C_O f^{(D-1)}$$

where

- $C_L$  liquid concentration of an element
- $C_O$  original liquid concentration
- $f$  residual liquid fraction
- $D$  bulk solid / liquid partition coefficient .

For  $D = 0$ , the equation reduces to  $C_L / C_O = 1/f$ . The relationship for two incompatible elements (*i.e.*  $D = 0$ ), then, simplifies to:

$$C_{L1}/C_{O1} = C_{L2}/C_{O2}$$

The two elements can then be plotted against one another as H versus H diagrams once the above relationship is written as:

$$C_{L2} = C_{L1} (C_{O2} / C_{O1}).$$

This equation is a linear regression of the form ( $y = mx + b$ ) which is constrained to pass through the origin such that  $b$  equals zero.

Recognizing that the slope of the line is  $(C_{O2} / C_{O1})$  from the previous step, one can then evaluate from actual data whether one, or more than one, regression is necessitated. A divergence from a single linear array "best fit" could mean that:

- both elements plotted are not equally incompatible (*i.e.*  $D \neq 0$ ).  
However, this is not the case since I used the enrichment diagrams to determine which elements are similarly incompatible.
- both elements are equally incompatible (*i.e.*  $D = 0$ ). If this is the case, then two arrays require two different  $(C_{O2} / C_{O1})$  which means that the source is heterogeneous.

In summary, if the criteria  $D = 0$  is satisfied then a single line of best fit suggests *source homogeneity* (Figure 14a) and more than one line requires *source heterogeneity* (Figure 14b).

There are two distinct trends for many of the combinations of incompatible elements, which is indicative of a heterogeneous source. Melts from the central and eastern alignments define one trend whereas western alignment lavas define a second. This is illustrated by plots of Ce vs Th, Nb vs Zr, and Ta vs Nb. There are other combinations of elements, however, which do not require two linear regressions. For instance, Hf versus Zr imply source homogeneity. Therefore, the data show that: (1) several trace elemental combinations suggest source heterogeneity (Figures 16 - 21), and (2) others support homogeneity (Figures 22 - 25). The implications of this will be further explored by using plots of highly incompatible elements (H) with moderately incompatible elements (M) as H/M versus H diagrams (see Section 5.2.4) and the Sr, Nd and Pb isotopic systems (Section 5.4).

A further use of H versus H diagrams is that one may assess magmatic processes. The geochemistry is considered in light of temporal indicators. The trends from older to younger deposits are characteristic of either partial melting (PM) or fractional crystallization (FC) processes (Trueil *et al.*, 1977). Batch partial melting is reflected by the data (Figure 15, label "I") if there is younging with decreasing concentrations of the incompatible elements, illustrated by Figure 26a. If, in contrast, there is an increasing concentration with time (Figure 26b) then fractional crystallization has occurred, as depicted by Figure 15, label "II".

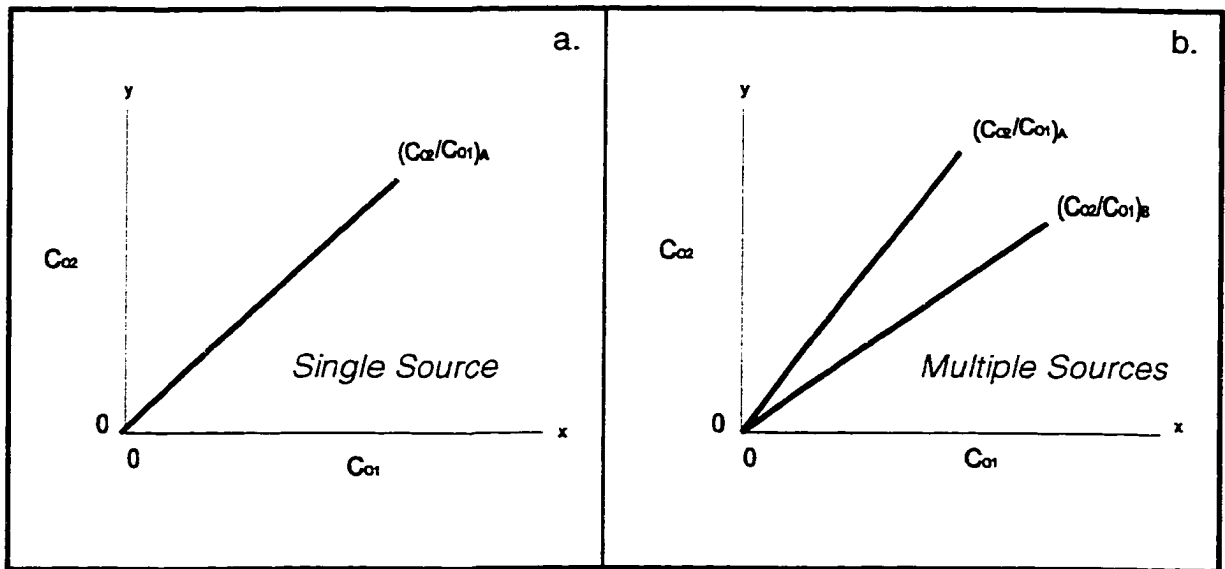


Figure 14. Plots of highly incompatible element concentration versus a different highly incompatible element concentration. (a) A single array is suggestive of a single melt source, whereas (b) represents more than one array, implying more than one melt source possible.

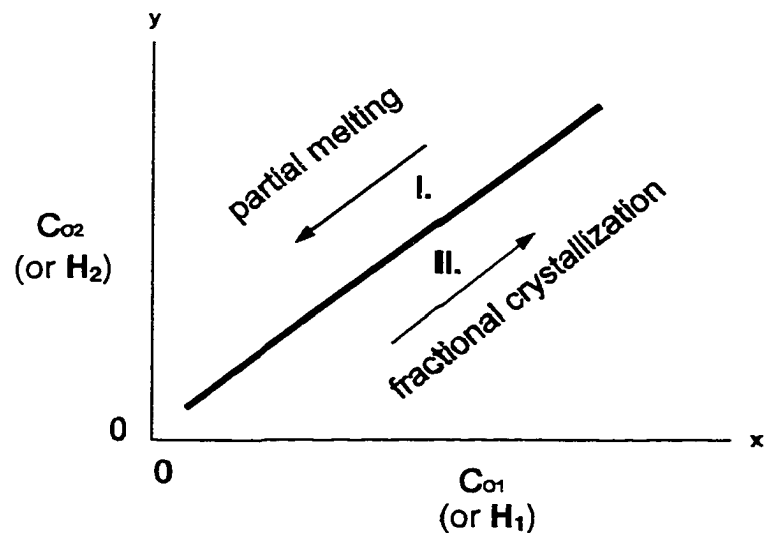


Figure 15. Time trends in an array may yield preliminary information about magmatic processes (younging in direction of arrow). Trend "I" indicates batch partial melting. Trend "II" corresponds to batch fractional crystallization. (After Trueill *et al.*, 1977).

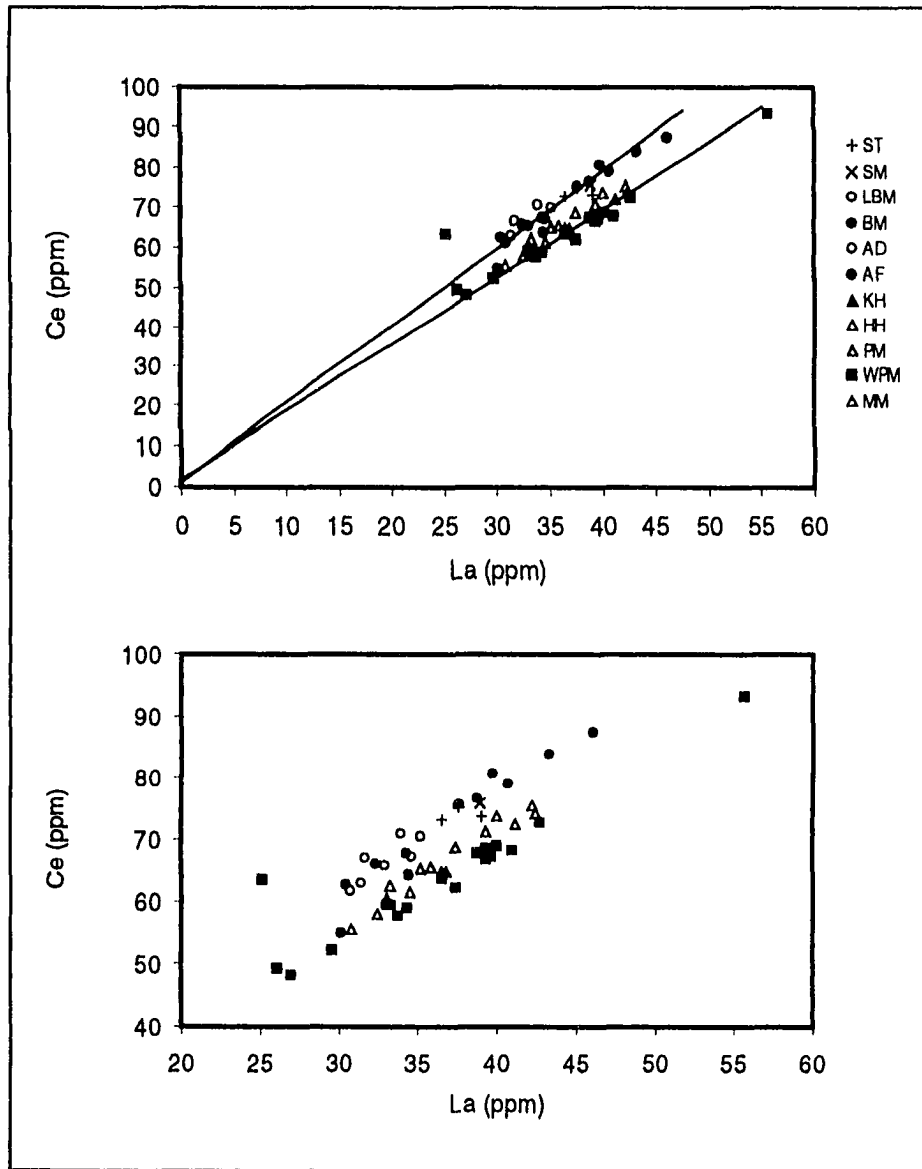


Figure 16. Highly incompatible element versus highly incompatible element diagrams (H vs H): La versus Ce. (a) With arrays and (b) closer view without arrays.

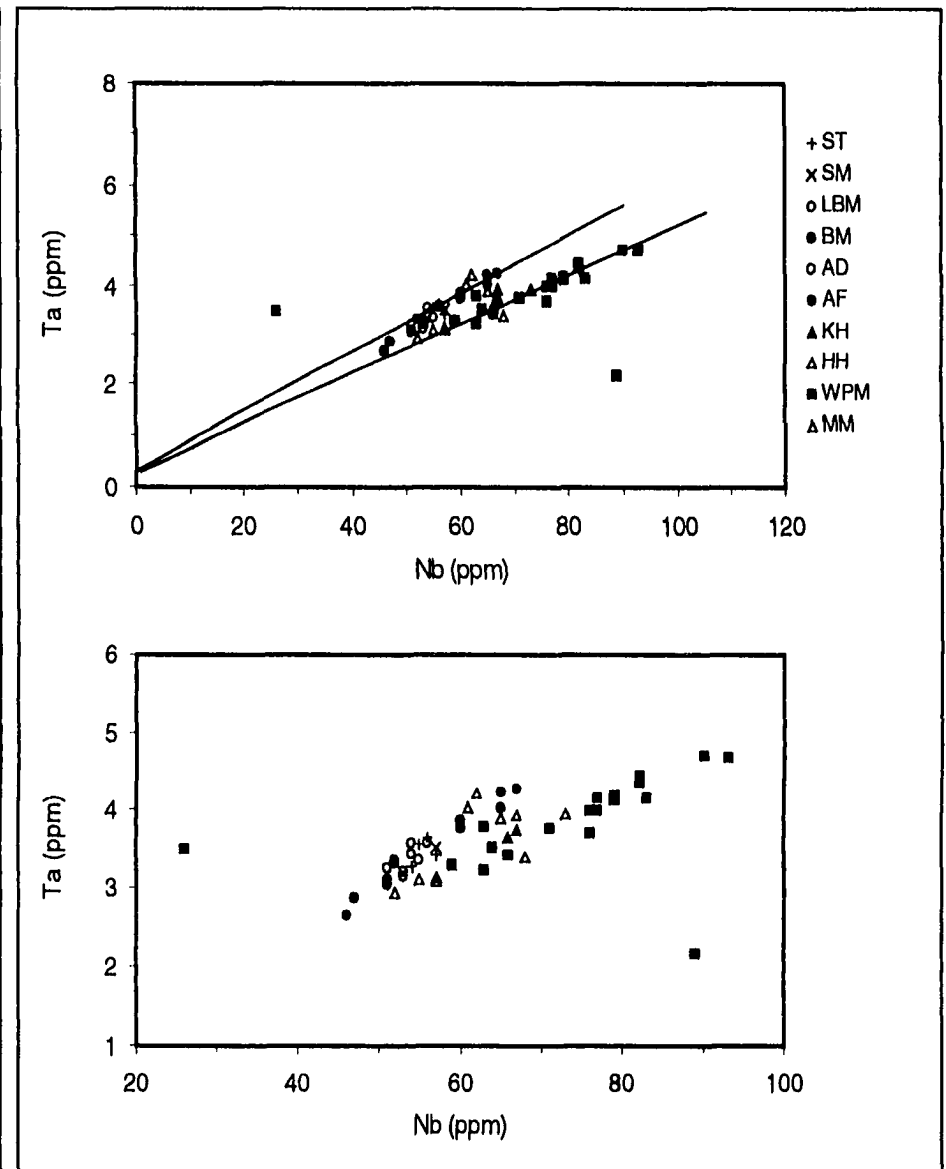


Figure 17. Highly incompatible element versus highly incompatible element diagrams (H vs H): Nb versus Ta. (a) With arrays and (b) closer view without arrays.

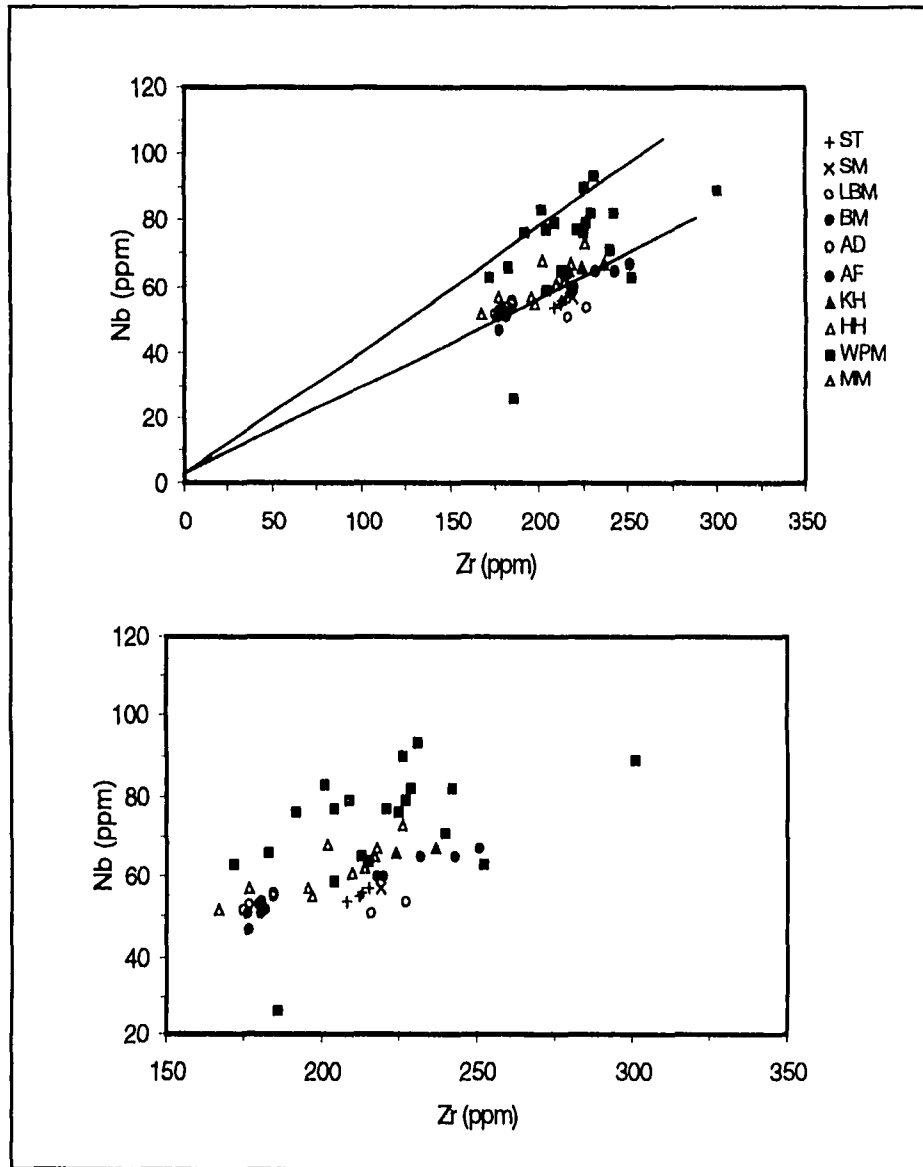


Figure 18. Highly incompatible element versus highly incompatible element diagrams (H vs H): Zr versus Nb. (a) With arrays and (b) closer view without arrays.

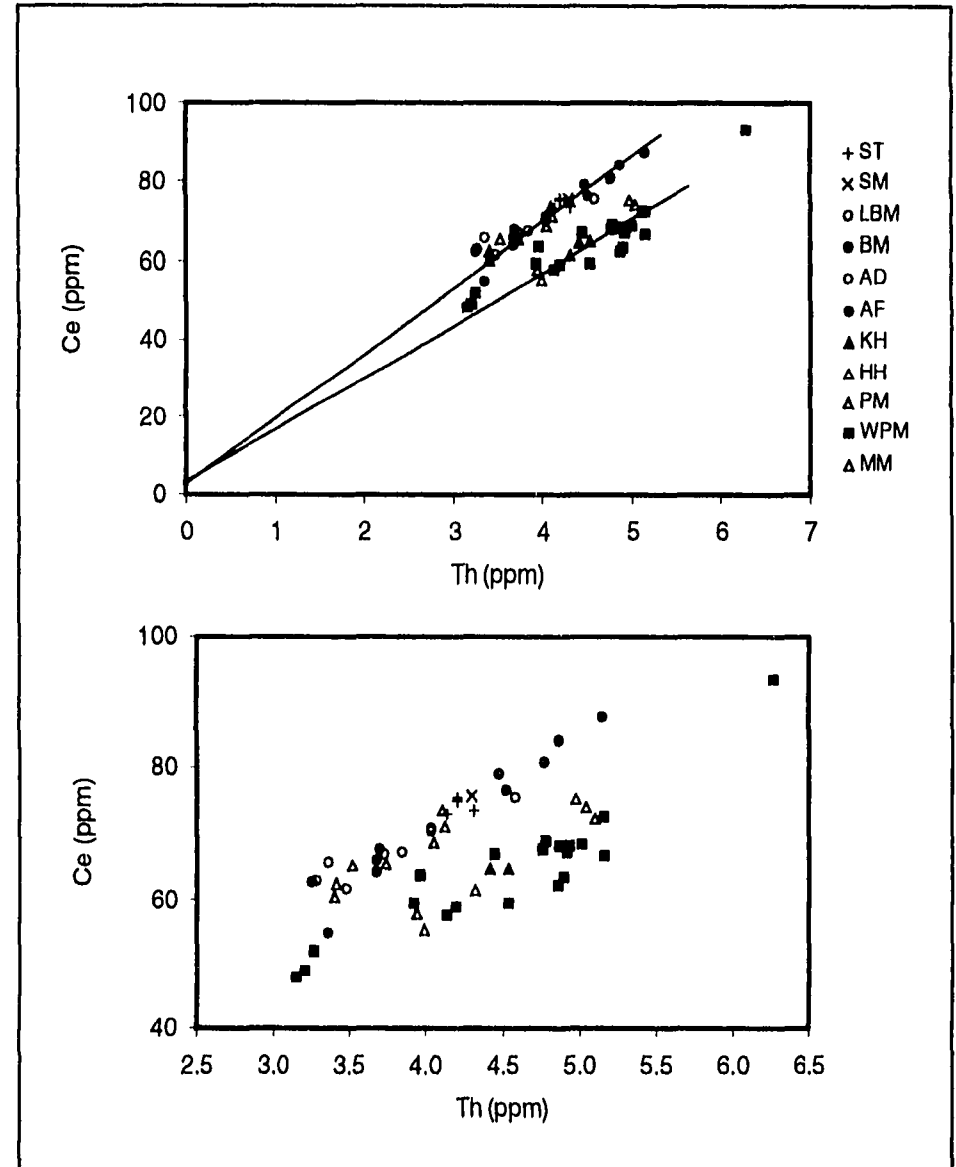


Figure 19. Highly incompatible element versus highly incompatible element diagrams (H vs H): Th versus Ce. (a) With arrays and (b) closer view without arrays.



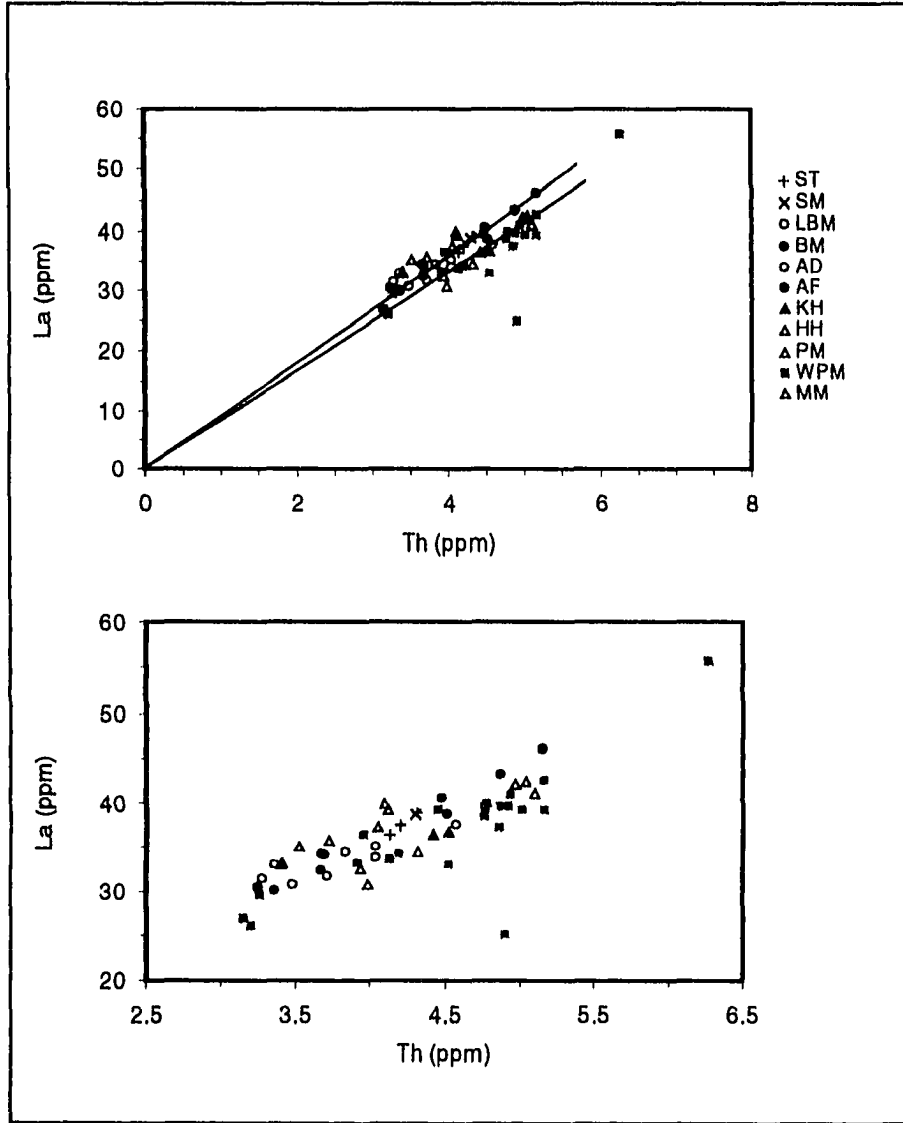


Figure 20. Highly incompatible element versus highly incompatible element diagrams (H vs H): Th versus La. (a) With arrays and (b) closer view without arrays.

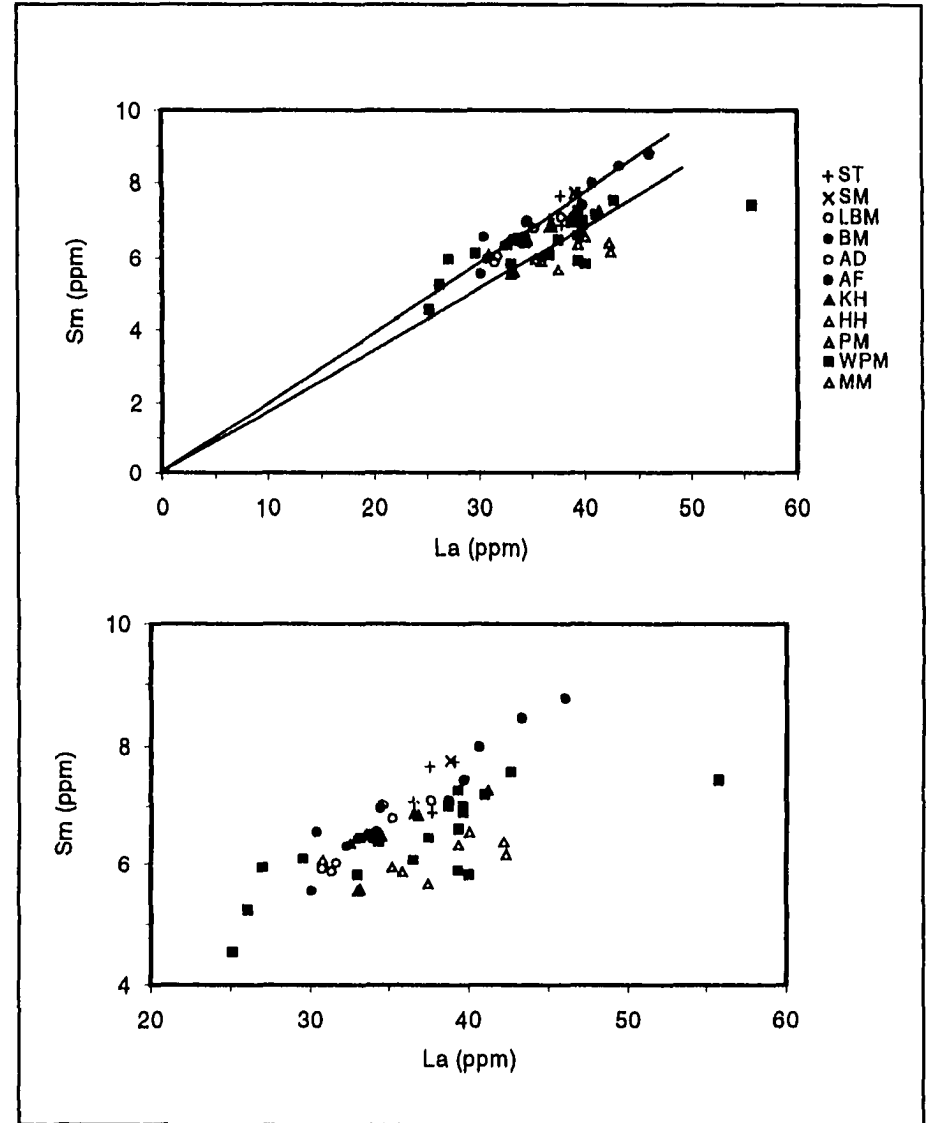


Figure 21. Highly incompatible element versus highly incompatible element diagrams (H vs H): La versus Sm. (a) With arrays and (b) closer view without arrays.

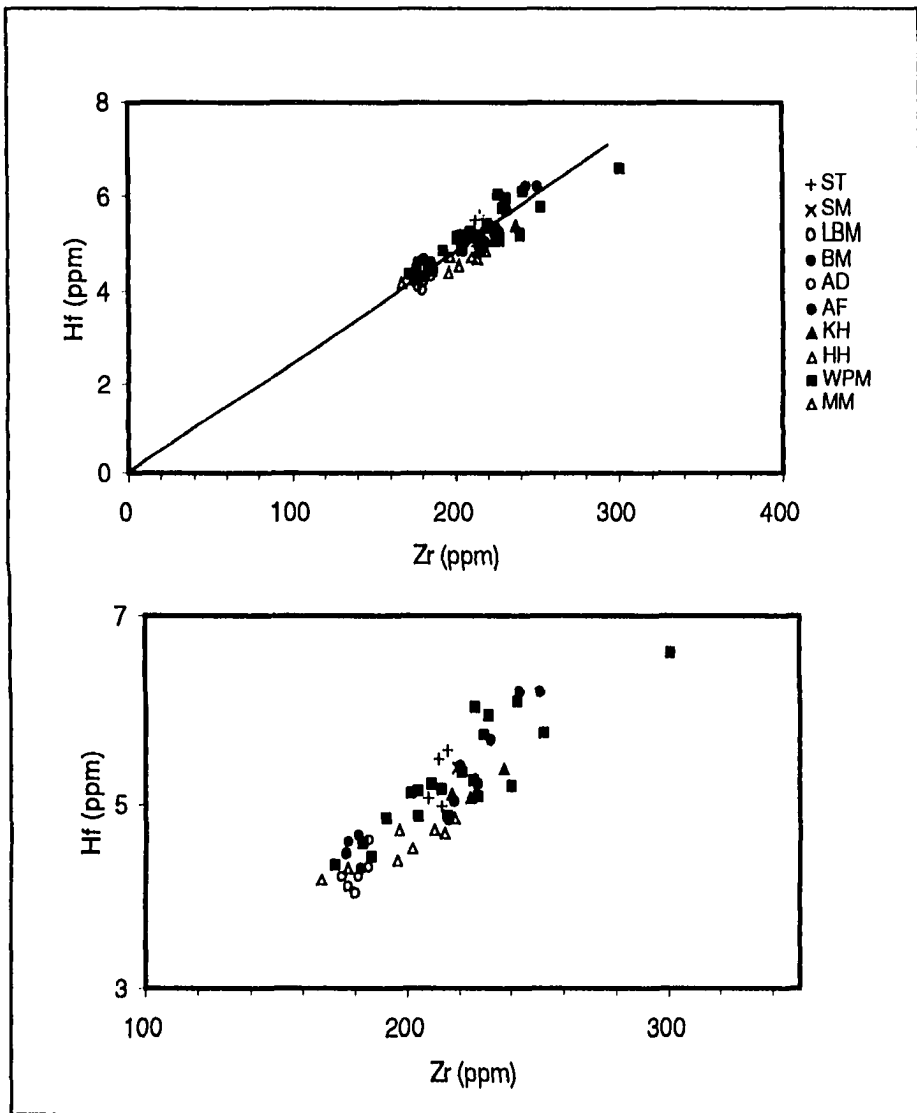


Figure 22. Highly incompatible element versus highly incompatible element diagrams (H vs H): Zr Versus Hf. (a) With array and (b) closer view without array.

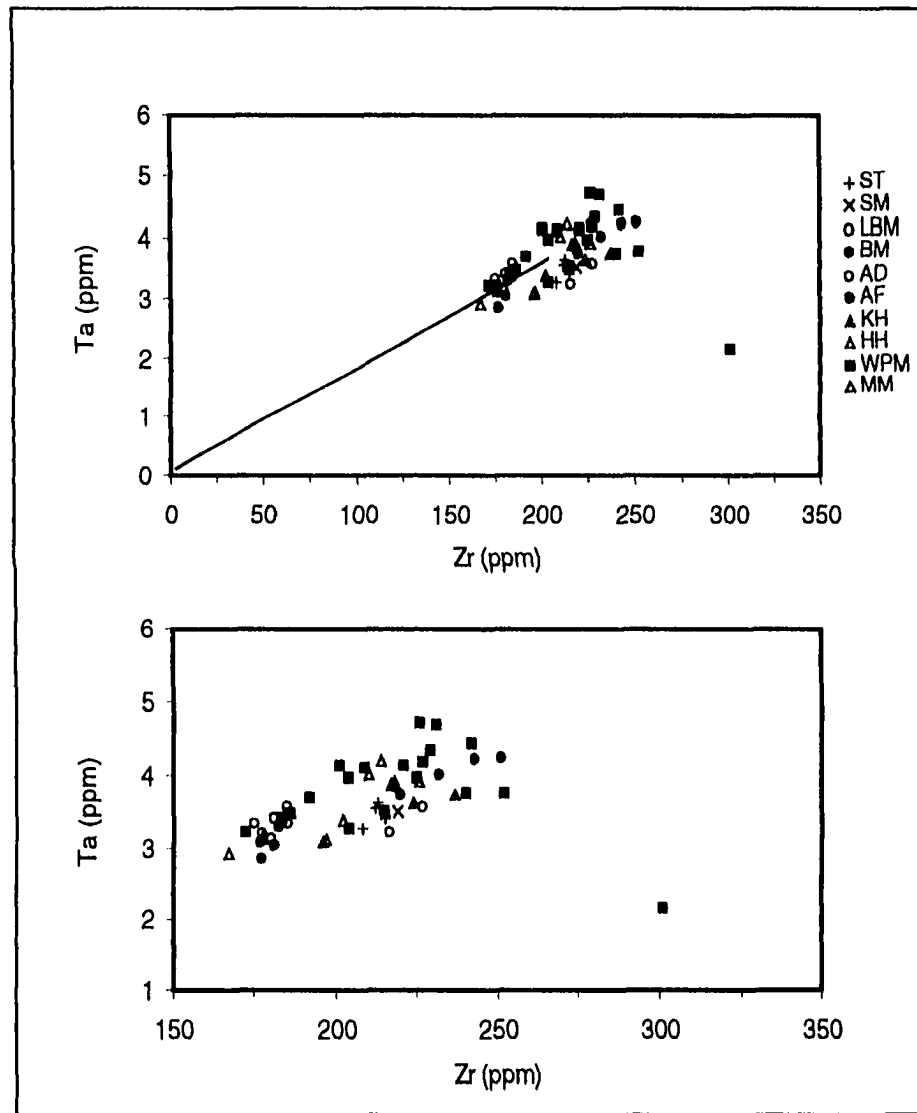


Figure 23. Highly incompatible element versus highly incompatible element diagrams (H vs H): Zr versus Ta (a) With array and (b) closer view without array.

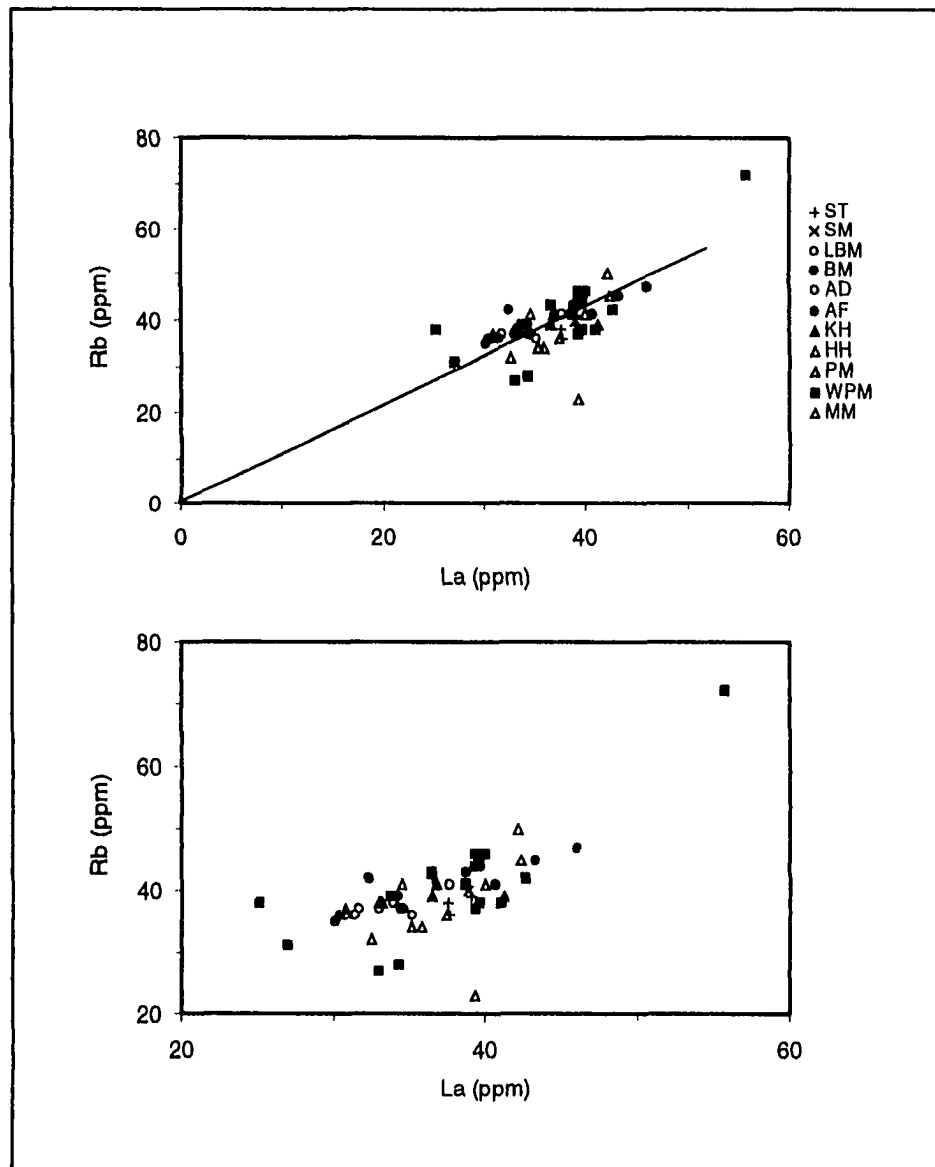


Figure 24. Highly incompatible element versus highly incompatible element diagrams (H vs H): La versus Rb. (a) With array and (b) closer view without array.

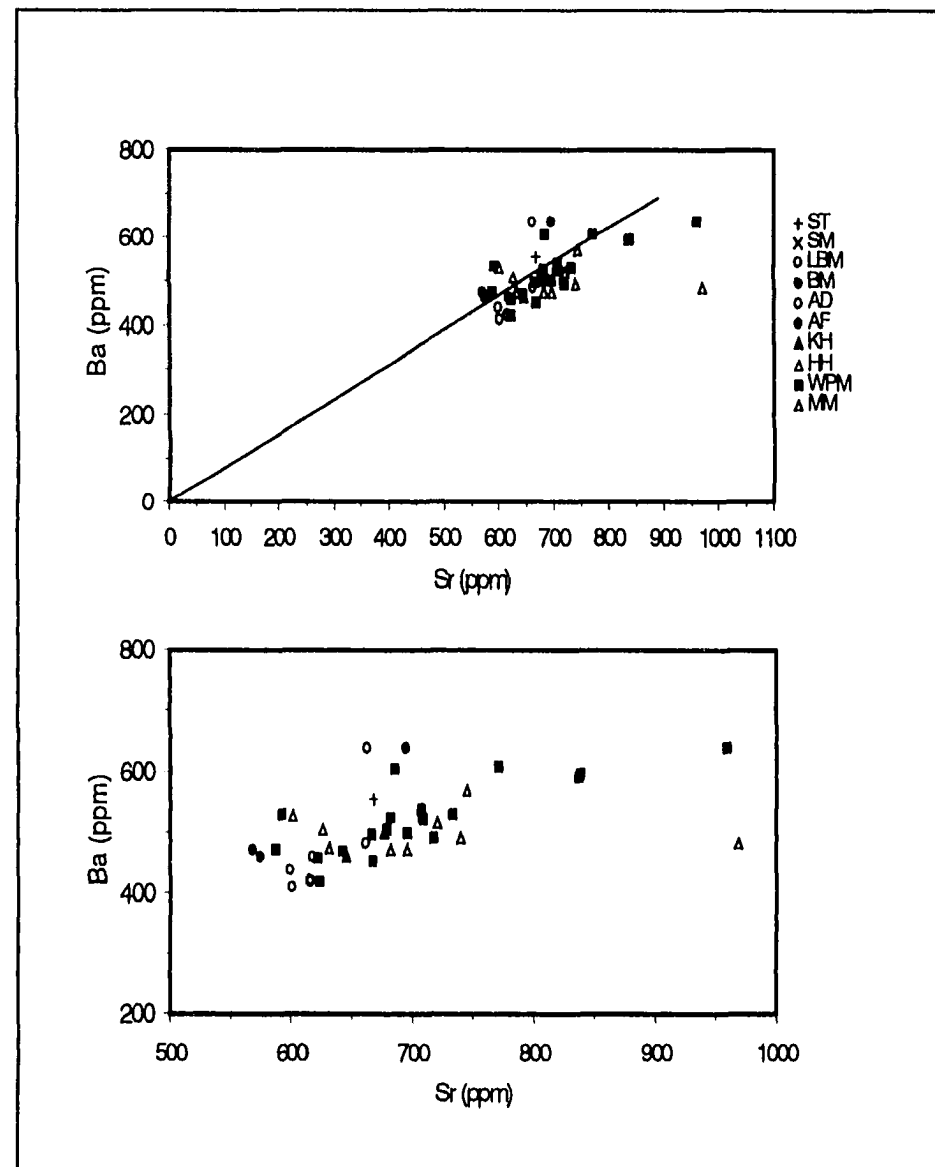


Figure 25. Highly incompatible element versus highly incompatible element diagrams (H vs H): Sr versus Ba. (a) With array and (b) closer view without array.

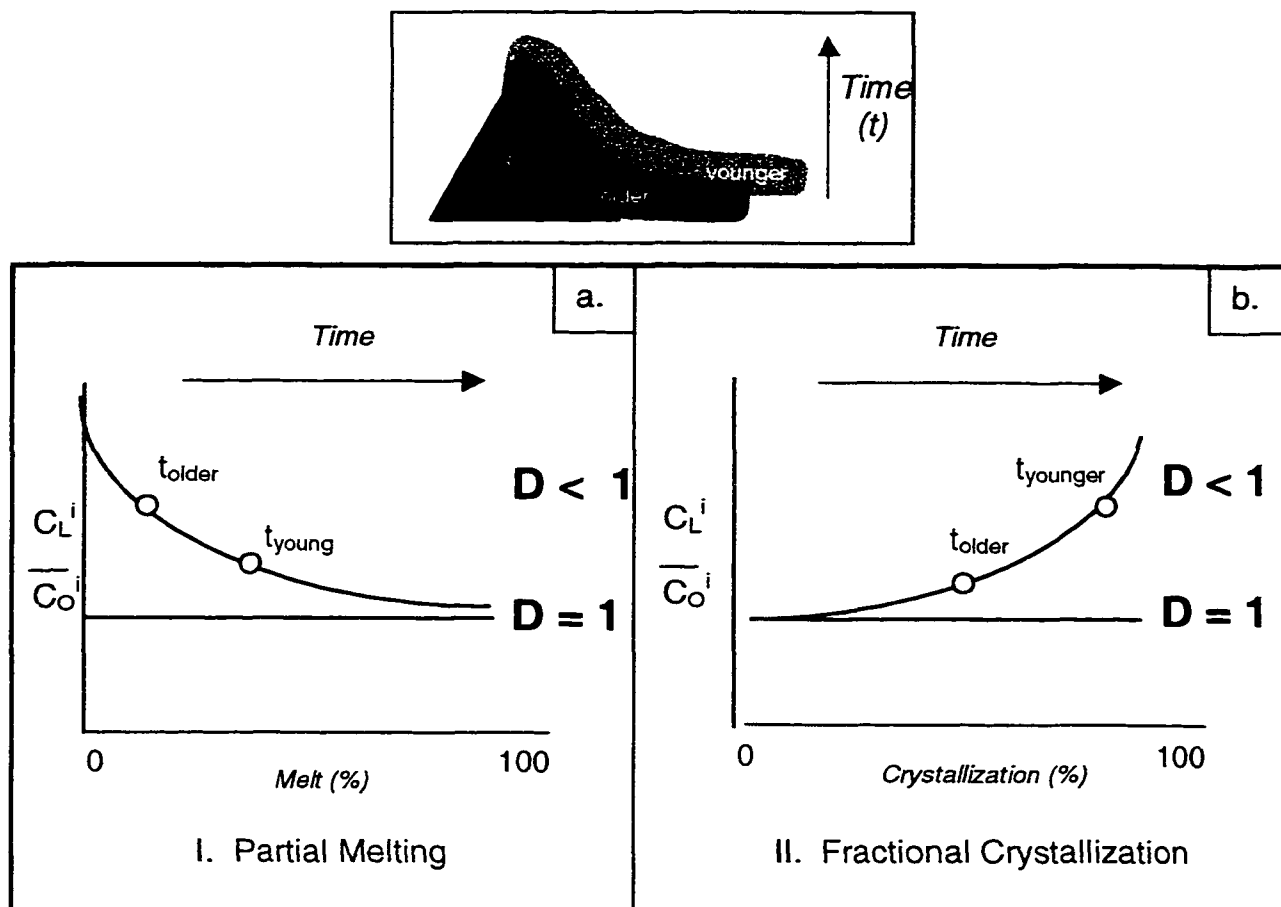


Figure 26. Degrees of magmatic processes as interpreted from incompatible element ratios with time: (a) batch partial melting processes will result in lowering of the ratio with increasing degree of melt extraction but (b) demonstrates the theory behind the correspondence of an increasing ratio with increasing percentage of batch fractional crystallization.

The lavas from the eastern and central alignments, which we know to be young, do not show any systematic changes with regard to the lavas from the western alignment, many of which we know to be old. In addition, systematic changes are not apparent within each of the three alignments. We can conclude from this that magmas in the Potrillo volcanic field represent neither continuous melt extraction from a homogeneous source nor periodic tapping of a continuously fractionating magma chamber.

#### **5.2.4 Incompatibles: H/M versus H**

Treuil *et al.* (1977) demonstrated that it is possible to develop H/M versus H diagrams that assist in distinguishing magmatic processes (Figure 27). This is accomplished by identifying correlations between highly (H) incompatible elements with moderately (M) or incompatible elements. As labeled in the figure, partial melting will produce an inclined positive sloping array such that higher ratios are associated with lower degrees of melting. Fractional crystallization processes will display a nearly horizontal trend such that greater highly incompatible concentrations are due to higher degrees of crystallization. Source heterogeneity will also show up on this diagram, therefore one must use a combination of H versus H and H/M versus H diagrams to fully understand the magmatic processes.

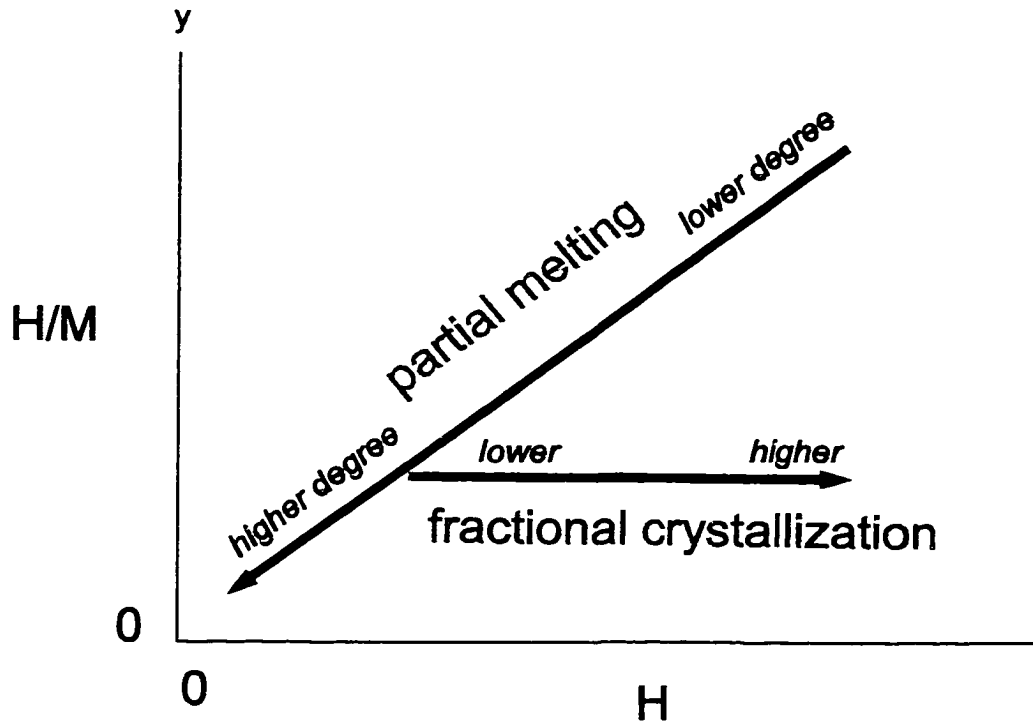


Figure 27. Magmatic process identification using a highly incompatible element concentration (H) versus the ratio H/M of the same highly incompatible element divided by a moderately incompatible element (after Trueill *et al.*, 1977). Partial melting processes are shown by a positively sloping array such that lower degrees of partial melting are associated with higher concentrations of incompatible elements, whereas higher degrees of partial melting are represented by lower elemental signatures. Fractional crystallization results in a horizontal to sub-horizontal array, with lower degrees of crystallization are correlated with lower amounts of H.

For application to the Potrillo volcanic field data, H and M elements were first selected using the enrichment diagrams included in Section 5.2.1. Those considered highly incompatible include Ce, La, Nb, Sr, Ta, Th, and Zr. These have been set as ratios with several moderately incompatible elements (such Sm and Yb). The following comments will be based upon Figures 28 through 35.

On the basis of H/M versus H plots, the majority of western melts are at high H/M with a broad range in the degree of partial melting and central melts are low on the partial melting trajectory and display much less variability. In contrast, the eastern lavas move off this trajectory toward one for fractional crystallization; however, these melts are anchored to lower partial melt characterizing the central compositions. This finding for the eastern lavas is consistent with the overall lower Mg #s determined for these melts, suggesting differentiation. This scenario is complicated by the presence of two arrays on the H versus H diagrams (Section 5.2.3) indicates that there is source heterogeneity involved such that the central plus eastern alignments define one array and the western alignment another. Thus, the position along an array or the trajectory must be some combination involving degree of partial melting and source heterogeneity. The relative contributions of these will be discussed in Chapter 6.

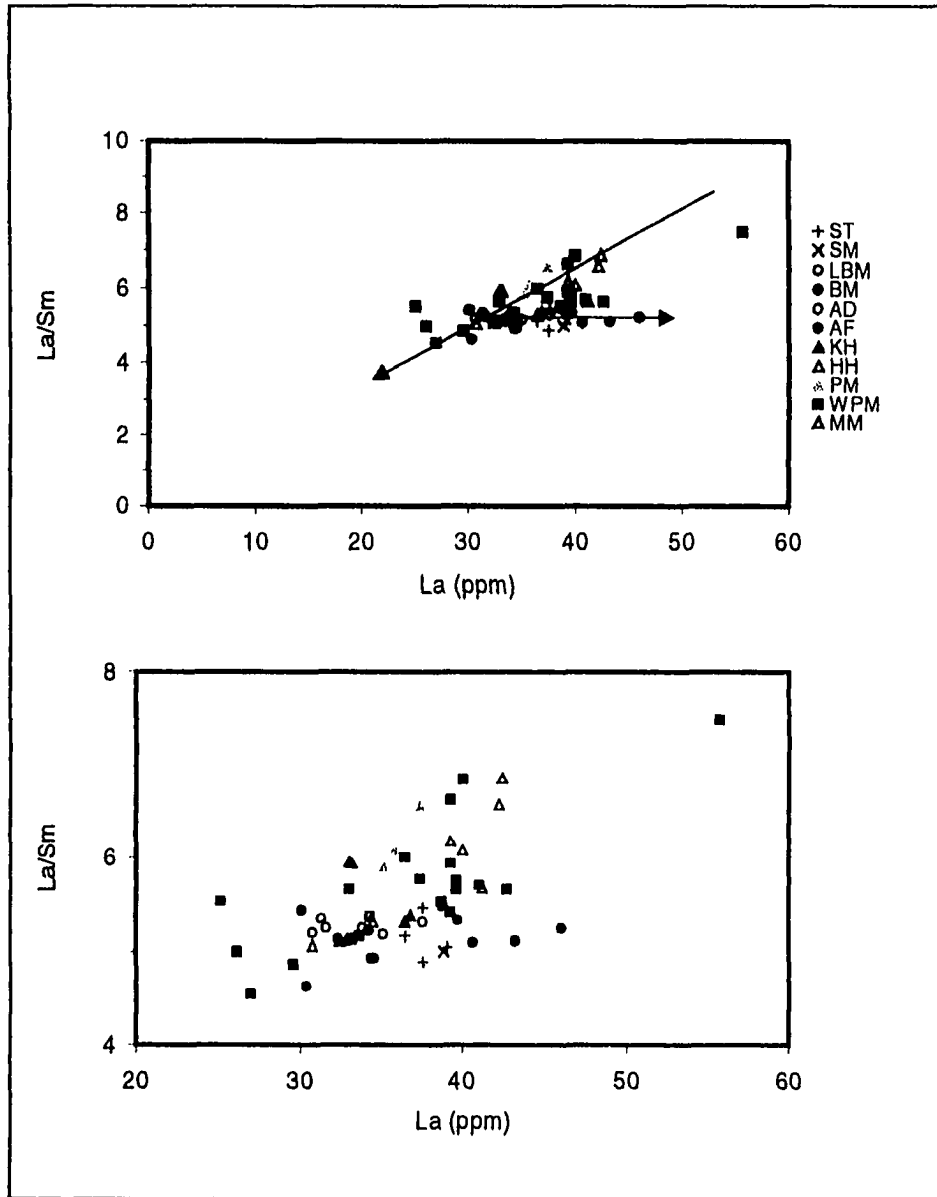


Figure 28. Highly incompatible element versus ratio of same highly incompatible element to moderately incompatible element plot for magmatic process identification: La versus La/Sm. (a) With arrays and (b) closer view without arrays.

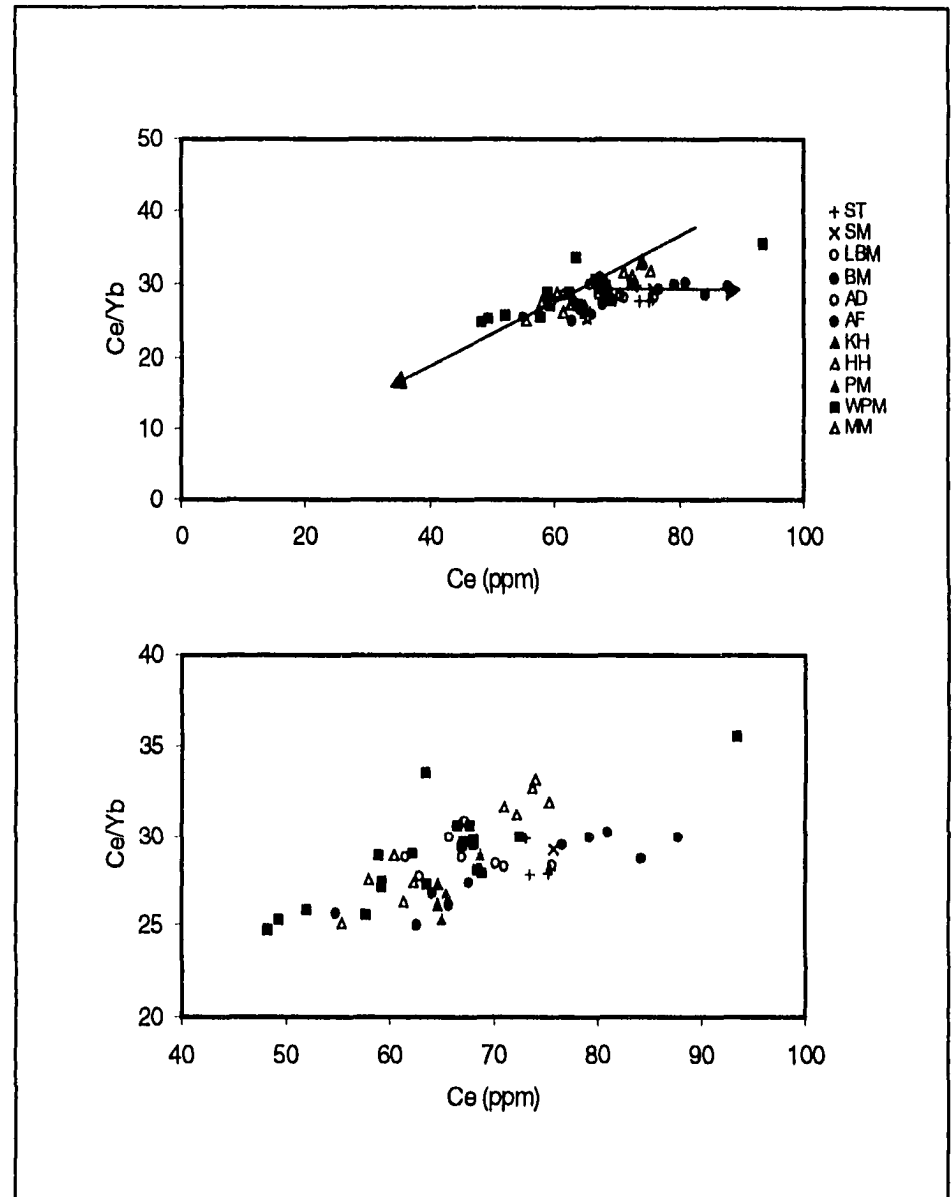


Figure 29. Highly incompatible element versus ratio of same highly incompatible element to moderately incompatible element plot for magmatic process identification: Ce versus Ce/Yb. (a) With arrays and (b) closer view without arrays.



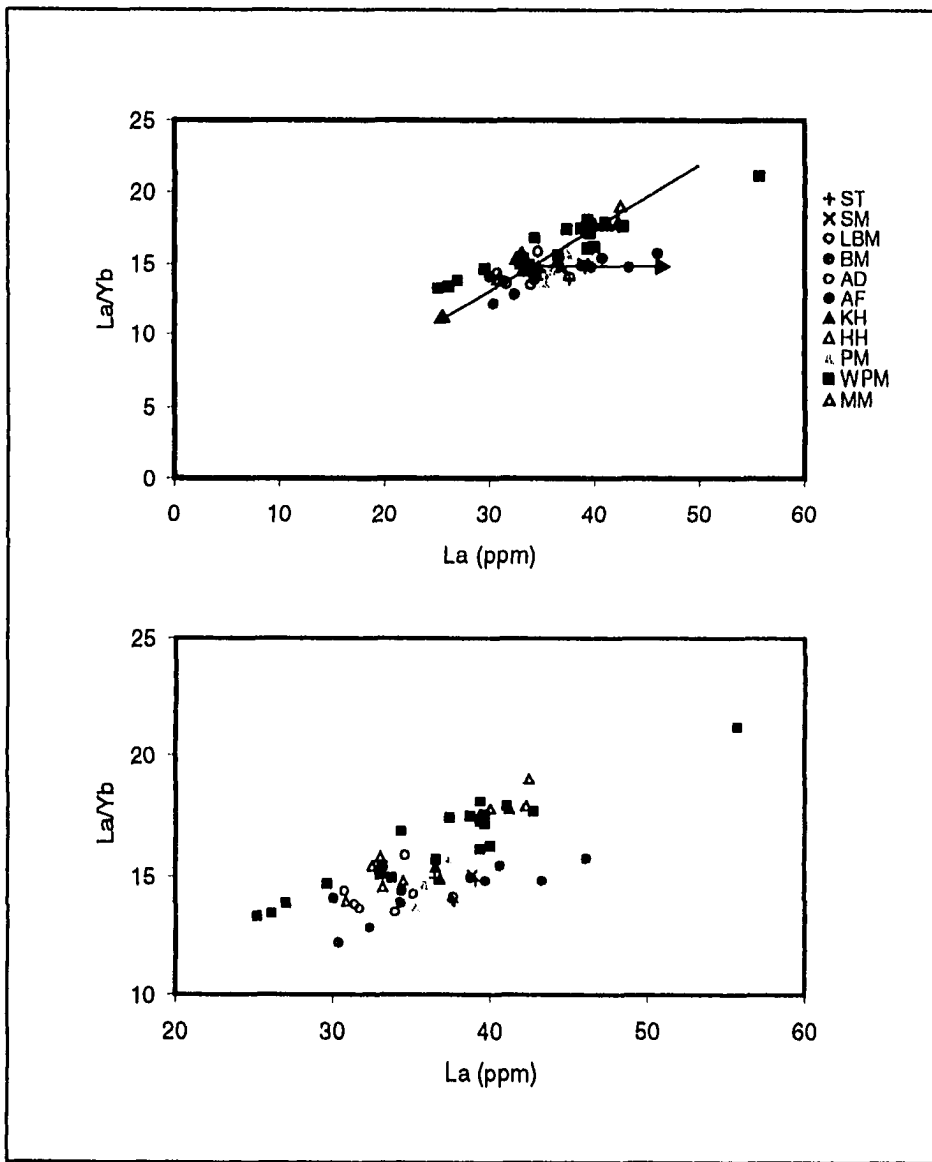


Figure 30. La versus La/Yb for Potrillo volcanic field. (a) With arrays superposed and (b) data with closer view without arrays.

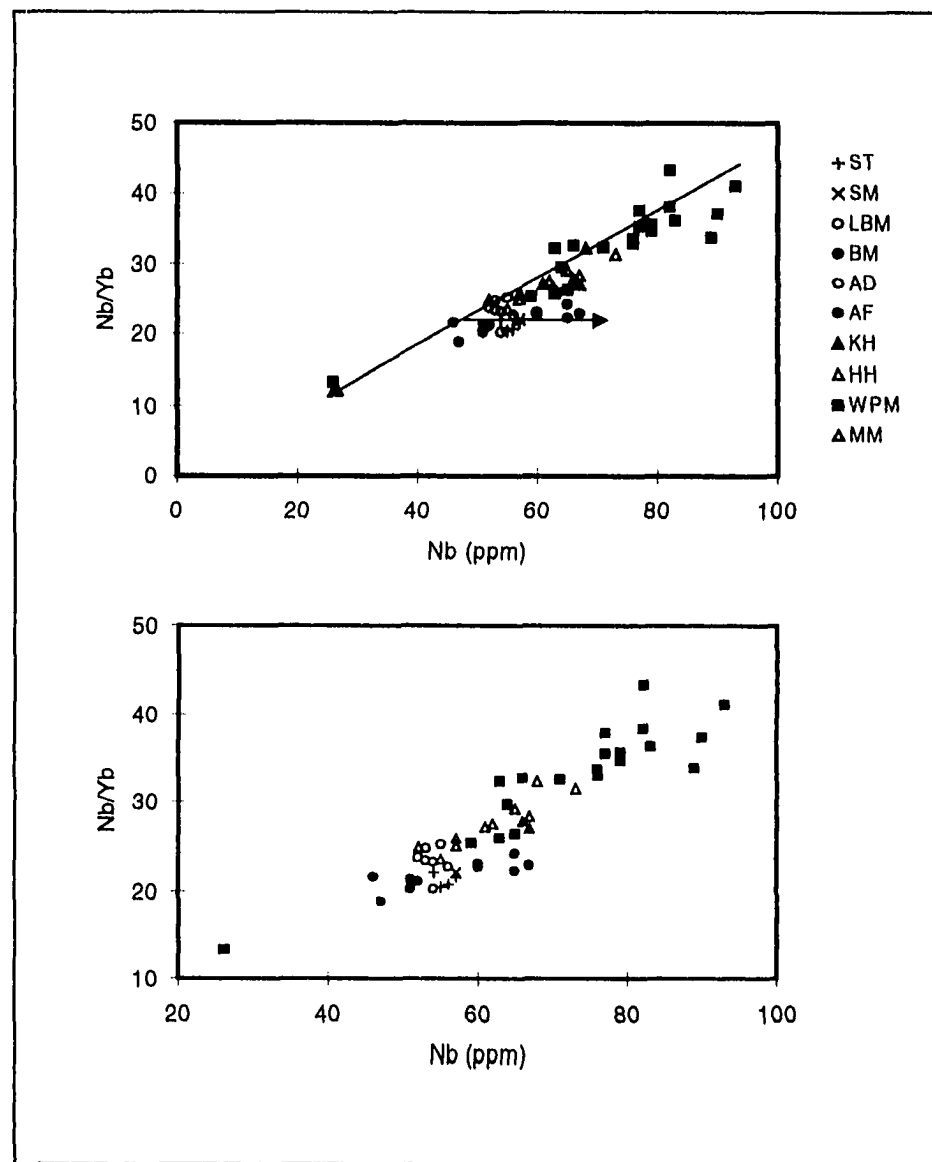


Figure 31. Nb vs Nb/Yb for Potrillo volcanic field. (a) With arrays superposed and (b) data with closer view without arrays.

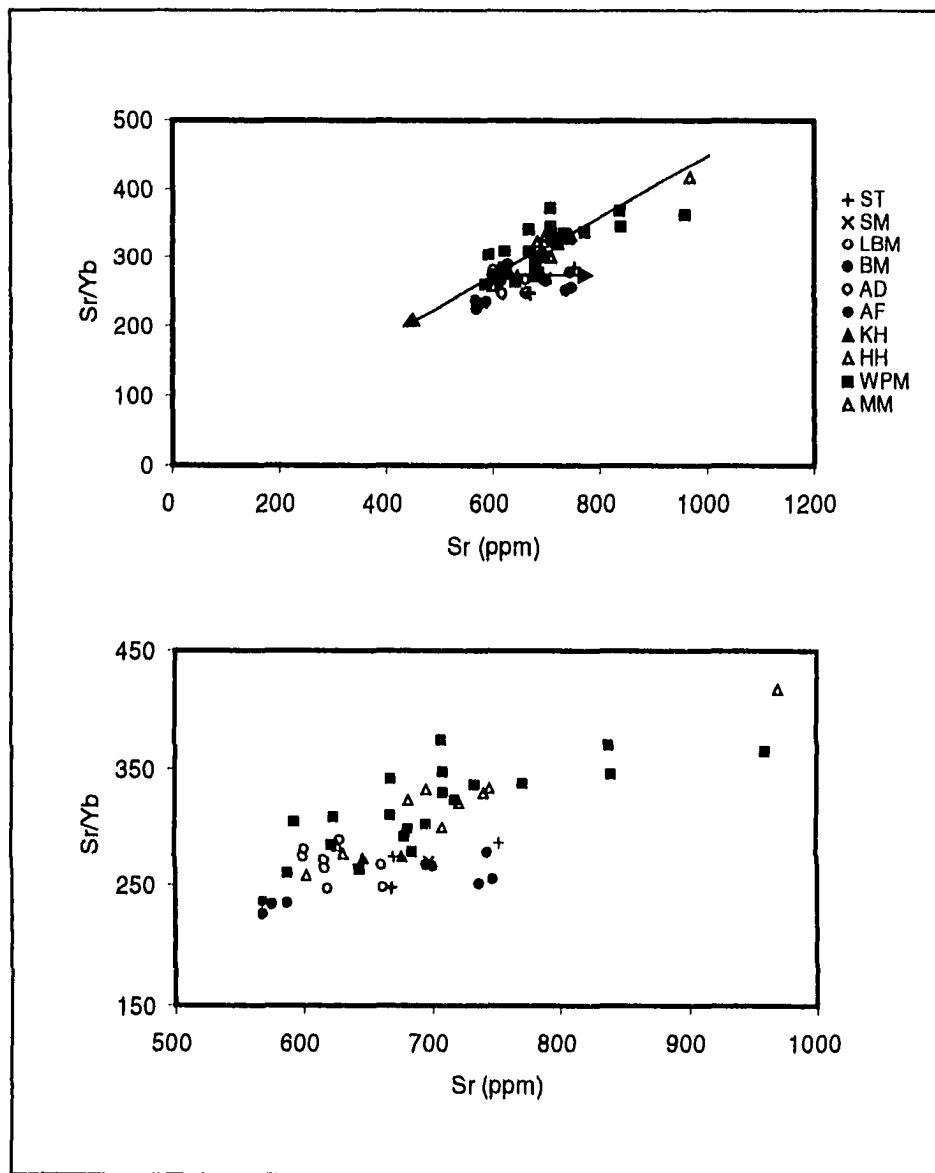


Figure 32. Sr Versus Sr/Yb for Potrillo volcanic field. (a) With arrays superposed and (b) data with closer view without arrays.

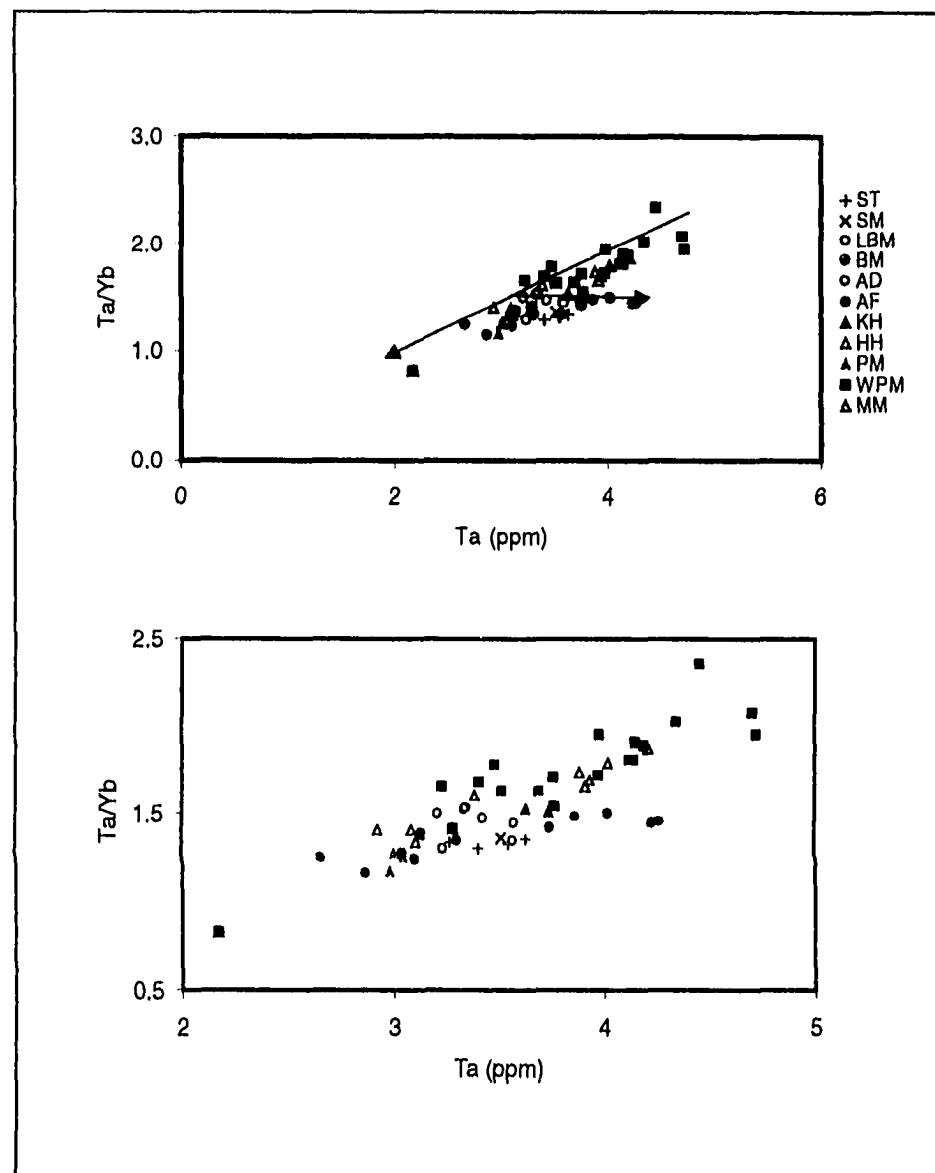


Figure 33. Ta Versus Ta/Yb for Potrillo volcanic field. (a) With arrays superposed and (b) data with closer view without arrays.

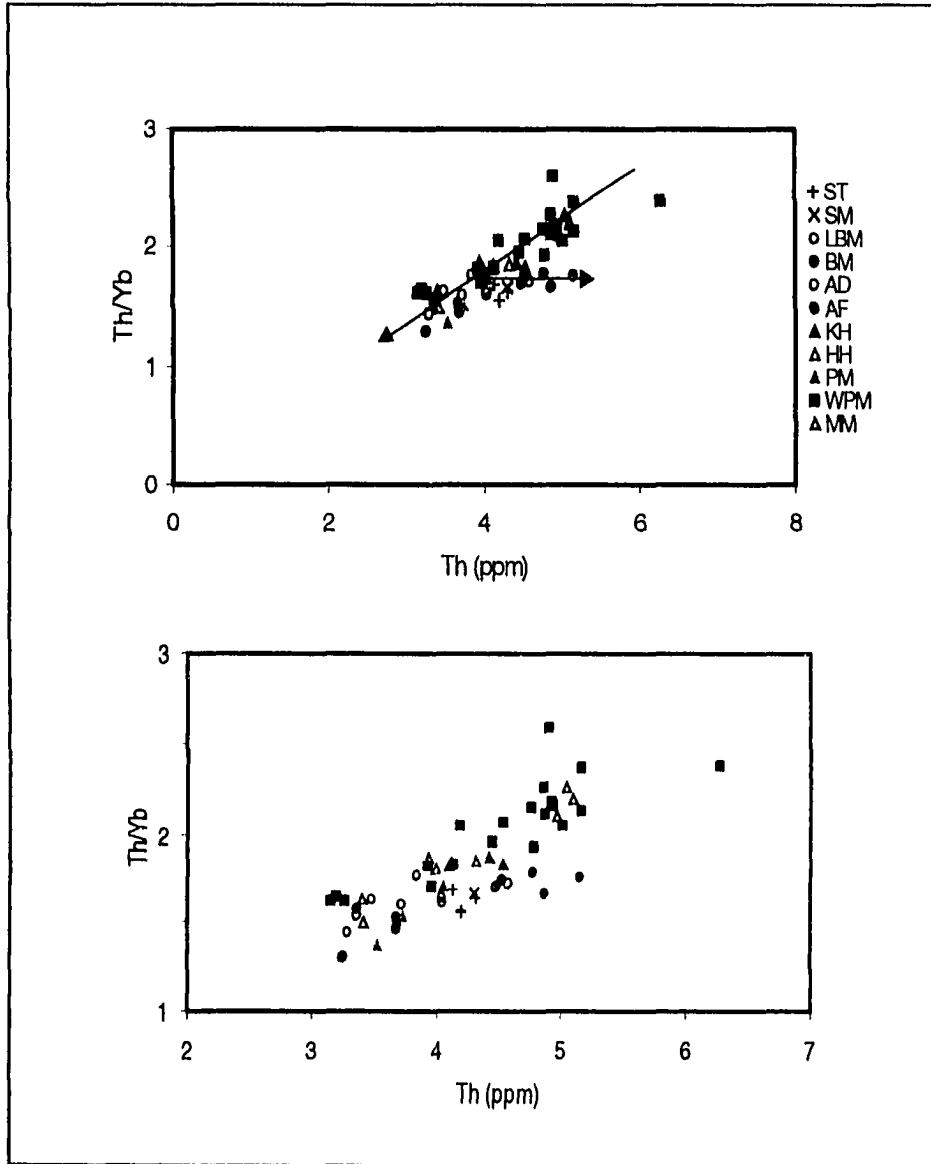


Figure 34. Th Versus Th/Yb. (a) Data with arrays and (b) closer view without arrays.

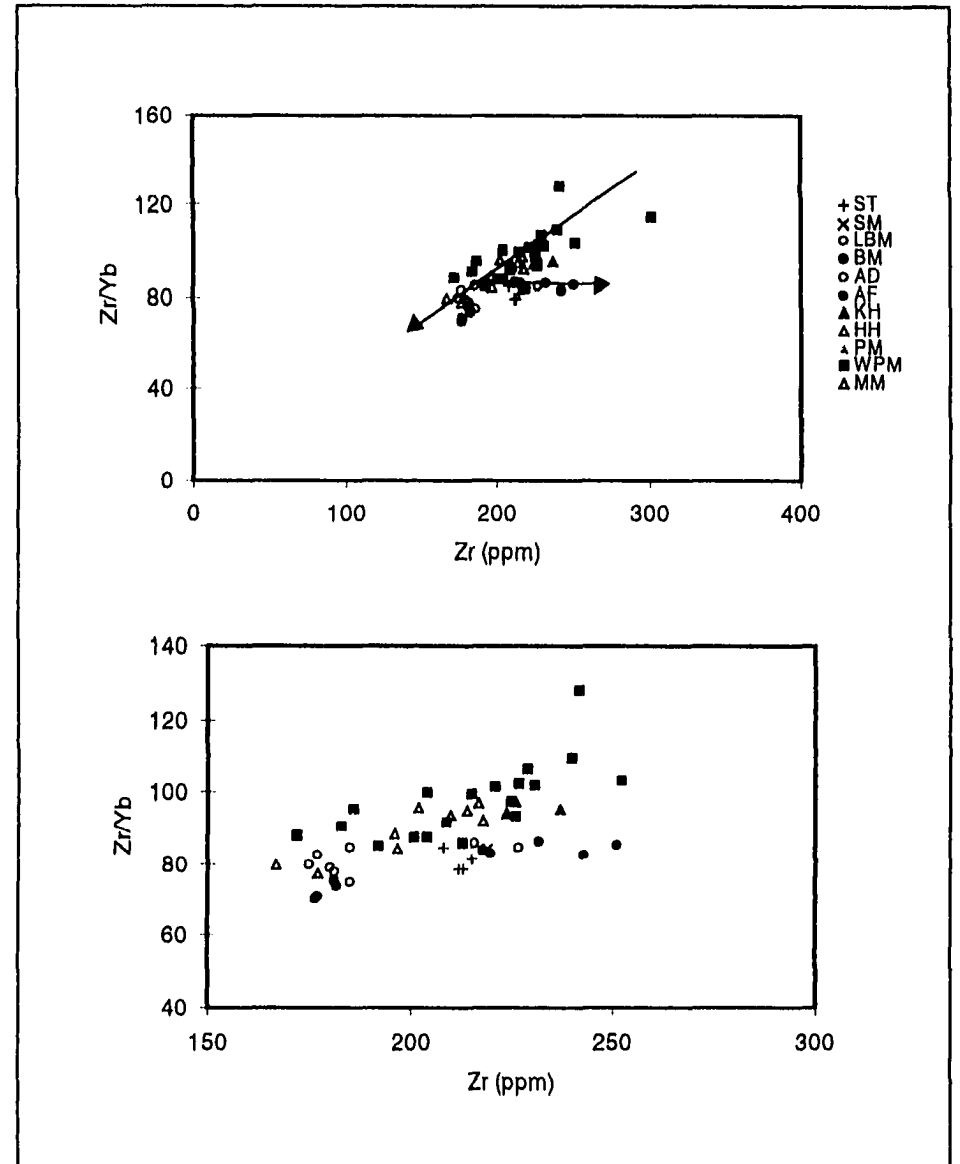


Figure 35. Zr Versus Zr/Yb . (a) Data with arrays and (b) closer view without arrays.

### 5.3 Relationship of Major and Trace (Incompatible) Elements

The role of phenocrystic plagioclase and clinopyroxene during the evolution of magmas can be understood using plots such as Figure 36 where Mg # is presented considering Sr and Sc behavior. Sr partitions into plagioclase whereas Sc goes into clinopyroxene during crystallization. Information from such plots includes recognizing that constant Sr with decreasing Mg # may indicate buffering of Sr during plagioclase fractionation, and that lower Sc contents with higher Mg # indicate clinopyroxene fractionation. If no phenocrysts are modally evident, the signature may indicate that during an earlier evolutionary stage this fractionation was important. This is the case with the Potrillo melts, where clinopyroxene is not a significant phenocrystic phase.

The data from the Potrillo volcanic field show two clusters. The first group is defined primarily by the eastern alignment. Recall that Mg # is indicative of the degree of magma evolution. Therefore, the eastern alignment shows higher degrees of crystal fractionation than the majority of both the central and western melts in that the Mg # decreases systematically as primitive mafic parent magmas fractionate olivine and clinopyroxene. As has been discussed above, this is supported by the modal mineralogy (Figure 12). Several West Potrillo Mountains flows (including 3 of the 4 reverse polarity flows) fall within the eastern range, particularly with respect to Sc and Mg #s. It may be that these older

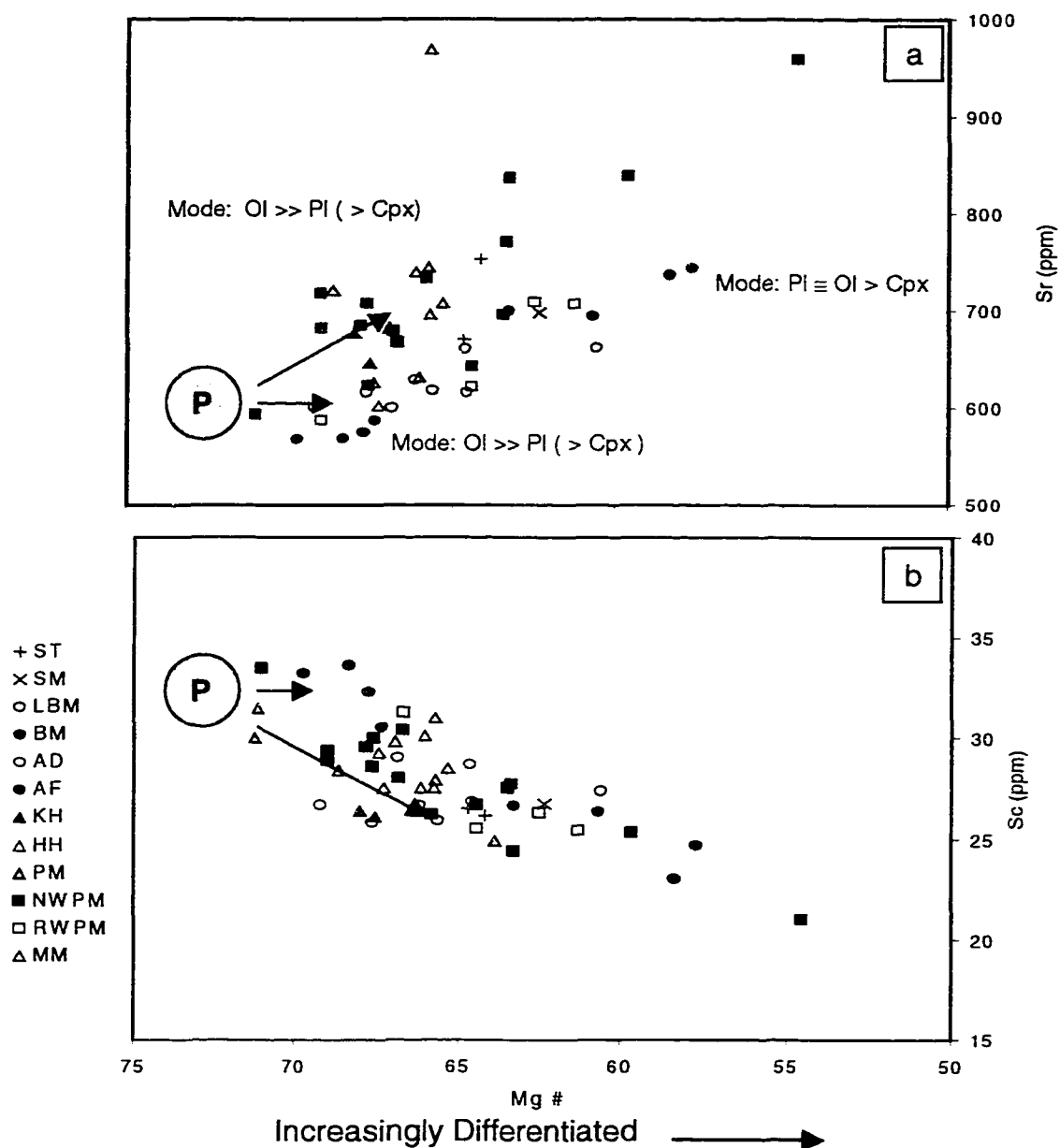


Figure 36. Plots showing relationship of Mg # versus two incompatible elements (Sr and Sc). (a) Mg # against Sr is sensitive to plagioclase (Pl) precipitation. Decreasing Sr concentration corresponds with increasing importance of plagioclase; this is not seen with the PVF data. (b) Mg # versus Sc shows current or prior history of clinopyroxene (Cpx) precipitation; decreasing Sc with decreasing Mg # corresponds with increasing role of Cpx. Modes are for phenocryst assemblages point-counted by Chen (1991). (P) indicates a hypothetical parent melt .

flows also underwent similar degrees of fractionation. A hypothetical parent magma is also denoted on Figure 36.

Thorium behaves incompatibly with respect to the melt, therefore it is a good indicator of the degree of partial melting. Experimental studies of partial melt in spinel peridotites show that until clinopyroxene is gone, increased melting leads to liquids with progressively decreased Th and  $\text{Al}_2\text{O}_3$  but progressively increased CaO and  $\text{CaO}/\text{Al}_2\text{O}_3$  concentrations. Stated differently, melting of a spinel peridotite in the presence of clinopyroxene causes CaO in the melt to increase and the  $\text{Al}_2\text{O}_3$  to decrease. It follows, then, that the  $\text{CaO}/\text{Al}_2\text{O}_3$  ratio would increase with the decreasing  $\text{Al}_2\text{O}_3$ . Also, a decrease in pressure results in progressively higher  $\text{Al}_2\text{O}_3$  in melts (Jacques and Green, 1980).

Luhr *et al.* (1995) compared the San Quintín volcanic field to several extensional intracontinental suites from Africa (Huri Hills), SE Australia, and Mexico (Ventura and La Brena) as well as non-extensional volcanism at Honolulu. I have plotted data for individual complexes with Mg #s greater than 64 from the Potrillo volcanic field along with data from the San Quintín volcanic field and these suites (adapted from Luhr *et al.*, 1995). This compilation is presented as Figure 37. Luhr *et al.* (1995) found that lavas with Mg #s greater than 64 from the San Quintín volcanic field display trends for Th versus CaO,  $\text{Al}_2\text{O}_3$  and  $\text{CaO} / \text{Al}_2\text{O}_3$ , which are different than the other intracontinental suites. For instance, the  $\text{Al}_2\text{O}_3$

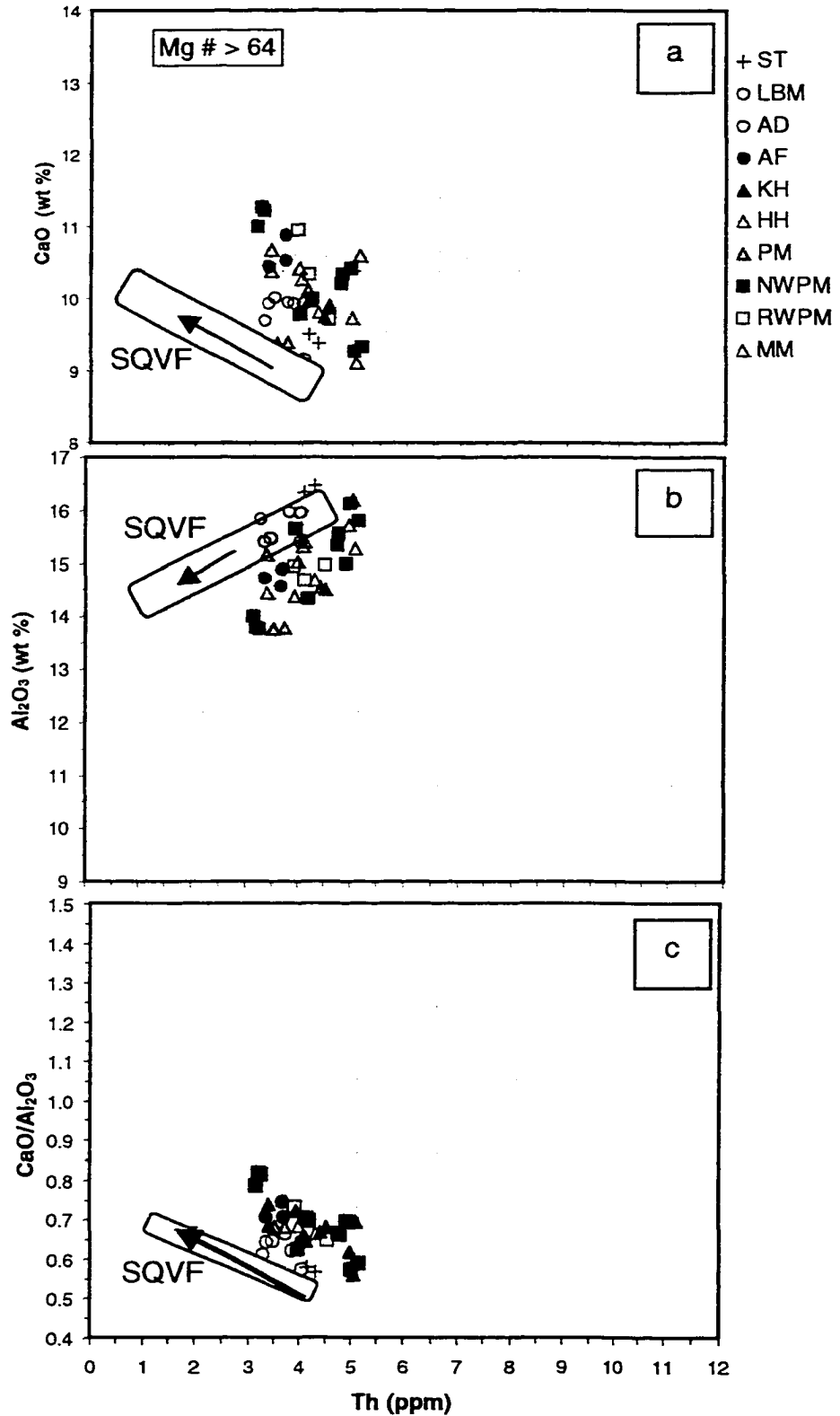


Figure 37. CaO, Al<sub>2</sub>O<sub>3</sub>, and CaO/ Al<sub>2</sub>O<sub>3</sub> versus Th for primitive samples from Potrillo volcanic field. SQVF – San Quintin volcanic field, Baja California Norte and other suites considered in Luhr *et al.* (1995) indicated by grey fields. Arrows denote general younging trends.

values for the San Quintín volcanic field are unusually high and CaO/ Al<sub>2</sub>O<sub>3</sub> unusually low. The Potrillo volcanic field has similar ranges, but higher Th values than primitive melts from San Quintín.

Luhr *et al.* (1995) interpret the difference between the San Quintín volcanic field and other intraplate, extensional volcanic fields to reflect that San Quintín melts are derived from shallow spinel mantle whereas the others are from deeper garnet mantle. The similarity of the Potrillo primitive melts to the San Quintín volcanic field, particularly with regard to high Al<sub>2</sub>O<sub>3</sub>, suggests that the Potrillo volcanic field might also tap shallow asthenospheric mantle. This would be consistent with the low P-wave velocities beneath the Potrillo volcanic field.

Whole rock Mg # versus Ni and K<sub>2</sub>O are presented in Figure 38. As can be seen in Figure 38a, Ni (which is a compatible element) decreases in abundance with decreasing Mg # (*i.e.* has a positively sloping trend). This correlation reflects the importance of olivine as an early phenocrystic phase throughout the history of the Potrillo volcanic field. Unlike Ni, the K<sub>2</sub>O values (Figure 38b) are considerably variable at essentially the same Mg # for the primitive melts. With the exception of Malpais, this spread is not seen in the maar samples. They show restricted K<sub>2</sub>O at 1.6 to 1.8 and Mg #s of 64 to 72. The variability in K<sub>2</sub>O probably results from the source heterogeneity discussed in earlier sections of this chapter. The overall trend of increasing incompatible concentrations with decreasing Mg # (*i.e.*



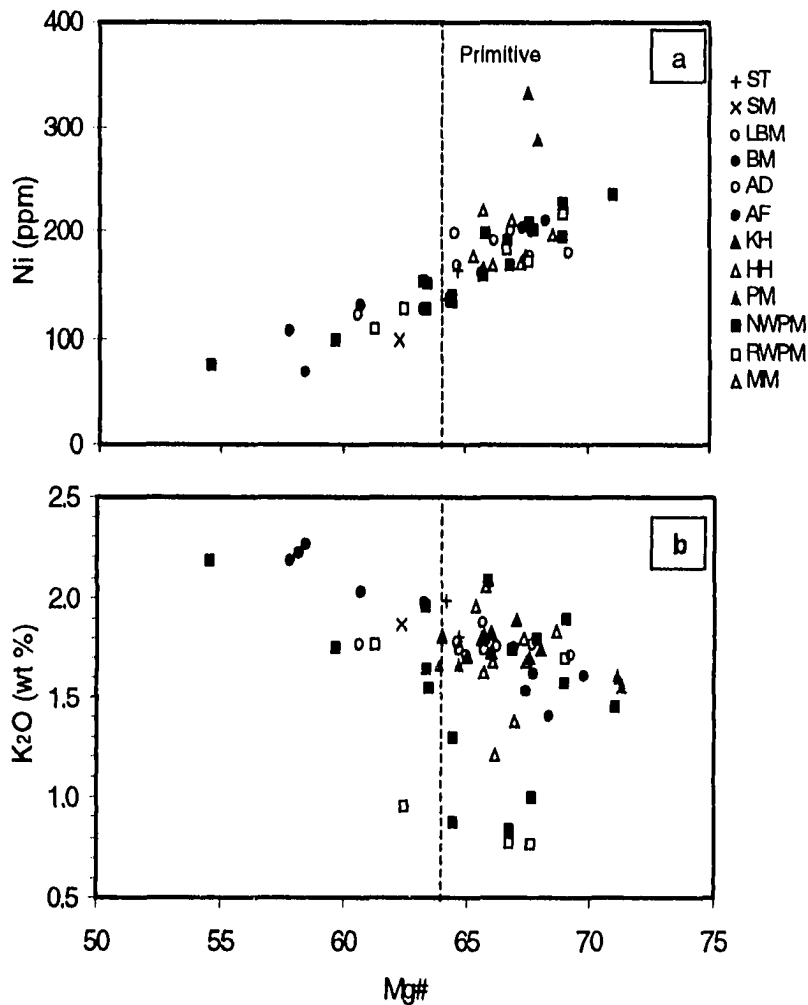


Figure 38. (a) Mg # Versus Compatible Ni. (b) Mg # Versus Incompatible K<sub>2</sub>O.

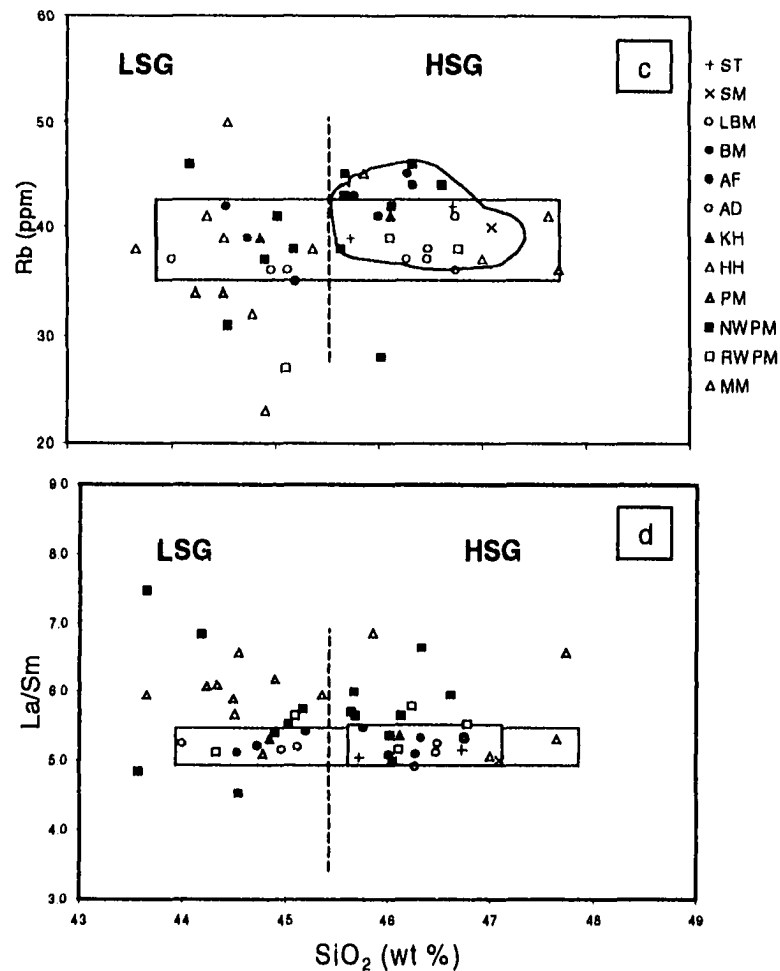


Figure 39. (a) SiO<sub>2</sub> Versus Rb (b) SiO<sub>2</sub> Versus La/Sm Note: LSG – Low Silica Group < 45 wt %; HSG – High Silica Group > 45 wt %; Red Domain – Eastern Alignment; Green Domain – Central Alignment.

a negatively sloping trend) is consistent with crystal fractionation of the non-primitive magmas.

The silica content is plotted versus Rb in Figure 39a. Rb ranges from a little over 20 ppm to approximately 50 ppm. This variability is mostly observed for lavas belonging to the Low Silica Group. The High Silica Group has a more restricted Rb content of 35 ppm to 48 ppm. According to Perry *et al.* (1987), and observed for lavas from Lathrop Wells (Perry and Crowe, 1992), the Rb content is a sensitive indicator of crustal contamination. The relationship of silica content to La/Sm, which represents a ratio of highly incompatible to moderately incompatible elements, is shown in Figure 39b. There is considerable scatter for samples from the West Potrillo Mountains whereas La/Sm is tightly constrained at approximately 5.0 – 5.5 for both the central and eastern alignments. The potential role of crustal contamination will be further evaluated using isotopic data, and then will be discussed in Chapter 6.

## **5.4 Isotopes**

Ten samples, with ages representing roughly 1 Ma to 20 ka ago, were selected from the Potrillo volcanic field. These samples are from the western and central alignments. Each was analyzed for their Nd, Sr, and Pb isotopic values. Results are reported in Table 7 and appendix Table E. Seven of the sampled

Table 7. Sr, Nd and Pb Isotopic Values

<b>Sample</b>	<b><math>^{87}\text{Sr}/^{86}\text{Sr}</math></b>	<b><math>\epsilon_{\text{Nd}}</math></b>	<b><math>^{206}\text{Pb}/^{204}\text{Pb}</math></b>	<b><math>^{207}\text{Pb}/^{204}\text{Pb}</math></b>	<b><math>^{208}\text{Pb}/^{204}\text{Pb}</math></b>
<b>NM1167</b>	0.703158	6.7	19.055	15.572	38.572
<b>NM1169</b>	0.703419	5.5	18.858	15.561	38.699
<b>M2</b>	0.703231	6.6	18.931	15.571	38.439
<b>NM879</b>	0.703105	6.6	19.081	15.584	38.615
<b>M5</b>	0.703087	6.5	18.949	15.568	38.478
<b>AF4</b>	0.703574	4.5	18.363	15.520	38.267
<b>PM-20</b>	0.703201	5.3	18.675	15.564	38.326
<b>KHSYN-1</b>	0.703343	6.2	18.936	15.583	38.546
<b>AD3</b>	0.703568	5.3	18.638	15.541	38.438
<b>HHSYN-1</b>	0.703917	4.4	18.558	15.554	38.192
	+/- .000024	+/- 0.5	+/- 0.1%	+/- 0.1%	+/- 0.1%

Note: See Appendix Table E for uncorrected lead data.

deposits have been dated using  $^3\text{He}$  methods. For these, magmatic  $^3\text{He}/^4\text{He}$  information is also reported (Table 1). Data have been plotted relative to global reservoirs using the compilations of Zindler and Hart (1986) and crustal xenolith information. Data are then also presented at a more local scale for evaluation of within field trends.

#### **5.4.1 Global Reservoirs**

Zindler and Hart (1986) came to the conclusion that any model for mantle systems presuming only two chemically viable mantle components is inaccurate. They proposed the use of a planar three-dimensional surface to represent the mantle, but caution that this too may be an oversimplification. The interrelationships among the isotopic values led them to recognize the following mantle components:

- (1) DMM A, which stands for depleted mantle and is characterized by mid-ocean ridge basalts (MORB).
- (2) HIMU. This stands for high  $\mu$ , which indicates signatures enriched in U and Th relative to Pb but not enriched with respect to its Rb/Sr ratio.
- (3) EM1 is “enriched” mantle. It is enriched in the sense that the Nd and Sr values exceed those of Bulk Earth (BE).
- (4) an undegassed mantle with high  $^3\text{He}/^4\text{He}$  ratios. These magmatic helium ratios are reported as  $R/R_a$ , which is the ratio of the sample

over the atmospheric ratio. Undegassed mantle is characterized by values in excess of 20  $R/R_a$ .

(5) PREMA, prevalent mantle. This component is defined by having

$$^{143}\text{Nd}/^{144}\text{Nd} = 0.5130 \text{ and } ^{87}\text{Sr}/^{86}\text{Sr} = 0.7033 .$$

Typical values for the above components are plotted on Figures 40 through 43, with the exception of the fourth. The  $^3\text{He}/^4\text{He}$  ratios for the Potrillo volcanic field are  $R/R_a$  less than 20 (reported in Table 1) and for that reason this undegassed reservoir is not relevant to this study. Data for mafic granulitic xenoliths from Ken Cameron (Personal Communication), silicic granulitic xenoliths from Reid (1989), and common lower crustal values (LC) from Nancy McMillan (Personal Communication) are also included. Their data define the nature of the lower crust underlying the Potrillo volcanic field, thus providing an additional potential reservoir for consideration.

Potrillo volcanic field samples are plotted on several global-scale diagrams (Figures 40 to 43). In the context of  $\epsilon_{\text{Nd}}$  versus  $^{87}\text{Sr}/^{86}\text{Sr}$  (Figure 40a), the Potrillo melts all plot in Quadrant I and within the range for typical oceanic and continental rift basalts. They plot within the field defined by DMM A, HIMU, and PREMA. Several samples from the central alignment do have higher  $^{87}\text{Sr}/^{86}\text{Sr}$  than most of these four reservoirs, thus indicating a potential role for either EM1 or Lower Crust.  $\epsilon_{\text{Nd}}$  versus  $^{206}\text{Pb}/^{204}\text{Pb}$  (Figure 40b) shows that the melts cluster

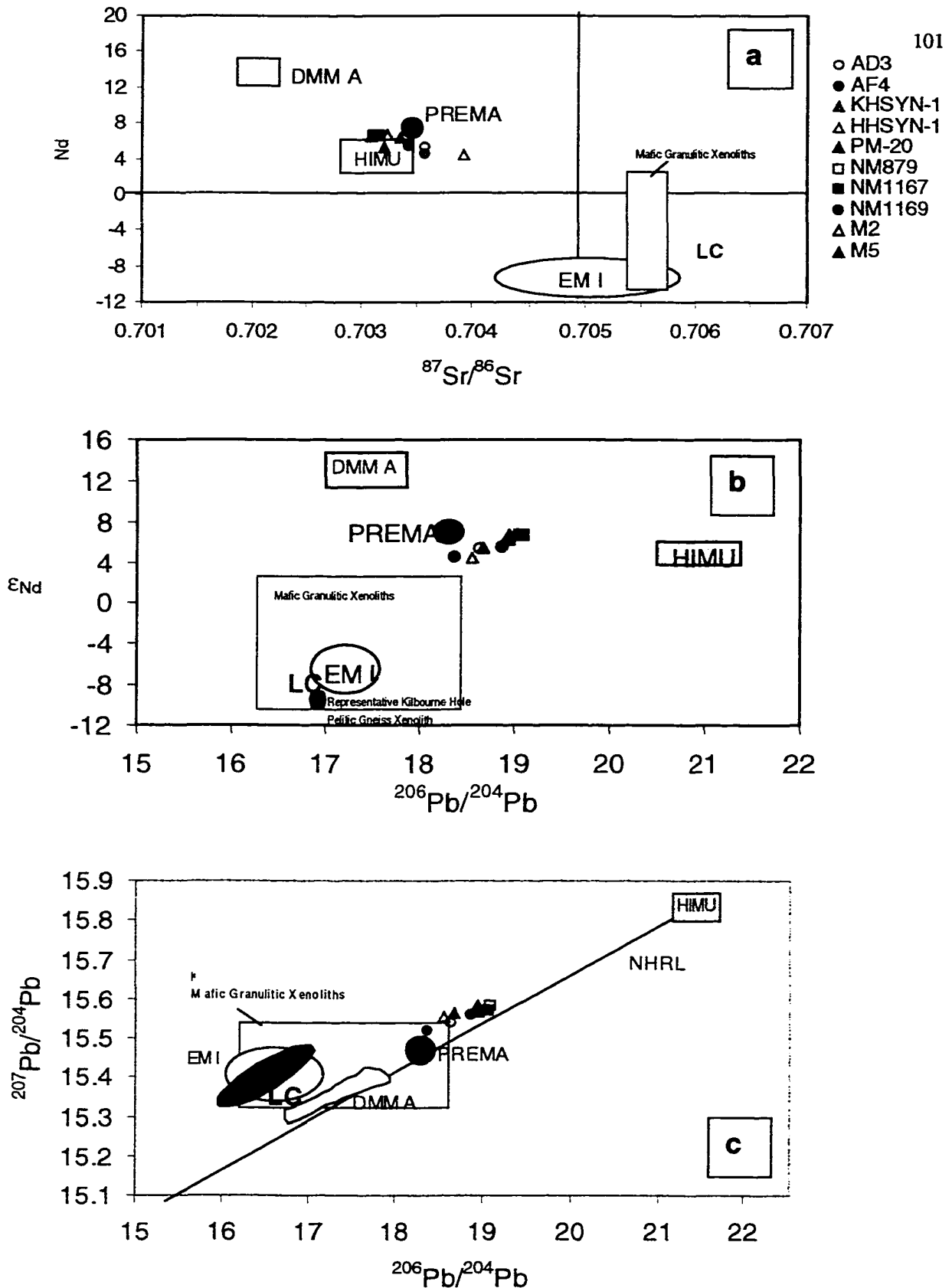


Figure 40. Isotopic results for PVF with respect to global reservoirs (Zindler and Hart, 1986), mafic granulitic xenoliths (green; K. Cameron, Personal Communication), silicic granulitic xenoliths (red; Reid, 1989) and representative lower crust (LC; McMillan, Personal Communication).

near PREMA with higher values for both isotopic ratios than documented for crustal xenoliths collected from the Potrillo volcanic field. It is important to note here that the crustal xenoliths are indistinguishable from EM1 with respect to these isotopes.

A diagram of  $^{207}\text{Pb}/^{204}\text{Pb}$  versus  $^{206}\text{Pb}/^{204}\text{Pb}$  (Figure 40c) shows that the Potrillo melts plot slightly to the left of the Northern Hemisphere Reference Line (NHRL), align with HIMU and PREMA, and are slightly more radiogenic than the mafic granulitic xenoliths from this volcanic field. The Potrillo samples have  $^{87}\text{Sr}/^{86}\text{Sr}$  and  $^{206}\text{Pb}/^{204}\text{Pb}$  ratios that are very similar to PREMA (Figure 41), in that they are intermediate to DMM A, HIMU, and EM1. When trends displayed in Figure 40c are also taken into account, this fact suggests that principle reservoirs may be EM1/LC, PREMA and HIMU. The necessity for a DMM A component is not substantiated by these observations.

$^{208}\text{Pb}/^{204}\text{Pb}$  versus  $^{206}\text{Pb}/^{204}\text{Pb}$  are shown in Figure 42 relative to the Northern Hemisphere Reference Line (NHRL). Samples from the West Potrillo Mountains (west alignment) and Kilbourne Hole (central alignment) are more radiogenic than Afton, Potrillo Maar (west alignment), Aden, and Hunt's Hole. The three central melts along with Potrillo Maar tend toward both mafic and silicic granulite crustal xenolith signatures.

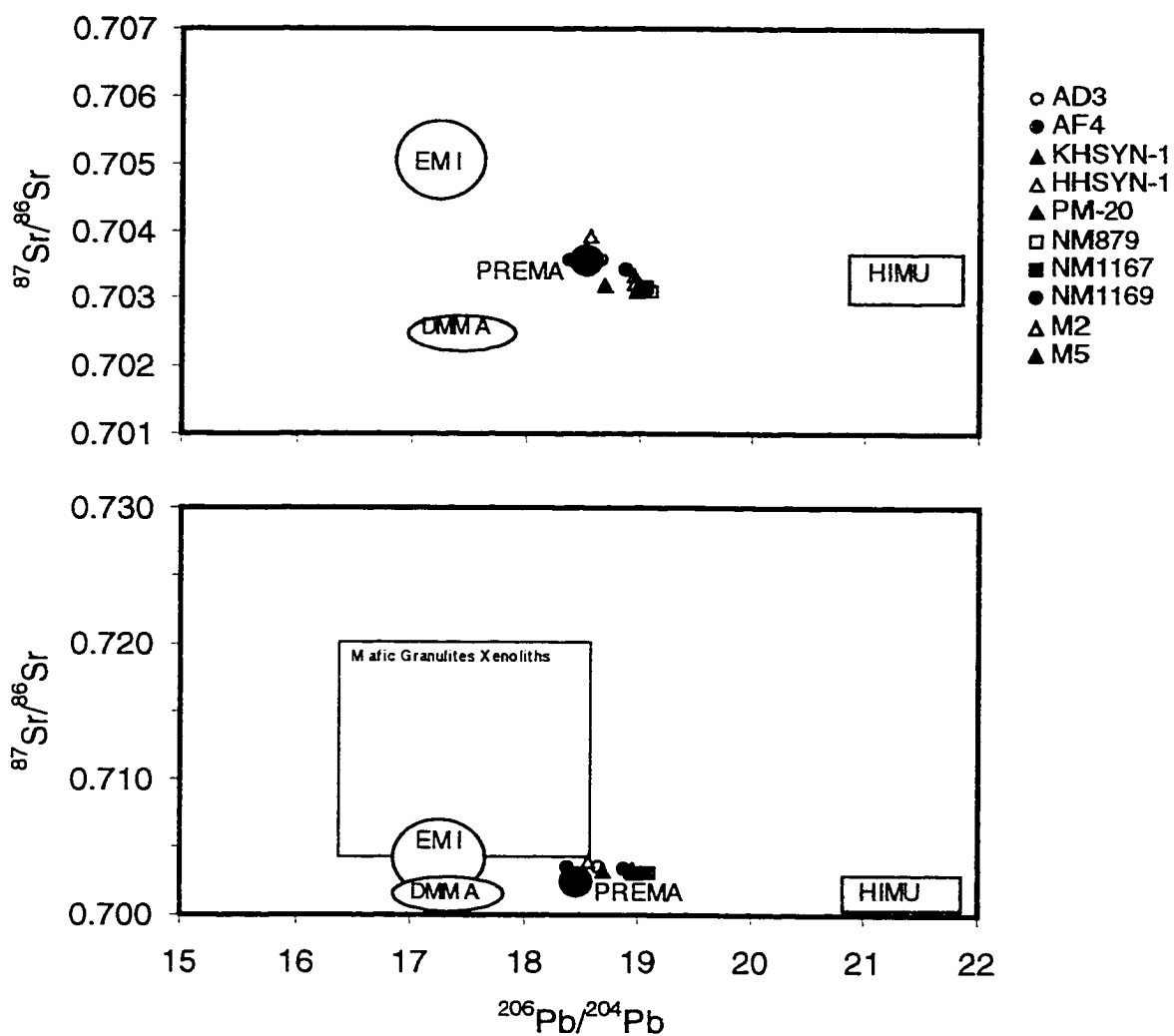


Figure 41. Relationship of Potrillo volcanic field isotopic results to  $^{206}\text{Pb}/^{204}\text{Pb}$  and  $^{87}\text{Sr}/^{86}\text{Sr}$  global reservoirs (Zindler and Hart, 1986) and range documented for mafic granulitic lower crustal xenoliths (K. Cameron, Personal Communication).



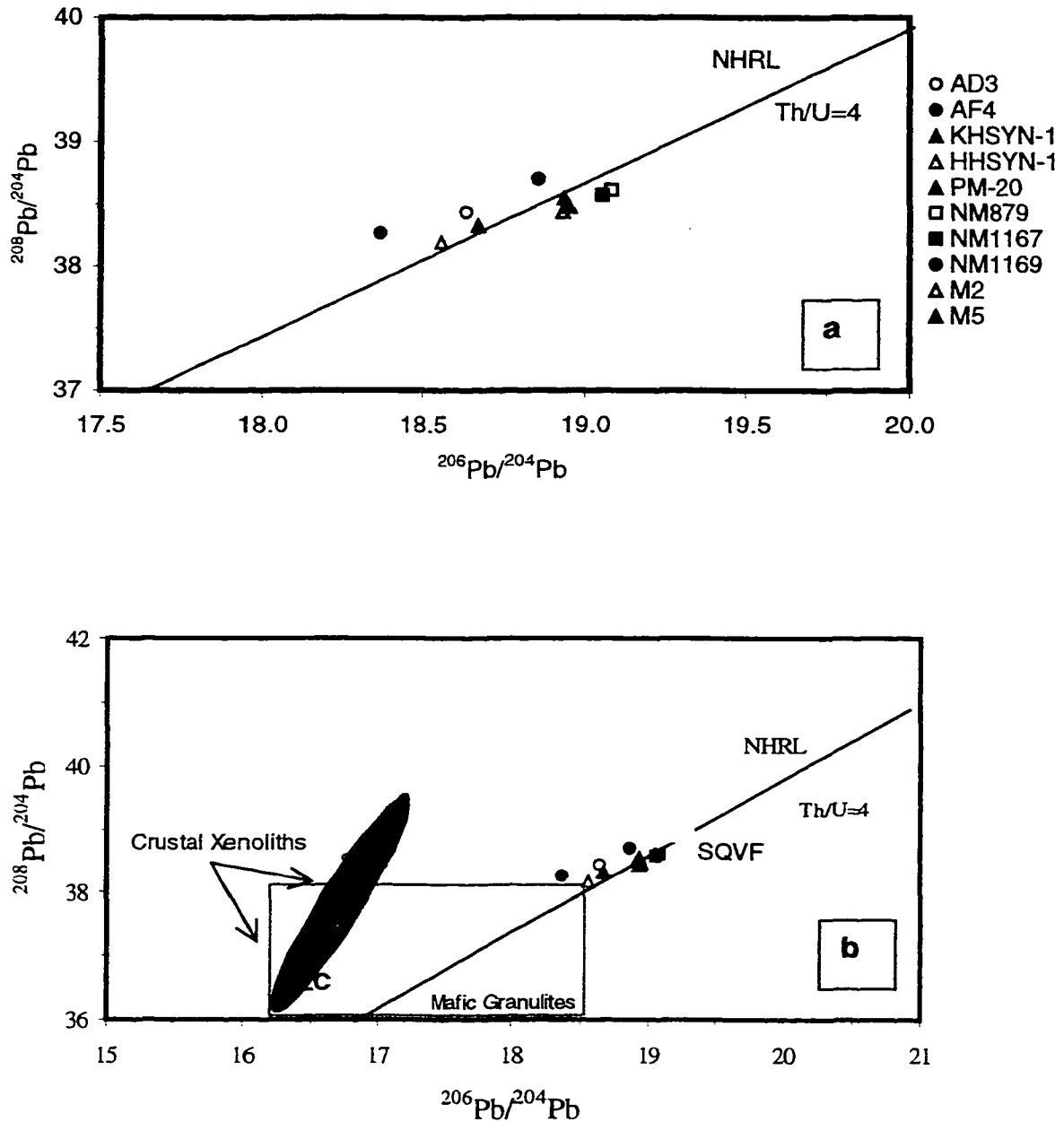


Figure 42.  $^{206}\text{Pb}/^{204}\text{Pb}$  versus  $^{208}\text{Pb}/^{204}\text{Pb}$  results for individual PVF samples, ranges of PVF crustal xenolith values, and cluster for the SQVF relative to the Northern Hemisphere Reference Line (NHRL). Mafic xenolith data from K. Cameron (Personal Communication), silicic xenolith data from Reid (1989), and representative lower crust (LC) from N. McMillan (Personal Communication).

Magmatic  $^3\text{He}/^4\text{He}$  ratios, measured during the crush procedure for surface exposure dating, can be considered in addition to  $^{147}\text{Sm}$ - $^{143}\text{Nd}$ ,  $^{87}\text{Rb}$ - $^{87}\text{Sr}$ ,  $^{238}\text{U}$ - $^{206}\text{Pb}$ ,  $^{235}\text{U}$ - $^{207}\text{Pb}$ , and  $^{232}\text{Th}$ - $^{208}\text{Pb}$  ratios. Seven of the ten samples analyzed for these other isotopes have helium information. These are reported in terms of  $R/R_a$ , the ratio of  $^3\text{He}/^4\text{He}$  for the sample over the atmospheric ratio. Note that data for the San Quintín volcanic field are also presented on this diagram for comparison with the Potrillo volcanic field. The San Quintín helium data are included in Part II of this dissertation. In Figure 43,  $^3\text{He}/^4\text{He}$  is plotted versus  $\epsilon_{\text{Nd}}$ ,  $^{87}\text{Sr}/^{86}\text{Sr}$  and  $^{206}\text{Pb}/^{204}\text{Pb}$ . The helium signatures are most similar to HIMU, with a potential shift towards DMM A (Figure 43c).

The samples from Potrillo volcanic field are most similar to HIMU, PREMA and EM1 and/or the Lower Crust collectively when considering all the isotopic data together. Thus these end members define a planar three-dimensional surface. It is not possible to tell which of the two reservoirs – EM1 or LC – has had a role due to the similarity in their isotopic ratios.

#### **5.4.2 Potrillo Volcanic Field**

Samples will now be evaluated for within field relationships. The following observations are based on the plots presented as Figures 44 through 49. I have kept the color scheme of the plots to reflect the geographic location within the

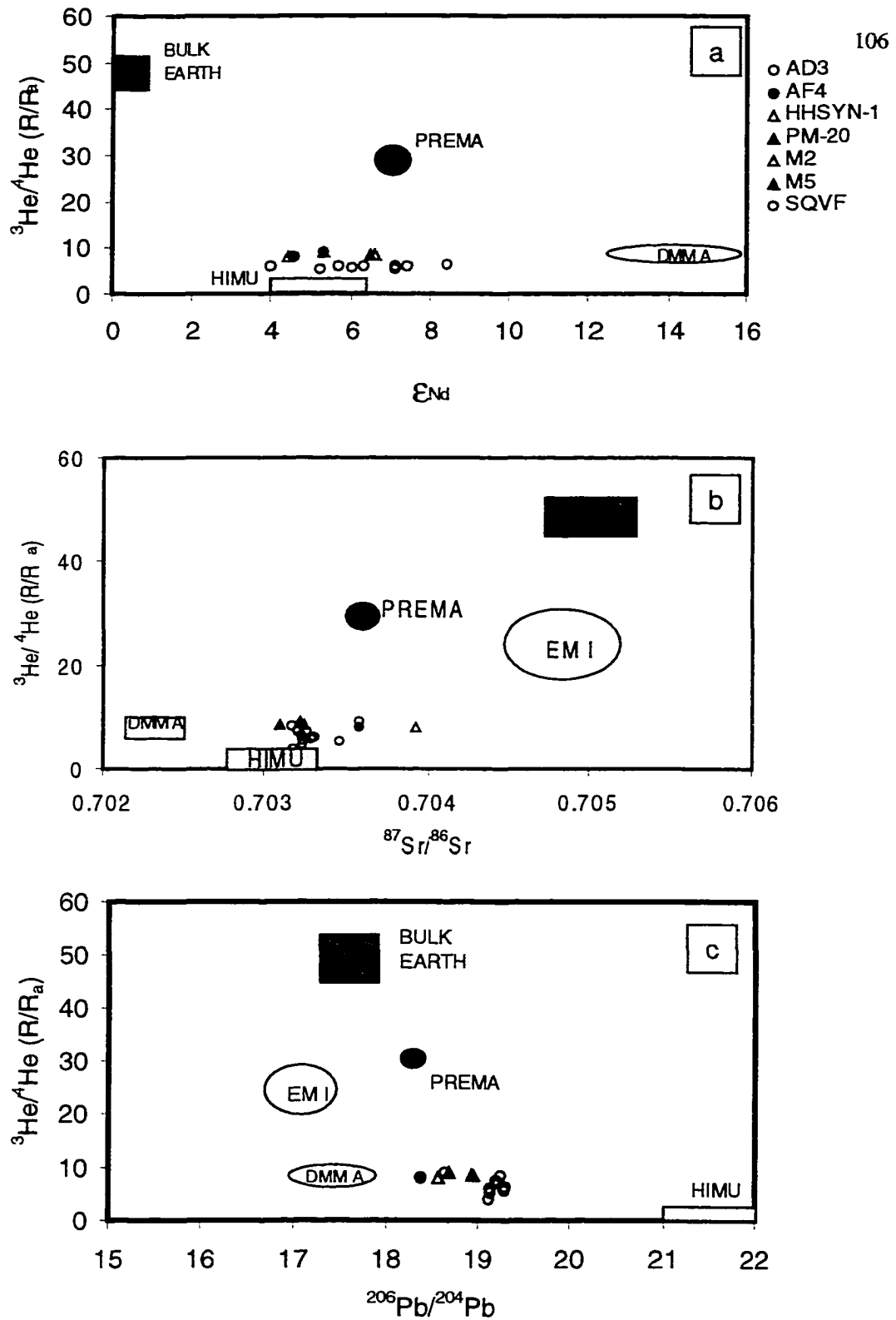


Figure 43. Global reservoirs for various isotopic systems (Zindler and Hart, 1986). Helium information only available for a subset of PVF isotopic analysis (corresponding to six lavas dated using the surface exposure method).

field (namely, green for the central alignment and blue for the western eruptive products).

$\epsilon_{\text{Nd}}$ ,  $^{87}\text{Sr}/^{86}\text{Sr}$ ,  $^{207}\text{Pb}/^{204}\text{Pb}$ , and  $^{208}\text{Pb}/^{204}\text{Pb}$  versus  $^{206}\text{Pb}/^{204}\text{Pb}$  are shown in Figures 44a through 44d. Three observations can be made on the basis of these plots:

- (1)  $\epsilon_{\text{Nd}}$ ,  $^{207}\text{Pb}/^{204}\text{Pb}$ , and  $^{208}\text{Pb}/^{204}\text{Pb}$  have a positive correlation with respect to  $^{206}\text{Pb}/^{204}\text{Pb}$  but  $^{87}\text{Sr}/^{86}\text{Sr}$  has a negative correlation.
- (2) There is a temporal trend with respect to  $\epsilon_{\text{Nd}}$  and  $^{87}\text{Sr}/^{86}\text{Sr}$ . The younger lavas display less radiogenic  $\epsilon_{\text{Nd}}$  but more radiogenic  $^{87}\text{Sr}/^{86}\text{Sr}$  signatures than do the older lavas. Further, these younger lavas have less radiogenic lead signatures.
- (3) The western alignment, consisting of breach and fissure-fed lavas, and the melts from maars which transported mantle xenoliths, consistently group together as Group I. The central alignment lavas and bomb coating from Hunt's Hole, which did not erupt mantle xenoliths, form the other association termed Group II.

Additional plots further illustrate these two groups. For example, Figure 45a shows the negative correlation between  $\epsilon_{\text{Nd}}$  and  $^{87}\text{Sr}/^{86}\text{Sr}$ , with Group I at high  $\epsilon_{\text{Nd}}$  and low  $^{87}\text{Sr}/^{86}\text{Sr}$ . A positive correlation between  $\epsilon_{\text{Nd}}$  and  $^{207}\text{Pb}/^{204}\text{Pb}$  is shown by Figure 45b.

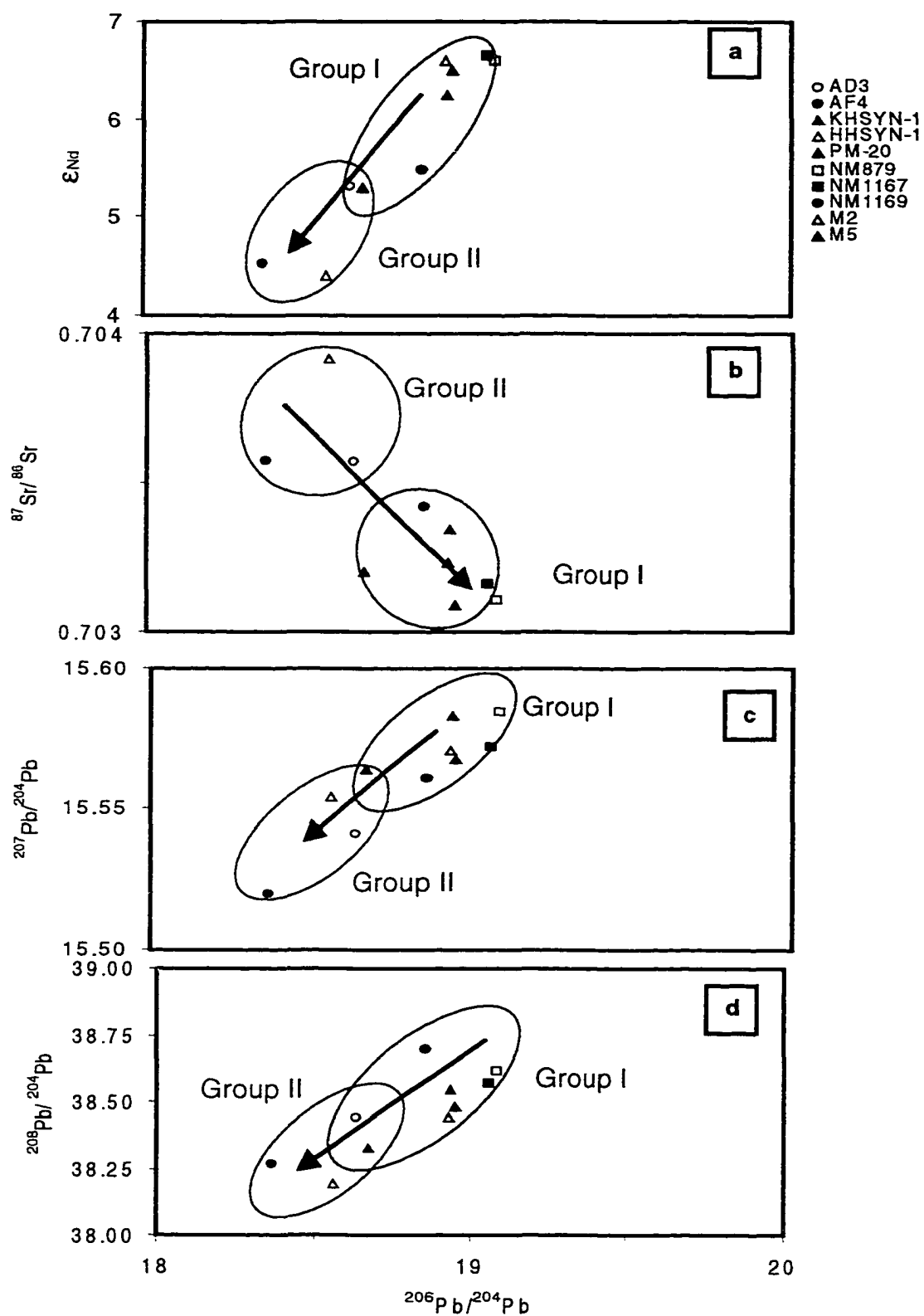
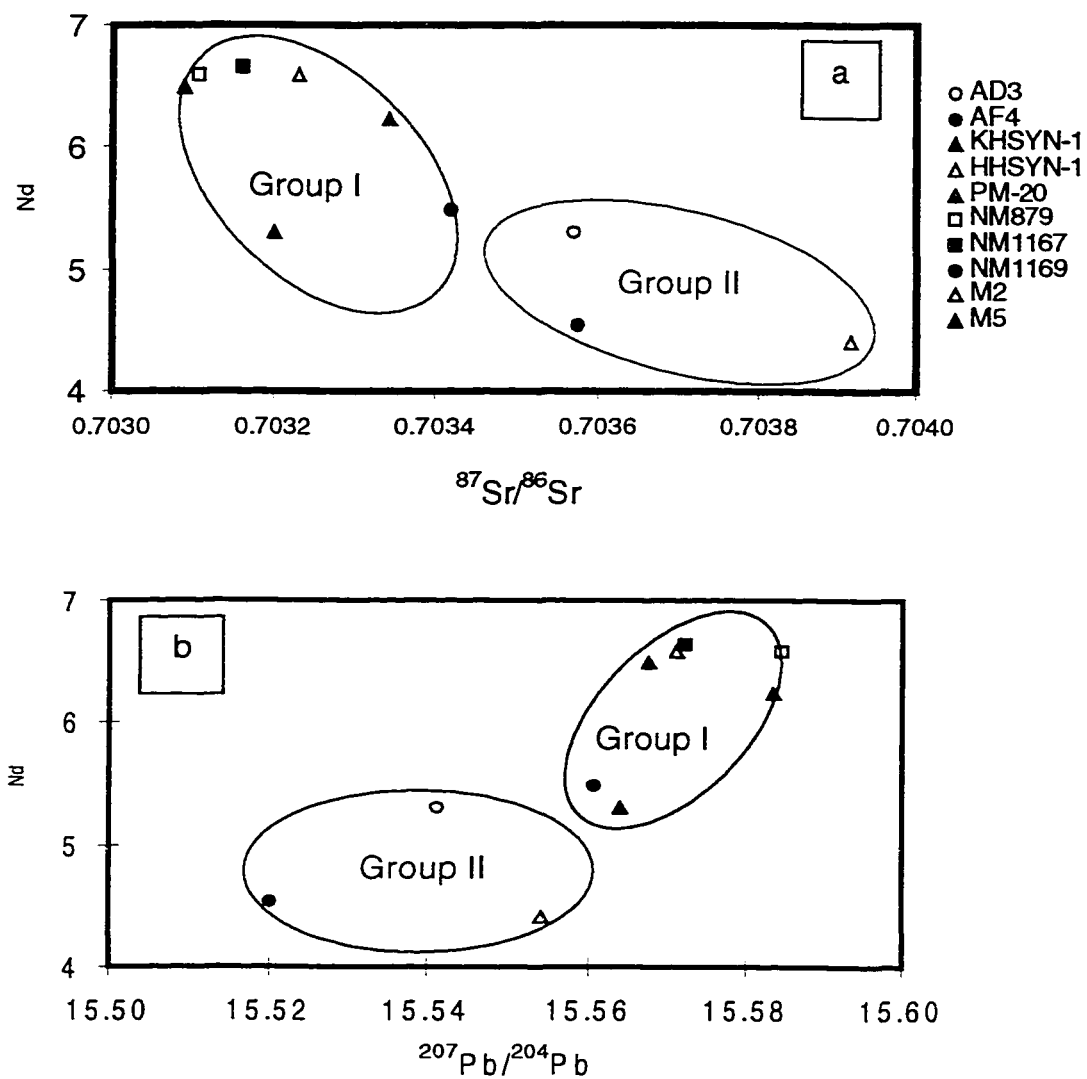


Figure 44. Potrillo volcanic field isotopic trends with Groups I and II denoted. Arrows indicate general younging trend.



Figures 45. Isotopic Groups I and II for  $^{87}Sr/^{86}Sr$  and  $^{207}Pb/^{204}Pb$  versus  $\epsilon_{Nd}$  for the Potrillo volcanic field. (a) Group I lower  $^{87}Sr/^{86}Sr$  whereas in (b) this group is more radiogenic with respect to lead.

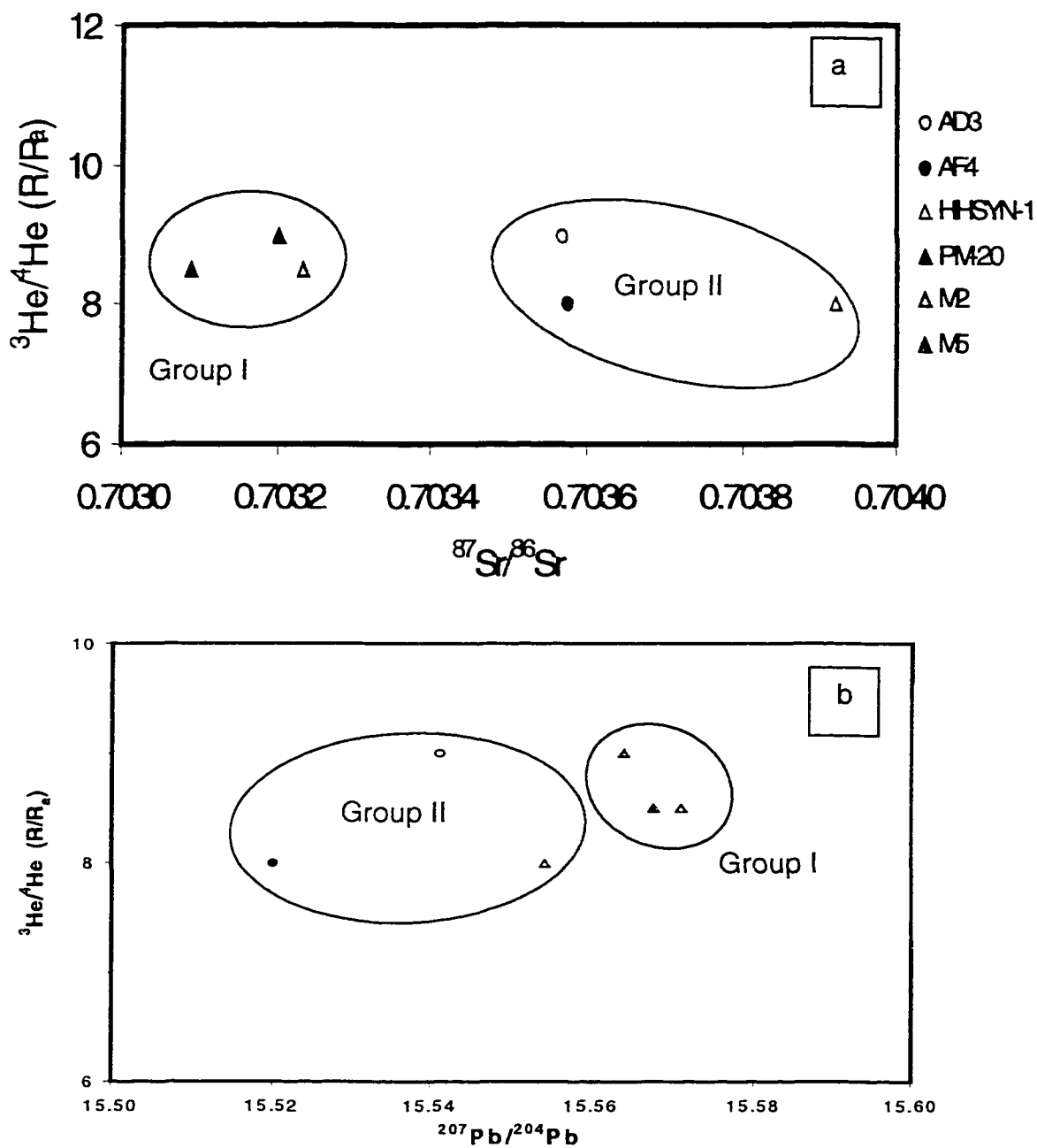


Figure 46. Magmatic helium signatures in relationship to the Sr and Pb data for the Potrillo volcanic field. (a)  $^{87}\text{Sr}/^{86}\text{Sr}$  versus  $^3\text{He}/^4\text{He}$  (R/R<sub>a</sub>) (b)  $^{207}\text{Pb}/^{204}\text{Pb}$  versus  $^3\text{He}/^4\text{He}$  (R/R<sub>a</sub>)

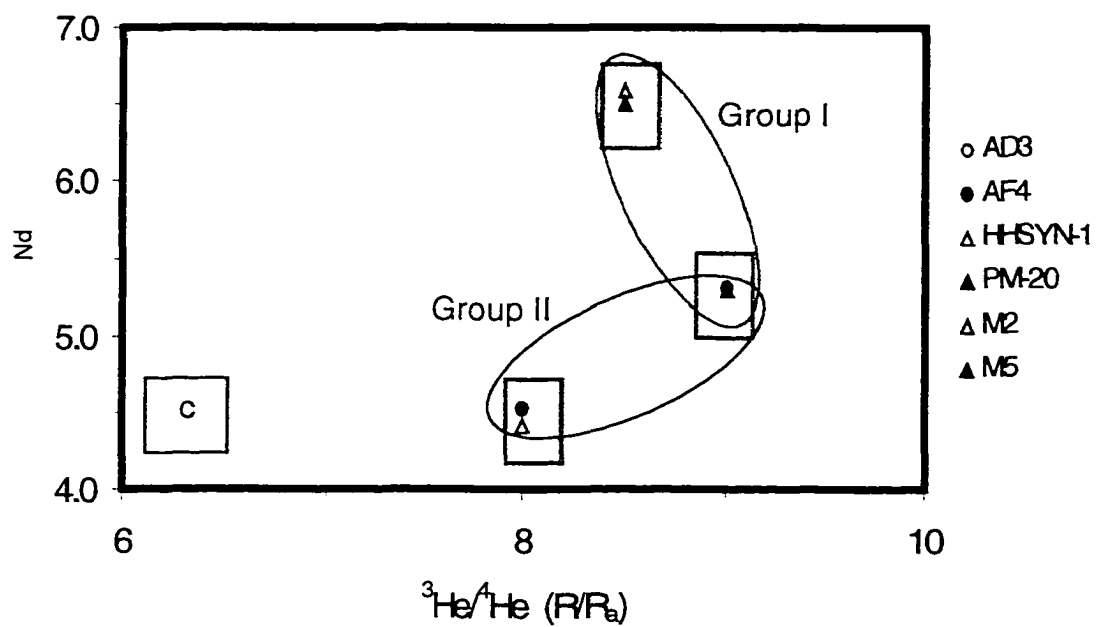


Figure 46c.  $\epsilon_{\text{Nd}}$  versus magmatic  $^3\text{He}/^4\text{He}$  ( $R/R_a$ ) with “pairing” of samples evident. Boxes delineate the three pairs. This plot fits within the continental mantle xenolith domain discussed by Reid and Graham (1996).



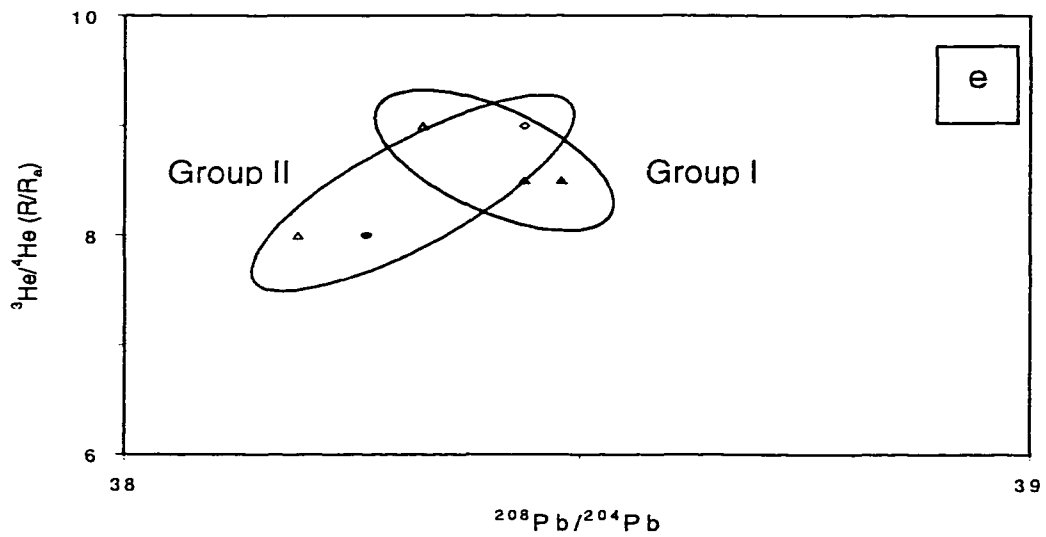
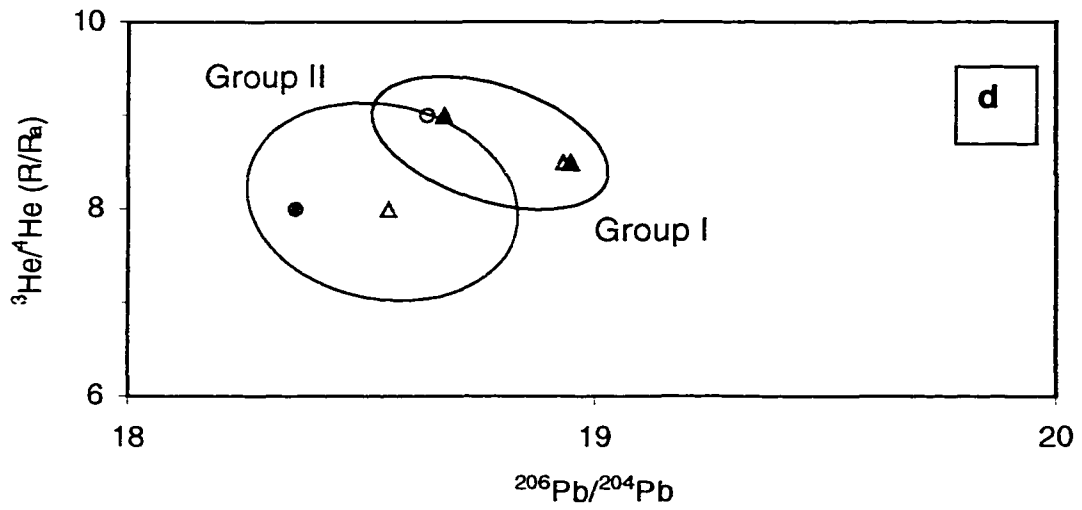


Figure 46. Magmatic helium relationship to lead isotopes for the Potrillo volcanic field. Groups I and II overlap. (a)  $^{206}\text{Pb}/^{204}\text{Pb}$  versus  $^3\text{He}/^4\text{He}$  (R/R<sub>a</sub>) (b)  $^{208}\text{Pb}/^{204}\text{Pb}$  versus  $^3\text{He}/^4\text{He}$  (R/R<sub>a</sub>)

The correlation of magmatic  $^3\text{He}/^4\text{He}$  ( $R/R_a$ ) with the radiogenic isotopes is more complex.  $^{87}\text{Sr}/^{86}\text{Sr}$  and  $^{207}\text{Pb}/^{204}\text{Pb}$  (Figure 46) separate into the same Group I and Group II associations, as previously discussed. However,  $R/R_a$  versus  $\epsilon_{\text{Nd}}$ ,  $^{206}\text{Pb}/^{204}\text{Pb}$  and  $^{208}\text{Pb}/^{204}\text{Pb}$  show varying amounts of overlap for the two groups. With respect to magmatic  $^3\text{He}/^4\text{He}$  versus  $\epsilon_{\text{Nd}}$ , the Nd isotopes form “pairs” (Figure 46c). Of the six samples, the following three pairs are evident:

- Pair A, which is defined by the syn- and post- Malpais maar analyses. The older syn-maar sample is M2 and the younger post-maar sample is M5.
- Pair B, which is defined by the older Afton (non maar) and younger syn-Hunt’s Hole.
- Pair C, which is defined by the older post-Potrillo maar (west half) and younger Aden (east half). This pair comprises the overlap between Group I and Group II.

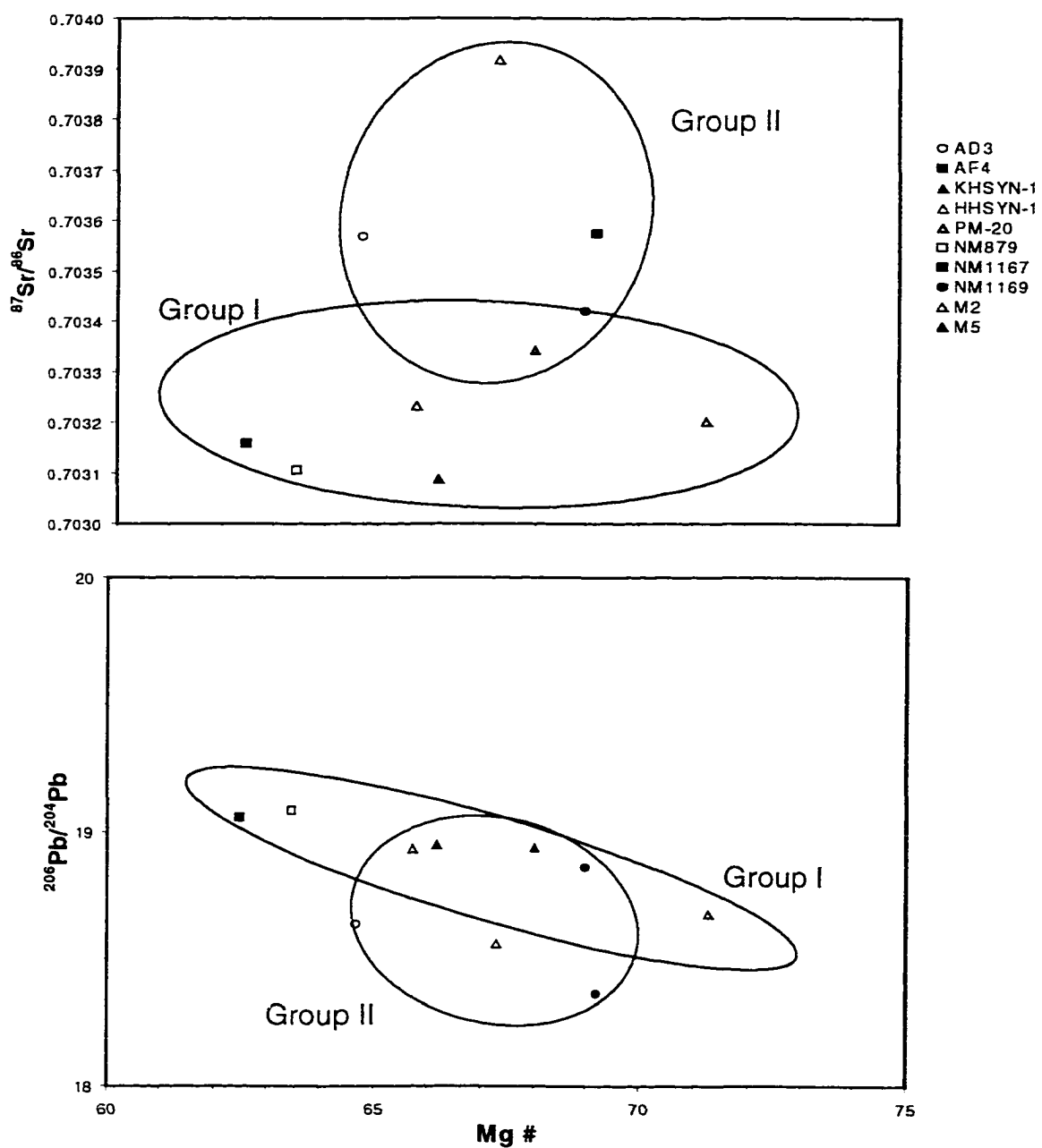
The centers forming Pair A and Pair B are spatially related. In the case of Pair A from the west half of the field, both samples are from within the Malpais Maar depression and so are construed as being from the same edifice. In the case of Pair B from the east half of the field, the Hunt’s hole eruption pierced the Afton flow; both events may have occurred along the same feeder conduit. Centers involved in Pair C, unlike the other two pairs, are not spatially close to one another. Potrillo Maar and Aden are separated by approximately 30 km; however, they are both immediately adjacent to the East Robledo fault. Finally, Figures 46d and 46e show that both  $^{206}\text{Pb}/^{204}\text{Pb}$  and  $^{208}\text{Pb}/^{204}\text{Pb}$  express the

same volcanic center pairs, but with more spread in the data. Again, both Groups I and II are evident, but with more overlap than observed for the  $\epsilon_{Nd}$  relationship with the magmatic helium ratio.

Reid and Graham (1996) discuss that the He – Nd isotopes for mafic lavas from the southwestern United States suggest that discrete mantle domains have experienced correlated He/Nd fractionation. They show that crustal thinning results in abrupt Nd isotope shifts, and they conclude that the discrete domains are successively involved in extensional volcanism. Results from this dissertation study are consistent with their hypothesis. The Potrillo volcanic field pairs plot within the southwest U.S. continental mantle xenoliths field depicted in their paper. Further, they comment that improved understanding of multiple mantle sources may be possible using He – Th – Nd isotopes, but that additional studies at the scale of volcanic fields and individual vents are needed. Therefore, this dissertation provides an addition toward that understanding.

## **5.5 Correlation of Isotopes and Elemental Data**

Mg # versus  $^{87}\text{Sr}/^{86}\text{Sr}$  and  $^{206}\text{Pb}/^{204}\text{Pb}$  is shown by Figure 47. Groups I and II are distinct from one another, especially for  $^{87}\text{Sr}/^{86}\text{Sr}$  with overlapping points being the syn-maar coatings from Kilbourne Hole and one sample from the West



Figures 47. Mg # versus  $^{87}\text{Sr}/^{86}\text{Sr}$  and  $^{206}\text{Pb}/^{204}\text{Pb}$  isotopes.

Potrillo Mountains (NM1169). Group I shows a weak negative correlation for Mg # versus  $^{206}\text{Pb}/^{204}\text{Pb}$  whereas Group II displays no correlation for either plot. La/Sm versus Nd, Sr and Pb isotopic data are considered. This ratio was selected because it showed good mantle heterogeneity in the H/M versus H diagrams (Figure 28) presented in Section 5.2.4. In Figure 48, groups break out with high La/Sm correlated to high  $\epsilon_{\text{Nd}}$  and  $^{206}\text{Pb}/^{204}\text{Pb}$  and low  $^{87}\text{Sr}/^{86}\text{Sr}$ . Note that the two groups again overlap with Kilbourne Hole and West Potrillo Mountains sample NM 1169.

Work at San Luis Potosí (Pier *et al.*, 1989), a maar-hosting alkaline mafic field in the Basin and Range province of México, also shows correlations among incompatible element abundances, lead and strontium isotopes, and ratios of highly incompatible to less incompatible elements. Pier *et al.* (1992) comment that although elemental correlations can be modified by fractional crystallization, isotopic and incompatible element ratios should not be affected. Therefore, the correlations depicted in Figure 48 imply that the processes and source regions controlling the generation and ascent of Group II (generally older melts) are definitely different from those for Group I (younger melts).

The correlation of magmatic helium with La/Sm is shown in Figure 49. Each plot has the same axes and scales, but depicts three different layers of information. Figure 49a shows Groups I and II, as defined previously. Boxes highlight data in

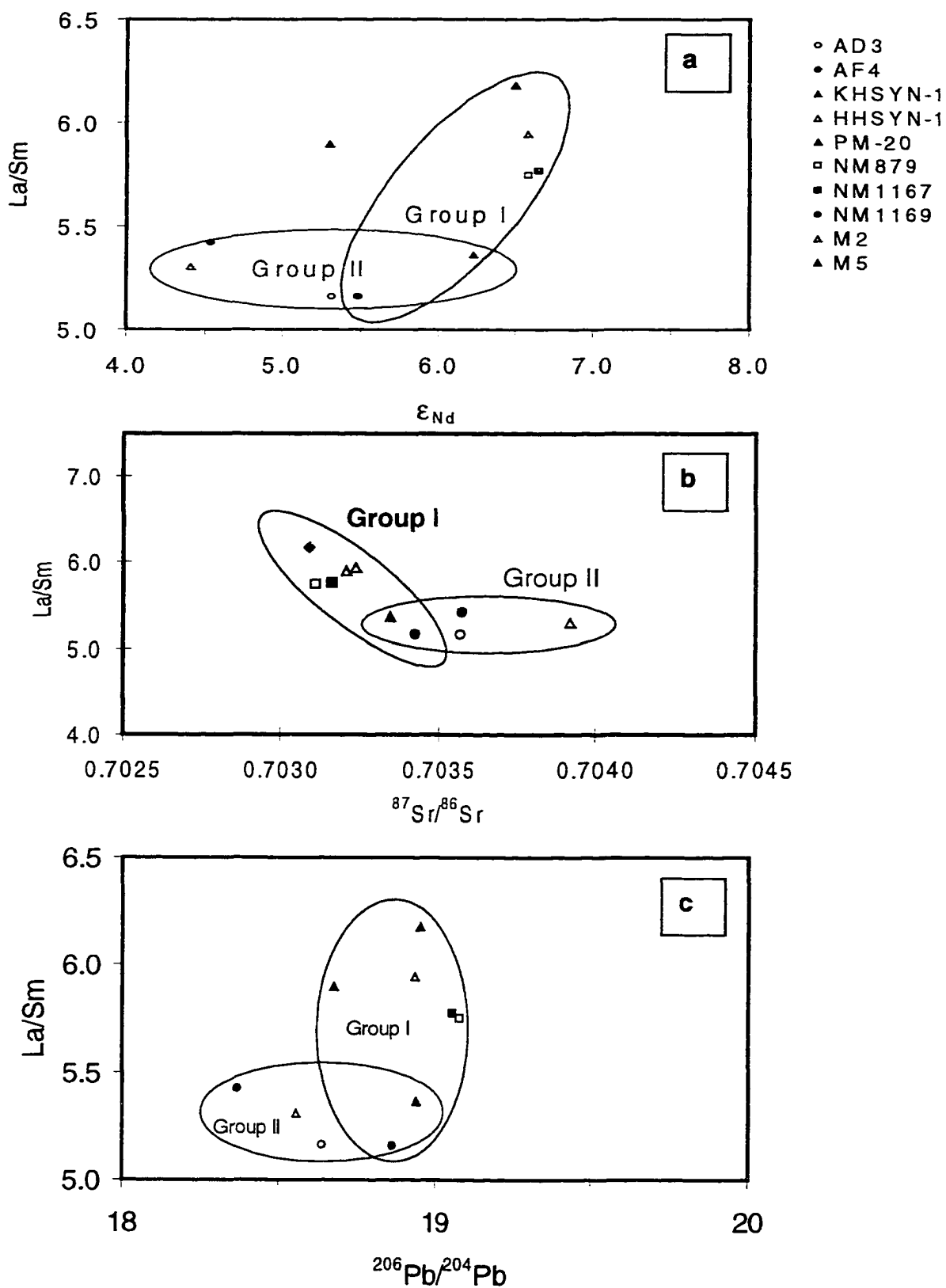


Figure 48 . Potrillo volcanic field isotopic Groups I and II displayed by  $\epsilon_{Nd}$ ,  $^{87}Sr/^{86}Sr$  and  $^{206}Pb/^{204}Pb$  plotted against  $La/Sm$ .

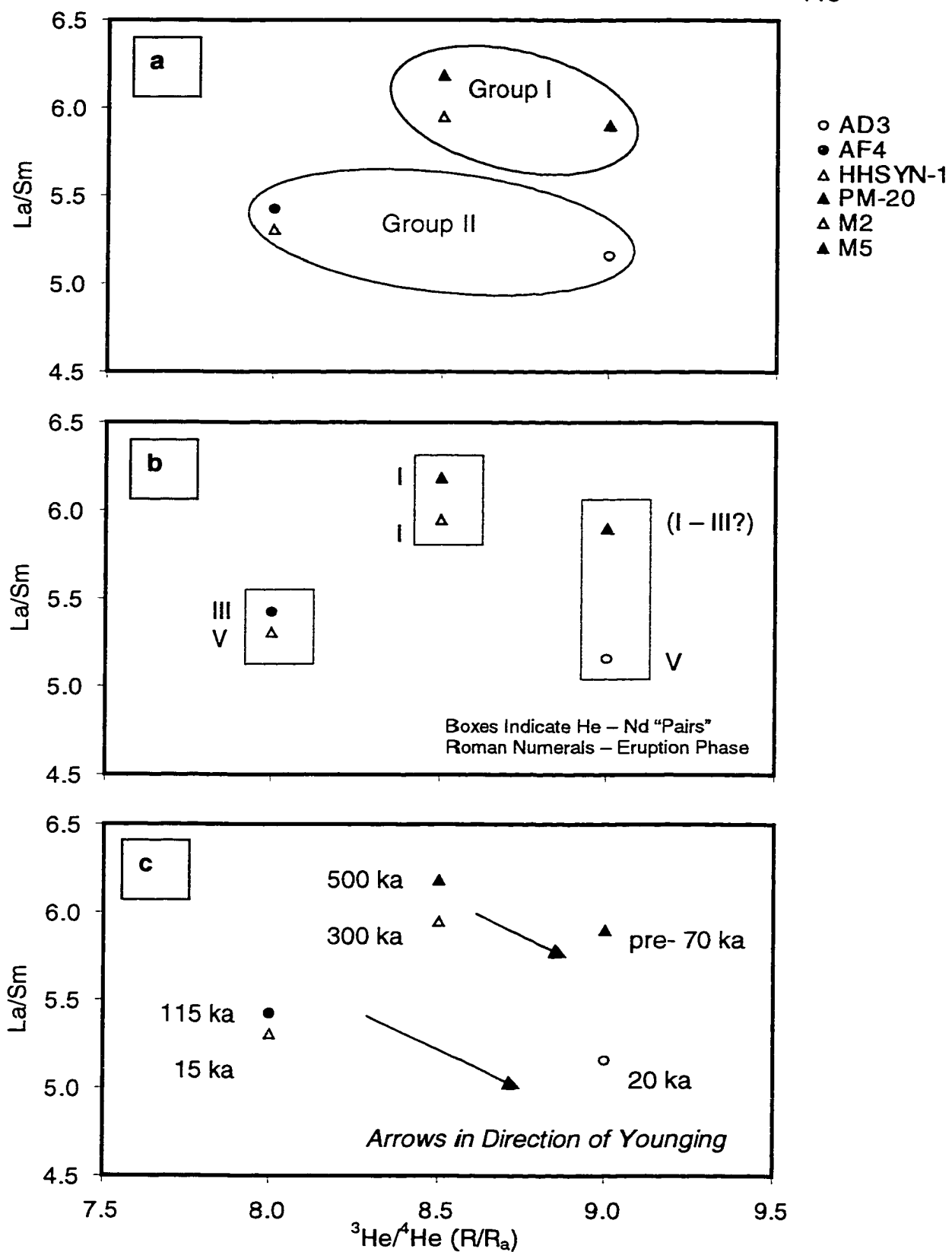


Figure 49 . Magmatic helium with respect to La/Sm as isotopic Groups I and II, "pairs", and eruption episodes.

Figure 49b to show which analyses combined as the three  $\epsilon_{Nd} - {}^3\text{He}/{}^4\text{He}$  pairs designated A, B and C. Use of these boxes is to point out that the same centers also pair with respect to La/Sm, especially for the spatially related pairs A and B. Also noted on this plot are the corresponding eruption Phases I (oldest) through V (youngest) discussed in the next chapter (Section 6.1). The final plot (Figure 49c) illustrates that, interestingly, helium and incompatible element ratios decrease with younging of deposits within Group I or Group II.



## **Chapter 6**

### **DISCUSSIONS AND CONCLUSIONS**

The following discussion is presented in three sections. First, Section 6.1 considers the physical evolution of the Potrillo volcanic field with time. In this section, there will be correspondence with the geographical nomenclature used in previous chapters. This entails beginning with the oldest eruptions forming the western alignment then assessing the central and eastern alignments together, due to their contemporaneous eruption activity. Section 6.2 examines the field with respect to geochemical and isotopic signatures. Section 6.3 will then synthesize temporal and chemical evolution into an integrated magmatic model for the Potrillo volcanic field.

#### **6.1 Physical, Spatial and Temporal Evolution**

The Potrillo volcanic field has evolved at least during the past one million years to as recently as twenty thousand years ago. Regional extension has caused variably trending normal faulting throughout the area. Mack and Seager (1995) document a NW-trending synclinal warp with superimposed graben structures and N to NE-trending fractures within the western part of this volcanic field. They designate this the “West Potrillo transfer zone” (Figure 3). Spatially and temporally, this volcanic field has seen most of its history concentrated in the

area west of the East Robledo fault (Figures 3 and 50). This area will henceforth be referred to as the “western half” of the field for the purposes of this discussion. The centers east of the East Robledo fault comprise the central and eastern alignments. These deposits will be referred to as the “eastern half.” The eastern half of the field is substantially less voluminous and represents much less of the total eruption history. However, it does have the most youthful activity in the entire Potrillo volcanic field. A summary of activity is provided by Figure 50. This is based on field relationships,  $^3\text{He}$  and  $^{40}\text{Ar}/^{39}\text{Ar}$  dates, and paleomagnetic data for centers throughout the field. Recognition of discrete time intervals leads me to propose five eruption phases. Interestingly, specific phases are not constrained to a given half of the field, given alignment, or *even* a given volcanic complex. The ensuing discussion and Figure 51 details this finding, first addressing the western half of the area.

In the western half, field and drill hole evidence supports early activity dominated by fissure-fed flows forming a plateau up to several hundred meters thick. Whole rock argon dates extend to approximately 980 ka, and paleomagnetic data document the reverse polarity Matayuma event. Later, eruptions took on a more point source style, resulting in greater than 100 scoria cones with and without associated breach flows. These flows are dominantly low aspect ratio pahoehoe-style. Argon dates document flows to be as young as approximately 70 ka old (*i.e.* the post-Potrillo Maar lavas).

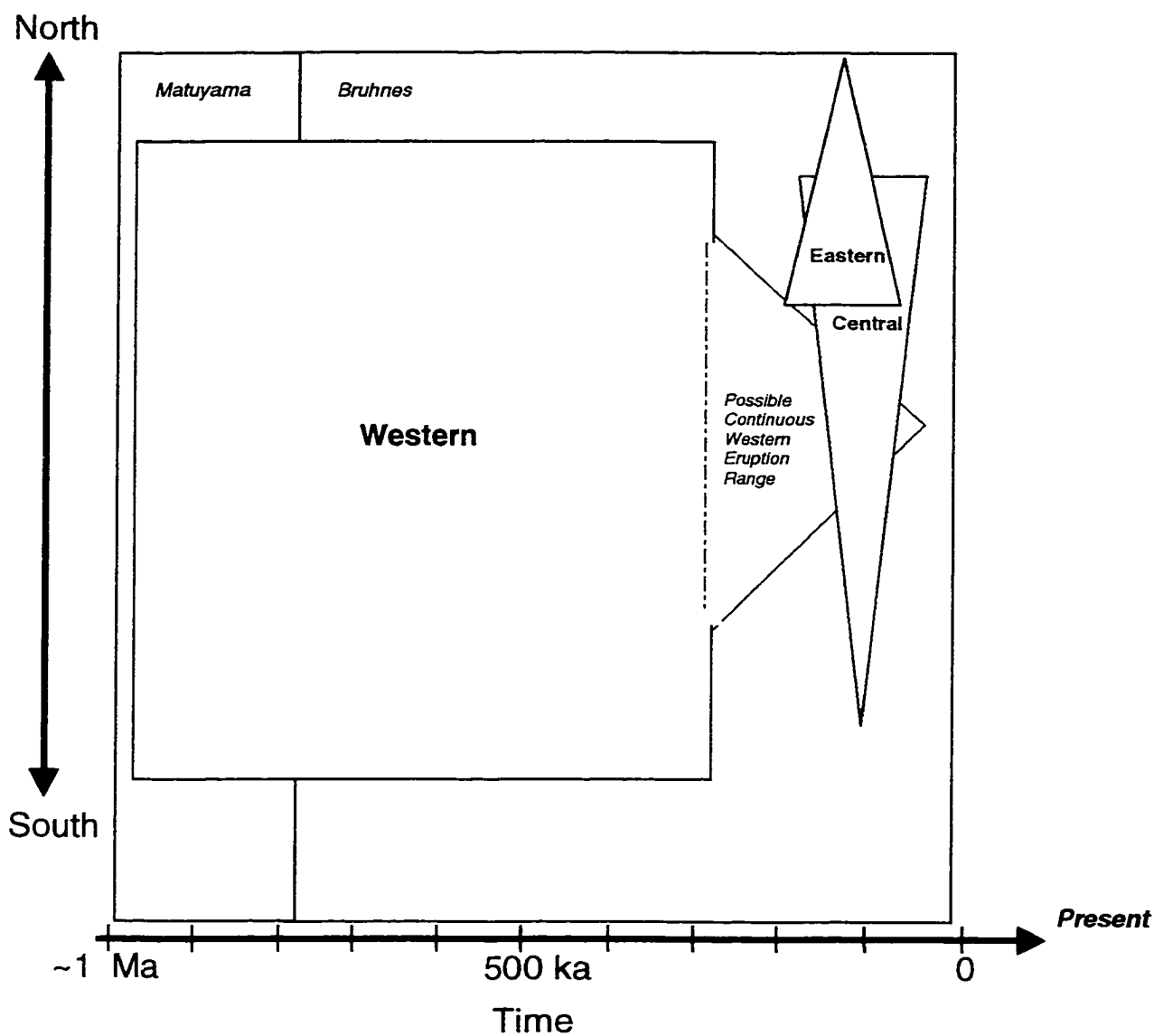


Figure 50. Schematic representation of map view spatial distribution and relative volume of lavas. Temporal framework based upon both  $^3\text{He}$  and  $^{40}\text{Ar}/^{39}\text{Ar}$  data. Paleomagnetic epochs include the Brunhes normal and Matuyama reversed events. Alignments are color-coded: western – blue, central – green, and eastern – red.

$^{40}\text{Ar}/^{39}\text{Ar}$  and  $^3\text{He}$  data compiled here add considerably to our understanding of the temporal history for the western half of the field. This area includes the oldest, most prolific outpourings. Therefore, it is *generally* designated Phase I (Figure 51a); the exception is that Potrillo Maar is included in Phase IV. But for the most part, the paucity of dates compared to the number of eruptive units present in this area does not provide enough detail for further discrimination of phases. The understanding of timing over this 1 Ma history could be used for regional estimates of episodicity.

There is more age control for the three recognized maars: Riley, Malpais and Potrillo. Recall from Chapter 4 (Figures 6 and 7) that Riley formed approximately 620 ka ago, syn-Malpais activity was bracketed from 610 and 510 ka ago, and post-Potrillo activity was around 70 ka ago. Within uncertainties, this suggests that the Riley and Malpais eruptions may have been contemporaneous. After a period of quiescence with respect to these two maars, phreatomagmatic activity shifted southeast within this western half and formed the Potrillo complex. However, eruptive foci jumped eastward roughly 20 km to initiate forming the eastern half of the field, emanating as the older flows in the eastern alignment. Therefore, magmatism initiated east of the East Robledo fault prior to the post-Potrillo maar activity, which is west of this fault.

At Potrillo Maar, paleomagnetic data place pre- and post-maar lavas as erupted during the normal polarity Bruhnes event. There is not a reliable date for the pre-maar flow cropping out to the northwest of the maar. Hence, it is not known if it would represent Phase I, II or III; however, post-maar flows are roughly 70 ka old. The syn-maar surge deposit is faulted, as exposed in a road cut across the northwest portion of the maar depression (Hoffer, Personal Communication). This fault may be a southern trace of the East Robledo fault defined by Mack and Seager (1995). Therefore, fault activity post-dates the syn-maar tuff ring emplacement. Whether or not the fault moved prior to, contemporaneously with, or after the post-maar volcanic episode at approximately 70 ka ago is yet unresolved.

The combined central and eastern alignments resulted in a smaller volume of material being emplaced (Phases II through V; Figure 51), which may reflect the two orders of magnitude less time represented by the deposits. The east half of the field has more youthful geomorphic features than those observed in the west. Stratigraphic relationships are vastly better understood, due to a combination of the lesser number of units "coalescing" and lesser degrees of subsequent burial of deposits, both by other magmatic materials and aeolian materials. The good exposure of surfaces and stratigraphic control made the use of helium dating

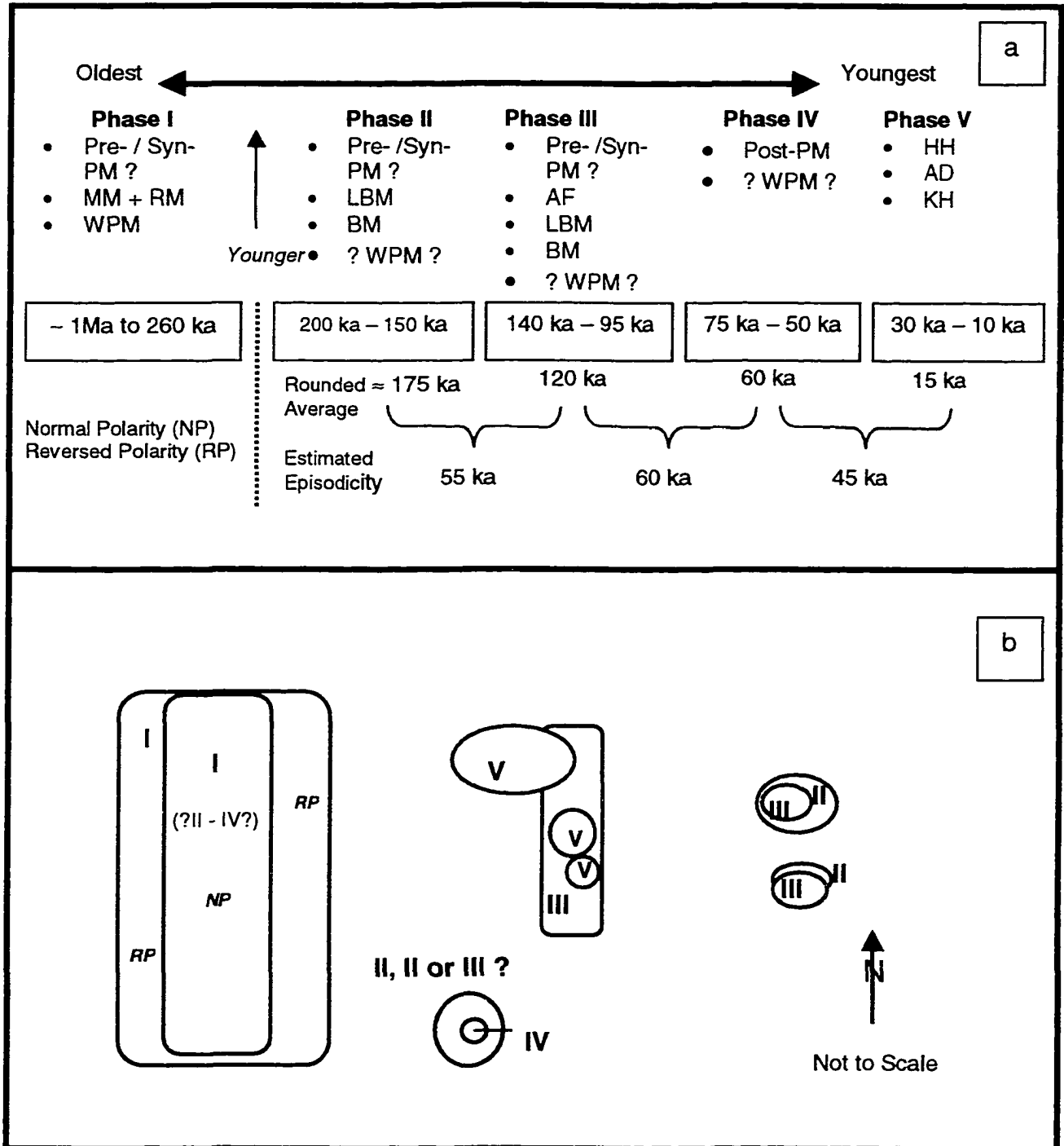


Figure 51. Identification of eruption Phases I through V and shift of eruption foci through time. (a) Tabulation of eruption dates, presented as ranges then rounded averages. Episodicity for the east half of the Potrillo volcanic field is estimated by averaging the length on time between Phases II through V. (b) Cartoon-style distribution of volcanic centers with eruptive phase indicated by I through V. This shows the shift in foci then re-occupation of previously used edifices (e.g. Black Mountain). Volcanic center name abbreviations and alignment color-coding found in Figure 4.

appropriate; argon/argon applications met with more limited success (as discussed in Chapter 4) mainly due to the youthfulness of the flows.

Identified here are four discrete eruption phases (Figure 51a) for centers in the east half of the Potrillo field. From oldest to youngest events, they are:

- Little Black Mountain and Black Mountain of the eastern alignment begin growing during Phase II (200 – 150 ka ago; rounded average = 175 ka).
- renewed eruptions at both Little Black Mountain and Black Mountain and emplacement of the Afton flows (central alignment) during Phase III (140 – 95 ka; rounded average = 120 ka).
- post-maar eruption of several scoria cones with small volume/high aspect ratio breach flows within the Potrillo Maar depression (western alignment) during Phase IV (75 – 50 ka ago; rounded average = 60 ka).
- the eruptions of the Afton complex, Kilbourne Hole, and Hunt's Hole (central alignment) during the most recent activity of Phase V (30 – 10 ka; rounded average = 15 ka).

Estimates for episodicity in this eastern sector are roughly  $50 \pm 10$  ka based on rounded averages of hiatus intervals between Phases II through V. In summary, volcanic activity forming the Potrillo volcanic field was not continuous throughout its 980 to 20 ka history. Rather, there has been punctuated activity with frequent shifts of foci and some reoccupation of edifices after 50 ka upwards to 100 ka of quiescence. This history of brief periods of eruptive activity separated by longer

periods of inactivity has been noted for Quaternary mafic centers in the southern Great Basin, U.S.A. (Crowe *et al.*, 1989), indicating that eruptive histories are more complicated than previously acknowledged (Wells *et al.*, 1989). This polycyclicality on the order of  $10^3$  to  $10^5$  years is now quantified for the Potrillo volcanic field as a result of this dissertation study.

## **6.2 Elemental and Isotopic Geochemical Evolution**

Process identification diagrams assist in discriminating between magmatic processes by showing the relative behaviors of highly (H) and moderately (M) incompatible elements during batch partial melting and fractional crystallization. They also help discern whether or not evidence of source heterogeneity is present. Two arrays were identified on several H versus H plots (Chapter 5), indicating source heterogeneity. The first array was consistently composed of eastern plus central alignment melts. The eastern lavas systematically plot at higher incompatible concentrations than do the central lavas. The second array was defined by the western alignment melts and had a lower trajectory than the first array.

In terms of H/M versus H (Chapter 5), the western alignment data defined a positively sloping array but the central and eastern data comprised a second, non-sloping trajectory. The ratio of highly to moderately incompatible elements will increase as the degree of partial melting decreases whereas the ratio will



stay almost constant or slightly increase for fractional crystallization. Figure 52 shows La/Sm plotted against La. The upper plot provides the position of each sample. The lower plot displays the data in terms of eruptive phase and delineates those data from the west half versus the east half. The west half, which formed during eruptive Phase I, plots over a large range and has a positively sloped trajectory. This range potentially reflects the longer eruptive history and greater variation in degrees of partial melting. In comparison, the centers in the east half of the field have a smaller range at higher degrees of partial melt and have been modified by shallow level fractional crystallization. Chen (1991) modeled the partial melting scenario primarily for the centers in the central and eastern alignments by using initial liquid concentrations derived from Mg / Fe<sup>2+</sup> against incompatible element concentrations. The calculations permit a two to three percent batch melting of the mantle.

Phases II, III and V all overlap Phase I at lower, constant La/Sm ratios. Phase IV is intermediate with respect to all other phases. The differences in La/Sm for a given La concentration cannot be the result of a single magma batch undergoing fractional crystallization (Perry and Crowe, 1992). Therefore, the presence of discrete domains elucidates that the data are consistent with a series of magma batches as opposed to derivation from one continuously fractionating batch.

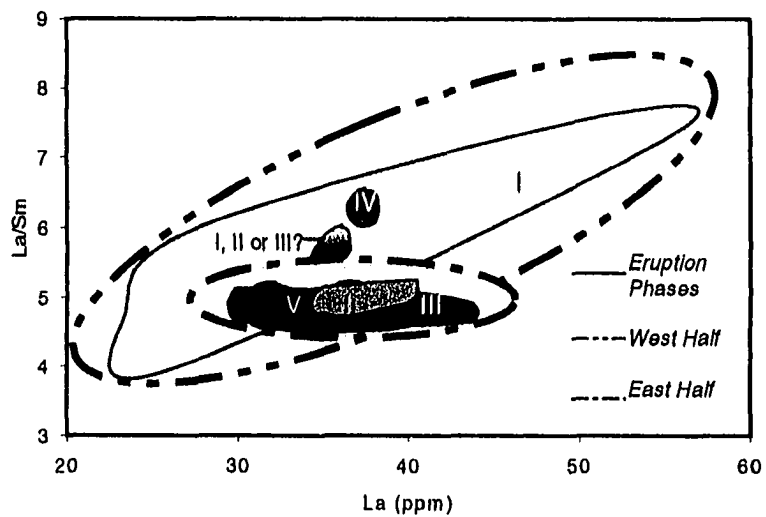
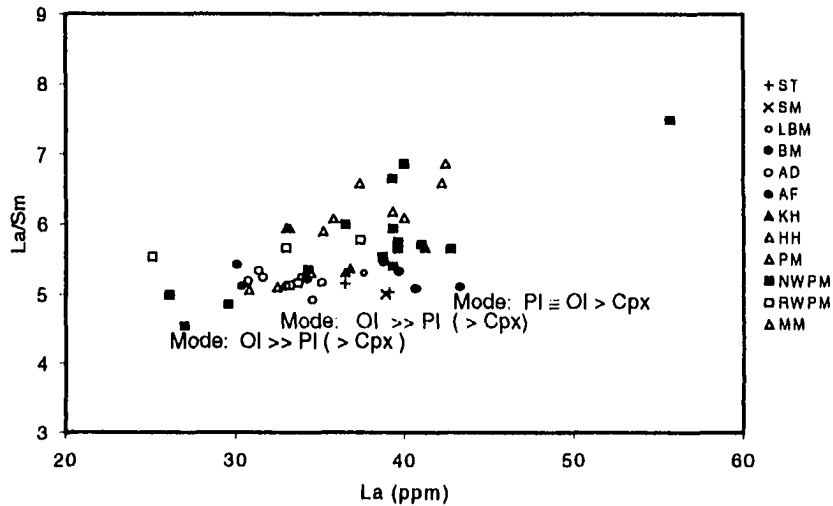


Figure 52. (a) La Versus La/Sm with Phenocryst Modes (b) Same plot with proposed eruption Phases I - V indicated.

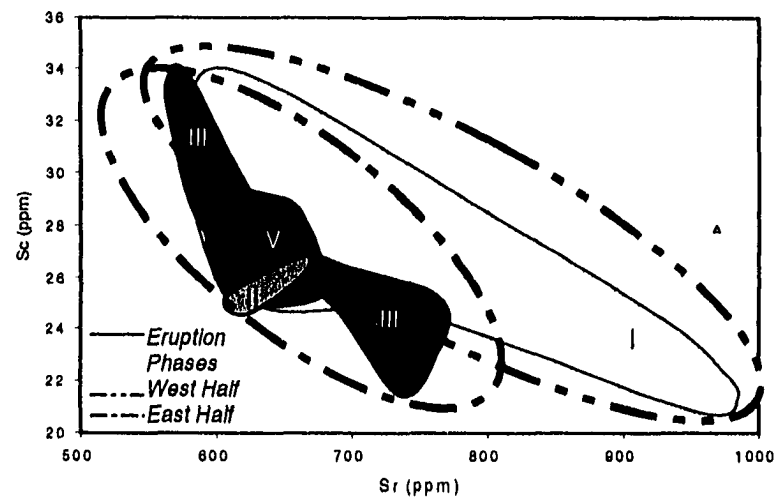
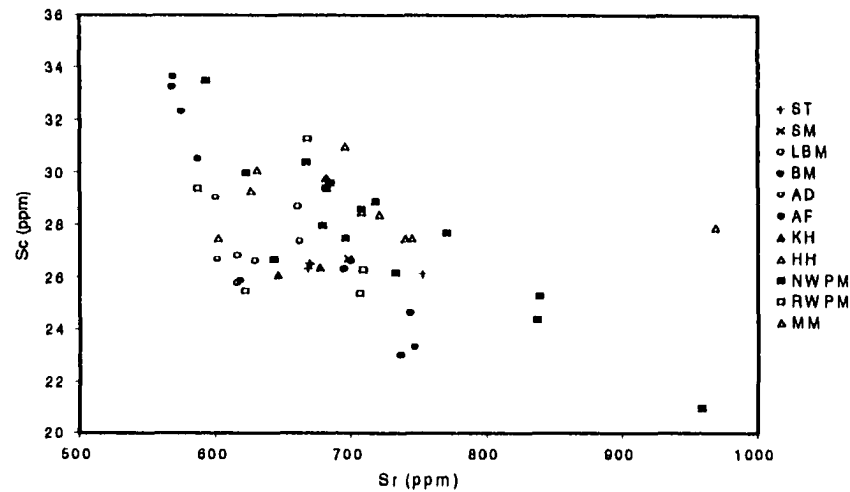


Figure 53. (a) Sr Versus Sc (b) same plot with proposed eruption Phases I - II and V indicated. Note: No Sr data available for IV.

Figure 53 shows the relationship of Sc versus Sr. Again, the upper plot provides the results for individual samples, with the exception of Potrillo Maar melts. Phase IV is not represented due to the lack of Sr data for this maar. This diagram clearly shows that all melts forming the Potrillo volcanic field indicate clinopyroxene crystallization at depth associated with early partial melting of asthenospheric mantle. Physical evidence of an early cumulate stage is potentially represented by clinopyroxene-dominated xenoliths brought to the surface by the Kilbourne Hole episode, for instance. Melts from the east half (mainly the eastern alignment centers) then experienced a shallow-level lithospheric mantle or crustal residency overprint.

Luhr *et al.* (1995) modeled trends for non-modal melting of a light rare earth enriched source. The source mineralogy is presented with respect to Yb versus La/Yb (Figure 54), with end members of 100% garnet lherzolite to 100% spinel lherzolite. This diagram illustrates that primitive (with respect to Mg # greater than 64) samples from the San Quintín volcanic field, characterized by high Yb and low La/Yb ratio values, plot close to a pure spinel lherzolitic source. In comparison, the primitive samples from the Potrillo volcanic field have higher La/Yb ratios but roughly the same range of high Yb concentrations. The Potrillo volcanic field tapped a source of predominantly shallow spinel lherzolite. This is similar to the San Quintín volcanic field, but with slightly more input from the deep, garnet lherzolitic mantle. The central and eastern alignments (*i.e.* the

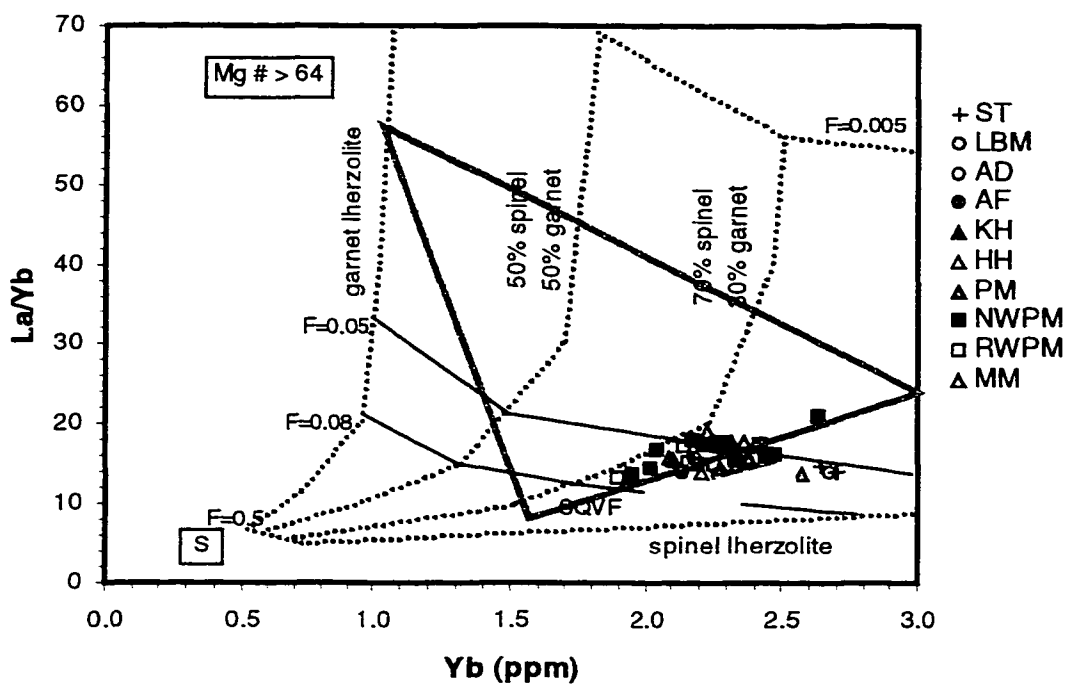


Figure 54. Yb versus La/Yb for primitive samples. This plot modified from Luhr *et al.* (1995); model of nonmodal partial melting of garnet and spinel lherzolite sources following the method in Class *et al.* (1994). Potrillo volcanic field center abbreviations as in Figure 4. San Quintín volcanic field samples provided as yellow domain. Aqua triangle encompasses other intraplate suites discussed in text (compiled in Luhr *et al.*, 1995). Potrillo sample “NWPM” are normal polarity WPM and “RWPM” are reversed polarity WPM.

younger east half of the field) are lower in La/Yb than the western alignment (*i.e.* the overall older west half of the field). Therefore, the source tapped by the younger eruptions is slightly depleted in the highly incompatible elements.

Two distinct associations are observed in the isotopic data, thus leading to the identification of two “groups” (Table 8). Group I melts are characterized by increasing  $\epsilon_{\text{Nd}}$ , decreasing  $^{87}\text{Sr}/^{86}\text{Sr}$ , increasing lead isotopes, and slightly higher magmatic  $^3\text{He}/^4\text{He}$  ( $R/R_a$ ) signatures. Group II displays the opposite signatures: decreasing  $\epsilon_{\text{Nd}}$ , increasing  $^{87}\text{Sr}/^{86}\text{Sr}$ , decreasing lead isotopes, and slightly lower to overlapping magmatic  $^3\text{He}/^4\text{He}$  ( $R/R_a$ ) signatures. In both groups,  $\epsilon_{\text{Nd}}$  -  $^3\text{He}/^4\text{He}$  ( $R/R_a$ ) pairs are documented. Isotopic Group I melts have higher concentrations of incompatible elements and represent lower degrees of partial melting. Group II melts have lower concentrations, thereby representing higher degrees of melting, and have undergone later crystal fractionation at shallow levels.

Preliminary modeling suggests three end member reservoirs are required to explain Group I and Group II (Figure 55). Based upon rationale set forth in Chapter 5, PREMA and HIMU (Zindler and Hart, 1986) are considered as reservoirs with high  $\epsilon_{\text{Nd}}$ , low  $^{87}\text{Sr}/^{86}\text{Sr}$ , and high lead isotopes. Both are consistent with “continental mantle.” These two sources are schematically depicted as Reservoir A and Reservoir B. The third end member, Reservoir C,

Table 8. Groups Determined from Isotopic Characteristics

Category	Attributes	Group I	Group II
Eruption Style	Breach or Fissure Lavas  Syn-Maar Lavas	Western (Mantle Xenolith/cryst-Bearing)  <ul style="list-style-type: none"> <li>Mantle and Crustal Xenolith/cryst-Bearing: RM, PM and KH</li> <li>Crustal Xenolith-Bearing: MM</li> </ul>	Central  <ul style="list-style-type: none"> <li>Crustal Xenolith-Bearing: HH</li> </ul>
Isotopes	$\epsilon_{Nd}$  $^{87}Sr/^{86}Sr$  $^{206}Pb/^{204}Pb$  $^3He/^4He (R/R_a)$	High  Low  High	Low  High  Low
Trace Elements	H/M vs H	High End	Low End

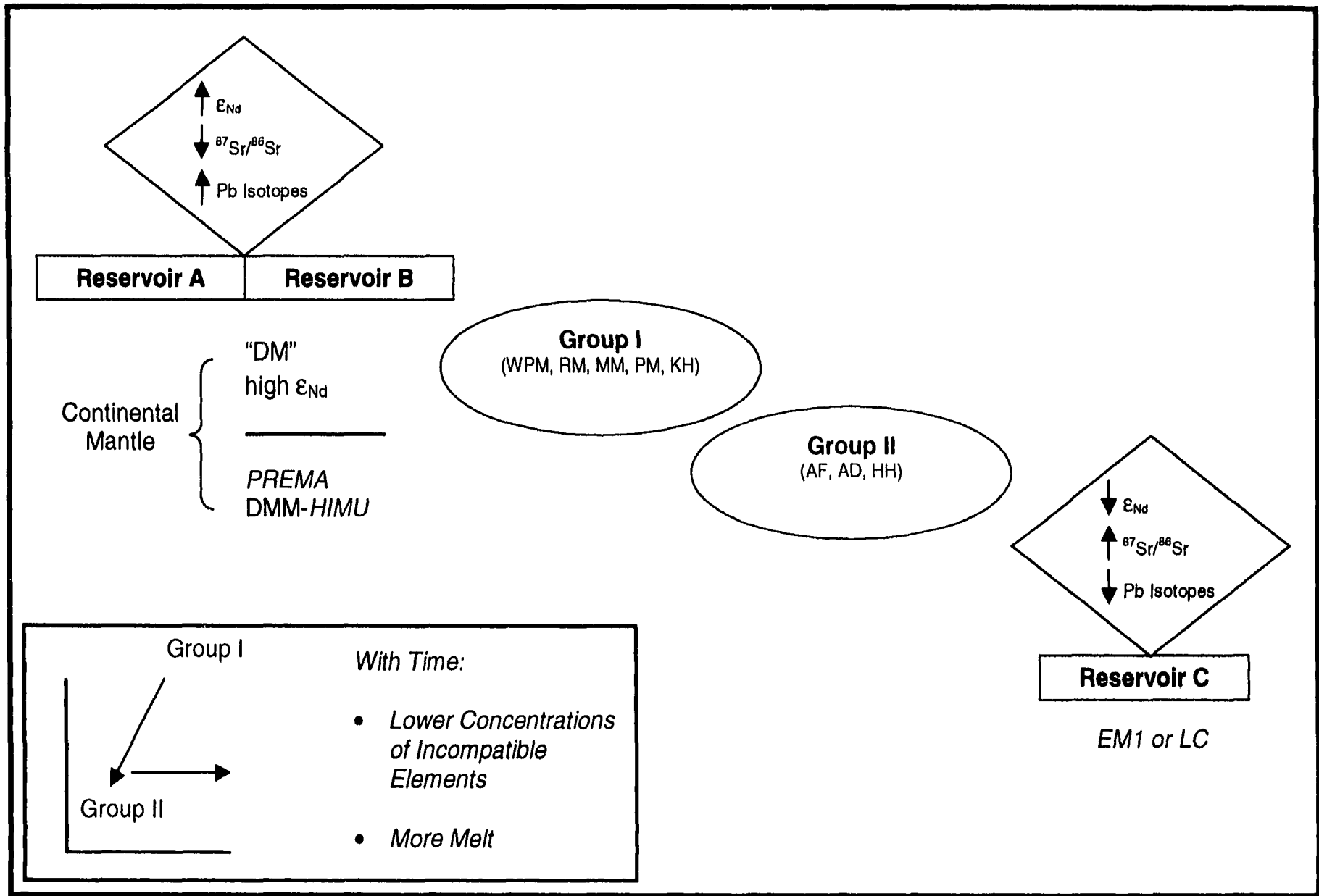


Figure 55. Schematic representation of the elemental and isotopic geochemical evolution for the Potrillo volcanic field.

may be either enriched mantle (EM1; Zindler and Hart, 1986) or lower crust (LC; see Chapter 5). Both elemental and isotopic evidence is equivocal, thus resolving which of these two candidates is Reservoir C is problematic.

### **6.3 Integrated Magma Dynamics Model**

Previous sections have outlined that temporal, physical, and chemical evidence suggest that the Potrillo volcanic field has formed as essentially two halves: the west and the east, relative to the East Robledo fault. Before presenting an integrated magma dynamics explanation for the observed correlations, it is necessary to consider mechanisms which allow mafic magma to ascend in the first place. To do this, I have included ideas from Takada (1995). His study evaluates magma emplacement modeled as “crack coalescence,” and then relates this to the formation of monogenetic and polygenetic mafic centers. Figure 56 is adapted from Takada (1989 and 1994). The four scenarios depict the vertical direction of crack propagation as controlled by density difference and stress gradient driving forces. Of the four, I believe that three cases can be applied to explain eruptions forming the Potrillo volcanic field.

Case 1c is the situation where melt is generated in the asthenosphere and begins to rise due to density differences between the liquid and the solid rock. However, the rising magma reaches a level of neutral buoyancy (LNB) above which it cannot ascend. Additional buoyancy can be achieved if superposition of



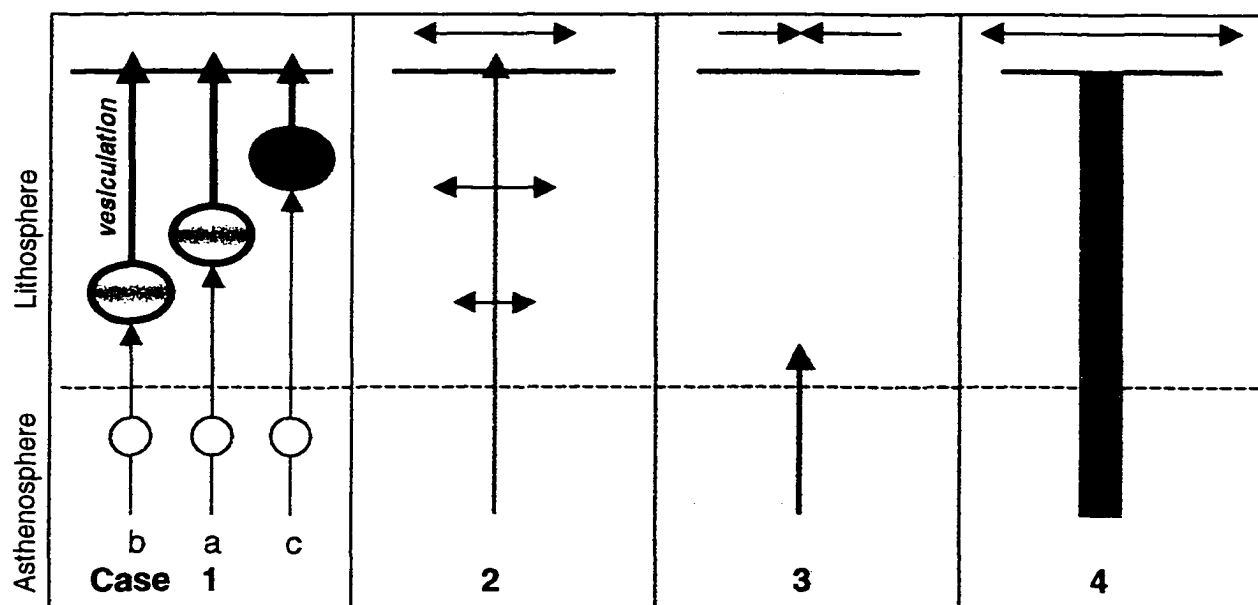



Figure 56. Adapted from Takada (1989 and 1994). Styles of vertical direction of crack propagation controlled by the driving force which is composed of both density difference between magma and host rocks and the stress gradient.

Case 1.  Magma is trapped at level of neutral buoyancy (LNB), or where driving force decreases abruptly, within lithosphere.

**Vesiculation** around LNB gives magma additional buoyancy:  
 (a) hydrostatic stress condition,  
 (b) superposition of compressional stress upon hydrostatic, or  
 (c) superposition of extensional stress upon hydrostatic.

Case 2. Superposition of stress gradient where **extensional stress** increases upward such that magma does not stall in lithosphere.

Case 3. Superposition of stress gradient where compressional stress increases upward (*i.e.* magma does not ascend in lithosphere).

Case 4. Superposition of stress gradient where **extreme extensional stress** increases upward such that any level of lithosphere is LNB.

an extensional stress upon the hydrostatic stress decreases lithostatic confining pressure, thus triggering vesiculation of the magma. This effectively drops the density of the magma, thereby permitting the melt to resume its ascent to the surface. This scenario does not call for protracted stalling of the melt at shallow levels prior to vesiculation. I believe that Takada's Case 1c explains the syn-maar eruption at Malpais Maar.

In the literature, there are two primary ways in which "maar" volcanoes (associated with tuff ring development, for example) develop. One hypothesis is that a few percent partial melt within the mantle results in magma charged with volatiles. This drops the density of the liquid dramatically and propels the material to the surface quite rapidly; field evidence in support of depth of generation and rapid transport is the frequent inclusion of mantle and crustal xenoliths in the tuffaceous phase of the eruption. The other hypothesis is that "maar" volcanoes are a violent, near surface phenomena due to magma intruding a water-saturated layer of crustal material, triggering a hydromagmatic explosion resulting in fragmentation and solidification of the melt as tuff.

Based upon field observations alone, the absence of mantle xenoliths and xenocrysts in the syn-maar tuff ring at Malpais Maar appears to indicate that the system did not tap deep sources. Rather, that it is a result of magma intersecting a watertable, triggering a purely hydromagmatic eruption resulting in

development of a tuff ring. However, the chemical signatures of syn-maar deposits do indicate a deep-seated origin in an apparent contradiction with the field evidence. I propose that the magma ascended to a level of neutral buoyancy (Figure 56, Case 1c), where it resided long enough for dense xenolithic and xenocrystic materials to settle but not sufficiently long enough to acquire crustal signatures. A vesiculation event was then triggered by a change in stress (e.g. seismic activity), bringing about the continued ascent and ensuing phreatomagmatic eruption forming Malpais Maar.

Case 2 in Figure 56 involves superposition of a stress gradient such that extensional stress increases upward and does not allow magma generated in the asthenosphere to stall while ascending through the lithosphere. In essence, there is no level of neutral buoyancy. I believe that this mechanism can be called upon to explain the eruptions of the west half of the field that is comprised of the West Potrillo Mountains, Riley Maar and Potrillo Maar. The Kilbourne Hole eruption in the east half is also best modeled using Case 2. All three maars have field evidence and chemical signatures supporting this scenario, which would allow for abundant mantle and crustal xenoliths and xenocrysts to be deposited at the surface (*i.e.* classic maar eruptions).

The third applicable scenario is Case 4. For this, superposition of a stress gradient is such that extreme extensional stress increases upward thus allowing

for any level of the lithosphere to become a level of neutral buoyancy with respect to ascending magmas generated in the asthenosphere. Vesiculation is *not* required. Depending upon the length and level of residency in the lithosphere, the magma may or may not undergo crystal fractionation and/or incorporate a crustal signature. I propose that this case documents the majority of centers forming the east half of the field: Black Mountain, Little Black Mountain, Afton, Aden, and Hunt's Hole.

Takada also considers the crack coalescence model in light of the style of formation of mafic centers possible; namely, whether they are monogenetic or polygenetic occurrences. He attributes the styles to correlation of magma input and differential stress. In the situation of monogenetic occurrences, there would be a lack of crack coalescence due to low magma input coupled with high differential stress. Conversely, polygenetic complexes would form due to the presence of crack coalescence related to high magma input and low differential stress. He further states that the coexistence of monogenetic and polygenetic volcanoes in areas of 30 km x 30 km, emplaced within 0.1 Ma periods, indicates changes in either magmatic input and/or differential stress with time.

The east half of the Potrillo volcanic field hosts both monogenetic and polygenetic centers with eruption dates within 100 ka or so of one another. Further, these two styles of volcanism occur within a 30 km x 30 km area.

Therefore, the crack coalescence model of Takada (1995) is directly applicable. The older centers of the eastern alignment and the Afton complex are polygenetic and document eruptions from approximately 200 to 100 ka ago (Phases II and III). In contrast, the younger centers are Aden, Kilbourne Hole and Hunt's Hole of the central alignment are monogenetic and erupted approximately 30 – 20 ka ago (Phase V). So there appears to have been a change from polycyclic to monocyclic, which implies a change in differential stress and/or magma input rate during the roughly 65 ka years of quiescence in the east half of the Potrillo volcanic field.

My integrated magma dynamics model (Figure 57) incorporates the physical, spatial, temporal, chemical, and emplacement mechanisms. Overwhelming evidence suggests that the East Robledo fault has played a major role in the development and character of the Potrillo volcanic field. This cartoon-style diagram presents a west to east section viewed from the south toward the north. It summarizes the distribution of major faults; alignments; volcano names; cone, maar or fissure; monocyclic (m) versus polycyclic (p) style; isotopic groups; eruption phases; and overall shift of eruption foci east of the East Robledo fault with time. The third dimension is added to help visualize the potential source reservoirs and the emplacement scenarios based upon the crack coalescence model by Takada (1995).

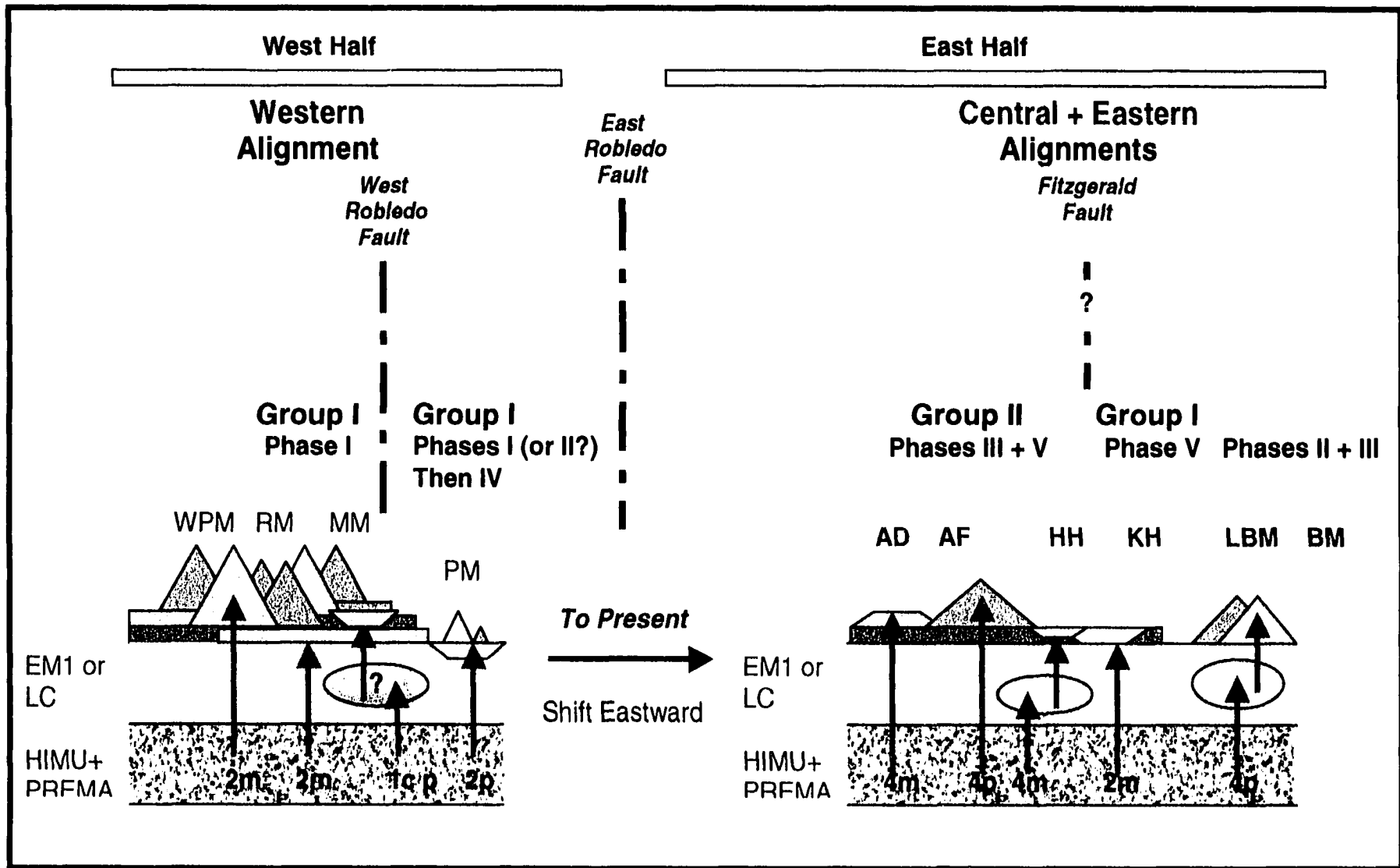


Figure 57. Integrated Magma Dynamics Model for the evolution of the Potrillo volcanic field with time. This is a cartoon-style W – E traverse, with the view from the south toward the north. Center abbreviations as in Figure 4. Above the corresponding centers are: (a) isotopic Groups I and II (b) eruption Phases I through V (c) red arrows indicate suggested path of melt (d) “m” stands for monogenetic and p for “polygenetic” (e) numbers refer to Takada’s Crack Coalescence Model Case number (e) potential reservoirs are also shown.

## REFERENCES

- Anders, E., and Ebihara, M. (1982) Solar abundances of the elements, *Geochimica et Cosmochimica Acta*, 46, 2363 – 2380.
- Anthony, E. Y., Hoffer, J. M., Williams, W. J. W., Poths, J., and Penn, B. (1998) Geochemistry and Geochronology of Quaternary Mafic Volcanic Rocks in the Vicinity of Carrizozo, New Mexico, *New Mexico Geological Society Guidebook* No. 49.
- Anthony, E. Y. (1993) Dating Techniques for Quaternary Lavas, *Eos, Transactions, American Geophysical Union*, 74, no. 31, 350.
- Anthony, E. Y., Hoffer, J., Waggoner, K., and Chen, W. (1992) Compositional diversity in late Cenozoic mafic lavas in the Rio Grande Rift and Basin and Range Province, southern New México: *Geological Society of America Bulletin*, v. 104, p. 973 - 979.
- Anthony, E. Y., McIntosh, W. C., Poths, J., Williams, W. J. W., Whitelaw, M., and Geissman, J. (1994) Geochronology and Paleomagnetism of the Quaternary Potrillo Volcanic Field, Rio Grande Rift, New Mexico, Eighth International Conference on Geochronology, Cosmochronology and Isotope Geology Abstracts Volume.
- Anthony, E. Y. and Poths, J. (1992)  $^3\text{He}$  surface exposure dating and its implications for magma evolution in the Potrillo volcanic field, Rio Grande Rift, New Mexico, USA, *Geochimica et Cosmochimica Acta*, 56, 4105 - 4108.
- Bard, E., Hamelin, B., Fairbanks, R. G., and Zindler, A. (1990) Calibration of the  $^{14}\text{C}$  timescale over the past 30,000 years using mass spectrometric U – Th ages from Barbados corals, *Nature*, 345, 405 – 410.
- Bersch, M. G. (1977) Petrography and Geology of the Southern West Potrillo Basalt Field, Dona Ana County, New Mexico, Unpublished M.S. Thesis, University of Texas at El Paso, 60 pp.
- Best, M. G. and Brimhall, W. H. (1974) Late Cenozoic alkali basalt magmas of the

- western Colorado Plateaus and the Basin and Range Transition Zone, U.S.A., and their bearing on mantle dynamics, *Geol. Soc. Am. Bull.*, 85, 1677 – 1690.
- Bierman, P. R. (1994) Using In-Situ Produced Cosmogenic Isotopes to Estimate Rates of Landscape Evolution -- A Review from the Geomorphic Perspective, *Journal of Geophysical Research*.
- Cerling, T. E. (1990) Dating geomorphic surfaces using cosmogenic  $^3\text{He}$ , *Quaternary Research*, 33, 148 - 156.
- Cerling, T. E. and Craig, H. (1994) Cosmogenic  $^3\text{He}$  production rates from 39° N to 46° N latitude, western U.S.A. and France, *Geochimica et Cosmochimica Acta*, 58, 249 – 255.
- Chen, W. (1992) Evolution of the Potrillo Volcanic Field, Unpublished M. S. Thesis, University of Texas at El Paso, 75 pp.
- Class, C., Altherr, R., Volker, F., Eberz, G., and McCulloch, M. T. (1994) Geochemistry of Pliocene to Quaternary alkaline basalts from the Huri Hills, northern Kenya, *Chemical Geology*, 113, 1 – 22.
- Craig, H. and Poreda, R. J. (1986) Cosmogenic  $^3\text{He}$  in terrestrial rocks: The summit lavas of Maui, *Proceedings of the National Academy of Science USA*, 83, 1970 - 1974.
- Crowe, B., Turrin, B., Wells, S., McFadden, L., Renault, C., Perry, F., Harrington, C., and Champion, D. (1989) Polycyclic volcanism: A common eruption mechanism of small volume basaltic volcanic centers of the southern Great Basin, U.S.A., IAVCEI Continental Magmatism Abstracts, New Mexico Bureau of Mines and Mineral Resources Bulletin 131, p 63.
- Crowley, J., Niemeyer, S. and Shaw, H. F. (1986) *Geo. Soc. Amer. Abs. Prog.*, 18, 577.
- DeHon, R.H. (1965) A maar origin for Hunts Hole, Doña Ana County, New Mexico, M.S. Thesis, Texas Tech College, 70 p.
- Dunker, K. E., Wolff, J. A., Harmon, R. S., Leat, P. T., Dickin, A. P., and Thompson,



- R. N. (1991) Diverse mantle and crustal components in lavas of the NW Cerros del Rio volcanic field, Rio Grande Rift, New Mexico: *Contributions to Mineralogy and Petrology*, v. 108, p. 331 - 345.
- Dungan, M. A., Lindstrom, M. M., McMillan, N. J., Moorbath, S., Hoefs, J., and Haskin, L. A. (1986) Open system magmatic evolution of the Taos Plateau volcanic field, Northern New México: 1. The petrology and geochemistry of the Servilleta basalt: *Journal of Geophysical Research*, v. 91, p. 5999 - 6028.
- Gibson, S. A., Thompson, R. N., Leat, P. T., Dickin, A. P., Morrison, M. A., Hendry, G. L., and Mitchell, J. G. (1992) Asthenosphere-derived magmatism in the Rio Grande rift, western U. S. A.: implications for continental break-up, from Storey, B.C., Alabaster, T. and Pankhurst, R. J. (eds) *Magmatism and the Causes of Continental Break-Up*, *Geo Soc Sp Pub* No. 68, pp. 61 – 89.
- Gile, L. H., Hawley, J. W. and Grossman, R. B. (1981) Soils and geomorphology in the Basin and Range area of southern New Mexico – Guidebook to the Desert Project: New Mexico Bureau of Mines and Mineral Resources, Circular 196, 43 pp.
- Gile, L. H. (1987) A pedogenic chronology for Kilbourne Hole, Southern New Mexico: I. Soils in the Tuff, *Soil Science Society of America Journal*, 51, 746 – 751.
- Harland, W. B., Armstrong, R. L., Cox, A. V., Craig, L. E., Smith, A. G., and Smith, D. G. (1990) *A Geologic Time Scale 1989*, Cambridge University Press, New York, 263 pp.
- Heatherington, A. L. (1988) Isotope systematics of volcanics from the south-central Rio Grande rift and the Western Mexican Volcanic Belt: Implications for magmatic and tectonic evolution of Cenozoic extensional regimes in western North America, Unpublished Ph.D., Washington University, 207 pp.
- Hill, B. E., Leslie, B. W., and Connor, C. B. (1993) A Review and Analysis of Dating Techniques for Neogene and Quaternary Volcanic Rocks, Nuclear Regulatory Commission Contract NRC-02-88-005, CNWRA 93-018, 79 pp.
- Hoffer, J. (1971) *Mineralogy and petrology of the Santo Tomas – Black Mountain*

- basalt field, Potrillo Volcanics, south-central New Mexico: *Geol Soc Amer Bull*, 82, 603 – 612.
- Hoffer, J. M. (1976) Geology of the Potrillo basalt field, south-central New Mexico, *New Mexico Bureau of Mines Circular* 149.
- Irving and Barager (1971) A guide to the chemical classification of the common volcanic rocks, *Canadian Journal of Earth Science*, 8, 523 – 548.
- Jacques, A. L. and Green, D. H. (1980) Anhydrous melting of peridotite at 0 – 15 kb pressure and the genesis of tholeiitic basalts, *Contrib. Mineral. Petrol.*, 73, 287 – 310, 1980.
- Jagoutz, E., Carlson, R. W., and Lugmair, G. W. (1980) Equilibrated Nd-unequilibrated Sr isotopes in mantle xenoliths, *Nature*, 286, 708 – 710.
- Johnson, C. M. and Thompson, R. A. (1991) Isotopic composition of Oligocene mafic volcanic rocks in the northern Rio Grande Rift: Evidence for contributions of ancient intraplate and subduction magmatism to evolution of the lithosphere: *Journal of Geophysical Research*, v. 96, p. 13593 - 13608.
- Keller, G. P., Morgan, P., and Seager, W. R. (1990) Crustal Structure, Gravity Anomalies and Heat Flow in the Southern Rio Grande Rift and Their Relationship to Extensional Tectonics, *Tectonophysics*, 174, 21 - 37.
- Knutson, J. and Green, T. H. (1975) Experimental duplication of a high-pressure megacryst/cumulate assemblage in a near-saturated hawaiiite, *Contrib Mineral. Petro.*, 52, 121 – 132.
- Kurz, M. D. (1986a) Cosmogenic helium in a terrestrial igneous rock, *Nature*, 320, 435 - 439.
- Kurz, M. D. (1986b) In situ production of terrestrial cosmogenic helium and some applications to geochronology, *Geochimica et Cosmochimica Acta*, 50, 2855 - 2862.
- Kurz, M. D., Colodner, D., Trull, T. W., Moore, R. B., and O'Brien, K. (1990) Cosmic ray exposure dating with in situ produced cosmogenic  $^3\text{He}$ : results from young Hawaiian lava flows, *Earth and Planetary Science Letters*, 97, 177 - 189.

- Lal, D. (1987) Production of  $^3\text{He}$  in terrestrial rocks, *Chemical Geology (Isotope Geoscience Section)* 66, 89 - 98.
- Lal, D. (1988) In situ-produced cosmogenic isotopes in terrestrial rocks, *Annual Review Earth and Planetary Science*, 16, 355 - 388.
- Lal, D. (1991) Cosmic ray labeling of erosion surfaces: in situ nuclide production rates and erosion models, *Earth and Planetary Science Letters*, 104, 424 - 439.
- Laughlin, A. W., Poths, J., Healey, H. A., Reneau, S., and WoldeGabriel, G. (1994) Dating of Quaternary basalts using the cosmogenic  $^3\text{He}$  and  $^{14}\text{C}$  methods with implications for excess  $^{40}\text{Ar}$ , *Geology*, 22, 135 - 138.
- Le Bas, M. J., Le Maitre, R. W., Streckeisen, A., and Zanettin, B. (1986) A chemical classification of volcanic rocks based on the total alkali-silica diagram, *Journal of Petrology*, 27, 745 - 750.
- Leavy, B. (1987) Surface exposure dating of young volcanic rocks using the in situ build-up of cosmogenic isotopes, Unpublished Ph.D., New Mexico Institute of Mining and Technology, 166 pp.
- Long, C. (1994) Ultramafic Xenoliths from Kilbourne Hole, Potrillo Volcanic Field, Unpublished M.S. Thesis, University of Texas at El Paso.
- Luhr, J. F., Aranda-Gomez, J. J., and Housh, T. B. (1995) San Quintín Volcanic Field, Baja California Norte, México: Geology, petrology, and geochemistry: *Journal of Geophysical Research*, v. 100, n. B7, pp. 10353 - 10380.
- McIntosh, W. C. (1994)  $^{40}\text{Ar}/^{39}\text{Ar}$  Geochronology of Late Miocene to Pleistocene Basalts of the Zuni-Bandera, Red Hills-Quemado, and Potrillo Volcanic Fields, New Mexico, *New México Geology*.
- Mack, G. H., Salyards, S. L. and James, W. C. (1991) Magnetostratigraphy of the Camp Rice Formation (Plio-Pleistocene in the southern Rio Grande rift, *Geol Soc Amer, Abs Prog*, 23, 45.
- Mack, G. H. and Seager, W. R. (1995) Transfer zones in the southern Rio Grande rift, *Journal of the Geological Society, London*, 152, 551 - 560.
- Marti, L. and Craig, H. (1987) Cosmic-ray-produced neon and helium in the summit

- lavas of Maui, *Nature*, 352, 335 - 337.
- Menzies, M. A., Kyle, P. R., Jones, M., and Ingram, G. (1991) Enriched and depleted source components for tholeiitic and alkaline lavas from Zuni-Bandera, New Mexico: Inferences about intraplate processes and stratified lithosphere: *Journal of Geophysical Research*, v. 96, p. 13645 - 13671.
- Menzies, M. A., Leeman, W. P., and Hawkesworth, C. J. (1983) Isotope Geochemistry of Cenozoic Volcanic Rocks Reveals Mantle Heterogeneity Below Western USA, *Nature*, 303, no. 5914, 205 - 209.
- Nishiizumi, K., Klein, J., Middleton, R., and Craig, H. (1990) Cosmogenic  $^{10}\text{Be}$ ,  $^{26}\text{Al}$  and  $^3\text{He}$  in olivine from Maui lavas, *Earth and Planetary Science Letters*, 98, 263 - 266.
- Nishiizumi, K., Lal, D., Klein, J., Middleton, R., and Arnold, J. R. (1986) Production of  $^{10}\text{Be}$  and  $^{26}\text{Al}$  by cosmic rays in terrestrial quartz in situ and implications for erosion rates, *Nature*, 319, 134 - 136.
- Nishiizumi, K. et al. (1991)  $^{10}\text{Be}$  -  $^{26}\text{Al}$  exposure ages at Meteor Crater, Arizona, *Geochimica et Cosmochimica Acta*, 55, 2699 - 2703.
- Omenda, P. (1997) Suswa Volcano, Kenya, Unpublished Ph.D., UTEP, 218 pp.
- Ortiz, T. G. (1981) Megacrysts and Mafic and Ultramafic Inclusions of the Southern West Potrillo Basalt Field, Dona Ana County, New Mexico, Unpublished M.S. Thesis, University of Texas at El Paso, 95 pp.
- Page, R. O. (1973) Stratigraphy and Structure of the Quaternary Malpais Maar Volcano, Dona Ana County, New Mexico, Unpublished M.S. Thesis, University of Texas at El Paso, 46 pp.
- Perry, F. V., Baldrige, W. S., and DePaolo, D. J. (1987) Role of Asthenosphere and Lithosphere in the Genesis of Late Cenozoic Basaltic Rocks from the Rio Grande Rift and Adjacent Regions of the Southwestern United States, *Journal of Geophysical Research*, 92, no. B9, 9193 - 9213.
- Perry, F. V., Baldrige, W. S., and DePaolo, D. J. (1988) Chemical and Isotopic

- Evidence for Lithospheric Thinning beneath the Rio Grande Rift, *Nature*, 332, no. 6163, 432 - 434.
- Perry, F. V., Baldrige, W. S., DePaolo, D. J., and Shafiqullah, M. (1990) Evolution of a magmatic system during continental extension: The Mount Taylor volcanic field, New México: *Journal of Geophysical Research*, v. 95, p. 19327 - 19348.
- Perry, F. V. and Crowe, B. (1992)
- Phillips, F. M., Dunbar, N. and Zreda, M. (1997) A test of chlorine-36 for dating of late basaltic volcanoes, *EOS Transaction AGU, Fall meeting supplement*, v 78, n 46, p. F760.
- Phillips, F. M., Zreda, M. G., Smith, S. S., Elmore, D., Kubik, P. W., Dorn, R. I., and Roddy, D. J. (1991) Age and geomorphic history of Meteor Crater, Arizona, from cosmogenic  $^{36}\text{Cl}$  and  $^{14}\text{C}$  in rock varnish, *Geochimica et Cosmochimica Acta*, 55, 2695 - 2698.
- Pier, J. G., Luhr, J. F., Podosek, F. A., and Aranda-Gomez, J. J. (1992) The La Breña – El Jagüey Maar Complex, Durango, México: II. Petrology and Geochemistry, *Bulletin of Volcanology*, 54, 405 – 428.
- Pier, J. G., Podosek, F. A., Luhr, J. F., Brannon, J. C., and Aranda-Gomez, J. J. (1989) Spinel-lherzolite-bearing, Quaternary volcanic centers in San Luis Potosí, México, 2. Sr and Nd isotopic systematics, *Journal of Geophysical Research*, 94, 7941 – 7951.
- Reeves, C. C., Jr., and DeHon, R. A. (1965) Geology of Potrillo maar, New Mexico and northern Chihuahua, Mexico, *American Journal of Science*, 263, 401 – 409.
- Reid, M. R. (1989) Compositional dependence of Pb isotopic signatures in the lower crust exhibited by xenoliths from Kilbourne Hole, New Mexico, *IAVCEI Continental Magmatism Abstracts*, New Mexico Bureau of Mines and Mineral Resources Bulletin 131, p 222.
- Reid, M. R. and Graham, D. W. (1996) Resolving lithospheric and sub-lithospheric contributions to helium isotope variations in basalts from the southwestern U.S., *Earth and Planetary Science Letters*, 144, 213 – 222.

- Renault, J. (1970) Major-Element Variations in the Potrillo, Carrizozo, and McCarty's Basalt Fields, New Mexico, New Mexico State Bureau of Mines and Mineral Resources Circular 113, 22 pp.
- Roden, M. F., Irving, A. J., and Murthy, V. R. (1988) Isotopic and trace element compositions of the upper mantle beneath a young continental rift: Results from Kilbourne Hole: *Geochimica et Cosmochimica Acta*, v. 52, p. 461 – 473.
- Salyards, S. L. (1991) A preliminary assessment of the seismic hazard of the southern Rio grande rift, New Mexico, *New Mexico Geological Society Guidebook*, 42<sup>nd</sup> Field Conference, 199 – 202.
- Sarda, P., Staudacher, T., Allegre, J., and Lecomte, A. (1993) Cosmogenic neon and helium at Reunion: measurement of erosion rate, *Earth and Planetary Science Letters*, 119, 405 - 417.
- Seager, W. R. and Morgon, R. (1979) Rio Grande rift in southern New Mexico, west Texas, and northern Chihuahua in rio Grande rift: *Tectonics and Magmatism*, American Geophysical Union, 87 – 106.
- Sheffield, T. M. (1981) Petrography and Geochemistry of the West Potrillo Basalt Field, Dona Ana County, New Mexico, Unpublished M.S. Thesis, University of Texas at El Paso, 91 pp.
- Staudacher, T. and Allegre, C. J. (1993) Ages of the second caldera of Piton de la Fournaise volcano (Reunion) determined by cosmic ray produced <sup>3</sup>He and <sup>21</sup>Ne, *Earth and Planetary Science Letters*, 119, 395 - 404.
- Takada, A. (1989) Magma transport and reservoir formation by a system of propagating cracks, *Bulletin of Volcanology*, 52, 118 – 126.
- Takada, A. (1994) The influence of regional stress and magmatic input on styles of monogenetic and polygenetic volcanism, *Journal of Geophysical Research*, 99, B7, 13563 – 13573.
- Treuil, M., Joron, J. L., and Jaffrezic, H. (1977) Trace Element Geochemistry of Magmatic Rock Series of Converging and Diverging Plate Boundaries, *Journal of Radioanalytical Chemistry*, 38, 351 – 362.

- Wells, S. G., Renault, C. E., and McFadden, L. D. (1989) Geomorphic and pedologic criteria for recognizing polycyclic volcanism at small basaltic centers in the western U.S.A., IAVCEI Continental Magmatism Abstracts, New Mexico Bureau of Mines and Mineral Resources Bulletin 131, p 289.
- Williams, W. J. W., Poths, J. and Anthony, E. Y. (In Revision) Helium isotopes and the geochronology of the Quaternary San Quintín volcanic field (Baja California Norte, México), *Journal of Volcanology and Geothermal Research*.
- Williams, W. J. W. and Poths, J. (1994) The Potrillo Volcanic Field, Southern Rio Grande Rift:  $^3\text{He}$  surface exposure dates and petrogenetic considerations, *New Mexico Geology*.
- Williams, W. J. W., McIntosh, W. C., Poths, J., Miller, J. G., and Anthony, E. Y. (1994) The Quaternary Western Potrillo Volcanic Field, Southern Rio Grande Rift:  $^{40}\text{Ar}/^{39}\text{Ar}$  geochronology and geochemistry [abs]: *EOS*, v. 75, p. 731.
- Williams, W. J. W., Anthony, E. Y., Poths, J., Healey, H. A., Whitelaw, M., and Geissman, J. (1993)  $^3\text{He}$  surface exposure dates and chemistry of the Potrillo volcanic field, Rio Grande rift, and magmatic  $^3\text{He}/^4\text{He}$  signatures of Quaternary lavas of the southwestern United States, International Association of Volcanologists and Chemists of the Earth's Interior General Assembly in Canberra, Australia, Abstracts Volume, 123.
- Williams, W. J. W., Poths, J., Anthony, E. Y., Miller, J. G., Luhr, J. F., Aranda-Gomez, J. J., and T. B. Housh (1995) Cosmogenic Helium Surface Exposure Dating of the Quaternary Mafic San Quintín Volcanic Field, Baja California Norte, México, Geological Society of America National Meeting in New Orleans, *GSA Abstract with Programs*.
- Williams, W. J. W., Poths, J., Anthony, E., Olinger, C. T., Whitelaw, M., and Geissman, J. (1992) Magmatic  $^3\text{He}/^4\text{He}$  signatures,  $^3\text{He}$  surface exposure dating and paleomagnetism of Quaternary volcanics in the Rio Grande rift, New Mexico, *EOS*, 73, 610.
- Zindler and Hart (1986) Chemical geodynamics, *Annual Review of Earth and Planetary*

Sciences, 14, 493 – 573.

Zreda, M. G., Phillips, F. M., Kubik, P. W., Sharma, P., and Elmore, D. (1993)  
Cosmogenic  $^{36}\text{Cl}$  dating of a young basaltic eruption complex, Lathrop Wells,  
Nevada, *Geology*, 21, 57 - 60.



## APPENDIX

Table A. <sup>3</sup>He Surface Exposure Dating Sample Descriptions

<b>Eruptive Center</b> <small><sup>3</sup>He Date Sample<sup>1</sup></small>	<b>Latitude</b> <b>(North)</b>	<b>Longitude</b> <b>(West)</b>	<b>Elevation</b> <b>(meters)</b>	<b>Thickness</b> <b>(cm)</b>	<b>OI</b> <b>(%)</b>
<b>Little Black Mountain</b>					
29#1	32° 07' 20"	106° 47' 20"	1283	5	92
29#2	32° 07' 20"	106° 47' 20"	1283	5	
<b>Black Mountain</b>					
21T	32° 04' 19"	106° 47' 36"	1320	3	
21B	32° 04' 19"	106° 47' 36"	1320	3	
27#1	32° 04' 16"	106° 47' 36"	1372	5	
27#2	32° 04' 16"	106° 47' 36"	1372	5	
<b>Aden Flows</b>					
23C#1				3	
23C#2				3	
24B				3.5	
24C				3.5	
25A				4.5	
65B#1	32° 05' 16"	106° 58' 11"	1291	3	95
65B#2	32° 05' 16"	106° 58' 11"	1291	3	97
<b>Syn-Hunt's Hole</b>					
62C#1	31° 55' 06"	106° 57' 40"	1259	5	
62C#2	31° 55' 06"	106° 57' 40"	1259	5	
<b>Syn-Kilbourne Hole</b>					
KHPRS13	31° 57' 30"	106° 57' 30"	1256	5	
<b>Afton Flows</b>					
22B#1	32° 03' 05"	106° 54' 43"	1286	3	
22B#2	32° 03' 05"	106° 54' 43"	1286	3	
22D	32° 03' 05"	106° 54' 43"	1286	3	
58B#1	31° 53' 15"	106° 58' 15"	1253	4	96
58B#2	31° 53' 15"	106° 58' 15"	1253	4	
58C#1	31° 53' 15"	106° 58' 15"	1253	4	
28#2	32° 58' 34"	106° 57' 29"	1311	5	
58A#1	31° 53' 15"	106° 58' 15"	1253	4	
<b>Spatter Near Hunt's Hole</b>					
63A#1	31 56' 08"	106 58' 11"	1273		

**Notes:**

1 Sample Density Used for Date

Calculations = 2.2 g/cc

2 Point counts on grain mounts conducted on random oi and px separations to determine percentage of oi analyzed.

3 Shielded sample of the lower Afton flow.

Excavated from under 2.3 m of tuff.

Table A.  $^3\text{He}$  Surface Exposure Dating Sample Descriptions

<b>Eruptive Center</b> <small><math>^3\text{He}</math> Date Sample<sup>1</sup></small>	<b>Latitude</b> <b>(North)</b>	<b>Longitude</b> <b>(West)</b>	<b>Elevation</b> <b>(meters)</b>	<b>Thickness</b> <b>(cm)</b>	<b>Ol*</b> <b>(%)</b>
<b>Post-Potrillo Maar</b>					
<b>52A#1</b>	31° 45' 45"	107°	1297	5	
<b>52A#2</b>	31° 45' 45"	107°	1297	5	
<b>52C#1</b>	31° 45' 45"	107°	1297	5	
<b>Post-Potrillo Maar</b>					
<b>56A#1</b>	31° 46' 23"	107°	1268	4	89.2
<b>56A#2</b>	31° 46' 23"	107°	1268	4	
<b>56A#3</b>	31° 46' 23"	107°	1268	4	
<b>56B#1</b>	31° 46' 23"	107°	1268	4	
<b>Post-Malpais Maar</b>					
<b>M3#1</b>	31° 48' 38"	107° 11' 48"	1317	3	
<b>M5#1</b>	31° 48' 18"	107° 12' 16"	1277	4	92
<b>M5#2</b>	31° 48' 18"	107° 12' 16"	1277	4	
<b>Carrizozo, New Mexico</b>					
<b>CF1#1</b>	33° 42' 06"	105° 56' 04"	1608	5	
<b>CF2#1</b>	33° 42' 06"	105° 56' 04"	1608	5	

**Notes:**

1 Sample Density Used for Date

Calculations = 2.2 g/cc

2 Point counts on grain mounts conducted

on random ol and px separations to

determine percentage of ol analyzed.

Table B. Comprehensive Major Element and Normative Mineralogy

Source Center	Chen (1991)										
	Afton flows				Aden Flows						
<b>Sample</b>	<b>AF4</b>	<b>AF8/26</b>	<b>AF2</b>	<b>AF1</b>	<b>AD6</b>	<b>AD5</b>	<b>AD4</b>	<b>AD3</b>	<b>AD3A</b>	<b>AD2</b>	<b>AD1</b>
SiO <sub>2</sub>	45.20	44.80	44.53	44.73	46.47	46.75	45.12	44.96	46.44	44.00	46.27
TiO <sub>2</sub>	2.18	2.10	2.18	2.18	2.33	2.24	2.38	2.29	2.33	2.21	2.31
Al <sub>2</sub> O <sub>3</sub>	14.73	14.50	14.56	14.89	15.40	15.84	15.48	15.41	15.94	14.91	15.96
Fe <sub>2</sub> O <sub>3</sub>	12.24	11.10	12.04	12.15	11.87	11.27	11.07	11.36	11.04	11.51	11.23
MnO	0.17	0.19	0.18	0.18	0.16	0.16	0.17	0.16	0.16	0.16	0.16
MgO	10.84	10.96	11.14	10.93	10.27	10.09	10.67	8.92	8.78	9.00	9.43
CaO	10.44	10.83	10.88	10.52	9.93	9.69	10.01	9.93	10.06	9.95	9.93
Na <sub>2</sub> O	3.38	3.14	2.95	2.96	3.43	3.19	3.34	3.29	3.38	3.36	3.56
K <sub>2</sub> O	1.53	1.61	1.40	1.62	1.76	1.77	1.72	1.75	1.72	1.78	1.76
F <sub>2</sub> O <sub>5</sub>	0.47	0.47	0.45	0.51	0.50	0.51	0.51	0.54	0.54	0.50	0.54
<b>Mg#</b>	<b>67.38</b>	<b>69.72</b>	<b>68.33</b>	<b>67.72</b>	<b>66.87</b>	<b>67.63</b>	<b>69.20</b>	<b>64.67</b>	<b>64.96</b>	<b>64.59</b>	<b>66.19</b>
Or	9.0	9.5	8.3	9.6	10.4	10.5	10.2	10.3	10.2	10.5	10.4
Ab	8.5	7.0	7.2	7.8	12.1	14.6	9.4	12.0	14.9	9.3	12.9
An	20.5	20.7	22.4	22.6	21.4	23.7	22.2	22.1	23.2	20.3	22.4
Ne	10.9	10.7	9.6	9.3	9.1	6.7	10.2	8.6	7.4	10.4	9.3
Cpx	22.8	24.1	23.2	21.2	19.8	16.8	19.4	19.1	18.7	20.9	18.9
Ol	20.5	19.3	21.1	21.1	20.0	20.2	20.0	17.4	16.9	17.2	18.2
Mt	2.7	2.4	1.7	2.6	2.6	2.5	2.4	2.5	2.4	2.5	2.4
Il	4.1	4.0	4.1	4.1	4.4	4.3	4.5	4.3	4.4	4.2	4.4
Ap	1.1	1.1	1.1	1.2	1.2	1.2	1.2	1.3	1.3	1.2	1.3
Total	100.12	98.80	98.63	99.59	101.10	100.32	99.51	97.62	99.42	96.38	100.17

Notes: **Bolded sample designations indicate a Hawaaitite rather than Trachybasalt ( $Na_2O - 2 > K_2O$ ; Le Bas *et al.*, 1986).**  
**Bolded and italicized sample designations indicate a Hawaaitite-Trachybasalt ( $Na_2O - 2 = K_2O$ ; Le Bas *et al.*, 1986).**

Table B. Comprehensive Major Element and Normative Mineralogy

Source Center	Santo Tomas			San Miguel			Little Black Mnt.			Black Mountains		
	AD1H	SAT5	SAT4	SAM7	LBM1	LBM2	BM5	BM5H	BM3	BM2		
SiO <sub>2</sub>	46.58	46.72	45.73	47.09	46.48	46.75	46.28	47.29	45.76	46.33		
TiO <sub>2</sub>	2.30	2.27	2.30	2.28	2.20	2.33	2.42	2.44	2.29	2.50		
Al <sub>2</sub> O <sub>3</sub>	15.53	16.35	16.47	16.80	15.94	16.65	17.16	17.23	15.97	17.28		
Fe <sub>2</sub> O <sub>3</sub>	11.30	11.07	10.70	10.66	11.36	11.32	10.50	10.50	10.99	10.37		
MnO	0.15	0.16	0.16	0.16	0.16	0.16	0.16	0.16	0.15	0.16		
MgO	9.27	8.70	8.22	7.56	9.31	7.46	6.33	6.26	7.28	6.09		
CaO	9.78	9.50	9.37	9.76	9.15	9.71	9.53	9.41	9.34	9.77		
Na <sub>2</sub> O	3.49	3.95	3.87	3.88	3.71	4.16	4.29	4.29	4.08	4.19		
K <sub>2</sub> O	1.75	1.81	1.99	1.88	1.88	1.77	2.27	2.22	2.03	2.19		
F <sub>2</sub> O <sub>5</sub>	0.52	0.56	0.58	0.58	0.58	0.57	0.69	0.66	0.58	0.65		
Mg#	65.69	64.69	64.18	62.33	65.65	60.59	58.43	58.16	60.68	57.79		
Or	10.3	10.7	11.8	11.1	11.1	10.5	13.4	13.1	12.0	12.9		
Ab	14.8	14.8	13.1	16.4	14.9	15.6	13.6	16.6	13.9	14.1		
An	21.5	21.5	21.7	22.9	21.3	21.5	20.9	21.2	19.3	21.9		
Ne	8.0	10.1	10.7	8.9	8.9	10.6	12.3	10.7	11.2	11.6		
Cpx	19.1	17.8	17.0	17.7	16.3	18.6	17.8	17.3	18.9	18.2		
OI	18.0	17.2	16.3	14.8	19.2	14.9	12.2	12.3	14.4	11.5		
Mt	2.5	2.4	2.3	2.3	2.5	2.5	2.3	2.3	2.4	2.3		
Il	4.4	4.3	4.4	4.3	4.2	4.4	4.6	4.6	4.3	4.7		
Ap	1.2	1.3	1.4	1.4	1.4	1.4	1.6	1.6	1.4	1.5		
Total	99.68	100.13	98.44	99.72	99.67	99.90	98.73	99.57	97.72	98.64		

Notes:

Table B. Comprehensive Major Element and Normative Mineralogy

Source Center	Potrillo Maar						(Williams, this study) West Potrillo Mtns				
Sample	BM1	13	SM.20	USF8/24	POST.16	8/23	NM 1103	NM1167	NM1168	NM1169	NM1171
SiO <sub>2</sub>	46.01	44.65	44.49	44.23	47.73	47.35	46.05	46.24	46.77	46.11	43.58
TiO <sub>2</sub>	2.27	2.17	2.17	2.19	2.08	2.08	2.44	2.37	2.24	2.33	2.54
Al <sub>2</sub> O <sub>3</sub>	16.52	13.82	13.76	13.79	16.52	16.24	13.78	14.61	14.90	14.69	13.76
Fe <sub>2</sub> O <sub>3</sub>	10.89	11.89	11.82	11.90	10.36	10.38	11.44	11.83	11.55	10.47	11.39
MnO	0.15	0.19	0.20	0.19	0.16	0.17	0.19	0.20	0.19	0.17	0.18
MgO	8.05	12.54	12.57	12.59	7.86	8.15	9.66	8.44	7.74	10.09	10.16
CaO	9.51	9.32	9.38	9.39	9.49	9.28	11.27	10.06	8.57	10.33	11.21
Na <sub>2</sub> O	3.92	3.38	3.35	3.48	4.01	4.07	3.23	4.03	3.69	3.01	2.31
K <sub>2</sub> O	1.98	1.61	1.55	1.59	1.67	1.67	0.84	0.96	1.77	1.70	0.77
P <sub>2</sub> O <sub>5</sub>	0.58	0.46	0.46	0.45	0.52	0.52	0.44	0.51	0.52	0.46	0.46
Mg#	63.27	71.09	71.26	71.16	63.89	64.68	66.74	62.46	61.25	68.97	67.58
Or	11.7	9.5	9.2	9.4	9.9	9.9	4.96	5.67	10.45	10.04	4.55
Ab	13.2	5.6	8.6	7.2	19.3	18.7	15.45	18.06	20.44	12.42	13.12
An	21.6	17.8	17.9	17.3	22.1	21.1	20.62	18.93	18.86	21.55	24.90
Ne	10.8	10.8	10.7	12.1	7.9	8.5	6.43	8.68	5.83	7.06	3.47
Cpx	17.6	20.5	20.6	21.2	17.5	17.4	26.27	22.53	16.54	21.54	22.41
Ol	15.9	24.1	2.6	23.9	15.4	18.0	17.38	17.06	17.76	18.89	19.49
Mt	2.4	2.6	4.1	2.6	2.2	2.3	2.76	2.87	2.79	2.53	2.76
Il	4.3	4.1	1.1	4.2	4.0	4.0	4.63	4.50	4.25	4.42	4.82
Ap	1.4	1.1		1.1	1.2	1.2	1.04	1.20	1.23	1.08	1.08
Total	98.94	96.10	74.70	98.76	99.51	101.10	99.54	99.50	98.15	99.53	96.60

Notes:

Table B. Comprehensive Major Element and Normative Mineralogy

Source Center	PVF1	PVF7	PVF8	PVF10	PVF11	PVF15A	NM877	NM878	NM879	NM880	NM1170	WPM6
SiO <sub>2</sub>	46.13	45.68	45.64	44.90	44.54	46.02	46.61	45.03	45.18	45.10	44.32	44.18
TiO <sub>2</sub>	2.68	2.66	2.48	2.61	2.45	2.59	2.52	2.66	2.33	2.08	2.54	2.37
Al <sub>2</sub> O <sub>3</sub>	15.63	14.99	14.98	15.18	14.00	14.33	15.79	15.34	15.47	14.96	14.94	15.56
Fe <sub>2</sub> O <sub>3</sub>	12.35	11.77	10.53	11.98	11.06	11.39	11.46	11.04	11.88	11.15	11.89	11.61
MnO	0.20	0.20	0.17	0.19	0.17	0.18	0.19	0.18	0.21	0.20	0.19	0.17
MgO	7.76	8.85	9.91	8.93	11.52	10.18	9.41	10.44	8.91	8.68	10.00	10.86
CaO	9.90	9.31	10.42	10.16	11.00	10.00	9.32	10.21	10.09	9.71	10.95	10.34
Na <sub>2</sub> O	3.82	3.81	3.27	3.49	2.48	3.38	3.82	3.63	3.61	3.20	3.76	2.97
K <sub>2</sub> O	1.76	1.96	1.58	1.65	1.45	1.00	2.09	1.90	1.55	0.88	0.78	1.80
P <sub>2</sub> O <sub>5</sub>	0.56	0.59	0.57	0.53	0.38	0.45	0.58	0.64	0.52	0.43	0.45	0.61
<b>Mg#</b>	<b>59.65</b>	<b>63.29</b>	<b>68.97</b>	<b>63.37</b>	<b>71.03</b>	<b>67.62</b>	<b>65.84</b>	<b>68.99</b>	<b>63.46</b>	<b>64.45</b>	<b>66.71</b>	<b>67.80</b>
Or	10.40	11.58	9.33	9.75	8.56	5.90	12.35	11.22	9.15	5.20	4.60	10.63
Ab	13.49	12.25	11.84	10.23	7.66	17.13	11.92	6.72	11.16	19.36	10.12	5.67
An	20.30	18.01	21.52	20.88	22.78	20.97	19.76	19.95	21.42	23.85	21.58	23.80
Ne	10.19	10.82	8.57	10.45	7.21	6.21	11.05	12.99	10.49	4.17	11.75	10.53
Cpx	20.57	19.77	21.35	21.20	23.60	20.78	18.38	21.40	20.53	17.48	24.16	18.99
Ol	16.70	18.35	18.56	18.28	21.21	20.03	19.59	19.73	18.65	18.84	19.04	22.27
Mt	3.00	2.87	2.56	2.91	2.68	2.76	2.76	2.66	2.87	2.69	2.87	2.81
Il	5.08	5.05	4.71	4.95	4.65	4.91	4.78	5.05	4.42	3.95	4.82	4.50
Ap	1.32	1.39	1.35	1.25	0.90	1.06	1.37	1.51	1.23	1.01	1.06	1.44
Total	101.05	100.09	99.79	99.90	99.25	99.75	101.96	101.23	99.92	96.55	100.00	100.64

Notes:

Table B. Comprehensive Major Element and Normative Mineralogy

Source Center	Malpais Maar											
	WPM7	WPM8	WPM10	M4	M2	MWC3	M1	M3	M5	MPRS6	MPRS7	MSYN8
SiO <sub>2</sub>	46.33	43.66	45.67	45.36	43.66	44.54	45.85	44.34	44.90	44.78	44.50	44.98
TiO <sub>2</sub>	2.01	2.27	2.48	2.52	2.33	2.48	2.47	2.52	2.50	2.45	2.53	2.61
Al <sub>2</sub> O <sub>3</sub>	16.12	15.69	15.64	15.16	14.44	15.70	16.20	15.31	15.41	14.37	15.27	15.51
Fe <sub>2</sub> O <sub>3</sub>	11.22	12.82	11.58	12.40	12.78	11.41	11.29	10.72	11.31	11.51	11.22	11.48
MnO	0.18	0.21	0.16	0.17	0.18	0.17	0.16	0.17	0.17	0.18	0.18	0.19
MgO	8.56	6.98	10.08	10.74	10.99	9.22	9.39	9.98	9.47	9.94	8.94	9.47
CaO	9.26	8.93	9.78	10.39	10.68	9.73	9.11	10.12	9.97	10.41	10.59	10.29
Na <sub>2</sub> O	3.73	4.30	3.30	3.44	2.36	3.86	3.63	3.75	4.29	2.97	3.47	3.72
K <sub>2</sub> O	1.30	2.19	1.75	1.68	1.63	1.96	2.06	1.84	1.21	1.38	1.81	1.80
F <sub>2</sub> O <sub>5</sub>	0.47	0.73	0.56	0.52	0.55	0.56	0.58	0.63	0.65	0.56	0.58	0.65
<b>Mg#</b>	<b>64.46</b>	<b>54.58</b>	<b>66.83</b>	<b>66.06</b>	<b>65.72</b>	<b>65.33</b>	<b>65.76</b>	<b>68.62</b>	<b>66.16</b>	<b>66.95</b>	<b>65.72</b>	<b>65.59</b>
Or	7.68	12.94	10.34	9.92	9.63	11.58	11.87	10.87	7.15	8.15	10.69	10.63
Ab	18.27	8.08	11.33	4.94	5.94	7.12	12.08	6.45	11.73	12.11	7.39	7.96
An	23.40	17.04	22.69	20.96	23.99	19.72	21.97	19.50	19.21	21.80	20.74	20.30
Ne	7.19	15.33	8.98	13.08	7.59	13.83	10.09	13.69	13.30	7.05	11.89	12.73
Cpx	15.84	18.51	17.94	24.50	20.60	20.19	15.75	21.46	21.06	21.21	22.72	21.47
Ol	19.34	16.97	21.07	20.78	23.24	18.59	20.33	18.71	18.58	19.67	16.95	18.52
Mt	2.71	3.10	2.79	3.00	3.08	2.75	2.72	2.59	2.74	2.78	2.71	2.76
Il	3.81	4.31	4.71	4.78	4.42	4.71	4.69	4.78	4.74	4.65	4.80	4.95
Ap	1.11	1.72	1.32	0.12	1.30	1.32	1.37	1.49	1.53	1.32	1.37	1.53
Total	99.35	98.00	101.17	102.08	99.79	99.81	100.87	99.54	100.04	98.74	99.26	100.85

Notes:

Table B. Comprehensive Major Element and Normative Mineralogy

Source Center	Kilbourne		Hunt's		Kilbourne (Bahar, 1991)					
	KHSYN1	KHSYN2	HHSYN1	HHSYN2	XPN-1	XPN-2	XPN-3	XP1-A	XP1-D	
SiO <sub>2</sub>	46.12	44.85	47.64	47.00	48.28	47.02	46.36	48.56	49.15	
TiO <sub>2</sub>	2.34	2.23	2.16	2.30	2.12	2.21	2.21	1.95	2.02	
Al <sub>2</sub> O <sub>3</sub>	14.51	14.56	14.68	15.03	14.36	14.51	14.80	14.51	13.85	
Fe <sub>2</sub> O <sub>3</sub>	12.21	11.89	10.86	11.25	11.01	11.49	11.55	10.44	10.78	
MnO	0.20	0.19	0.18	0.19	0.19	0.20	0.20	0.17	0.18	
MgO	11.10	10.45	9.49	10.16	9.46	10.02	10.00	9.56	9.31	
CaO	9.91	9.74	9.80	10.28	9.73	9.07	9.37	9.34	9.12	
Na <sub>2</sub> O	3.57	3.56	3.26	3.24	3.44	3.75	3.67	3.77	3.70	
K <sub>2</sub> O	1.75	1.70	1.80	1.68	1.81	1.73	1.83	1.71	1.89	
F <sub>2</sub> O <sub>5</sub>	0.62	0.57	0.50	0.42	-	-	-	-	-	
Mg#	67.99	67.55	67.28	67.43	64.00	66.00	66.00	65.00	67.00	
Or	10.34	10.04	10.63	9.92						
Ab	9.74	8.92	16.83	12.88						
An	18.39	18.72	20.10	21.50						
Ne	11.08	11.48	5.82	7.87						
Cpx	21.62	20.96	20.45	21.64						
OI	22.49	21.35	18.80	19.83						
Mt	2.95	2.87	2.62	2.72						
Il	4.44	4.23	4.10	4.36						
Ap	1.46	1.35	1.18	0.99						
Total	102.51	99.92	100.53	101.71						

Notes:



Table C. Major Element Analyses

Sample	NM 1103	NM 1103*	NM 1103**	NM1167	NM1167*	NM1168	NM1168*	NM1169	NM1169*	NM1171	NM1171*	PVF1
Experiment	WPVFA	WPVFA	WPVFB	WPVFA	WPVFA	WPVFA	WPVFA	WPVFA	WPVFA	WPVFA	WPVFA	WPVFA
SiO <sub>2</sub>	46.05		46.18	46.24		46.77		46.11		43.58		46.13
TiO <sub>2</sub>	2.44		2.45	2.37		2.24		2.33		2.54		2.68
Al <sub>2</sub> O <sub>3</sub>	13.78		13.58	14.61		14.90		14.69		13.76		15.63
Fe <sub>2</sub> O <sub>3</sub> (Total)	11.22	11.39	11.71	11.83	11.83	11.41	11.68	10.58	10.37	11.36	11.43	12.24
report avg	11.44			11.83		11.55		10.47		11.39		12.35
Fe <sub>T</sub>	7.85	7.97	8.19	8.27	8.27	7.98	8.17	7.40	7.25	7.94	7.99	8.56
Fe <sup>(2+)</sup>	0.12	0.12	0.12	0.13	0.13	0.12	0.12	0.11	0.11	0.12	0.12	0.13
MnO	0.19		0.18	0.20		0.19		0.17		0.18		0.20
MgO	9.66		10.00	8.44		7.74		10.09		10.16		7.76
Mg	0.24		0.25	0.21		0.19		0.25		0.25		0.19
CaO	11.11	11.74	10.97	9.63	10.49	9.17	7.96	10.10	10.56	11.46	10.96	9.36
report avg	11.27			10.06		8.57		10.33		11.21		9.90
Na <sub>2</sub> O	3.26	3.27	3.15	3.96	4.09	3.69	1.27	2.98	3.04	2.29	2.33	3.75
report avg	3.23			4.03		3.69		3.01		2.31		3.82
K <sub>2</sub> O	0.84		0.84	0.96		1.77		1.70		0.77		1.76
P <sub>2</sub> O <sub>5</sub>	0.44		0.42	0.51		0.52		0.46		0.46		0.56
LOI	1.37		1.29	1.78		0.93		0.75		3.69		0.74
Total <sub>(Fe Tot)</sub>	100.71			101.03		98.86		100.12		100.05		101.53
Mg# <sub>(0.85)</sub>	66.74		66.56	62.46		61.25		68.97		67.58		59.65

Note: All concentrations expressed in weight percent.  
 Major element analyses provided by Texas Tech.  
 \*Indicates NAA (24-Hour Count) done at UT-El Paso.  
 \*\*Run as a blind with experiment WPVFB.  
 \*\*\*Run as a blind with experiment WPVFA.  
 $Mg \# = [\text{molar } (Mg / (Mg + Fe^{2+})) \times 100]$   
 Iron distribution calculated from Fe<sub>2</sub>O<sub>3</sub> (Total) as follows:  
 (1)  $Fe_T = Fe_2O_3 \text{ (Total)} \times 0.699$   
 (2)  $Fe^{2+} = [(Fe_T * 0.85) / 55.847]$

Table C. Major Element Analyses

<b>Sample</b>	<b>PVF1*</b>	<b>PVF7</b>	<b>PVF7*</b>	<b>PVF8</b>	<b>PVF8*</b>	<b>PVF10</b>	<b>PVF10*</b>	<b>PVF11</b>	<b>PVF11*</b>	<b>PVF11**</b>	<b>PVF15A</b>	<b>PVF15A*</b>
<b>Experimen</b>	<b>WPVFA</b>	<b>WPVFA</b>	<b>WPVFA</b>	<b>WPVFA</b>	<b>WPVFA</b>	<b>WPVFA</b>	<b>WPVFA</b>	<b>WPVFA</b>	<b>WPVFA</b>	<b>WPVFB</b>	<b>WPVFA</b>	<b>WPVFA</b>
<b>SiO<sub>2</sub></b>		45.68		45.64		44.90		44.54		45.80	46.02	
<b>TiO<sub>2</sub></b>		2.66		2.48		2.61		2.45		2.51	2.59	
<b>Al<sub>2</sub>O<sub>3</sub></b>		14.99		14.98		15.18		14.00		14.18	14.33	
<b>Fe<sub>2</sub>O<sub>3</sub> (Total)</b>	12.46	11.96	11.57	10.39	10.68	12.03	11.93	10.95	10.92	11.31	11.36	11.43
<b>report avg</b>		11.77		10.53		11.98		11.06			11.39	
<b>Fe<sub>T</sub></b>	8.71	8.37	8.09	7.27	7.47	8.41	8.34	7.66	7.64	7.91	7.94	7.99
<b>Fe<sup>(2+)</sup></b>	0.13	0.13	0.12	0.11	0.11	0.13	0.13	0.12	0.12	0.12	0.12	0.12
<b>MnO</b>		0.20		0.17		0.19		0.17		0.18	0.18	
<b>MgO</b>		8.85		9.91		8.93		11.52		11.30	10.18	
<b>Mg</b>		0.22		0.25		0.22		0.29		0.28	0.25	
<b>CaO</b>	10.43	9.08	9.54	10.32	10.51	10.16	10.16	11.02	10.74	11.25	9.77	10.23
<b>report avg</b>		9.31		10.42		10.16		11.00			10.00	
<b>Na<sub>2</sub>O</b>	3.88	3.82	3.80	3.21	3.34	3.47	3.51	2.46	2.48	2.50	3.27	3.49
<b>report avg</b>		3.81		3.27		3.49		2.48			3.38	
<b>K<sub>2</sub>O</b>		1.96		1.58		1.65		1.45		1.57	1.00	
<b>P<sub>2</sub>O<sub>5</sub></b>		0.59		0.57		0.53		0.38		0.43	0.45	
<b>LOI</b>		0.87		0.95		0.47		0.88		0.79	1.77	
<b>Total<sub>(Fe Tot)</sub></b>		100.68		100.49		100.09		99.93			101.28	
<b>Mg#<sub>(0.85)</sub></b>		63.29		68.97		63.37		71.03		69.96	67.62	

Table C. Major Element Analyses

Sample	PVF15B	PVF15B*	NM877	NM877*	NM878	NM878*	NM879	NM879*	NM880	NM880Duf	NM880*	NM1170
Experimen	WPVFA	WPVFA	WPVFB	WPVFB	WPVFB	WPVFB	WPVFB	WPVFB	WPVFB	WPVFB	WPVFB	WPVFB
SiO <sub>2</sub>	44.51		46.61		45.03		45.18		45.10	45.05		44.32
TiO <sub>2</sub>	2.56		2.52		2.66		2.33		2.08	2.07		2.54
Al <sub>2</sub> O <sub>3</sub>	15.44		15.79		15.34		15.47		14.96	14.78		14.94
Fe <sub>2</sub> O <sub>3</sub> (Total)	11.20	11.30	11.38	11.54	10.94	11.13	11.96	11.79	11.16	11.32	10.97	11.63
report avg	11.25		11.46		11.04		11.88		11.15			11.89
Fe <sub>T</sub>	7.83	7.90	7.96	8.07	7.65	7.78	8.37	8.25	7.81	7.92	7.67	8.13
Fe <sup>(2+)</sup>	0.12	0.12	0.12	0.12	0.12	0.12	0.13	0.13	0.12	0.12	0.12	0.12
MnO	0.18		0.19		0.18		0.21		0.20	0.20		0.19
MgO	10.48		9.41		10.44		8.91		8.68	8.79		10.00
Mg	0.26		0.23		0.26		0.22		0.22	0.22		0.25
CaO	10.20	10.22	9.33	9.30	10.36	10.06	10.27	9.91	9.64	9.77		11.13
report avg	10.21		9.32		10.21		10.09		9.71			10.95
Na <sub>2</sub> O	3.94	3.91	3.78	3.85	3.64	3.61	3.60	3.62	3.20	3.27	3.13	3.80
report avg	3.93		3.82		3.63		3.61		3.20			3.76
K <sub>2</sub> O	1.09		2.09		1.90		1.55		0.88	0.87		0.78
P <sub>2</sub> O <sub>5</sub>	0.66		0.58		0.64		0.52		0.43	0.43		0.45
LOI	0.98		-0.02		0.20		1.05		2.81	2.81		1.39
Total(Fe Tot)	101.29		101.76		101.26		100.80		99.20			101.20
Mg# (0.85)	68.57		65.84		68.99		63.46		64.45	64.41		66.71

Table C. Major Element Analyses

<b>Sample</b>	<b>NM1170*</b>	<b>MPRS6</b>	<b>MPRS6*</b>	<b>MPRS7</b>	<b>MPRS7*</b>	<b>MSYN8</b>	<b>MSYN8D<sub>u</sub></b>	<b>KHSYN1</b>	<b>KHSYN1*</b>	<b>KHSYN2</b>	<b>KHSYN2*</b>	<b>HHSYN1</b>
<b>Experimen</b>	<b>WPVFB</b>	<b>WPVFB</b>	<b>WPVFB</b>	<b>WPVFB</b>	<b>WPVFB</b>	<b>WPVFB</b>	<b>WPVFB</b>	<b>WPVFB</b>	<b>WPVFB</b>	<b>WPVFB</b>	<b>WPVFB</b>	<b>WPVFB</b>
<b>SiO<sub>2</sub></b>		44.78		44.50		44.98	44.72	46.12		44.85		47.64
<b>TiO<sub>2</sub></b>		2.45		2.53		2.61	2.59	2.34		2.23		2.16
<b>Al<sub>2</sub>O<sub>3</sub></b>		14.37		15.27		15.51	15.38	14.51		14.56		14.68
<b>Fe<sub>2</sub>O<sub>3</sub> (Total)</b>	12.14	11.44	11.57	10.87	11.57	11.58	11.38	12.18	12.24	11.70	12.08	10.76
<b>report avg</b>		11.51		11.22		11.48		12.21		11.89		10.86
<b>Fe<sub>T</sub></b>	8.49	8.00	8.09	7.60	8.09	8.10	7.96	8.52	8.56	8.18	8.45	7.53
<b>Fe<sup>(2+)</sup></b>	0.13	0.12	0.12	0.12	0.12	0.12	0.12	0.13	0.13	0.12	0.13	0.11
<b>MnO</b>		0.18		0.18		0.19	0.19	0.20		0.19		0.18
<b>MgO</b>		9.94		8.94		9.47	9.30	11.10		10.45		9.49
<b>Mg</b>		0.25		0.22		0.23	0.23	0.28		0.26		0.24
<b>CaO</b>	10.76	10.41	10.40	10.38	10.79	10.26	10.32	9.95	9.86	9.81	9.67	9.68
<b>report avg</b>		10.41		10.59		10.29		9.91		9.74		9.80
<b>Na<sub>2</sub>O</b>	3.71	2.89	3.05	3.39	3.56	3.75	3.69	3.54	3.59	3.46	3.66	3.21
<b>report avg</b>		2.97		3.47		3.72		3.57		3.56		3.26
<b>K<sub>2</sub>O</b>		1.38		1.81		1.80	1.78	1.75		1.70		1.80
<b>P<sub>2</sub>O<sub>5</sub></b>		0.56		0.58		0.65	0.60	0.62		0.57		0.50
<b>LOI</b>		1.19		1.48		0.31	0.31	-0.10		0.02		0.31
<b>Total<sub>(Fe Tot)</sub></b>		99.73		100.57		101.01		102.22		99.76		100.68
<b>Mg#<sub>(0.85)</sub></b>		66.95		65.72		65.59	65.58	67.99		67.55		67.28

Table C. Major Element Analyses

<b>Sample</b>	<b>HHSYN1*</b>	<b>HHSYN2</b>	<b>HHSYN2*</b>	<b>WPM6</b>	<b>WPM6*</b>	<b>WPM7</b>	<b>WPM7*</b>	<b>WPM7**</b>	<b>WPM8</b>	<b>WPM8*</b>	<b>WPM10</b>	<b>WPM10*</b>
<b>Experimen</b>	<b>WPVFB</b>	<b>WPVFB</b>	<b>WPVFB</b>	<b>MAOVL</b>	<b>MAOVL</b>	<b>MAOVL</b>	<b>MAOVL</b>	<b>WPVFB</b>	<b>MAOVL</b>	<b>MAOVL</b>	<b>MAOVL</b>	<b>MAOVL</b>
<b>SiO<sub>2</sub></b>		47.00		44.18		46.33		46.07	43.66		45.67	
<b>TiO<sub>2</sub></b>		2.30		2.37		2.01		2.06	2.27		2.48	
<b>Al<sub>2</sub>O<sub>3</sub></b>		15.03		15.56		16.12		15.48	15.69		15.64	
<b>Fe<sub>2</sub>O<sub>3</sub> (Total)</b>	10.96	11.44	11.06	12.02	11.20	11.00	11.30	11.37	13.54	12.10	11.66	11.50
<b>report avg</b>		11.25		11.61		11.22			12.82		11.58	
<b>Fe<sub>T</sub></b>	7.67	8.00	7.74	8.41	7.83	7.69	7.90	7.95	9.47	8.46	8.16	8.04
<b>Fe<sup>(2+)</sup></b>	0.12	0.12	0.12	0.13	0.12	0.12	0.12	0.12	0.14	0.13	0.12	0.12
<b>MnO</b>		0.19		0.17		0.18		0.20	0.21		0.16	
<b>MgO</b>		10.16		10.86		8.56		8.31	6.98		10.08	
<b>Mg</b>		0.25		0.27		0.21		0.21	0.17		0.25	
<b>CaO</b>	9.92	10.49	10.06	10.07	10.60	9.17	9.13	9.48	9.01	8.85	9.68	9.88
<b>report avg</b>		10.28		10.34		9.26			8.93		9.78	
<b>Na<sub>2</sub>O</b>	3.31	3.25	3.22	3.00	2.94	3.80	3.66	3.73	4.49	4.10	3.36	3.23
<b>report avg</b>		3.24		2.97		3.73			4.30		3.30	
<b>K<sub>2</sub>O</b>		1.68		1.80		1.30		1.28	2.19		1.75	
<b>P<sub>2</sub>O<sub>5</sub></b>		0.42		0.61		0.47		0.46	0.73		0.56	
<b>LOI</b>		0.33		0.86		1.80		1.96	1.69		0.13	
<b>Total<sub>(Fe Tot)</sub></b>		101.87		101.33		100.98			99.47		101.13	
<b>Mg#<sub>(0.85)</sub></b>		67.43		67.80		64.46		63.01	54.58		66.83	

Table C. Major Element Analyses

<b>Sample</b>	<b>M4</b>	<b>M4*</b>	<b>M2</b>	<b>M2*</b>	<b>MWC3</b>	<b>M1</b>	<b>M1*</b>	<b>M3</b>	<b>PVFM3***</b>	<b>M3*</b>	<b>M5</b>	<b>M5*</b>
<b>Experiment</b>	<b>CHEN</b>	<b>CHEN</b>	<b>MAOVL</b>	<b>MAOVL</b>	<b>CHEN</b>	<b>MAOVL</b>	<b>MAOVL</b>	<b>CLKHA</b>	<b>WPVFA</b>	<b>CLKHA</b>	<b>CLKHA</b>	<b>CLKHA</b>
<b>SiO<sub>2</sub></b>	45.36		43.66		44.54	45.85		44.34	43.93		44.90	
<b>TiO<sub>2</sub></b>	2.52		2.33		2.48	2.47		2.52	2.68		2.50	
<b>Al<sub>2</sub>O<sub>3</sub></b>	15.16		14.44		15.70	16.20		15.31	15.20		15.41	
<b>Fe<sub>2</sub>O<sub>3</sub> (Total)</b>	12.86	11.93	13.36	12.20	11.41	11.40	11.19	10.64	10.83	10.70	11.29	11.33
<b>report avg</b>	12.40		12.78		11.41	11.29		10.72			11.31	
<b>Fe<sub>T</sub></b>	9.00	8.34	9.34	8.53	7.98	7.97	7.83	7.44	7.57	7.48	7.90	7.92
<b>Fe<sup>(2+)</sup></b>	0.14	0.13	0.14	0.13	0.12	0.12	0.12	0.11	0.12	0.11	0.12	0.12
<b>MnO</b>	0.17		0.18		0.17	0.16		0.17	0.18		0.17	
<b>MgO</b>	10.74		10.99		9.22	9.39		9.98	10.56		9.47	
<b>Mg</b>	0.27		0.27		0.23	0.23		0.25	0.26		0.23	
<b>CaO</b>	10.09	10.69	10.65	10.70	9.73	9.37	8.85	10.02	10.19	10.16	9.79	10.14
<b>report avg</b>	10.39		10.68		9.73	9.11		10.12			9.97	
<b>Na<sub>2</sub>O</b>	3.42	3.45	2.33	2.38	3.86	3.77	3.50	3.73	3.82	3.69	4.33	4.25
<b>report avg</b>	3.44		2.36		3.86	3.63		3.75			4.29	
<b>K<sub>2</sub>O</b>	1.68		1.63		1.96	2.06		1.84	1.74		1.21	
<b>P<sub>2</sub>O<sub>5</sub></b>	0.52		0.55		0.56	0.58		0.63	0.65		0.65	
<b>LOI</b>	-0.49		0.53		-0.32	0.07		0.47	0.48		0.18	
<b>Total<sub>(Fe Tot)</sub></b>	101.88		100.12		99.31	100.80		99.85			100.06	
<b>Mg#<sub>(0.85)</sub></b>	66.06		65.72		65.33	65.76		68.62	69.45		66.16	

Table D. Comprehensive Trace Element Analyses

Sample	NM 1103	NM 1103*	NM 1103**	NM1167	NM1167*	NM1168	NM1168*
Experiment	WPVFA	WPVFA	WPVFB	WPVFA	WPVFA	WPVFA	WPVFA
Na <sub>2</sub> O	3.27		3.26	4.09	3.96	1.27	3.69
CaO	11.74		11.11	10.49	9.63	7.96	9.17
Sc	30.4		29.8	26.3	26.1	25.4	25.0
Average	30.1			26.2		25.2	
Ti			2.5				
V			244		233		205
Cr	357		247	292	308	259	257
Average	302			300		258	
Fe <sub>2</sub> O <sub>3</sub>	11.39		11.22	11.83	11.83	11.68	11.41
Co	49.4			44.2		43.9	
Ni			191	130	126	118	102
Average	191			128		110	
Cu			38.00		33.60		29.50
Zn			75.0	84.7	73.6	89.3	79.1
Average	75.0			79.2		84.2	
Rb			14	21		38	
Average	14			21		38	
Sr	665	667	657	691	709	695	707
Report		667			709		707
Zr	212	186	190	272	229	282	242
Report		186			229		242
Nb		26	67		82		82
Ba	564	496	466	635	521	668	538
Report		496			521		538
La	26.1			37.4		25.1	
Ce	49.3			62.2		63.4	
Nd	24.9			27.7		29.5	
Sm	5.23			6.48		4.54	
Eu	1.95			2.05		2.11	
Y			26		27		26
Tb	0.75			0.78		0.78	
Yb	1.946			2.146		1.890	
Lu	0.30			0.35		0.31	
Hf	4.44			5.73		6.09	
Ta	3.48			4.34		4.45	
Th	3.15			4.86		4.90	
U						0.89	

Note: All concentrations in ppm.

NAA analyses (WPVFA 24-hour and WPVFB 8-hour counts) determined at UT-EI Paso.

\* Indicates ICP (AAS for Rb) determinations provided by Texas Tech.

\*\*Run as a blind with experiment WPVFB.

\*\*\*Indicates XRF analyses by W. Chen through the NM Bureau of Mines and Geology.

<sup>1</sup> NAA run as experiment CKLHA (24-hr counts). Peaks originally picked by C. Long. Peaks re-picked by W. Williams under experiment label "WJWMM" for comparison.

<sup>2</sup> NAA run as CKLHA (24-hr counts). Split run as blind with WPVFA ICP analyses.

Table D. Comprehensive Trace Element Analyses

NM1169 WPVFA	NM1169* WPVFA	NM1171 WPVFA	NM1171* WPVFA	PVF1 WPVFA	PVF1* WPVFA	PVF7 WPVFA	PVF7* WPVFA
3.04	2.98	2.33	2.29	3.88	3.75	3.80	3.82
10.56	10.10	10.96	11.46	10.43	9.36	9.54	9.08
29.9	28.9	32.4	30.0	25.3	23.5	24.4	23.9
29.4		31.2		24.4		24.1	
	230		263		208		212
331	365	315	340	156	148	262	255
348		328		152		258	
10.37	10.58	11.43	11.36	12.46	12.24	11.57	11.96
46.8		48.1		45.5		43.6	
190	241	168	175		99	153	153
216		172		99		153	
	33.70		38.00		31.70		30.70
69.8	76.2	69.5	71.8	95.0	87.3	84.2	84.6
73.0		70.7		91.1		84.4	
39		20		42		45	
39		20		42		45	
618	587	623	623	792	839	786	837
	587		623		839		837
241	192	230	183	275	226	290	231
	192		183		226		231
	76		66		90		93
605	471	529	419	764	596	716	592
	471		419		596		592
33.7		29.6		42.7		39.6	
57.7		52.1		72.5		67.1	
25.0		25.3		34.2		30.8	
6.53		6.10		7.56		7.01	
1.96		1.98		2.41		2.20	
	29		26		29		28
0.82		0.78		0.92		0.83	
2.257		2.017		2.419		2.261	
0.36		0.33		0.37		0.37	
4.85		4.59		6.03		5.94	
3.69		3.41		4.72		4.70	
4.13		3.26		5.16		4.92	
						1.35	



Table D. Comprehensive Trace Element Analyses

PVF8 WPVFA	PVF8* WPVFA	PVF10 WPVFA	PVF10* WPVFA	PVF11 WPVFA	PVF11* WPVFA	PVF15A WPVFA	PVF15A* WPVFA
3.34	3.21	3.51	3.47	2.48	2.46	3.49	3.27
10.51	10.32	10.47	10.16	10.74	11.02	10.23	9.77
29.2	29.6	27.7	31.4	32.0	35.1	28.5	28.8
29.4		29.6		33.5		28.6	
	213		225		242		225
267	281	162	170	366	390	294	321
274		166		378		307	
10.68	10.39	11.93	12.03	10.92	10.95	11.43	11.36
48.1		47.0		52.2		50.6	
182	208	131	126	227	242	183	235
195		128		235		209	
	36.50		37.00		39.60		30.40
71.8	63.6	78.8	86.8	70.3	65.6	80.3	66.4
67.7		82.8		68.0		73.3	
38		37		31		28	
38		37		31		28	
678	682	758	771	575	593	707	708
	682		771		593		708
250	201	259	209	204	172	240	204
	201		209		172		204
	83		79		63		77
665	526	751	607	672	531	657	526
	526		607		531		526
41.0		39.3		27.0		34.2	
68.1		67.0		48.3		58.9	
31.1		33.3		25.6		27.3	
7.19		7.28		5.95		6.41	
2.22		2.25		1.86		2.05	
	29		30		26		26
0.85		0.86		0.76		0.81	
2.289		2.276		1.948		2.039	
0.36		0.37		0.31		0.32	
5.12		5.22		4.36		5.15	
4.14		4.12		3.23		3.98	
4.94		4.45		3.15		4.19	
				0.85			

Table D. Comprehensive Trace Element Analyses

PVF15B WPVFA	PVF15B* WPVFA	NM877 WPVFB	NM877* WPVFB	NM878 WPVFB	NM878* WPVFB	NM879 WPVFB	NM879* WPVFB
3.91	3.94	3.85	3.78	3.61	3.64	3.62	3.60
10.22	10.20	9.30	9.33	10.06	10.36	9.91	10.27
27.8	28.5	27.3	25.1	29.6	28.1	28.0	27.0
28.1		26.2		28.9		27.5	
			2.5		2.7		2.3
	223		204		225		203
283	291	256	277	264	280	226	238
287		267		272		232	
11.30	11.20	11.54	11.38	11.13	10.94	11.79	11.96
49.8		49.2		50.6		47.8	
180	194	169	228	199	254	155	148
187		199		227		151	
	34.70		34.00		43.00		46.00
74.4	73.5	85.2	78.0	70.8	72.0	83.6	78.0
74.0		81.6		71.4		80.8	
31		44	44	41	40	39	36
31		44		41		38	
724	730		733		718		696
	730		733		718		696
247	203	205	238	230	224	215	235
	203	avg 221		avg 227		avg 225	
	74		77		79		76
639	516	589	530	577	492	558	499
	516		530		492		499
41.6		39.3		38.7		39.6	
67.7		66.6		67.7		68.1	
31.3		31.8		34.2		32.7	
7.04		6.62		7.00		6.89	
2.15		2.14		2.22		2.19	
	29		27		30		30
0.85		0.85		0.89		0.91	
2.192		2.175		2.215		2.307	
0.34		0.34		0.34		0.36	
4.95		5.34		5.09		5.25	
3.89		4.15		4.19		3.97	
4.76		5.16		4.76		4.87	
		1.27		1.02		1.31	

Table D. Comprehensive Trace Element Analyses

NM880 WPVFB	NM880* WPVFB	NM1170 WPVFB	NM1170* WPVFB	MPRS6 WPVFB	MPRS6* WPVFB	MPRS7 WPVFB	MPRS7* WPVFB
3.13	3.20	3.71	3.80	3.05	2.89	3.56	3.39
	9.64	10.76	11.13	10.40	10.41	10.79	10.38
25.7	25.3	32.5	30.2	30.8	28.8	29.3	26.6
25.5		31.3		29.8		27.9	
	2.1		2.5		2.4		2.4
	163		197		223		208
246	268	316	324	310	311	235	225
257		320		310		230	
10.97	11.24	12.14	11.63	11.57	11.44	11.57	10.87
45.2		53.4		52.2		48.8	
133	135	174	195	199	222	168	159
134		184		210		164	
	60.00		43.00		41.00		35.00
78.7	81.0	81.3	81.0	78.5	74.0	82.5	72.0
79.9		81.2		76.2		77.3	
29	26		7	31	33	41	36
27		7		32		39	
	622		668		682		969
	622		668		682		969
232	248	221	210	214	190	234	217
avg 240		avg 215		avg 202		avg 226	
	71		64		68		73
521	459	529	452	546	473	571	482
	459		452		473		482
33.0		33.2		32.5		41.2	
59.3		59.3		58.0		72.3	
29.3		30.1		30.8		35.2	
5.84		6.48		6.37		7.27	
1.90		2.12		2.09		2.32	
	29		29		29		30
0.78		0.86		0.83		0.97	
2.190		2.158		2.106		2.319	
0.35		0.34		0.32		0.37	
5.19		4.87		4.54		5.27	
3.76		3.52		3.39		3.93	
4.53		3.92		3.94		5.10	
1.33				1.14		1.22	

Table D. Comprehensive Trace Element Analyses

KHSYN1 WPVFB	KHSYN1* WPVFB	KHSYN2 WPVFB	KHSYN2* WPVFB	HHSYN1 WPVFB	HHSYN1* WPVFB	HHSYN2 WPVFB	HHSYN2* WPVFB
3.59	3.54	3.66	3.46	3.31	3.21	3.22	3.25
9.86	9.95	9.67	9.81	9.92	9.68	10.06	10.49
27.2	25.5	27.3	24.9	28.6	26.5	29.7	28.9
26.4		26.1		27.5		29.3	
	2.3		2.2		2.1		2.2
	207		198		202		216
395	381	405	422	248	239	247	259
388		414		244		253	
12.24	12.18	12.08	11.70	10.96	10.76	11.06	11.44
53.3		53.4		49.5		50.7	
277	298	260	404	182	158	185	168
287		332		170		176	
	39.00		42.00		38.00		38.00
89.0	83.0	87.5	81.0	78.1	69.0	71.6	74.0
86.0		84.3		73.6		72.8	
43	40	40	38	42	40	37	36
41		39		41		37	
	677		646		602		626
	677		646		602		626
250	224	237	211	196	197		196
avg 237		avg 224		avg 197		196	
	67		66		55		57
568	499	541	460	583	529	574	505
	499		460		529		505
36.8		36.5		34.5		30.8	
64.7		64.6		61.4		55.4	
32.5		32.9		31.7		31.0	
6.86		6.87		6.50		6.08	
2.14		2.17		2.04		1.92	
	31		31		29		30
0.92		0.89		0.87		0.80	
2.476		2.373		2.333		2.209	
0.39		0.37		0.36			
5.37		5.07		4.73		4.40	
3.74		3.63		3.11		3.09	
4.53		4.42		4.32		3.99	
1.29		1.35		1.00		1.14	

Table D. Comprehensive Trace Element Analyses

WPM6 MAOVL	WPM7 MAOVL	WPM8 MAOVL	WPM10 MAOVL	M4 CHEN	M2 MAOVL	MWC3 CHEN	M1 MAOVL
2.94	3.66	4.10	3.23	3.45	2.38	3.86	3.50
10.60	9.13	8.85	9.88	10.69	10.70	9.73	8.86
29.6	26.7	21.0	28.0	30.1	31.0	28.5	27.5
29.6	26.7	21.0	28.0	30.1	31.0	28.5	27.5
278	231	91	255	282	346	229	241
278	231	91	255	282	346	229	241
11.20	11.30	12.10	11.50				
52.1	44.1	38.9	50.1	56.8	58.6	48.3	50.1
202	140	75	168	172	220	177	160
202	140	75	168	172	220	177	160
46	46	72	43	38	38	50	45
46	46	72	43	38	38	50	45
685	643	959	679	631	696	708	745
685	643	959	679	631	696	708	745
213	252	301	204	177	167	218	217
213	252	301	204	177	167	218	217
65	63	89	59	57	52	67	65
605	470	638	506	474	473	540	569
605	470	638	506	474	473	540	569
40.0	39.3	55.7	36.5	33.2	33.0	42.2	42.4
68.9	68.4	93.4	63.6	62.4	60.4	75.4	74.0
31.3	30.9	40.9	30.6	26.3	26.6	30.2	30.4
5.83	5.91	7.44	6.09	5.59	5.55	6.40	6.17
2.18	1.74	2.51	1.81	2.12	2.10	2.24	2.19
26	27	31	28	25	25	28	26
0.89	0.86	0.98	0.92	0.90	0.81	1.01	0.90
2.470	2.440	2.630	2.330	2.280	2.090	2.360	2.230
0.34	0.37	0.40	0.35	0.35	0.35	0.37	0.35
5.16	5.76	6.61	4.88	4.31	4.19	4.86	5.10
	3.77	2.17	3.29	3.13	2.93	3.91	3.88
4.78	5.01	6.27	3.96	3.41	3.40	4.97	5.04
1.59	1.81	1.93	1.14	0.69	0.74	1.28	1.19

Table D. Comprehensive Trace Element Analyses

M3 CLKHA	M3* CLKHA	M3 WJWMM <sup>1</sup>	M3* WJWMM <sup>2</sup> (Averaged)	M3 NAA	M5 CLKHA	M5* CLKHA	M5 WJWMM <sup>1</sup>
3.73	3.73	3.60	3.82	3.67	4.22	4.33	4.21
11.2	10.02	9.25	10.19	10.23	10.37	9.79	10.26
29	28.5	29.3	26.8	29.2	27.7	26.8	27.9
28.4					27.5		
			228				
242	268	241	259	242	246	268	245
253					253		
10.79	10.64	10.73		10.76	11.32	11.29	11.33
49.1		49.0		49.1	49.4		50.3
188	223	186	190	187	162	181	160
197					168		
			40				
			68				
38	43			38	22	24	
41					23		
640	748		693	640	632	740	
avg 721						740	
227	207	220	200	224	211	209	211
avg 214					avg 210		
	62		83			61	
508	540	534	492	521	520	492	516
avg 516						492	
39.8		40.2		40.0	39.0		39.5
72.6		74.7		73.7	69.9		72.1
34.4		32.8		33.6	31.0		31.5
6.6		6.54		6.57	6.38		6.33
2.11		2.10		2.11	2.06		2.05
	29.7		30.4			29	
0.908		0.900		0.904	0.875		0.860
2.25		2.25		2.25	2.23		2.24
0.34		0.34		0.34	0.34		0.33
4.71		4.69		4.70	4.73		4.72
4.22		4.20		4.21	4.00		4.03
4.11		4.08		4.10	4.13		4.10

Table D. Comprehensive Trace Element Analyses

M5 NAA (Averaged)	AF4 CHEN	PM824 CHEN	PM20 CHEN	PM16 CHEN
4.22	3.24	3.53	3.49	3.92
10.32	10.64	11.85	9.83	9.86
27.8	29.5	31.5	30.0	24.9
	29.5	31.5	30.0	24.9
246	358	438	528	229
	358	438	528	229
11.33	11.10	12.23	12.46	10.30
49.9	54.8	61.9	63.2	44.7
161	203	306	340	106
	203	306	340	106
22	35***	34***	34***	36***
	35	34	34	36
632	558***	582***	574***	640***
	558	582	574	640
211	172***	194***	198***	214***
	172	194	198	214
	46***	49***	49***	50***
518	484	437	500	490
	484	437	500	490
39.3	30.1	35.8	35.2	37.4
71.0	54.9	65.4	65.1	68.7
31.3	25.6	27.3	27.9	27.3
6.36	5.55	5.89	5.97	5.68
2.06	2.01	2.21	2.23	2.09
	26	27	28	27
0.868	0.95	0.90	0.93	0.82
2.24	2.14	2.45	2.57	2.38
0.34	0.36	0.39	0.40	0.40
4.73	4.08	4.58	4.80	4.86
4.02	2.66	3.05	2.98	3.01
4.12	3.36	3.73	3.52	4.05
	0.92	0.84	0.80	0.99

Table E. Sr, Nd and Pb Isotopic Data

Sample	$^{87}\text{Sr}/^{86}\text{Sr}$	$^{143}\text{Nd}/^{144}\text{Nd}$	$\epsilon_{\text{Nd}}$	$^{206}\text{Pb}/^{204}\text{Pb}$ (uncorrected for fractionation)	$^{207}\text{Pb}/^{204}\text{Pb}$ (uncorrected for fractionation)	$^{208}\text{Pb}/^{204}\text{Pb}$ (corrected for 0.11%amu mass fractionation)	$^{206}\text{Pb}/^{204}\text{Pb}$ (corrected for 0.11%amu mass fractionation)	$^{207}\text{Pb}/^{204}\text{Pb}$	$^{208}\text{Pb}/^{204}\text{Pb}$
NM1167	0.703158	0.512979	6.7	19.0127	15.5207	38.4026	19.055	15.572	38.572
NM1169	0.703419	0.512919	5.5	18.8165	15.5095	38.5299	18.858	15.561	38.699
M2	0.703231	0.512976	6.6	18.8899	15.5196	38.2709	18.931	15.571	38.439
NM879	0.703105	0.512976	6.6	19.0396	15.5331	38.4462	19.081	15.584	38.615
M5	0.703087	0.512971	6.5	18.9074	15.5163	38.3099	18.949	15.568	38.478
AF4	0.703574	0.51287	4.5	18.3224	15.469	38.0992	18.363	15.520	38.267
PM-20	0.703201	0.51291	5.3	18.6344	15.5127	38.1581	18.675	15.564	38.326
KHSYN-1	0.703343	0.512958	6.2	18.8945	15.532	38.3774	18.936	15.583	38.546
AD3	0.703568	0.51291	5.3	18.5968	15.49	38.2699	18.638	15.541	38.438
HHSYN-1	0.703917	0.512864	4.4	18.5175	15.503	38.0243	18.558	15.554	38.192
	+/- .000024		+/- 0.5				+/- 0.1%	+/- 0.1%	+/- 0.1%

Note: Analyses run at UT-Austin.



## Part II

# COSMOGENIC HELIUM SURFACE EXPOSURE DATING OF THE QUATERNARY MAFIC SAN QUINTÍN VOLCANIC FIELD, BAJA CALIFORNIA NORTE, MÉXICO

Wendi J. W. Williams<sup>1</sup>

<sup>1</sup>Department of Geological Sciences, University of Texas, El Paso, TX  
79968-0555 [wjwwilliams@hotmail.com](mailto:wjwwilliams@hotmail.com)

Jane Poths<sup>2</sup>

<sup>2</sup>CST-7, Los Alamos National Laboratory, Los Alamos, NM 87545

### ABSTRACT

A better understanding of eruption ages, episodicity, and spatial distribution of Quaternary volcanism can allow detailed petrogenetic modeling and assessment of neotectonic events. Previous <sup>3</sup>He surface exposure dating of young, mafic volcanism within the southwestern United States has demonstrated the promising application of this method to pahoehoe surfaces located above 1000 meters elevation. We have now gathered helium data for the San Quintín field in México to determine not only the timing of eruption events, but also to evaluate this dating method for samples collected from both aa and pahoehoe surfaces located near sea level. Multiple lava flows from 9 of the 10 exposed complexes were sampled for cosmogenic helium dating, yielding eruption dates from 165 ±

were sampled for cosmogenic helium dating, yielding eruption dates from  $165 \pm 13$  ka to  $22 \pm 5$  ka ( $1 \sigma$ ). Two major episodes of volcanic activity occurred along parallel lineations trending roughly N40°W. The younger trend of three centers ( $31 \pm 4$  ka,  $27 \pm 5$  ka and  $22 \pm 5$  ka) steps outboard to the southwest from the older alignment. The older dated surfaces range from  $165 \pm 13$  ka to  $84 \pm 10$  ka, where these bracketing dates happen to be for two distinct lavas associated with nested cinder cones comprising the Woodford complex. The data provide quantitative geochronologic evidence for multiple eruptions (*i.e.* polycyclicality) from a single mafic volcanic center which are separated by a time gap discernible within the resolution of the helium technique. Comparison of  $^3\text{He}$  to  $^{40}\text{Ar}/^{39}\text{Ar}$  dating for the field yields agreement within the uncertainties of the these dating methods: 1) a flow from the Kenton complex yields a helium date of  $145 \pm 14$  ka and argon date of  $126 \pm 8$  ka and 2) for a Media Luna flow,  $^3\text{He}$  yields  $106 \pm 9$  ka (weighted average of two surfaces from the same flow) whereas the step-heated argon analysis of groundmass results in  $90 \pm 10$  ka. An interesting petrologic insight is provided by the helium trapped in the olivine and clinopyroxene mineral separates. Geochemical and isotopic signatures documented by Luhr and others (1995) support incorporation of crustal components by ascending magmas forming Ceniza and Monte Mazo centers. Lavas from those two centers and the other 7 centers we analyzed yield  $^3\text{He}/^4\text{He}$

values ranging from  $4.9 \pm 0.9 R/R_a$  to  $7.4 \pm 1.1 R/R_a$ , which may reflect addition of crustal helium ( $<0.1 R/R_a$ ) to melts derived from a MORB ( $8 \pm 1 R/R_a$ ) source. However, the San Quintín trapped component determinations do overlap within analytical error. If the  $5.52 \pm 2.42$  weighted average is considered instead of individual  $R/R_a$  values for this field, the trapped component composition may represent the low end of the range reported by Graham and others (1992) for MORB rather than a crustal signature.

## INTRODUCTION

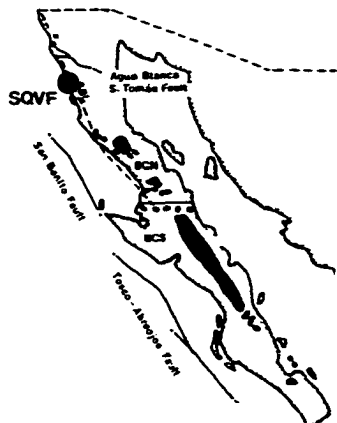
Previous  $^3\text{He}$  surface exposure dating of young, mafic volcanism within Hawaii and the southwestern United States has demonstrated the promising application of this method to pahoehoe lava flow surfaces (for instance: Kurz (1986a,b), Kurz and others (1990), Craig and Poreda (1986), Marti and Craig (1987), Cerling (1990), Anthony and Poths (1992), Poreda and Cerling (1992), Cerling and Craig (1994), and Laughlin *et al.* (1994)). We have now gathered helium data for the San Quintín field to determine not only the timing of eruption events, but also to evaluate this dating method for samples collected from both rough aa and pahoehoe lava flow surfaces located near sea level.

Numerous studies have been done concerning the San Quintín volcanic field, beginning with Woodford's geologic study published in 1928. A comprehensive review of the literature, as well as detailed investigation of geology, petrology and geochemistry for this volcanism, has recently been completed by Luhr *et al.* (1995). They consider this volcanic occurrence as representing the westernmost expression of the Basin and Range extension in northern México. The field (Figure 1) forms a Y-shaped bay along the Pacific coast of Baja California Norte, approximately 260 km south of the México - United States border. It consists of 10 discrete complexes dominated by cinder cones with both aa and pahoehoe flows. Our study provides helium determinations for flows from 9 of these centers. There is evidence of subaqueous eruptions building subaerially to shield-type cones as the bases to later developing cinder-type cone and flow deposits. A possible 11<sup>th</sup> complex is partially exposed in a seacliff west of Basu. Luhr and others (1995) have completed detailed mapping, identifying 41 different eruptive units. According to their stratigraphic assessment, the complexes are (from oldest to youngest): Ceniza, Riveroll, Kenton, Woodford, Basu, Media Luna, Isla San Martín, Sudoeste, Monte Mazo, and Picacho Vizcaíno. For ease of correlation, we have adopted the field-based sample designations made by Luhr *et al.* (1995) as part of our sample names (e.g. Media Luna Flow B is "LBL" whereas a lava lake associated with Woodford Cone C is "WC").

## ANALYTICAL METHODS AND RESULTS

Well-preserved breach-flow or lava lake surface samples were analyzed for 9 of the volcanic centers (Figure 1). In some instances, several surfaces from a single flow were collected. Noble gases were determined (Table 1) for olivine + clinopyroxene mixtures separated from these surfaces. Sample locations and descriptions are provided in Table 2. For analytical procedures, see Anthony and Poths (1992) and Laughlin and others (1994).

The concentration and isotopic compositions of helium and neon were determined for the trapped component by crushing approximately 0.3 grams of mineral separates on-line to a Nier mass spectrometer. The resulting powder was melted under vacuum, releasing a mixture of cosmogenic and residual trapped components. In several cases, additional powder splits were crushed off-line in a nitrogen atmosphere to increase the amount of powder later run in the furnace. The number of packages melted is reflected in the total weights provided in Table 1: one equals about 0.3 g, two yields closer to 0.5 g and three hold roughly 0.8 g. Cosmogenic  $^3\text{He}$  was determined by subtracting the trapped values from the total  $^3\text{He}$  released during the melt procedure. This trapped helium was assumed to be equal to the amount of  $^4\text{He}$  released in the melt step



## San Quintín Volcanic Field

### Baja California Norte

### México

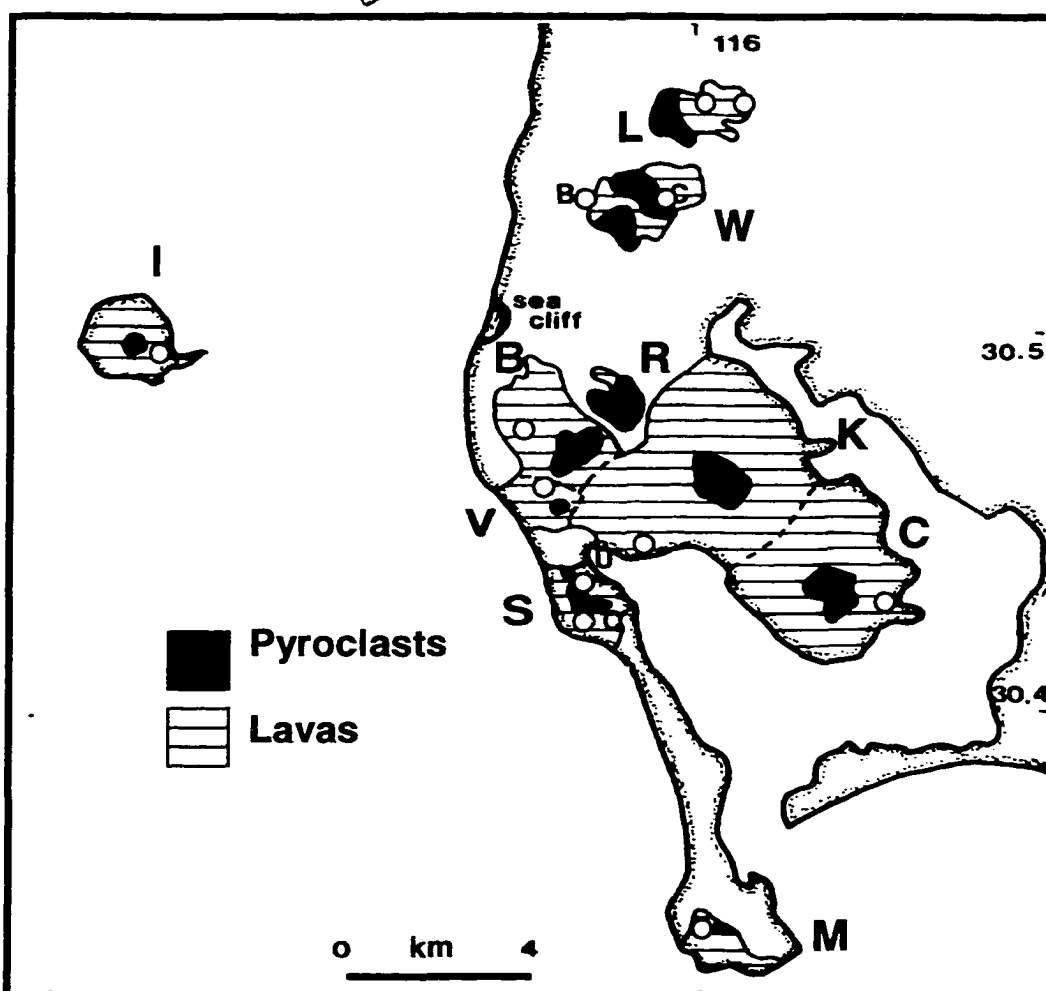


Figure 1. Local map of the San Quintín volcanic field, Baja California Norte, México. Pyroclasts indicate scoria cone positions. Complexes present: L – Media Luna; W – Woodford; B – Basu; V – Picacho Vizcaíno; S – Sudoeste; M – Monte Mazo; K – Kenton; C – Ceniza; and I – Isla San Martín. (Modified from Luhr *et al.*, 1995).

multiplied by the  $^3\text{He}/^4\text{He}$  released in the crush step. The correction for trapped helium ranged from 6% to 38%, however values are typically either approximately 10 % or 30 %.

All data in Table 1 have been corrected for mass discrimination and blank. Errors are reported as one sigma analytical uncertainties. The concentration of cosmogenic  $^3\text{He}$  and the dates include propagated uncertainties for analysis, blank and correction for the trapped  $^3\text{He}$  in the melt step. The trapped  $^3\text{He}/^4\text{He}$  values vary for different flows and therefore have not been averaged for the trapped correction. We have used production rates based on work by Cerling and Craig (1994): a value of 440 atoms/grams/year at 1445 m and 39°N latitude, adjusted for latitude and altitude using the work of Lal (1991). Production of  $^3\text{He}$  in olivine and clinopyroxene was assumed identical within analytical error, based upon conclusions drawn by Laughlin and others (1994). We have further decreased the production rate by 18% to incorporate the recalibration of the  $^{14}\text{C}$  timescale by Bard *et al.* (1990).

There are two types of averaging included in Table 1. In the case of two surfaces collected several meters apart on the same Media Luna flow "B", the line associated with sample LBL1+2#1 presents weighted averages for the two separate crush-melt analyses of LBL1#1 and LBL2#1. In contrast, dates

Table 1. Noble gases for cosmogenic helium dates from olivine and clinopyroxene fractions.

Sample	Crush			Melt							
	<sup>4</sup> He mol/g	R/R <sub>a</sub>	<sup>20</sup> Ne 10 <sup>-10</sup> mol/g	Wt g	[ <sup>4</sup> He] mol/g	[ <sup>1</sup> He <sub>c</sub> ] mol/g	[ <sup>3</sup> He <sub>c</sub> ] atoms/g	<sup>3</sup> He Prod Rate atoms g <sup>-1</sup> yr <sup>-1</sup>	<sup>3</sup> He Dates (ka)		
<i>Medla Luna</i>											
LBL1#1	7.88E-09 +/- 2.37E-10	8.45 +/- 2.26	3.17 +/- 0.19	0.2707	4.18E-09 +/- 2.2E-10	4.74E-13 +/- 5.58E-14	1.19E+07 +/- 1.59E+06	102	125 +/- 15		
LBL2#1	2.60E-08 +/- 7.81E-10	5.15 +/- 0.96	5.48 +/- 0.21	0.4763	4.45E-09 +/- 2.3E-10	3.85E-13 +/- 4.11E-14	9.78E+06 +/- 1.14E+06	102	149 +/- 25		
LBL1+2#1*	1.69E-08 +/- 3.60E-10	6.8 +/- 1.14	4.33 +/- 0.14		4.32E-09 +/- 1.6E-10	4.30E-13 +/- 3.42E-14	1.08E+07 +/- 9.60E+05				
<i>Woodford</i>											
WBL1#1	2.69E-08 +/- 7.77E-10	4.89 +/- 0.92	6.03 +/- 0.25								
WBL1#2	1.86E-08 +/- 5.69E-10	6.48 +/- 1.18	3.76 +/- 0.19								
WBL1#1+2**	2.23E-08 +/- 4.72E-10	5.69 +/- 0.74	4.90 +/- 0.18	0.5251	1.28E-08 +/- 6.6E-10	7.07E-13 +/- 4.98E-14	1.69E+07 +/- 1.40E+06	102	173 +/- 14		
WC1#1	1.84E-09 +/- 5.62E-11	10.13 +/- 6.71	1.94 +/- 0.10								
WC1#2	2.61E-09 +/- 7.64E-11	2.19 +/- 4.70	2.88 +/- 0.18								
WC1#1+2**	2.18E-09 +/- 4.69E-11	6.16 +/- 4.03	2.41 +/- 0.10	0.5789	2.91E-09 +/- 1.7E-10	3.52E-13 +/- 3.51E-14	9.01E+06 +/- 1.06E+06	107	89 +/- 10		
<i>Basu</i>											
BAL1#1	3.60E-08 +/- 1.05E-09	7.13 +/- 0.84	4.69 +/- 0.22	0.5452	2.62E-08 +/- 1.3E-09	6.87E-13 +/- 4.95E-14	1.17E+07 +/- 1.52E+06	104	118 +/- 15		
<i>Picacho Vizcalno</i>											
VBL1#1	7.26E-09 +/- 2.19E-10	8.36 +/- 2.18	1.18 +/- 0.14	0.8214	2.79E-09 +/- 1.4E-10	1.13E-13 +/- 1.68E-14	2.27E+06 +/- 5.23E+05	104	23 +/- 5		
<i>Sudoestre</i>											
SUL1#1	2.12E-08 +/- 6.36E-10	7.41 +/- 1.07	1.54 +/- 0.14	0.8610	5.04E-09 +/- 2.5E-10	1.52E-13 +/- 1.75E-14	2.79E+06 +/- 5.18E+05	102	29 +/- 5		
<i>Monte Mazo</i>											
MXL1#1	2.69E-09 +/- 8.16E-11	3.30 +/- 4.83	9.52 +/- 0.34								
MXL1#2	2.01E-09 +/- 6.12E-11	0.62 +/- 6.42	3.52 +/- 0.18								
MXL1#1+2**	2.35E-09 +/- 5.05E-11	1.91 +/- 3.98	6.52 +/- 0.18								
<i>Kenton</i>											
KDL1#1	1.93E-08 +/- 5.80E-10	5.63 +/- 1.14	5.12 +/- 0.24	0.5506	1.99E-08 +/- 1.0E-09	6.94E-13 +/- 4.73E-14	1.51E+07 +/- 1.54E+06	104	151 +/- 15		
<i>Ceniza</i>											
CCL1#1	3.36E-08 +/- 1.01E-09	6.08 +/- 0.79	2.30 +/- 0.13								
CCL1#2	2.67E-08 +/- 8.02E-10	5.93 +/- 0.95	2.79 +/- 0.13								
CCL1#1+2**	3.02E-08 +/- 6.40E-10	6.01 +/- 0.61	2.55 +/- 0.09	0.5275	2.29E-08 +/- 1.1E-09	6.80E-13 +/- 5.06E-14	1.30E+07 +/- 1.50E+06	104	131 +/- 15		
<i>Isla San Martin</i>											
ICL2#1	9.31E-09 +/- 2.80E-10	4.01 +/- 1.75	2.42 +/- 0.16	0.8214	1.32E-09 +/- 1.1E-10	1.22E-13 +/- 1.66E-14	3.19E+06 +/- 4.70E+05	104	32 +/- 5		

\* Averages for the two samples collected from different locations on the same lava surface.

\*\*Averages for crusher splits of the same sample collected.

These values were propagated through melt calculations since both powder splits were combined for the single furnace analysis .



derived for Woodford (flows “B” and “C”) and Ceniza were done using powders crushed as two separate on-line analyses (for example, splits WBL1#1 and WBL1#2) that were then combined as two packages for one furnace analysis. The two separate crush data were combined as a weighted average for propagation into the melt-step spreadsheets. We determined one surface exposure date using these average values with the singular-run melt data (WBL1#1+2 yields  $165 \pm 13$  ka, for instance).

We have determined eruption dates from  $165 \pm 13$  ka to  $22 \pm 5$  ka (Figure 2, Table 2). From oldest to youngest, they include: Woodford (flow “B”;  $165 \pm 13$  ka), Kenton ( $145 \pm 14$  ka), Ceniza ( $125 \pm 14$  ka), Basu ( $113 \pm 14$  ka), Media Luna (two dates from the same surface average  $106 \pm 9$  ka), Woodford (flow “C”;  $84 \pm 10$  ka), Isla San Martín ( $31 \pm 4$  ka), Sudoeste ( $27 \pm 5$  ka), and Picacho Vizcaíno ( $22 \pm 5$  ka).

## **DISCUSSION**

Field observations of cone and flow geomorphology (Luhr *et al.*, 1995) and results of this geochronologic study (Figure 2) combined suggest that two major episodes of volcanic activity occurred along roughly parallel lineations trending

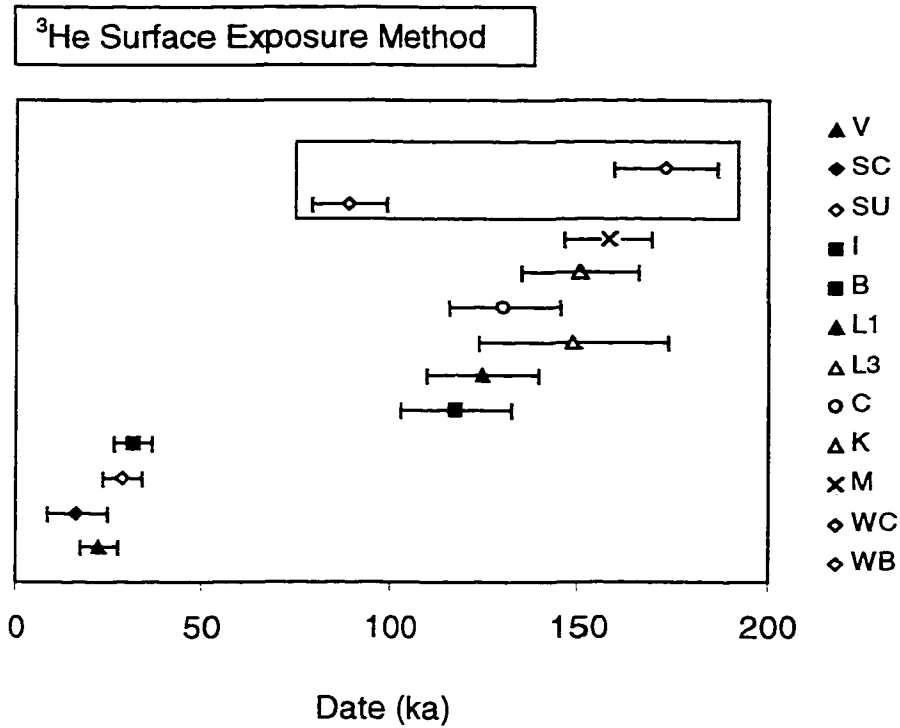


Figure 2.  $^3\text{He}$  surface exposure date determinations by complex. Abbreviations same as in Figure 1. Box identifies distinct polycyclic activity at the Woodford complex. Yellow hashures denote lack of eruption activity. Complex abbreviations in Figure 1 caption: first letter for center name, second letter for distinctly separate flow unit.

Table 2. Sample Descriptions and  $^{40}\text{Ar}/^{39}\text{Ar}$  Information

$^3\text{He}$ Date	Latitude	Longitude	Elevation*	$\rho$	Thickness	OI **	$^{40}\text{Ar}/^{39}\text{Ar}^*$ **
Sample	(North)	(West)	(meters)	(g/ cc)	(cm)	(%)	(ka)
<u>Media Luna</u>							
LBL1	30° 32.7'	115° 59.8'	20	2.6	5.0	75	90 +/- 10
LBL2	30° 33.0'	115° 59.5'	20	2.1	5.0	90	90 +/- 10
<u>Woodford</u>							
WBL1	30° 31.7'	116° 01.0'	20	2.9	4.5	80	
WC1	30° 31.9'	116° 00.8'	80	1.7	5.0	75	
<u>Basu</u>							
BAL1	30° 28.3'	116° 01.3'	40	1.4	5.0	100	
<u>Picacho</u>							
<u>Vizcaíno</u>							
VBL1	30° 28.1'	116° 02.1'	40	2.5	6.0	95	
<u>Sudoeste</u>							
SUL1	30° 26.9'	116° 01.6'	20	2.4	5.0	70	
<u>Monte Mazo</u>							
MXL1	30° 22.2'	115 ° 59.9'	20	2.3	5.0	83	
<u>Kenton</u>							
KDL1	30° 27.5'	116° 01.4'	40	2.4	6.0	100	126 +/- 8
<u>Ceniza</u>							
CCL1	30° 26.4'	115° 58.0'	40	2.3	5.0	90	
<u>Isla San</u>							
<u>Martín</u>							
ICL2	30° 29.2'	116° 06.5'	45	2.4	5.0	75	

\* Determined from topographic sheets. Except Isla, where a map is not Available. This elevation was determined using a Brunton Compass transit siting from sample location to sea level (within line of sight), combined with estimated map distances then calculated using trigonometry).

\*\* Mixtures of olivine and clinopyroxene phenocrysts.

\*\*\*Determinations by Berkeley Geochronology Laboratory (Luhr *et al.*, 1995).

roughly N40°W. Further, eruptions within a trend appear to have occurred synchronously. The older series includes: Woodford (“WBL”), Kenton (“KDL”), Ceniza (“CCL”), Basu (“BAL”), Media Luna (“LBL”), and Woodford (“WC”; lava lake surface). The younger, outboard series comprises Isla San Martín (ICL), Sudoeste (“SUL”) and Picacho Vizcaíno (“VBL”). We would like to note that there is very good agreement between the stratigraphic order resolved by these two studies, illustrating that good mapping is still essential for thorough geologic assessments of Quaternary volcanism.

The data plotted as Figure 2 indicates volcanic quiescence for roughly 50 ka. L1 and L2 are two samples from the same Media Luna flow surface collected over 50 meters apart, demonstrating reproducibility on this pahoehoe surface sample. The determinations for this flow agree within 1  $\sigma$ . WB and WC are two samples (breach flow and lava lake surface, respectively) from two different cones within the Woodford complex. The dates for these can be resolved as two distinctly separate eruption events (denoted by the significant time gap between them).

If the two determinations for the Woodford complex represent dates from well-preserved surfaces (which we believe they do), then there have been multiple eruptions from a single mafic volcanic center separated by a time gap discernible within the resolution of the helium technique. According to Luhr *et al.*

(1995), Monte Mazo and Picacho Vizcaíno each only have 2 eruptive units. The other 7 complexes we sampled, though, have from 4 to 8 distinguishable units each. We believe that several of these would also have polycyclic activity discernable with the  $^3\text{He}$  surface exposure dating technique. Kenton, Ceniza and Sudoeste are similar to Woodford in that they have geomorphic characteristics supporting significant time has passed between eruptions within each center. These volcanoes would be good candidates for further study of polycyclic development of mafic edifices.

Three surfaces were sampled from flows with argon dates performed by the Berkeley Geochronology Center (published in Luhr *et al.* (1995)).  $^3\text{He}$  to  $^{40}\text{Ar}/^{39}\text{Ar}$  dating for the field yields agreement within the uncertainties of these two dating methods. A weighted average of two surfaces from the same flow at Media Luna yields a cosmogenic date of  $106 \pm 9$  ka in comparison to the argon determination of  $90 \pm 10$  ka. Similarly, our determination for the Kenton flow is  $145 \pm 14$  ka, whereas the argon date is  $126 \pm 8$  ka.

The low  $^3\text{He}/^4\text{He}$  trapped components for this volcanic field may reflect a crustal contribution of helium. Geochemical and isotopic signatures previously documented for some of the centers support incorporation of crustal

components by ascending magmas. Luhr and others (1995) cite low Ce/Pb,  $\epsilon_{Nd}$ , and  $^{206}\text{Pb}/^{204}\text{Pb}$  in combination with high  $^{87}\text{Sr}/^{86}\text{Sr}$  values as evidence of crustal contamination of Monte Mazo and Ceniza magmas. Lavas from those two centers and the other 7 centers we analyzed yield  $^3\text{He}/^4\text{He}$  values ranging from  $4.9 \pm 0.9 R/R_a$  to  $7.4 \pm 1.1 R/R_a$  (Table 1), which may reflect addition of crustal helium ( $<0.1 R/R_a$ ) to melts derived from a MORB ( $8 \pm 1 R/R_a$ ) source. If it is crustal contamination with a helium contribution, then all of the lavas show some degree of decoupling from Sr, Nd, Pb, and trace elements. The San Quintín trapped component determinations do overlap within analytical error, however; the weighted average is  $5.52 \pm 2.42 R/R_a$ . If melts did not assimilate crust, then another possibility is that the low  $R/R_a$  values may reflect a non-MORB mantle source beneath this field. Whether the average value or individual  $R/R_a$  values for this field are considered, the trapped component composition may likewise represent the low end of the range reported by Graham and others (1992) for MORB (rather than a crustal signature).

## CONCLUSIONS

- 1) Lavas from 9 volcanic complexes within the San Quintín volcanic field in México, yield helium surface exposure dates between  $165 \pm 13$  ka and

- 22 ± 5 ka (1 σ). Their spatial distributions suggest eruption activity along two sub-parallel lineations trending N40°W. The older series erupted approximately 50 ka before the younger, outboard series. There is also evidence of synchronous eruption activity within each series.
- 2) We have documented a time gap discernible within the resolution of the helium technique. Data for two flows fed by two separate cinder cones in the Woodford complex provide quantitative geochronologic evidence for polycyclic activity at a Quaternary mafic volcanic center.
  - 3) <sup>3</sup>He and <sup>40</sup>Ar/<sup>39</sup>Ar dates for this field agree within the uncertainties of the two dating methods.
  - 4) Trapped components range from 4.9 ± 0.9 R/R<sub>a</sub> to 7.4 ± 1.1 R/R<sub>a</sub>, which is lower than most MORB-source values.

## **ACKNOWLEDGMENTS**

This study constitutes a part of WJWW's doctoral research at the University of Texas at El Paso. We thank WJWW's advisor, Elizabeth Y. Anthony, for her contributions. We also thank Jim F. Luhr, Jose J. Aranda-Gomez and Todd B. Housh for accompanying WJWW in the field to assure samples collected would correspond to their recently published study. Joseph G. Miller helped with

sample preparation at the University of Texas at El Paso. William Phillips and Joseph Banar provided valuable analytical support while WJWW used the Nier Noble Gas Mass Spectrometer at Los Alamos National Laboratory. This material is based in part upon work supported by the Texas Advanced Research Program under Grant No. 003661-010 to E.Y. Anthony. Our work is also supported by the U.S. Department of Energy (JP) and the Association of Western Universities, Inc. (WJWW).

## REFERENCES

- Anthony, E., and Poths, J., 1992,  $^3\text{He}$  surface exposure dating and its implications for magma evolution in the Potrillo volcanic field, Rio Grande rift, New Mexico, USA: *Geochimica et Cosmochimica Acta*, v. 56, p. 4105 - 4108.
- Bard, E., Hamelin, B., Fairbanks, R. G., and Zindler, A., 1990, Calibration of the  $^{14}\text{C}$  timescale over the past 30,000 years using mass spectrometric U-Th ages from Barbados corals: *Nature*, v. 345, p. 405 - 410.
- Cerling, T., 1990, Dating geomorphic surfaces using cosmogenic  $^3\text{He}$ : *Quaternary Research*, v.33, p. 148 - 156.
- Cerling, T., and Craig, H., 1994, Cosmogenic  $^3\text{He}$  production rates from 39°N to



46°N latitude, western USA and France: *Geochimica et Cosmochimica Acta*, v. 57, p. 249 - 255.

Craig, H., and Poreda, R., 1986, Cosmogenic  $^3\text{He}$  in terrestrial rocks: The summit lavas of Maui: *National Academy of Sciences Proceedings*, v. 83, p. 1970 - 1974.

Kurz, M.D., 1986a, Cosmogenic helium in a terrestrial igneous rock: *Nature*, v. 320, p. 435 - 439.

Kurz, M. D., 1986b, In situ production of terrestrial cosmogenic helium and some applications to geochronology: *Geochimica et Cosmochimica Acta*, v. 50, p. 2855 - 2862.

Kurz, M. D., Colodner, D., Trull, T. W., Moore, R. B., and O'Brien, K., 1990, Cosmic ray exposure dating with in situ produced cosmogenic  $^3\text{He}$ : Results from young Hawaiian lava flows: *Earth and Planetary Science Letters*, v. 97, p. 177 - 189.

Graham, D. W., Jenkins, W. J., Schilling, J.-G., Thompson, G., Kurz, M. D., and Humphris, S. E., 1992, Helium isotope geochemistry of mid-ocean ridge basalts from the South Atlantic: *Earth and Planetary Science Letters*, v. 110, p. 133 - 147.

Lal, D., 1991, Cosmic ray labeling of erosion surfaces: In situ nuclide production rates and erosion models: *Earth and Planetary Science Letters*, v. 104, p. 424 - 439.

- Laughlin, A. W., Poths, J., Healey, H. A., Reneau, S., and WoldeGabriel, G., 1994, Dating of Quaternary basalts using the cosmogenic  $^3\text{He}$  and  $^{14}\text{C}$  methods with implications for excess  $^{40}\text{Ar}$ : *Geology*, v. 22, p. 135 - 138.
- Luhr, J. F., Aranda-Gómez, J. J., and Housh, T. B., 1995, San Quintín volcanic field, Baja California Norte, México: geology, petrology, and geochemistry: *Journal of Geophysical Research*, v. 100, n. B7, p. 10,353 - 10,380.
- Marti, K., and Craig, H., 1987, Cosmic-ray produced neon and helium in the summit lavas of Maui: *Nature*, v. 325, p. 335 - 337.
- Poreda, R. J., and Cerling, T. E., 1992, Cosmogenic neon in recent lavas from the western United States: *Geophysical Research Letters*, v. 19, p. 1863 - 1866.
- Woodford, A. O., 1928, The San Quintín volcanic field, lower California: *American Journal of Science*, v. 15, p. 493 - 573.

Table 2. Sample Descriptions and  $^{40}\text{Ar}/^{39}\text{Ar}$  Information

$^3\text{He}$ Date	Latitude	Longitude	Elevation*	$\rho$	Thickness	OI **	$^{40}\text{Ar}/^{39}\text{Ar}^{**}$
Sample	(North)	(West)	(meters)	(g/cc)	(cm)	(%)	(ka)
<u>Media Luna</u>							
LBL1	30° 32.7'	115° 59.8'	20	2.6	5.0	75	90 +/- 10
LBL2	30° 33.0'	115° 59.5'	20	2.1	5.0	90	90 +/- 10
<u>Woodford</u>							
WBL1	30° 31.7'	116° 01.0'	20	2.9	4.5	80	
WC1	30° 31.9'	116° 00.8'	80	1.7	5.0	75	
<u>Basu</u>							
BAL1	30° 28.3'	116° 01.3'	40	1.4	5.0	100	
<u>Picacho</u>							
<u>Vizcaíno</u>							
VBL1	30° 28.1'	116° 02.1'	40	2.5	6.0	95	
<u>Sudoeste</u>							
SUL1	30° 26.9'	116° 01.6'	20	2.4	5.0	70	
<u>Monte Mazo</u>							
MXL1	30° 22.2'	115 ° 59.9'	20	2.3	5.0	83	
<u>Kenton</u>							
KDL1	30° 27.5'	116° 01.4'	40	2.4	6.0	100	126 +/- 8
<u>Ceniza</u>							
CCL1	30° 26.4'	115° 58.0'	40	2.3	5.0	90	
<u>Isla San</u>							
<u>Martín</u>							
ICL2	30° 29.2'	116° 06.5'	45	2.4	5.0	75	

\* Determined from topographic sheets. Except Isla, where a map is not Available. This elevation was determined using a Brunton Compass transit siting from sample location to sea level (within line of sight), combined with estimated map distances then calculated using trigonometry).

\*\* Mixtures of olivine and clinopyroxene phenocrysts.

\*\*\*Determinations by Berkeley Geochronology Laboratory (Luhr *et al.*, 1995).

## ***CURRICULUM VITAE***

Wendi Joan Whitehead was born on 10 January 1963 in Panama City, Florida, U.S.A. The first child to Donald G. and Joan C. Whitehead, she demonstrated the propensity toward the earth sciences in pre-school, making the most of baking mud pies and collecting shiny natural baubles. Wendi graduated from Western Hills High School in Fort Worth, Texas, in 1981. She attended Texas Christian University and Tarrant County Junior College then transferred into the Geology Program at the University of Texas in Arlington. There she discovered the wonders of things petrologic and jumped both feet into volcanoes. She was included in "Who's Who in American Colleges and Universities" and was active in the campus' Science Constituency Council.

After earning her Bachelor's of Science in Geology in 1985, Wendi married, adding yet another "W" to her name, and relocated to southern California. It is there that she gained experience as a geologist with a consulting business, then returned to pursue a Master's of Science degree in the Geosciences through the University of California at Riverside with Advisor Dr. Mike McKibben. Her research topic involved characterizing hydrothermal gold deposits hosted by Miocene felsic volcanic deposits, but did have opportunity to assist in research concerning active geothermal systems; her degree was conferred in December 1992. Wendi then joined Riverside County as an Engineering Geologist, now jumping with both feet into backhoe trenches to

study the San Andreas fault and associated features with the interests of public safety in mind.

In 1992, Wendi entered the Graduate School at The University of Texas at El Paso as a Patricia Roberts Harris Fellow. In 1995, Wendi relocated to Austin and joined the efforts of colleagues at Austin Community College. It was then she coordinated a Texas team of educators from the community college, UT-Austin, Texas Bureau of Economic Geology and local independent school districts that was selected by the Geological Society of America to participate in their Earth and Space Science Technological Education Project.

Wendi is presently teaching at North Harris College in Houston and has been awarded a Partnership in Energy and Technology Education Internship for curriculum development. She will join with high school faculty and staff at the Big Thicket National Preserve to develop field-enriched activities according to the National Science Standards.

Above all else, Wendi's greatest joy to date is being the wife of Jeffrey Lynn Williams and mother of Sarah Gayle, who's arrival improved their existence in 1996. Fingerpaints, giggles, and all.

Permanent Address:       15911 Boulder Oakes  
                                     Houston, TX 77084

This dissertation was prepared by Wendi Williams using Microsoft Office on a PC.